Marine biogeochemical cycling during extreme climate events

Exploring the importance of benthic-pelagic processes with models

By

DOMINIK HÜLSE

School of Geographical Sciences
UNIVERSITY OF BRISTOL

A thesis submitted to the University of Bristol
in accordance with the requirements of the degree
of DOCTOR OF PHILOSOPHY in the Faculty of Science.

School of Geographical Sciences

JANUARY 2018

Word count: 65,880

Abstract

The production and degradation of organic matter (OM) in the marine realm and its removal to the sediments, exerts a dominant control on biogeochemical cycles in the ocean and, on longer timescales, atmospheric CO_2. Marine surface sediments are key components in this inter-connected system as they host the largest carbon reservoir within the surficial Earth system, provide the primary long term sink for atmospheric CO_2 and recycle nutrients. Despite this fundamental importance most Earth system models either neglect sediment dynamics or treat them in a very simplistic way. For this reason OMEN-SED, a new, one-dimensional analytical early diagenetic model resolving OM cycling and associated biogeochemical dynamics in marine sediments is developed. OMEN-SED is able to reproduce observed pore water profiles across a wide range of depositional environments and simulated terminal electron acceptor fluxes fall well within the range of observed fluxes. Coupled to the Earth system model cGENIE, the model captures global patterns of surface sediment OM content, oxygen penetration depths and biogeochemical reaction rates. The new model framework is applied to study the most prominent oceanic anoxic event during the Cretaceous (OAE2). Model simulations reveal: (1) the importance of benthic-pelagic coupling for the development of ocean anoxia and euxinia, (2) biogeochemical feedbacks in the marine system lead to significantly enhanced OM preservation, (3) observed patterns of OM-rich black shales are reproduced by the model and (4) rapid OM sulfurization in the water column has the potential to intensify OM burial. Coupled to an Earth system model, OMEN-SED is thus a powerful tool that will not only help elucidate the role of benthic-pelagic exchange processes in the evolution and, in particular, the termination of extreme climate events, but will also allow a direct comparison of model output with the sedimentary record - the most important climate archive on Earth.

ACKNOWLEDGEMENTS

Sandra and Andy, thank you so much for introducing me to biogeochemical modelling, for being inspiring and encouraging, and for giving me lots of freedom but also advice and support whenever needed. Thank you both for hosting me in either Brussels or Riverside after you both abandoned me in Bristol ;-). Thank you for sharing lovely evenings together, for letting me haul brush up a hill and for delicious baked goods which kept me alive over the last months. I really enjoy working with you!

Thank you Pierre Regnier, Guy Munhoven, Jamie Wilson and Stuart Daines for helping with editing my research manuscripts, for providing advice and ideas or for digging deep into boundary matching problems and MATLAB programming.

Thanks a lot to Andy Dale, Christof Meile, Filip Meysman, Jack Middelburg, Fanny Monteiro, Claire Reimers, Katherina Seiter and Martin Thullner for providing data sets to evaluate my model. Thank you Francesca Pianosi for opening my eyes to the power and beauty of sensitivity analysis and for implementing the SAFE toolbox (and of course for becoming a friend)!

Thanks a lot to the biogeochemical modelling group in Bristol (Fanny Monteiro, Jamie Wilson, Ros De'Ath, Sandy Kirtland-Turner and Sarah Greene) for very helpful discussions and good times in the pub and in the National Parks.

Thanks to my office mates Ciaran, Harry, Hazel and Thom. You made my Bristol experience to something very special! I will miss you guys!

Thank you Alex for becoming an amazing friend, for listening to my moaning, for understanding me better than I do it myself, for hosting me when I was homeless (again) and for kicking my ass on the trails!

Thank you Kristine for buying the whisky, for hosting me when I was homeless (again) and for being awesome!

Danke, Mama, Papa und Jenni, für euer Verständnis das mit mir Dinge doch häufiger mal anders kommen als geplant.

AUTHOR'S DECLARATION

I declare that the work in this dissertation was carried out in accordance with the requirements of the University's Regulations and Code of Practice for Research Degree Programmes and that it has not been submitted for any other academic award. Except where indicated by specific reference in the text, the work is the candidate's own work. Work done in collaboration with, or with the assistance of, others, is indicated as such. Any views expressed in the dissertation are those of the author.

SIGNED: ..... DATE: .....

TABLE OF CONTENTS

List of Tables

List of Figures

CHAPTER 1

INTRODUCTION

Contributions and acknowledgements

Section 1.1 of this chapter is adapted from a research article published in Earth-Science Reviews [Hülse et al., 2017]. All co-authors (S. Arndt, J.D. Wilson, G. Munhoven and A. Ridgwell) provided assistance with editing and advised on aspects of this work. Two anonymous referees gave insightful comments on a previous version of the published manuscript. All work presented in this chapter is my own.

1.1 Understanding the global carbon cycle and the biological carbon pump

On a wide range of geologically-relevant and resolvable time-scales, from 10^3 to $>10^6$ years, the climate system is thought to be largely driven by variations in atmospheric CO_2, itself controlled by a dynamic balance between varying CO_2 inputs from volcanoes and metamorphic alteration of rock, and the removal of CO_2 from the ocean-atmosphere system through weathering and burial of carbon in marine sediments [Fig. 1.1; Berner, 1991; Berner and Caldeira, 1997; Kump et al., 2000; Ridgwell and Zeebe, 2005]. A key motivator of paleoclimate research is hence to understand the controls, characteristic time-scales and the dynamic balance between carbon sources and sinks as well as its possible feedbacks with global climate. This endeavour rests heavily on numerical models to help quantify potential dynamic behaviours and sensitivities of responses and to test hypotheses. To be successful however, these models must include appropriate representations of the key carbon cycle processes and/or exhibit real-world relevant dynamics. To what degree this is true is the topic of the review study presented in Chapter 2 which is focused around marine

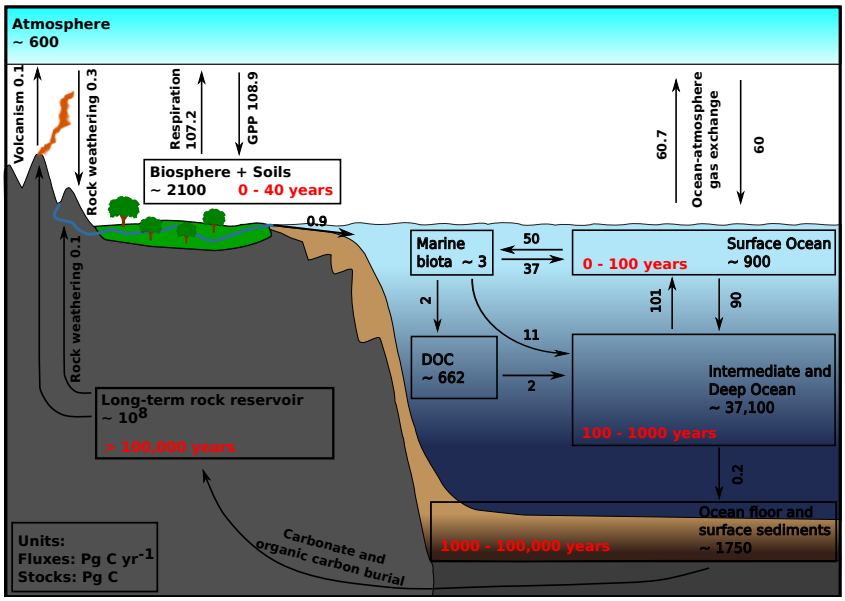

Figure 1.1: A simplified view of the global carbon cycle showing the approximate carbon stocks in Pg C and main annual fluxes in Pg C yr^{-1} for the preindustrial era (largely based on IPCC 2013 [Ciais et al., 2014] and Hain et al. [2014], GPP: Gross Primary Production). Years in red indicate the time-scales at which the reservoirs exert control on atmospheric CO_2 concentrations. Thus, the biological carbon pump in the ocean is important on time-scales shorter than about 1000 years, whereas the sediments become influential on time-scales of 1000 to 100,000 years.

carbon cycling and in particular the sequence of processes that create and transfer carbon from the ocean surface to the underlying sediments.

In the modern carbon cycle, the net transfer of CO_2 from the atmosphere to the oceans and then sediments, is primarily a direct consequence of the combined effect of the solubility and biological pump [Volk and Hoffert, 1985]. The solubility pump describes the exchange of CO_2 between ocean surface and atmosphere, and its redistribution as dissolved inorganic carbon within the ocean interior by large-scale circulation. It is estimated to account for only ~10% of the surface-to-deep gradient of (preindustrial) dissolved inorganic carbon (DIC) [Sarmiento and Gruber, 2006] and cannot itself lead to carbon removal from the surficial system. As its potential for modifying atmospheric CO_2 is limited and it mostly acts on a sub-kyr time-scale, I do not address the paleo role of this process in any detail in Chapter 2 or in this thesis. The biological carbon pump, for which I will expand on more common definitions for the geological context, refers here to both the organic and inorganic carbon fixed by primary producers in the euphotic zone, the efficiency of its transfer to the underlying ocean interior, *and* the efficiency with which it is buried in the underlying sediments [Fig. 1.2; Volk and Hoffert, 1985]. The growth of phytoplankton in the light-flooded surface layer of the global ocean removes nutrients and carbon from the water and transforms them into cellular material and/or inorganic carbonates. Upon organism death, part of this produced particulate organic and inorganic carbon (POC, PIC)

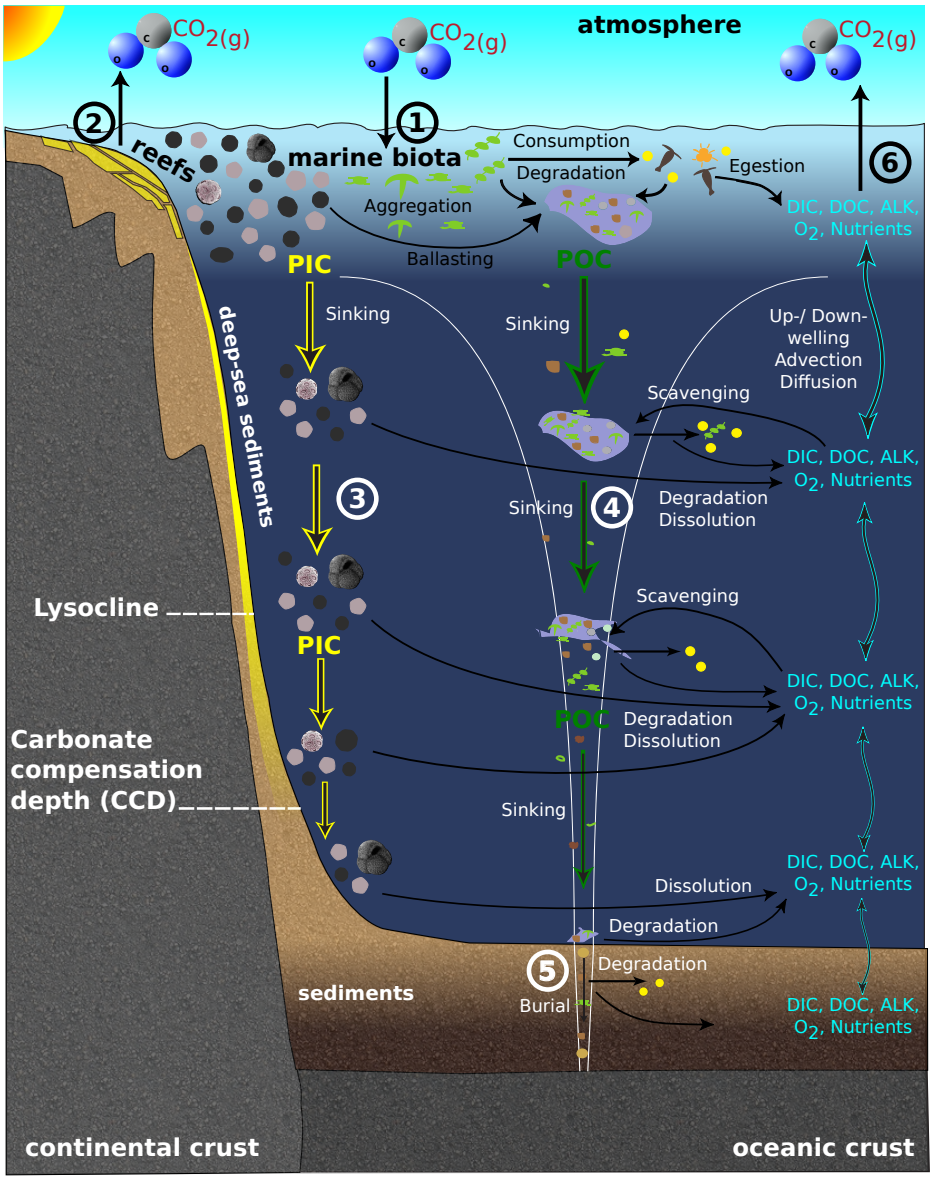

Figure 1.2: Schematic of the main processes constituting the ocean's solubility and biological pump (labelled 1 to 6). **1**: Air-sea gas exchange of CO_2, used by phytoplankton to form cellular material. Through complex recycling and aggregation pathways, agglomerations of POC and PIC are formed, heavy enough to sink out of the euphotic zone. **2**: Precipitation of $CaCO_3$ by, e.g., coccolithophores and foraminifera in the open ocean or by corals and coralline algae in the shallow-water contributing to the formation of reefal structures, resulting in higher pCO_2 at the surface and therefore a transfer of CO_2 to the atmosphere. ($Ca^{2+} + 2HCO_3^- \rightarrow CaCO_3 + CO_{2(aq)} + H_2O$). **3**: Carbonate sinking into the deeper ocean and forming deep-sea sediments. At the lysocline the rate of dissolution increases dramatically until below the CCD no $CaCO_3$ is present in the sediment any more. **4**: Vertical settling flux of POC (in combination with PIC) that decreases approximately exponentially with depth. **5**: Deposition of organic carbon in the deep sea. Only a small fraction escapes degradation and is buried in the sediments. **6**: DIC in the upper ocean is created through degradation and egestion processes and upwelling of DIC rich subsurface waters. These processes contribute to raise surface water pCO_2, driving a transfer of CO_2 to the atmosphere.

sinks out of the euphotic zone. In addition, dissolved organic carbon (DOC) is either scavenged by particle aggregates and sinks to the deep ocean or is redistributed into the deeper layers by ocean circulation. In today's well oxidised ocean a large fraction of the gross primary production of organic matter is remineralised by bacterial activity in the water column and less than ~ 0.5% of it is ultimately buried in marine sediments [Fig. 1.1 + 1.2; Burdige, 2007; Hedges and Keil, 1995; Middelburg and Meysman, 2007].

Despite intense ocean upwelling and mixing, the biological pump results in distinct ocean depth gradients of carbon, nutrients and oxygen. In particular its control on surface ocean DIC concentration, which is next to temperature, wind speed and ambient pH one of the main drivers of air-sea carbon dioxide fluxes, is of fundamental importance for the global carbon cycle and thus global climate [Volk and Hoffert, 1985]. In fact, modelling studies have shown that atmospheric CO_2 concentrations would be significantly higher above an abiotic ocean [Archer et al., 2000b; Sarmiento and Toggweiler, 1984]. Sarmiento and Gruber [2006] show that the organic part of the biological pump is responsible for about 70% and the inorganic part for 20% of the total preindustrial dissolved inorganic carbon transfer from the surface to the deeper ocean. (The remaining 10% are attributed to DIC variations driven by temperature variations, ocean mixing and the solubility pump.)

The efficiency of the biological pump depends not only on the rate of carbon fixation and export out of the surface layer, but also on the depth at which the organic and inorganic carbon is respired or dissolved. This depth determines the time during which carbon is isolated from the atmosphere and therefore atmospheric CO_2 concentration exhibits an inverse relationship to the efficiency of the biological pump [Boyd and Trull, 2007; Yamanaka and Tajika, 1996]. Estimates for global organic carbon exported from the surface to the deeper ocean are in the range of 5-11 Pg C yr^{-1} [Dunne et al., 2007; Henson et al., 2011; Laws et al., 2000]. The inorganic carbon flux is also strongly coupled to the organic carbon flux by the biologically driven carbonate precipitation and the effect of organic matter remineralisation on carbonate preservation [see Box 1 in Chapter 2 or, e.g., Hales, 2003; Ridgwell and Zeebe, 2005].

In marine sediments, carbon is buried as organic matter or carbonate minerals. As mentioned before, in today's well oxidized ocean, only a small fraction of the organic matter produced in the photic zone escapes microbial degradation and is ultimately buried and preserved in the deep sediment [e.g. Burdige, 2007; Emerson and Hedges, 1988; Middelburg and Meysman, 2007]. Nevertheless, organic matter burial rates have been shown to vary significantly through geological history [e.g., Arthur et al., 1985] and the relative fraction of the deposited organic matter that is ultimately buried can range from 0 to almost 100% across different environments [e.g., Canfield, 1994]. Most biogeochemical cycles and diagenetic reactions in the surface sediments as well as the direction and rate of sediment-water interface fluxes can be related either directly or indirectly to the degradation of organic matter [Arndt et al., 2013; Boudreau and Ruddick, 1991; Middelburg et al., 1993]. The degradation process releases reduced compounds (e.g. NH_4, H_2S) as well as

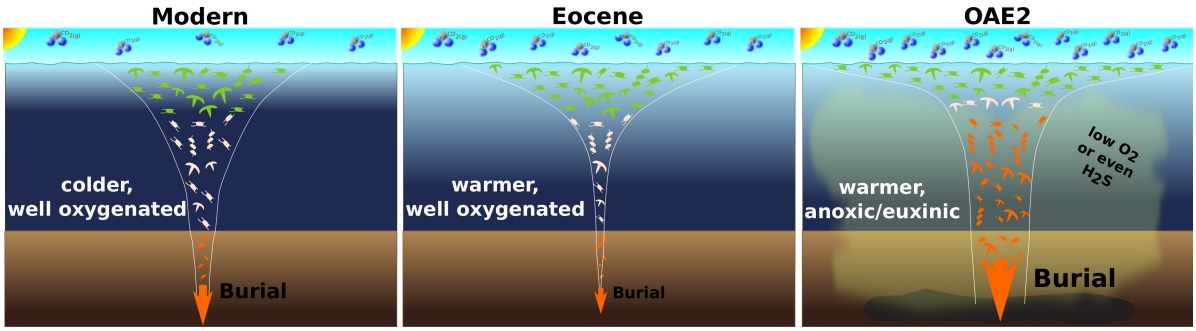

Figure 1.3: Schematic representation of the potential functioning of the biological pump in the modern world (left), during the Eocene (middle) and the oceanic anoxic event 2 (right, OAE2). There is much evidence that global mean ocean temperatures exceeded those of the modern day by several degrees during the Eocene epoch (55.5-33.7 Ma) and theory predicts that elevated temperatures should cause a decrease in the efficiency of the biological pump as sinking POC is more quickly remineralised. In contrast, during OAE2 (ca. 93.5 Ma) the ocean exhibited widespread oxygen depletion and photic zone euxinia (occurrence of hydrogen sulphide (H_2S)). At the same time the marine sediments are characterised by enhanced deposition of organic carbon-rich black layers.

DIC, alkalinity and PO_4 to the water column. On the other hand, sediments take up terminal electron acceptors (e.g. O_2, NO_3, SO_4) from the water-column which are either used to degrade organic matter or for the reoxidation of reduced compounds [e.g. Cappellen and Wang, 1996]. Therefore, the fate of organic matter in the sediments plays a crucial role for the global cycling of carbon, oxygen, phosphorus and sulphur and thus for the development of ocean anoxia and euxinia [occurrence of H_2S; Kraal et al., 2010; Van Cappellen and Ingall, 1994].

Over the geological past, the functioning and intensity of the marine carbon cycle has very likely experienced important variability linked to extreme climate events and perturbations of the global carbon cycle [compare Fig. 1.3 and e.g. John et al., 2014; Kohfeld et al., 2005; Ma et al., 2014; Sigman and Boyle, 2000]. This complex system involves a myriad of interconnected biological, chemical, and physical processes. For this reason alone, linking observations, often highly abstracted in the form of proxies, to the primary processes involved and ultimately to explanatory hypotheses for specific geological events and transitions, is challenging. The past few decades has seen a progressive improvement in theoretical and process-based understanding of the various components that make up the marine carbon cycle and hand-in-hand with this, the development of numerical model representations of the complete system [Hülse et al., 2017].

1.2 Oceanic anoxic events

As a test case for our understanding of biogeochemical dynamics under extreme conditions I use the Cenomanian-Turonian oceanic anoxic event (OAE2, ~93.5 Ma). In general, oceanic anoxic events (OAEs) represent severe disturbances of the global carbon, oxygen and nutrient cycles of

the ocean and were common during the Cretaceous period [de Graciansky et al., 1984; Jenkyns, 2010; Schlanger and Jenkyns, 1976]. The archetypal example is OAE2, which is characterized by extreme atmospheric CO_2 concentrations [Bice et al., 2006; Takashima et al., 2006], widespread bottom water anoxia [e.g., Brumsack, 2006; Goldberg et al., 2016; Owens et al., 2012] and photic zone euxinia [Kuypers et al., 2002; Pancost et al., 2004; Sinninghe Damsté and Köster, 1998]. In addition the formation of isotopically light organic carbon-rich black-shales was so increased [Stein et al., 1986] that the atmospheric and oceanic CO_2 reservoirs became relatively enriched, leading to positive excursions in the sedimentary $\delta^{13}C$ record [Arthur et al., 1987; Schlanger et al., 1987].

Although OAEs have been described more than 40 years ago [Schlanger and Jenkyns, 1976], the mechanisms triggering widespread ocean anoxia and enhanced organic carbon burial are still topics of intense debate [Jenkyns, 2010; Meyer and Kump, 2008]. One mechanism to explain the evolution of anoxia during OAE2 is increased O_2 demand due to enhanced primary productivity [Kuypers et al., 2002; Monteiro et al., 2012; Ozaki et al., 2011]. Potential nutrient sources to fuel primary productivity include elevated weathering rates due to warmer temperatures [Blättler et al., 2011; Pogge von Strandmann et al., 2013], leaching of nutrients from flooded continental shelves due to sea level rise [Jones and Jenkyns, 2001; Voigt et al., 2006] and increased hydrothermal activity associated with large-scale submarine volcanism due to the formation of the Caribbean and/or Arctic Large Igneous provinces [Du Vivier et al., 2014; Snow et al., 2005]. Once bottom waters became anoxic additional nutrient inputs may have come from marine sediments as the burial efficiency of phosphorus declines when bottom waters become anoxic [Kraal et al., 2010; Van Cappellen and Ingall, 1994]. Furthermore, Cretaceous oceans were susceptible to anoxia because of generally elevated sea-surface temperatures [Bice et al., 2006; Forster et al., 2007] and thus lower oxygen solubility in seawater. The most important feedbacks considered responsible for OAE2 are summarised in Figure 1.4.

Even though the mechanisms triggering OAE2 are still under debate, the feedbacks responsible for its termination are even more enigmatic. The Earth system has a number of possible "recovery" mechanisms through which elevated atmospheric CO_2 concentrations can be ameliorated. One way to permanently remove CO_2 from the atmosphere (and reduce O_2 demand in the ocean) is to bury carbon in the form of organic matter (OM) in marine sediments and the geological record shows that the burial of OM was more efficient during OAE2 than in the modern ocean [Arthur and Sageman, 1994; Stein et al., 1986]. A number of possible controls on enhanced OM preservation or reduced rates of OM degradation have previously been proposed and assessed, such as elevated depositional fluxes and higher clay mineral availability [Kennedy et al., 2002]. More often, the enhanced burial of organic matter is related to reduced oxygenation of the depositional environment [e.g. Demaison and Moore, 1980; Emerson, 1985; Hartnett et al., 1998] which is explained by the lower free energy gains through anaerobic degradation [LaRowe and Van Cappellen, 2011], the need for more complex bacterial consortia, reduced bioturbation

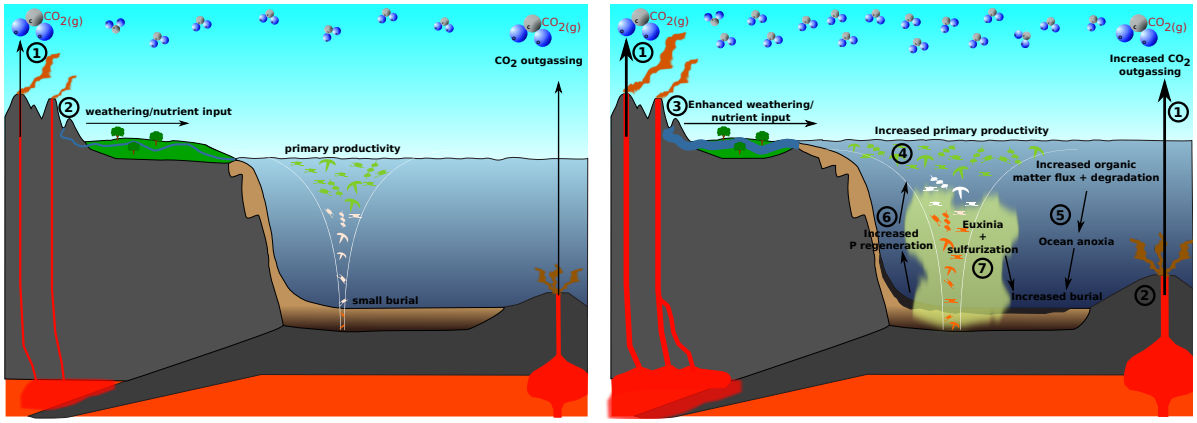

Figure 1.4: Schematic of potential feedbacks during OAE2. **Left:** Pre-OAE2, with background CO_2 outgassing (1) and nutrient input to the ocean (2). **Right:** Peak-OAE2, with increased CO_2 outgassing (1,2), enhancing the nutrient input (3) and PP (4), causing anoxia (5), this results in P regeneration from sediments (6), which in turn fuels PP (4). This further increases anoxia and develops into euxinia, which results in OM sulfurization (7) and increased OM burial, therefore oxygenating the ocean and drawing down atmospheric CO_2.

and grazing or the presence of non-hydrolyzable substrates that resist degradation, in anoxic environments [Canfield, 1994; Hedges and Keil, 1995].

Over the last decades, an additional mechanism has been proposed to explain increased organic matter burial - sulfurization [Arndt et al., 2009; Hebting et al., 2006; Sinninghe Damsté and Köster, 1998]. During organic matter sulfurization, functionalized lipids and carbohydrates react through their functional groups with reduced inorganic sulfur species (e.g. H_2S), resulting in the formation of organic sulfur compounds which are less prone to bacterial degradation [Sinninghe Damsté et al., 1989b]. Thus, under euxinic environmental conditions, sulfurisation of organic matter could be an important emergency recovery mechanism within the Earth system. Although studies indicate the global significance of this process for OAE2 [Raven et al., 2016; Werne et al., 2008], its implications on Cretaceous benthic-pelagic coupling and thus OAE2 evolution and recovery has not yet been quantified and tested with a 3D Earth system model. The reason for this knowledge gap is that an appropriate representation of the coupled atmosphere-ocean-sediment system which is able to model widespread ocean euxinia and all relevant processes and feedbacks over geological time-scales currently does not exist. The major hurdle is the high computational cost of simulating the essential redox reactions in marine sediments, which are critical to quantify OM burial rates and benthic recycling fluxes of chemical compounds.

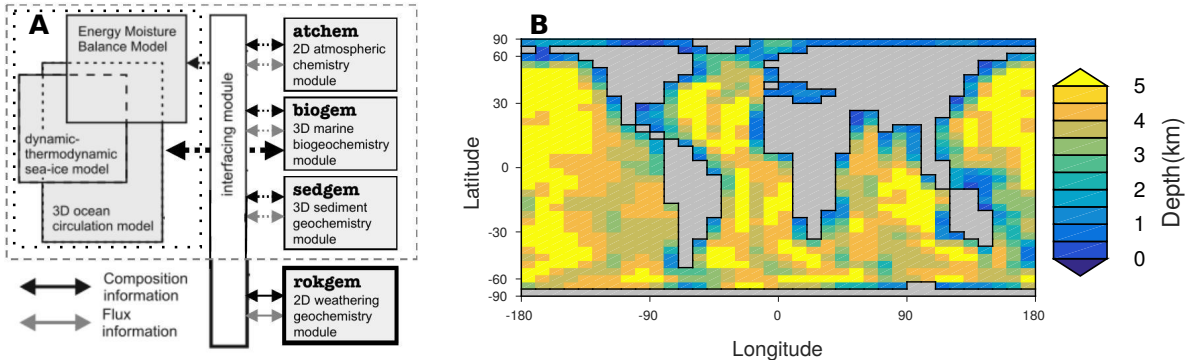

Figure 1.5: Schematic describing the relationship between the different model components comprising the cGENIE model (A) and gridded continental configuration and ocean bathymetry of the preindustrial 16-level version of cGENIE (B). **A:** Delineated by a dotted box is the underlying climate model "C-GOLDSTEIN" [Edwards and Marsh, 2005], the dashed box comprises the ocean-atmosphere-sediment carbon cycle and climate model as described in Ridgwell and Hargreaves [2007], while the weathering module RoKGeM [Colbourn et al., 2013] is outlined in bold. Figure adapted from Colbourn et al. [2013].

1.3 Numerical modelling: The cGENIE Earth system model

The carbon-centric version of the "Grid ENabled Integrated Earth system model" [cGENIE, Ridgwell and Hargreaves, 2007; Ridgwell et al., 2007] is used in this thesis. cGENIE is a model of intermediate complexity based on the "C-GOLDSTEIN" model [Edwards and Marsh, 2005; Marsh et al., 2011] which couples a 3D-ocean circulation model to a fast 2D energy-moisture balance model (EMBM) of the atmosphere and a dynamic-thermodynamic sea-ice model (Fig. 1.5A). The reduced physics ocean model produces circulation fields similar to General Circulation Models (GCMs), but is significantly faster to run [Marsh et al., 2011]. The ocean model is implemented on a 36×36 equal-area horizontal grid, resulting in 10° increments in longitude and uniform increments in sine of latitude (i.e. ~ 3.2° at the equator increasing to 19.2° in the highest latitude band). The vertical resolution is flexible and can be defined as 8 or 16 variably spaced depth levels. The grid and bathymetry for the preindustrial 16 level model setup is shown in Figure 1.5B. Temperature and salinity are the prognostic variables of C-GOLDSTEIN and its horizontal and vertical transport through advection, convection and diffusion are calculated along with the passive transport of biogeochemical tracer concentrations [Edwards and Marsh, 2005; Marsh et al., 2011]. Surface exchange of heat and moisture between the ocean, atmosphere and sea-ice is performed by the coupling scheme of the EMBM of the atmosphere [Marsh et al., 2011].

The 3-D ocean circulation model has been extended with the marine "BIOGEochemistry Model" [BIOGEM Ridgwell et al., 2007] and later with the "SEDiment GEochemistry Model" [SEDGEM Ridgwell and Hargreaves, 2007] to explore the role of ocean biogeochemistry and marine sediments within the global carbon cycle and in regulating atmospheric CO_2 concentra-

tions on multimillenial timescales. BIOGEM accounts for the biogeochemical redistribution of ocean tracers occurring by other means than ocean circulation. Therefore, biological productivity in the euphotic zone of the ocean is estimated based on the availability of light and nutrients (either with phosphate as the only limiting nutrient or a multi-nutrient description depending on phosphate, nitrate and iron). Nutrients and dissolved inorganic carbon (DIC), together with alkalinity (ALK) are removed from solution and coupled to oxygen production using canonical molar ratios [Anderson and Sarmiento, 1994; Redfield, 1963]. The resulting particulate organic and inorganic carbon (POC, PIC or calcium carbonate) is exported from the surface ocean and sinks down the water column (assuming constant sinking speed) while it is subject to degradation and dissolution, thus releasing its constituents back into solution. At the ocean floor, the remaining particulates are either entirely remineralised/dissolved or, in case the sediment module SEDGEM is coupled, PIC is incorporated in the surface layer of the sediments where it is subject to carbonate dissolution [Ridgwell and Hargreaves, 2007]. The terrestrial rock weathering model "Rock Geochemical Model" [RokGeM Colbourn et al., 2013] can then be used to close the geological cycle of carbon. As SEDGEM and RoKGeM are not in the focus of this thesis, I will not discuss these modules in further detail here. However, more information on representations of marine carbon cycling and benthic-pelagic coupling in Earth system models in general, and of cGENIE in particular, is provided in Chapter 2.

Although cGENIE represents the terrestrial-atmosphere-ocean-sediment carbon cycle the model is still computationally efficient and has been shown to simulate > 1,000 years per (2.4 GHz) CPU hour using a standard desktop PC [Ridgwell and Hargreaves, 2007]. Thus, cGENIE represents a powerful tool for sensitivity analyses using large model ensembles and for model runs of 10,000 years or more which is necessary for ocean biogeochemistry to equilibrate. However, as I discuss in Chapter 2, the representation of marine and diagenetic biogeochemistry has important limitations, particularly with respect to the lack of an appropriate representation of organic carbon degradation and related biogeochemical reactions in marine sediments. These processes are specifically important for controlling ocean oxygen, phosphate, nitrate and sulphate concentrations and enhanced organic carbon burial may have been important for the termination of OAEs occurring during Earth history [Jenkyns, 2010]. Due to the current simple parameterisation of the benthic-pelagic boundary the importance of sediment-water interface fluxes and organic carbon burial for the development and termination of these events cannot be explicitly assessed.

1.4 Objectives and outline of the thesis

The research challenge described in this thesis was to review, evaluate and extent the current state of marine carbon cycle modelling with a specific focus on the representation of benthic-pelagic coupling in paleoclimate Earth system models. The presented research thus covers four

components: (1) Chapter 2 reviews and evaluates the three dominant processes involved in the cycling of organic and inorganic carbon in the marine system and how they are represented in numerical models, namely: biological productivity at the ocean surface, remineralisation/dissolution of particulate carbon within the water column, and the benthic-pelagic coupling at the seafloor. (2) In order to address one of the main limitations in modelling marine carbon cycling as identified in Chapter 2, Chapter 3 presents the new, one-dimensional, analytical diagenetic model OMEN-SED. OMEN-SED is the first analytical model to explicitly describe organic matter cycling as well as associated dynamics of the most important terminal electron acceptors (i.e. O_2, NO_3, SO4), related reduced substances (NH_4, H_2S), the full suite of secondary-redox reactions, macronutrients (PO_4) and associated pore water quantities (ALK, DIC). An extensive sensitivity analysis is performed to identify which model parameters have the largest impact on the different model outputs. Thereafter, the stand-alone version of OMEN-SED is validated by comparing simulated pore water profiles and terminal electron acceptor fluxes with observations and results from a more complex, numerical diagenetic model. (3) Chapter 4 describes the coupling of OMEN-SED to the carbon-centric version of the "GENIE" Earth system model. Sensitivity studies with the coupled model framework are carried out and simulated organic matter concentrations in the surface sediments are compared to a global database. (4) Chapter 5 and 6 apply the new Earth system model framework to questions in the paleo-context and constrain model results with observations for seafloor anoxia, photic zone euxinia and organic matter content in the sediments. Chapter 5 investigates the importance of benthic-pelagic coupling for the development of ocean anoxia and euxinia during OAE2 and compares the new, coupled model with simpler representations of the sediments. Finally, Chapter 6 employs the new model to investigate feedbacks between water column anoxia/euxinia and enhanced organic matter preservation in Cretaceous sediments.

CHAPTER 2

UNDERSTANDING THE CAUSES AND CONSEQUENCES OF PAST MARINE CARBON CYCLING VARIABILITY THROUGH MODELS

Contributions and acknowledgements
This chapter is adapted from a research article published in Earth-Science Reviews [Hülse et al., 2017]. All co-authors (S. Arndt, J.D. Wilson, G. Munhoven and A. Ridgwell) provided assistance with editing and advised on aspects of this work. Two anonymous referees gave insightful comments on a previous version of the published manuscript. All work presented in this chapter is my own.

2.1 Introduction

The complex interplay and strong feedback between fluxes and transformations of carbon in the ocean-sediment system limit our predictive ability of the global climate system and its evolution throughout Earth's history and critically disguise the underlying physical and biogeochemical process interplay behind our paleo observations that simply reflect the net process outcome [Falkowski et al., 2000]. Appropriate mathematical models can help as they allow us to elucidate the various rates of biogeochemical processes and related fluxes that comprise the net result (ideally, but rarely, quite equal to the observation). They also present the opportunity to formally and quantitatively test hypotheses that arise from observations. Furthermore, they allow us to explore and discover behaviours and dynamics that may not necessarily have ever occurred in Earth history, or more usefully, behaviours and dynamics that we did not *a priori* suspect were taking place until their possibility was revealed by a model.

The great challenge in successfully applying paleoclimate models arises because of practical

temporal and spatial constraints on computation, unconstrained and uncertain boundary conditions, but also simply because of the lack of mechanistic knowledge. It is impossible therefore for paleoclimate (or indeed, any) models to capture the full complexity of the complete carbon cycle, at least not perfectly [Cox et al., 2000; Friedlingstein et al., 2006, 2003]. Simplification is necessary and ideally would be based on a sound mechanistic understanding of the underlying processes and be consistent and traceable between models. Instead, the choices of how to parameterise processes and which processes to neglect altogether, vary between models and can depend on the specific questions or paleo events being addressed. It is hence critical that we have a good understanding of the consequences of these choices and what the implications are for the degree of confidence we can draw from model results when applied in the paleo realm. Particular care is needed in respect of the applicability of parametrisations that are derived from observations of the present-day ocean-sediment system because environmental conditions may be very different during past extreme events (compare Fig. 1.3).

Unlike in the case of modern [IPCC, Randall et al., 2007] and past climate dynamics [PMIP, whose aim is to test the ability of General Circulation Models (GCMs) to reproduce feedbacks and large changes in the climate system, e.g. Kageyama et al., 2016; Lunt et al., 2017], there has not yet been any systematic review study of the marine carbon cycle dynamics represented in paleoclimate models, a process which could help to substantially upgrade the performance of these models and raise the degree of confidence in their results. The geologic context also requires sediment dynamics to be considered, a component not typically considered as part of the biological carbon pump, as benthic-pelagic coupling plays an important role for carbon cycling and Earth's recovery from global warming events, especially on longer time-scales (>1000 years; Fig. 1.1). Conversely, to simplify the analysis, we omit shorter time-scale processes that impact upon the biological carbon pump such as ocean circulation, which at least in the modern/future context, are discussed in detail elsewhere [e.g. IPCC, Ciais et al., 2014]. Furthermore, this study does not aim to provide an exhaustive review of all critical aspects of ocean biogeochemistry, particularly since facets such as the marine iron cycle and its influence on the biological pump are relatively poorly studied and represented even in models of the modern ocean [Tagliabue et al., 2016]. Instead, we focus on the core behaviours and dynamics of three key aspects of marine organic and inorganic carbon cycling and their encapsulation into Earth system models: biological productivity at the ocean surface, remineralisation/dissolution of carbon within the water column and the benthic-pelagic coupling at the seafloor. The crux of the issue addressed here is then the range of formulations used to represent these key carbon cycle processes and the resulting divergence of predictions for carbon cycle change under different boundary conditions, such as increased global temperatures, ocean anoxia or euxinia (Fig. 1.3).

The structure of this chapter is as follows. First, different types of paleoclimate models are presented and compared; and an overview for their characteristic time-scales of application is given (Section 2.2). Thereafter, the focus of the chapter is on reviewing the three key processes

of the biological carbon pump and evaluating their representation in paleoclimate models by testing their ability to predict the response of carbon cycling under different extreme climate conditions (Section 2.3). The final part (Section 2.4), highlights the importance for applying models of different complexities, and summarises two key outstanding modelling issues.

2.2 Overview of numerical models commonly employed in paleoclimate research

Numerical models are essential tools that help us to understand the complex Earth system dynamics, including how climate and the biological pump have changed in the past and how they may evolve in the future [see e.g. Alverson et al., 2003; McGuffie and Henderson-Sellers, 2005; Randall et al., 2007]. Existing Earth system models vary considerably in complexity from highly parametrised conceptual models (e.g., box models) to comprehensive coupled General Circulation Models (GCMs), with different scientific questions often being tackled with different model approaches. Writing a fully comprehensive review of all available models including a representation of the biological pump would be an impossible task and quickly out of date. We have hence chosen to focus on more computationally efficient models, such as box models (Section 2.2.1) and intermediate complexity models (Section 2.2.2), which include a minimum set of components representing the biological carbon pump. Furthermore, the particular models we include have all been used to study biogeochemical cycling for some interval in Earth history and have generated simulations that span order 10^4 years or more (and thus are able to model processes involving the deep ocean and the marine sediments). We hence omit higher resolution ocean models and fully coupled GCMs, that while encompassing sophisticated representations of ocean biogeochemistry and circulation and describing many details of fluxes between the ocean-atmosphere systems [see e.g. Washington and Parkinson, 2005], generally focus on time scales of a few thousands of years or less, and generally do not take into account sediment processes (examples of GCMs that have been used for paleo studies with a focus on the biological pump are: MPIOM, Heinze and Ilyina [2015] and CCSM3, Winguth et al. [2012]).

Historically, paleoclimate models with a focus on the ocean's biological pump have evolved along two distinct paths. Global carbon cycle box models were designed around simplified multi-box or advection-diffusion models of the ocean circulation and global carbon cycling, while Earth System Models of Intermediate Complexity [EMICs; Claussen et al., 2002] can be considered as coarse resolution Earth system models [e.g. Eby et al., 2013]. We hence make a distinction between the two and discuss them largely separately. Box models and EMICs can also mostly be separated by the general absence of explicit climate feedback with carbon cycling in the former, and inclusion in the latter (see Table 2.1 and 2.2), although most EMICs include few of the atmospheric feedbacks (e.g. internal climate oscillations such as ENSO, changes with climate in wind strength and zonal position, cloud cover and albedo) that fully coupled GCMs can be

thought of as specializing in.

2.2.1 Global carbon cycle box models

Global carbon cycle box models (GCCBMs) are a very conceptualised representations of the Earth system that focus on the global carbon cycle and are employed to test hypotheses and to quantify large scale processes. Due to their high computational efficiency they allow the investigation of long-term dynamics in the Earth system and its biogeochemical evolution (compare Fig. 2.1). Sarmiento and Toggweiler [1984] for instance, simulated with a simple 4-box model of the ocean-atmosphere the substantial influence of high latitude surface ocean productivity and thermohaline overturning rate on atmospheric CO_2 fluctuations during glacial-interglacial cycles. However, GCCBMs incorporate highly simplified representations of both the atmosphere and ocean systems with the notable exception of the GEOCLIM family of models which use the biogeochemical ocean-atmosphere model COMBINE [Goddéris and Joachimski, 2004] and couple it to the three-dimensional climate model FOAM [Donnadieu et al., 2006a]. In general, the atmosphere is encapsulated into a simple one-box model and atmospheric processes are reduced to simple gas and sometimes heat exchange [e.g., DCESS Shaffer et al., 2008]. Without a fully-resolved atmosphere, the upper oceanic boundary conditions (wind stress, heat flux, equilibrium state with fixed boundary conditions and fresh-water flux) can also not be defined in a physically rigorous way. Therefore, the representation of ocean circulation in these models is highly parametrised and ranges from simple multi-box models with prescribed exchange fluxes [e.g., BICYCLE, Köhler et al., 2005] to advection-diffusion box models (e.g. DCESS, Shaffer et al. [2008]; GEOCLIM *reloaded*, Arndt et al. [2011]). Ice sheet dynamics are generally neglected due to the simplicity of the ocean-atmosphere models. Terrestrial vegetation and weathering fluxes are generally integrated in form of simplified rate laws [e.g., BICYCLE; Köhler et al., 2005].

2.2.2 Earth system Models of Intermediate Complexity

Earth system Models of Intermediate Complexity (EMICs) have been developed to close the gap between the computationally efficient, but conceptual box models and the computationally expensive general circulation models [Claussen et al., 2002]. The first EMIC-like models that already included and coupled important parts of the Earth system were developed in the early 1980s [Chalikov and Verbitsky, 1984; Petoukhov, 1980]. The spatial resolution of EMICs is coarser than that of "state-of-the-art" GCMs. However, they explicitly simulate, in an interactive mode, the basic components of the Earth system, including the atmosphere, ocean, cryosphere and land masses, over a very wide range of temporal scales, from a season to hundreds of thousands and even millions of years. In addition, EMICs include, although often in parametrised form, most of the processes described in GCMs [Claussen et al., 2002]. On the other hand, they are efficient enough to resolve climate dynamics on the event-scale (kyrs) and are thus especially useful for the study of paleoclimate dynamics since they allow exploring the complex behaviour of Earth's

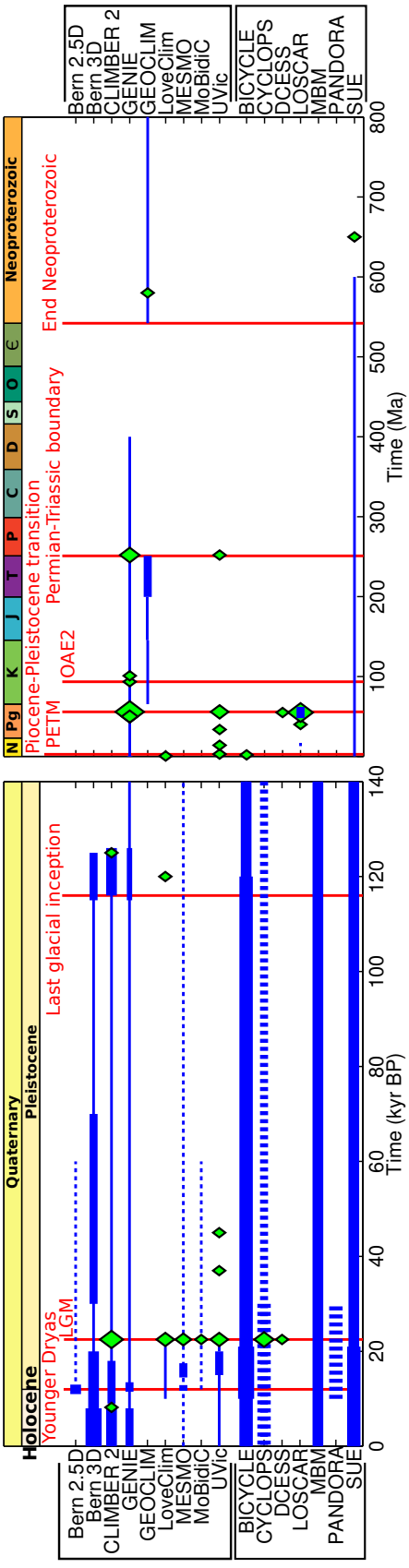

Figure 2.1: Timeline for EMIC and Earth system box model applications. Diamonds represent steady-state studies, solid lines display transient simulations for the specific time period and dotted lines steady-state studies for the respective period without a specified time. The size of the diamonds and thickness of the lines reflect the number of studies for this time period (also compare Table A.1). The geological timescale abbreviations for the periods are: N: Neogene, Pg: Paleogene, K: Cretaceous, J: Jurassic, T: Triassic, P: Permian, C: Carboniferous, D: Devonian, S: Silurian, O: Ordovician, ∈: Cambrian. Note the change of timescale!

climate system as an integrated multi-component system with non-linearly coupled processes. Often EMICs incorporate more sub-component models (e.g. sediments) and climatic variables than GCMs [Petoukhov et al., 2005]. Furthermore, they facilitate large ensemble experiments needed for climate sensitivity studies to external forcings [e.g. Dalan et al., 2005; Goodwin et al., 2009] and can provide guidance for more detailed investigations using more complex GCMs. Also, due to their fast computation, EMICs are able to integrate long-term processes like carbonate preservation in marine sediments [Ridgwell and Hargreaves, 2007; Tschumi et al., 2011] which is important for regulating atmospheric CO_2 concentrations on time-scales of thousands to tens of thousands of years [Ridgwell and Zeebe, 2005]. The model design is generally driven by the underlying scientific questions, the considered temporal and spatial scales, as well as by the expertise of the research group. As a consequence, different components of the climate system are described with different levels of complexity. Most EMICs emerged from comprehensive, dynamic climate models that were used to study contemporary climate change and thus rely on sophisticated coupled ocean-atmosphere GCMs with integrated ice sheet dynamics [e.g. McGuffie and Henderson-Sellers, 2005]. Terrestrial vegetation and weathering dynamics in EMICs are often included on the basis of dynamic models (such as VECODE in CLIMBER-2; Brovkin et al., 2002a; or RoKGeM in GENIE; Colbourn et al., 2013, respectively). A major caveat of many existing models is the lack of a sophisticated sedimentary biogeochemical model for organic carbon (compare Section 2.3.3). Notable exceptions are Bern 3D which includes a vertically-integrated, dynamic model considering oxic degradation and denitrification of organic carbon [Tschumi et al., 2011]; the box model MBM, integrating a vertically-resolved advection-diffusion-reaction model for solid and solute species [MEDUSA, Munhoven, 2007]; and DCESS, using a semi-analytical, iterative approach considering (oxic and anoxic) organic matter remineralisation [Shaffer et al., 2008].

2.3 Overview of the primary processes involved in marine carbon cycling

Over the geological past, the intensity of the biological pump has probably experienced significant spatial and temporal variability that can be directly linked to perturbations of the global carbon cycle and climate [e.g. John et al., 2014; Kohfeld et al., 2005; Ma et al., 2014; Sigman and Boyle, 2000]. Therefore, the description of the biological carbon pump exerts an important control on the performance and predictive abilities of Earth system models. Simulating the ocean's carbon pump is made difficult by the plethora of processes that govern the formation of particulate organic and inorganic carbon (POC, PIC) and dissolved organic carbon (DOC) in the euphotic zone, its export to depth and its subsequent degradation, dissolution or burial in the sediments. Unlike for ocean circulation, a fundamental set of first principle equations that govern nutrient cycling still remains to be defined, assuming they even exist. Thus a wide range

Table 2.1: Overview of EMICs mentioned in this study and their characteristics related to the biological pump.

Models	Ocean Model	Ocean Carbon Cycle			Sediments
	Resolution	Surface Production	Tracers	Degradation	
EMICs					
Bern 2.5D	Zonally averaged, 3-basin circulation model, 14 vertical layers Marchal et al. (1998)	Michaelis-Menten kinetics, PO_4 limiting nutrient and relation to temperature. Marchal et al. (1999)	DOC, DIC, C, $\delta^{13}C$, $\delta^{14}C$, PO_4, ALK, O_2, $CaCO_3$; Marchal et al. (1998b)	Power law (Martin)	No sediment representation
Bern 3D	3-D, horizontal 36x36 equal area boxes, 10°x(3.2-19.2)°, 32 vertical layers; Müller et al. (2006)	Fully coupled carbon cycle, Michaelis-Menten nutrient uptake kinetics, limited by PO_4, Fe and light. Parekh et al. (2008); Tschumi et al. (2008)	CFC-11, PO_4, DOP, DIC, DOC, $\delta^{13}C$, $\delta^{14}C$, $\delta^{39}Ar$, Ar, ALK, O_2, FeT; Müller et al. (2008), Parekh et al. (2008)	Power law (Martin)	Vertically integrated, dynamic model of top 10cm: oxic respiration and denitrification. $CaCO_3$, opal, POM, clay and DIC, ALK, PO_4, NO_3, O_2, silicic acid; Tschumi et al. (2011)
CLIMBER-2	3 zonally averaged basins, 2.5° (meridional), 20 vertical layers	Fully coupled carbon cycle (HAMOCC3) + ecosystem model, Six and Maier-Reimer (1996)	DIC, DOC, PO_4, O_2, Alkalinity, silicate, isotopes (^{12}C, ^{13}C,^{14}C, ^{39}A), $\delta^{18}O$; Brovkin et al. (2002)	Power law (Suess)	$CaCO_3$ model with oxic-only sediment respiration (Archer, 1996a)
GENIE	3-D, horizontal 36x36 equal area boxes, 10° x (3.2-19.2)°, 8/16 vertical layers	Fully coupled carbon cycle, Michaelis-Menten nutrient uptake kinetics, limited by PO_4, NO_3, Fe and light, Ridgwell et al. (2007)	Ca. 56 dissolved and various solid tracers; see www.seao2.info/mycgenie.html	Double Exponential / Temp dependent / Power Law / Ballasting	Vertically integrated model: u.a. $CaCO_3$, detrital material, $\delta^{13}C$, $\delta^{14}C$; Ridgwell and Hargreaves (2007)
GEOCLIM	3 zonally averaged basins, 2.5° (meridional), 20 vertical layers (uses CLIMBER-2)	Fully coupled carbon cycle model, PO_4 limiting nutrient (using COMBINE, Goddéris and Joachimski (2004))	PIC, POC, PO_4, O_2, DIC, ALK, pH, $\delta^{13}C$, $\delta^{18}O$, Ca^{2+}, $CaCO_3$	Recycling rate linear function of $[O_2]$	Simple org. C, P model (COMBINE): oxic layer (C:P ratio ~ $[O_2]$) and constant sulfate reduction zone; Goddéris and Joachimski (2004)
LOVECLIM	3-D, 3° x 3°, 30 vertical layers; Goosse et al. (2010)	Fully coupled carbon cycle; LOCH:Mouchet and Francois (1996); rain ratio depends on silica, tmp, $CaCO_3$)	DIC, Alkalinity, dissolved inorganic phosphorous, DOC, POC, O_2, org. and inorg. $\delta^{13}C$, $\delta^{18}O$, $CaCO_3$, silica, opal	Power law (Martin)	Constant part of POC & PIC is preserved; Goosse et al. (2010)
MESMO	3-D, horizontal 36x36 equal area boxes, 10° x (3.2-19.2)°, 16 vertical layers	Fully coupled carbon cycle, Michaelis-Menten nutrient uptake kinetics, limited by PO_4, NO_3, CO_2, Fe, light and tmp; Matsumoto et al. (2008)	CFC-11, NO_3, N*, ^{15}N, PO_4, O_2, DIC, $CaCO_3$, ALK, POC, DOC, $\delta^{13}C$, ^{14}C	Temp dependent	Vertically integrated model: u.a. $CaCO_3$, detrital material, $\delta^{13}C$, $\delta^{14}C$; Ridgwell and Hargreaves (2007)
MoBidiC	3 zonally averaged basins, 5° (meridional), 19 vertical layers	Fully coupled carbon-cycle, PO_4 limiting nutrient, Michaelis-Menten kinetics, Crucifix, (2005)	DIC, DI^{13}C, DOC, DO^{13}C, ALK, PO_4,O_2, ^{14}C, POC, $CaCO_3$	Single exponential	No sediment representation
UVic	3-D, 1.86° (meridional) x 3.6° (zonal), 19 vertical layers	Fully coupled carbon cycle + NPZD ecosystem representation + dynamic iron cycle; e.g. Schmittner et al. (2008), Keller et al. (2012), Nickelsen et al. (2015)	Phytoplankton (nitrogen fixers and others), NO_3, PO_4, O_2, DIC, $CaCO_3$, ALK, zooplankton, particulate detritus, POC, DOC, $\delta^{13}C$, $\delta^{18}O$, Fe, Fe_p	Single exponential	$CaCO_3$ model with oxic-only sediment respiration (Archer, 1996a)

Glossary				
	Circulation & Temp feedback; reduced complexity atm. GCM	Ecological model	Double exponential / Temp dependent	Vertically integrated, organic and inorganic carbon burial
	Circulation & Temp feedback; highly simplified or basic dynamics atm.	Export production model (10 or more tracers)	Power law or single exponential	Vertically integrated inorganic carbon burial - no organic carbon burial
	No or simplified feedbacks (e.g. weathering)	Export production model (less than 10 tracers) or simpler model	Linear/fixed fraction	Constant preservation

Table 2.2: Overview of global carbon cycle box models mentioned in this study and their characteristics related to the biological pump (Glossary of Table 2.1 applies here as well).

Models	Ocean Model	Ocean Carbon Cycle			Sediments
	Resolution	Surface Production	Tracers	Degradation	
Box models					
BICYCLE	10 homogeneous boxes (5 surface, 2 intermediate, 3, deep); Köhler et al. (2005)	Fixed fraction of PO_4, Munhoven and François (1996)	PIC, POC, PO_4, O_2, DIC, ALK, $\delta^{13}C$, $\delta^{14}C$	Fixed fraction	No sediment representation or restoration of prescribed lysocline or $[CO_3^{2-}]$
CYCLOPS	14/13 homogeneous boxes, e.g. Keir 1988, 1990; later 18 boxes, Hain et al. 2010	Fixed fraction of PO_4 depending on latitude, Keir (1988)	PO_4, O_2, DIC, ALK, $\delta^{13}C$, $\delta^{14}C$, POC, $CaCO_3$	Fixed fraction depending on latitude	1. Similar to LOSCAR (but const. porosity); 2. Respiration driven $CaCO_3$ dissolution, Sigman et al. (1996)
DCESS	2 x 55 boxes, 1 hemisphere, 100m vertical resolution, Shaffer et al. 2008	Export production model, PO4 limiting nutrient, Yamanaka and Tajika (1996)	POC, PO_4, O_2, DIC, ALK, $^{12,13,14}C$, $CaCO_3$	Single exponential	Semi-analytical, oxic respiration and denitrification, $CaCO_3$, Shaffer et al. 2008
LOSCAR	10 homogeneous boxes for modern ocean (13 e.g. for the P/E-version)	Biological uptake using Michaelis-Menten kinetics, PO_4 limiting nutrient	TCO_2, TA, PO_4, O_2, $\delta^{13}C$, pH, Mg/Ca	Fixed fraction	%$CaCO_3$ in the bioturbated layer as a fct. of sediment rain, dissolution, burial and chemical erosion - also variable porosity
MBM	10 homogeneous boxes (5 surface, 2 intermediate, 3, deep)	Similar to BICYCLE	DIC, TA, PO_4, O_2, CO_2, $\delta^{13}C$,$\delta^{14}C$, OM, calcite, aragonite	Power law (Martin)	Advection-diffusion-reaction model MEDUSA: solids (clay, calcite, aragonite, OM), solutes (CO_2, HCO_3, CO_3, O_2)
PANDORA	10/11 homogeneous boxes, e.g. Broecker and Peng (1986, 1987)	Limiting nutrients (PO_4, NO_3) with diff. residence times per box	PO_4, NO_3, O_2, DIC, ALK, $\delta^{13}C$, $\delta^{14}C$, POC, silica, $CaCO_3$, ^{39}Ar, ^3He, $^{13}C/^{12}C$	Fixed fraction	No sediment representation
SUE	Uses set-up of Bern 2.5D or PANDORA model	Export production model (siliceous and non-siliceous phytoplankton), limiting nutrients (PO_4, H_4SiO_4, Fe); Ridgwell (2001)	PO_4, H_4SiO_4, Fe, DIC, ALK, O_2, $CaCO_3$, POC, opal, DOM, $^{12,13}C$, $^{16,17,18}O$	Single exponential	$CaCO_3$ and opal as fct. of saturation state, Ridgwell et al. (2002), Archer (1991)

of model approaches of varying sophistication have been put forward for specific problems [e.g. Bacastow and Maier-Reimer, 1990; Maier-Reimer, 1993; Najjar et al., 1992; Sarmiento et al., 1993; Six and Maier-Reimer, 1996]. The following sections critically review important processes of the biological pump and their representation in paleoclimate models. They are separated into biological production in the surface ocean (2.3.1), carbon dynamics in the deeper ocean (2.3.2) and benthic processes (2.3.3). The numerical representations are generally described moving from simple/empirical to more dynamic/mechanistic approaches. Even though the silica cycle is strongly interrelated with the biological pump [e.g. opal as a ballasting material; Klaas and Archer, 2002] we limit our review to carbon containing compounds and refer the interested reader to Ragueneau et al. [2000] and Tréguer and Rocha [2013] for reviews on the ocean silica cycle.

2.3.1 Biological production

Biological production is controlled by the availability of light, nutrients, and trace metals, as well as phytoplankton speciation, temperature, and grazing. At steady state, nutrients removed from surface waters in the form of descending particulate matter are balanced by the upward advective and diffusive supply of dissolved nutrients that support new production in surface waters [Eppley and Peterson, 1979]. The production of PIC, POC and DOC in the surface ocean is

Export Production Models

Najjar et al. (1992); Maier-Reimer (1993); Yamanaka and Tajika (1996):

$$F_{\mathrm{POC}}(z) = (1-\delta)\cdot\int_0^{z_{\mathrm{eup}}} k_{\max}\cdot(NU-NU^*)dz \qquad \text{if} \quad NU > NU^* \tag{1}$$

$$F_{\mathrm{POC}}(z) = 0 \qquad \text{if} \quad NU \leq NU^*$$

or

$$F_{\mathrm{TOC}}(z) = \int_0^{z_{\mathrm{eup}}} k_{\max}\cdot\frac{NU}{NU+K_{\mathrm{NU}}}dz \tag{2}$$

$$F_{\mathrm{POC}}(z) = (1-\delta)\cdot F_{\mathrm{TOC}}(z) \tag{3}$$

$$F_{\mathrm{DOC}}(z) = \delta\cdot F_{\mathrm{TOC}}(z) \tag{4}$$

$$F_{\mathrm{PIC}}(z) = r_{\mathrm{PIC/POC}}\cdot F_{\mathrm{POC}}(z) \tag{5}$$

Biological Models

Mouchet and Francois (1996):

$$F_{\mathrm{POC}}(z) = \int_0^{z_{\mathrm{eup}}}\left(g_{\max}\cdot\frac{P}{P+K_{\mathrm{P}}}+d_{\mathrm{Ph}}\right)dz \tag{6}$$

$$F_{\mathrm{DOC}}(z) = 0$$

$$F_{\mathrm{PIC}}(z) = r_{\mathrm{PIC/POC}}\cdot F_{\mathrm{POC}}(z) \tag{7}$$

Six and Maier-Reimer (1996) (or similarly Schmittner et al., 2005):

$$F_{\mathrm{POC}}(z) = \int_0^{z_{\mathrm{eup}}}\left((1-\varepsilon_{\mathrm{her}})G\frac{P-P_{\min}}{P+P_0}Z + d_{\mathrm{Ph}}(P-P_{\min}) + (1-\varepsilon_{\mathrm{can}})d_{\mathrm{Zo}}(Z-Z_{\min})\right)dz \tag{8}$$

$$F_{\mathrm{DOC}}(z) = \int_0^{z_{\mathrm{eup}}}\left(\gamma_P(P-P_{\min})+\gamma_Z(Z-Z_{\min})\right)dz \tag{9}$$

$$F_{\mathrm{PIC}}(z) = r_{\mathrm{PIC/POC}}\cdot F_{\mathrm{POC}}(z) \tag{10}$$

Glossary

z	Water depth	z_{eup}	Bottom of euphotic zone
F_{A}	Flux of A	TOC	Total Organic Carbon
δ	Fraction of produced DOC	$k_{\max}$	Max. production rate
NU	Simulated nutrient concent.	NU^*	Fixed nutrient concentration
K_{NU}, K_P	Michaelis-Menten term	$r_{\mathrm{PIC/POC}}$	Rain ratio
$g_{\max}$	Max. grazing rate	d_{Ph}, d_{Zo}	Specific mortality rate
$(1-\varepsilon_{\mathrm{her}})$	Egestion as fecal pellets from herbivores	$(1-\varepsilon_{\mathrm{can}})$	Egestion as fecal pellets from carnivores
G	Available biomass	$P_{(\min)}$	(Min) phytoplankton concentration
P_0	Half-saturation concentration for phytoplankton ingestion		
$Z_{(\min)}$	(Min) zooplankton concentration	γ_P, γ_Z	Excretion rate of DOC

Figure 2.2: Overview of model approaches that are applied in paleoclimate models to calculate surface ocean production/export production.

thus driven by complex recycling and transformation pathways within the euphotic ecosystem [e.g. Sarmiento and Gruber, 2006]. High data requirements, excessive computational demands, as well as the limited transferability of existing comprehensive ecosystem model approaches to the geological timescale compromise the application of these models in a paleo-context. Therefore, paleoclimate models generally treat surface ocean biogeochemical dynamics in a simplified way (see Fig. 2.2 for an overview).

2.3.1.1 Organic carbon production

Model approaches can be broadly divided into two different classes (Fig. 2.2). A first class of models simply relates the whole-community export production directly to the availability of nutrients within the euphotic zone using either a nutrient restoration scheme towards a fixed concentration distribution [NU^*, e.g. Najjar et al., 1992], or a Michaelis-Menten term for uptake kinetics [e.g. Maier-Reimer, 1993]. These export production models sometimes account for the more refractory DOC pools by assuming that a fixed fraction, δ, of the produced carbon is converted to DOC in the production zone. The second class of models explicitly resolves, although in a very reduced and simplified way, part of the biological complexity that drives carbon production in the euphotic zone [Keller et al., 2012; Mouchet and François, 1996; Six and Maier-Reimer, 1996]. In these models, the export production is driven by a pool of phytoplankton whose growth is controlled by the availability of nutrients, light, as well as temperature. Upon death, organisms feed the fast sinking particulate organic carbon pool and POC export production is thus determined by grazing and mortality rates. The biological model of Mouchet and François [1996] applies a simple maximum grazing rate with a Michaelis-Menten term that allows for a non-linear closure of the system. Six and Maier-Reimer [1996] on the other hand explicitly resolve the dynamics of nutrients, phytoplankton, zooplankton and detritus (NPZD-model) in the euphotic layer and account for the production of fecal pellets by both carnivors and herbivores. Furthermore, their model assumes that DOC is produced by exudation from phytoplankton and zooplankton excretion.

All global carbon cycle box models integrate a simple export production model including highly parametrised maximum production terms, since their low spatial resolution does not permit the resolution of latitudinal temperature and light variations. Some EMICs also apply simple export production models, however, the maximum export production depends here on the ambient temperature and/or light conditions. The UVic model, CLIMBER-2 and LOVECLIM have more complex biological schemes, following Keller et al. [2012], Six and Maier-Reimer [1996] and Mouchet and François [1996], respectively. Although there is still a controversy about nitrogen or phosphorus being the ultimate limiter of oceanic primary production at geological time-scales [Falkowski et al., 1998; Smith, 1984; Tyrrell, 1999], most paleoclimate models estimate export production directly from available surface phosphate concentrations, implicitly assuming that nitrogen fixation compensates for a potential nitrogen limitation.

2.3.1.2 Pelagic calcium carbonate production

Box 1: Calcium carbonate thermodynamics primer

One of the most common minerals on Earth is calcium carbonate ($CaCO_3$) which is almost exclusively formed by biological processes. In the ocean $CaCO_3$ most commonly exists in two crystal forms: *calcite* and *aragonite*. Because calcite is the more thermodynamically stable phase it is more abundant in the ocean and forms almost all deep sea carbonate sediments. Aragonite, on the other hand, is found in shallow-water sediments (e.g. corals). Carbonate precipitation can be described by the following chemical reaction:

$$Ca^{2+} + 2HCO_3^- \rightarrow CaCO_3 + CO_{2(aq)} + H_2O$$

Whether $CaCO_3$ precipitates or dissolves can be directly linked to the concentrations of Ca^{2+} and CO_3^{2-} in sea-water which controls the stability of its crystal structure [Ridgwell and Zeebe, 2005]. This is expressed as the *saturation state* Ω of the solution and is defined as

$$\Omega = [Ca^{2+}] \times [CO_3^{2-}]/K_{sp},$$

where K_{sp} is a solubility constant which scales with increasing pressure [Zeebe and Wolf-Gladrow, 2001]. Calcium carbonate is thermodynamically favourable to precipitate at $\Omega > 1$ (i.e. in oversaturated environments) and prone to dissolution when Ω is smaller than unity. The saturation state of the ocean generally decreases with water depth in response to the combined effects of the pressure-induced increase in the solubility constant and the release of CO_2 through the degradation of sinking POC that decreases the ambient pH and thus the carbonate ion concentration [Ridgwell and Zeebe, 2005; Soetaert et al., 2007]. Oceanic waters become undersaturated (i.e. $\Omega < 1$) below the depth of the *saturation horizon* (i.e. $\Omega = 1$) and carbonates start to dissolve. However, the process of dissolution proceeds only extremely slowly in the beginning. The depth at which the dissolution rate increases considerably and impacts become noticeable is known as the *lysocline* [Broecker, 2003] (sometimes defined at $\Omega = 0.8$, Milliman et al. [1999]). Deeper still, the rate of dissolution becomes fast enough to exactly balance the rate of supply of carbonates to the sediments and therefore no carbonates are preserved. This is termed the *carbonate compensation depth* (CCD) (compare Fig. 1.2).

Today, the surface ocean is largely oversaturated with respect to carbonate phases [see Box 1 for a carbonate primer; Ridgwell and Zeebe, 2005]. Nevertheless, due to the kinetically unfavourable initial step of crystal nucleation, abiotic carbonate precipitation is rare and only occurs in extreme environments as cements or ooids [e.g. Morse and He, 1993; Schneider et al., 2006]. In the open ocean, the most important groups for the production of calcium carbonate ($CaCO_3$) are marine organisms like coccolithophores, foraminifera and pteropods. These three groups are responsible for up to 70% of global $CaCO_3$ precipitation [Milliman and Droxler, 1996]. Coccolithophores are a group of algae (mostly unicellular) that form an outer sphere of small calcite crystals, known as coccoliths. The other two groups are heterotrophic zooplankton. Foraminifera form skeletons made out of calcite and pteropods, a general term for a group of molluscs, produce crystals made out of aragonite (the thermodynamically less stable form of

calcium carbonate).

As these biological processes and their links to ocean geochemistry are very complex, most paleoclimate models calculate marine carbonate export production as a fixed fraction of POC export production [the $r_{\mathrm{PIC/POC}}$ "rain ratio", compare Fig. 2.2 and e.g. Yamanaka and Tajika, 1996]. However, there is no simple means of deriving the value of $r_{\mathrm{PIC/POC}}$ as it is highly dependent on the local ecosystem structure [Shaffer, 1993]. Paleoclimate models that integrate biological models generally apply a formulation that relates the rain ratio to the ecosystem structure. Otherwise, highly parametrised formulations on the basis of ambient temperature conditions [e.g. Archer et al., 2000b; Heinze et al., 1999; Maier-Reimer, 1993; Sarmiento et al., 2002] or the saturation state with respect to calcite are used [Arndt et al., 2011; Ridgwell et al., 2007]. Only a small number of paleoclimate models distinguish between calcite and aragonite fractions as most of the global PIC export is driven by low-Mg calcite from coccolithophores and foraminifera [Iglesias-Rodriguez et al., 2002; Morse et al., 2007]. The aragonite cycle is still poorly quantified and therefore, its rain ratio is considered in a few models only: LOCH/LOVECLIM [Mouchet and François, 1996], MBM [Munhoven, 2007; Munhoven and François, 1996], and optionally in Bern 3D [Gangstø et al., 2011]. Estimates for the fraction of aragonitic pteropods or heteropods in the global ocean carbonate rain are in the range of 10–50% [Berner, 1977; Berner and Honjo, 1981; Fabry, 1989].

2.3.2 Carbon (re)cycling in the ocean interior

The remineralisation of biogenic particles exported from the surface ocean redistributes carbon and nutrients in the ocean exerting an important influence on atmospheric CO_2 levels. Changes in the depth-distribution of POC remineralisation controls the sequestration of CO_2 in the water column on time-scales of decades to centuries [Kwon et al., 2009] whereas changes in the ratio of POC to $CaCO_3$ in fluxes reaching the sediment may change CO_2 over thousands to millions of years [Archer and Maier-Reimer, 1994; Roth et al., 2014]. However, despite considerable effort to identify potential processes that control the fate of organic carbon in water column (e.g., Joint Global Ocean Flux Study [JGOFS, Buesseler and Boyd, 2009]; VERtical Transport In the Global Ocean [VERTIGO, Trull et al., 2008]), the key processes are still not well understood [Boyd and Trull, 2007].

2.3.2.1 Particulate Organic Carbon

2.3.2.1.1 Observations Field observations across the global ocean show that a large fraction of particulate organic carbon is efficiently degraded by bacterial activity as it sinks through the water column and that the recycling process is exponentially faster in the mesopelagic layers of the ocean than in the deeper ocean [e.g. Honjo et al., 2008; Lutz et al., 2002; Martin et al., 1987, compare Fig. 1.2 and 2.4]. This is generally explained with either increasing particle sinking speeds with depths [Berelson, 2001] or a decrease in organic matter reactivity with

depth/age because as POC sinks, labile organic components are degraded more readily, leaving more refractory material behind [e.g. Dauwe et al., 1999]. However, the overall importance of this so-called selective preservation remains disputed [e.g. Gupta et al., 2007; Hedges et al., 2001], and little is known about the mechanistic control on decreasing organic matter degradability during sinking. Other mechanisms, such as physical protection [e.g. Keil and Hedges, 1993] likely also contribute to decreasing organic matter reactivity. Compilations of globally distributed sediment trap data show that the rate of attenuation with depth varies generally with latitude. However, very little is known about what controls this geographical variability and different observations are seemingly inconsistent [see e.g. Henson et al., 2012; Marsay et al., 2015]. Various mechanisms have been postulated to explain these spatial patterns, focusing again on either changes in the sinking rate or the degradation rate of POC.

As the density of typical organic matter ($\sim$1.05 g cm^{-3}, Logan and Hunt [1987]) is close to that of seawater ($\sim$1.02–1.03 g/cm^{-3}) POC needs to aggregate or a source of weight in order to contribute significantly to the organic matter flux to the deep ocean. Strong global correlations between inorganic minerals (such as $CaCO_3$, opal and lithogenic material) and POC fluxes in the deep ocean led to the hypothesis that the denser minerals increased the density, and therefore sinking rate, of POC (the "ballast hypothesis") [Armstrong et al., 2001; Klaas and Archer, 2002]. Deep ocean POC fluxes are thus driven by the local biomineral (i.e. high in calcite-dominated and low in opal-dominated regions.) However, analyses of these relationships on temporal [Lam et al., 2011] and spatial scales [Wilson et al., 2012] have questioned the relative role of minerals as ballast material. The correlations may also reflect other processes governing the association between POC and minerals such as the presence of transparent exopolymer particles (TEP) that stimulate aggregation De La Rocha et al. [2008]; Passow [2004]. Another explanation for the observed regional POC flux variability is a temperature dependence for the degradation of organic matter. Temperature is a primary determinant for bacterial degradation rates [Gillooly et al., 2001; Matsumoto, 2007] and it has been shown that degradation rates are more sensitive to temperature than photosynthesis [López-Urrutia et al., 2006; Regaudie-de Gioux and Duarte, 2012]. Thus, warmer waters are characterised by faster degradation rates and therefore shallower remineralisation [Marsay et al., 2015].

A hypothesis that combines elements of the previous mechanisms specifies ecosystem structure and specifically the extent of recycling of organic matter in the euphotic zone as an important factor governing the observed spatial variability in POC flux [Henson et al., 2012; Le Moigne et al., 2014, 2012]. The reasoning is that in high export production areas (generally colder high latitudes) aggregates are rather fresh and loosely packed as they are a result of strong, seasonal diatom blooms, making them prone to rapid degradation. In low export production areas (warmer low latitudes) the material being finally exported has been processed multiple times in the euphotic layer and is therefore tightly-packed, highly refractory and thus experiences reduced microbial degradation at mesopelagic depths [Henson et al., 2012].

An increasing number of mechanisms have been identified that may contribute to changes in the attenuation of POC flux in the water column. However, as highlighted above, these mechanisms are potentially interlinked and difficult to distinguish from current observations. This represents a significant source of uncertainty surrounding the magnitude and sign of ocean carbon cycle feedbacks to changes in atmospheric CO_2 and climate [Barker et al., 2003; Riebesell et al., 2009].

2.3.2.1.2 Numerical approaches Most Earth system models impose static POC depth profiles and are therefore based on simple fitting exercises to limited data sets rather than on a mechanistic understanding of the underlying processes. This is surprising, since more sophisticated models have long been used to study organic carbon degradation dynamics in soils and marine sediments over different time-scales [e.g. Arndt et al., 2013]. Even though still far from providing an appropriate representation of the plethora of different mechanisms that control organic carbon degradation, these models have proven useful in describing the degradation dynamics of organic carbon from different sources, in different environments, under changing redox-conditions and over time-scales [e.g. Arndt et al., 2013]. The applied approaches in ocean biogeochemical models can be broadly divided into two groups: the primarily empirical approaches and more mechanistic approaches of various levels of complexity.

In the early 1980's net primary productivity (NPP) in the surface waters was assumed to be most important for vertical POC flux. The empirical algorithm of Suess [1980] (equation (1) in Fig. 2.3) describes POC flux to depth as a function of NPP, scaled to depth below the sea-surface. However, Bishop [1989] demonstrated that export (or new) production of POC (i.e. POC exported from the euphotic zone) predicts POC flux in deeper waters more reliably and is used until now in biogeochemical models. Other empirically derived relationships used in paleoclimate models are intentionally or unintentionally related to more mechanistic descriptions of organic carbon degradation. Power-law [Martin et al., 1987], single exponential [Heinze et al., 1999; Shaffer, 1996; Volk and Hoffert, 1985] or double exponential [Andersson et al., 2004; Lutz et al., 2002] relationships are applied in most of the paleoclimate models (Table 2.1). Although these models are usually empirical as well, they can be directly derived from the kinetic first-order rate law of organic matter degradation:

$$\frac{d\mathrm{POC}}{dt} = k \cdot \mathrm{POC}. \tag{2.1}$$

and the chosen function reflects certain assumptions about the organic matter pool and its degradation rate k. Therefore, the representation may be more directly related to some underlying bioenergetic drivers [Berner, 1980a; Boudreau, 1997]. The rate constant of organic carbon degradation, k, is usually interpreted as a measure of the reactivity of the macromolecular organic matter towards hydrolytic enzymes and is thus assumed to primarily depend on the macromolecular composition of organic matter. It therefore encompasses not only the original composition of the exported organic carbon, but also its evolution during sinking [Arndt et al.,

Suess Model

Suess (1980):

$$F_{\mathrm{POC}}(z) = \frac{C_{\mathrm{NPP}}}{0.0238 \cdot z + 0.212} \tag{1}$$

Single Exponential Model

e.g., Heinze et al. (1999)

$$F_{\mathrm{POC}}(z) = F_{\mathrm{POC}}(z_{\mathrm{eup}}) \cdot \exp\left(-\frac{z - z_{\mathrm{eup}}}{L_{\mathrm{POC}}}\right) = F_{\mathrm{POC}}(z_{\mathrm{eup}}) \cdot \exp\left(-\frac{k}{w}(z - z_{\mathrm{eup}})\right) \tag{2}$$

Martin Model

Martin et al. (1987):

$$F_{\mathrm{POC}}(z) = F_{\mathrm{POC}}(z_{\mathrm{eup}}) \cdot \left(\frac{z}{z_{\mathrm{eup}}}\right)^{-b} \tag{3}$$

Double Exponential Model

e.g., Lutz et al. (2002) or Andersson et al. (2004):

$$F_{\mathrm{POC}}(z) = f \cdot F_{\mathrm{POC}}(z_{\mathrm{eup}}) \cdot \exp\left(-\frac{k_1}{w_1}(z - z_{\mathrm{eup}})\right) + (1 - f) \cdot F_{\mathrm{POC}}(z_{\mathrm{eup}}) \cdot \exp\left(-\frac{k_2}{w_2}(z - z_{\mathrm{eup}})\right) \tag{4}$$

Reactive Continuum Model

Boudreau and Ruddick (1991):

$$F_{\mathrm{POC}}(z) = F_{\mathrm{POC}}(z_{\mathrm{eup}}) \cdot \left(\frac{a}{a + (z - z_{\mathrm{eup}})/w}\right)^{u} \tag{5}$$

Glossary

z	Water depth	z_{eup}	Bottom of euphotic zone
F_{POC}	Flux of POC	C_{NPP}	NPP of organic matter in surface
b	Flux attenuation factor	L_{POC}	POC degradation length scale
k_i	Degradation rate of POC	w_i	Sinking rate of POC
f	Labile fraction of POC	a	Average life-time of labile POC
u	Non-dimensional parameter		

Figure 2.3: Overview of model approaches that are applied in paleoclimate models to calculate the depth profiles of POC fluxes in the water column.

2013]. The simplest form of this approach assumes that the organic carbon constitutes one single pool, which is degraded at a constant rate. This approach is equivalent to the so-called 1G-Model of organic matter degradation [Berner, 1964a] that has been widely used in diagenetic modelling [Boudreau, 1997]. Its steady-state solution is given by a simple exponential decrease of organic carbon flux with depth that is controlled by the reactivity of organic carbon, k, and the settling velocity, w (equation (2) in Fig. 2.3; see Sarmiento and Gruber [2006] for a derivation). Yet, this simple exponential model represents merely a linear approximation of the complex degradation dynamics and the first-order degradation constant, k, represents a mean value for the heterogeneous mixture of organic compounds. It should be noted that such simplification is reasonable only if the degradability of different compounds does not vary by more than one order of magnitude [Arndt et al., 2013].

Under the assumption that the organic carbon degradation rate decreases linearly with depth, a power-law functionality for POC flux can be derived from kinetic first-order principles [compare supporting information of Lam et al., 2011]. Most commonly used is the description of [Martin et al., 1987] – equation (3) in Fig. 2.3. Martin et al. [1987] fitted a number of sediment trap POC flux measurements from six different locations in the northeast Pacific Ocean to a simple power-law. The expression scales deep fluxes to POC export from the euphotic zone (z_{eup}) and flux attenuation with depth is parametrised with a constant parameter $b = 0.858 \pm 0.1$. The majority of existing paleoclimate models integrate the Martin curve in its original form with a constant parameter b (Table 2.1) that does not change temporally or spatially. Its popularity mainly stems from the fact that a power-law represents a mathematically simple way to describe the sharp decrease of organic carbon fluxes in mesopelagic layers, while still maintaining a flux at depth.

Yet, in reality, the organic carbon flux to depth is composed of many specific and very heterogeneous compounds with a continuum of individual decay rates, distributed from very labile compounds that are degraded within several hours or days to highly condensed compounds that persist for hundreds of thousands or even millions of years. The assumption of a single organic carbon pool that is degraded with a constant or linear degradation rate is thus not consistent with natural conditions. The bulk POC flux can be subdivided into a number of compound classes that are characterised by different degradabilities k_i. This approach follows the multi-G approach proposed by Jørgensen [1978] and Berner [1980b] to describe organic carbon degradation in marine sediments. The rapid depletion of the more reactive compound class results in a decrease of total organic carbon degradability with water depth and therefore provides a more realistic representation of organic carbon degradation dynamics [Bishop, 1989; Wakeham et al., 1997]. Lutz et al. [2002] propose to describe organic carbon flux to depth using a double exponential equation including degradation length scales for a labile and a refractory fraction of POC (equation (4) in Fig. 2.3). For instance GENIE integrates such a double exponential expression that can capture the rapid flux attenuation in subsurface waters as well as the slower flux attenuation in deep waters. In theory, this 2G-Model could be expanded by introducing other POC compound classes, but as

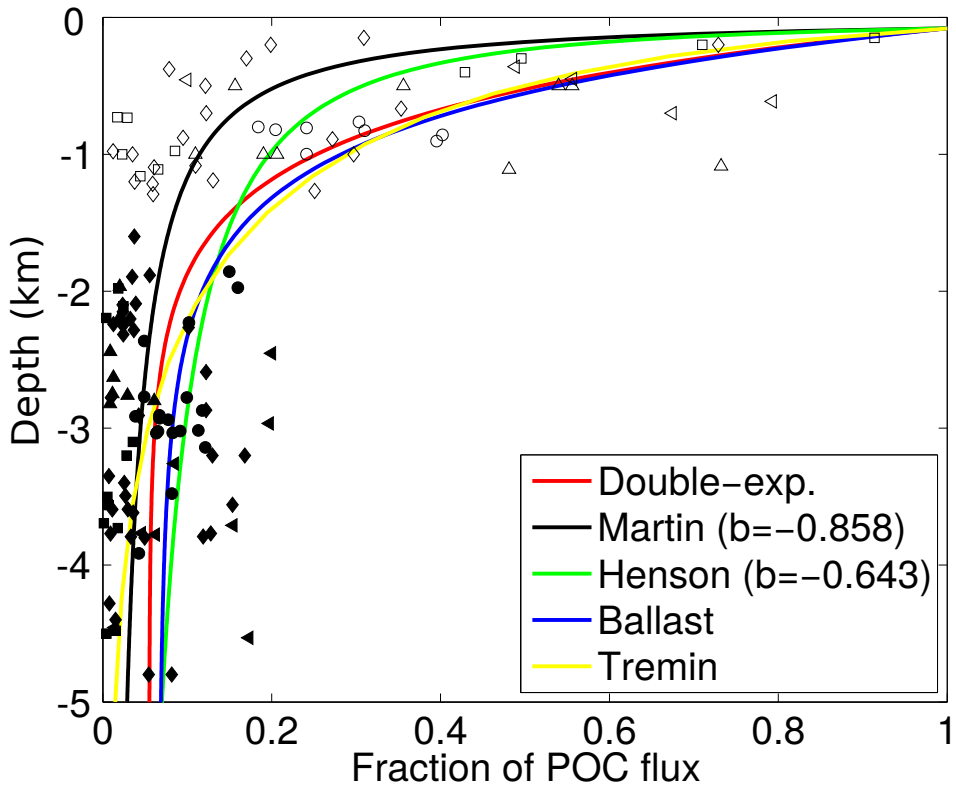

Figure 2.4: Comparison of discussed POC flux representations and global POC flux data from Lutz et al. [2002]. Observations shallower than 1.5 km have been divided by 0.4 to account for the potential undertrapping error (open symbols). Observations: ■/□: Atlantic Ocean, ♦/◇: Pacific Ocean, •/○: Indian Ocean, ▲/△: Greenland Sea. POC flux data has been normalised to regional POC export estimates given in Lutz et al. [2002] - Table 2.

they are difficult to identify from observational data their number is generally restricted to three [Jørgensen, 1978; Middelburg, 1989]. An alternative to these models are Reactive Continuum Models (RCMs) of organic matter degradation (equation (5) in Fig. 2.3). These models assume a continuous distribution of reactive types, thus avoiding the highly subjective partitioning of POC into a limited number of compound groups [e.g. Boudreau and Ruddick, 1991; Middelburg, 1989]. A newer version of GEOCLIM [GEOCLIM *reloaded*; Arndt et al., 2011] applies the RCM to quantify POC fluxes below the euphotic zone. The RCM provides a direct conceptual link between the composition of organic matter and its degradability. The total amount of organic matter is represented as the integral of the distribution function of reactive types over the entire range of possible degradation rate constants. Each member is degraded according to a first order rate law. The RCM thus explicitly integrates the effect of compound-specific reactivities on organic matter degradation and captures the decrease in organic matter degradability with depth/age. However, the RCM approach requires the determination of realistic differential reactivities of specific components rather than an average reactivity for the total POC pool which can be challenging.

2.3.2.1.3 Comparing numerical approaches Fig. 2.4 compares some of the discussed approaches with a compilation of globally distributed POC flux observations from the modern day [Lutz et al., 2002]. The Henson-approach uses the Martin equation but calculates the b-value in relation to local SST ($b = (0.024 \cdot SST) - 1.06$, compare Henson et al. [2012, Fig. 4f]). A mean SST of 17.4 °C leads to a global mean b-value of −0.643 and therefore predicts higher residual POC flux in the deep ocean as the Martin model, showing how sensitive this approach is to changing b-values. The ballasting-method assumes that part of the POC export is associated with a ballasting mineral (here calcium carbonate) and the excess POC is considered the labile fraction [Armstrong et al., 2001; Klaas and Archer, 2002]:

$$F_{\mathrm{POC}}(z) = \lambda_{\mathrm{Ca}} \cdot F_{\mathrm{Ca}}(z) + F_{\mathrm{labile}}(z), \tag{2.2}$$

where $F_{\mathrm{POC}}(z)$ is the total POC flux at depth z, $\lambda_{\mathrm{Ca}} = 0.126$ the carrying coefficient of $CaCO_3$, $F_{\mathrm{Ca}}(z)$ and $F_{\mathrm{labile}}(z)$ the total calcium carbonate and labile POC mass flux as calculated with GENIE. The temperature dependent remineralisation follows the description of John et al. [2014] using an Arrhenius-type equation to predict the temperature dependent remineralisation rate $k(T)$:

$$k(T) = A \cdot \exp(-\frac{E_{\mathrm{a}}}{RT}), \tag{2.3}$$

where R is the gas constant and T the absolute temperature. To distinguish between labile and refractory POC two activation energies E_{a} (55 and 80 kJ mol^{-1}, resp.) and two rate constants A (9×10^{11} and 1×10^{14} year^{-1}, resp.) were chosen [as calibrated in John et al., 2014]. The mean temperature profile for the global ocean has been taken from the World Ocean Atlas [Locarnini et al., 2013]. In principle, all shown formulations are able to capture the characteristic POC-flux profiles for the modern day ocean (Fig. 2.4). However, as the parameters applied in paleoclimate models are constrained to modern-day observations [e.g. Honjo et al., 2008; Martin et al., 1987] and the performance of the models strongly depend on the parameter choice, their predictive ability under different climatic conditions is seriously compromised.

To illustrate the impact of using a static versus a mechanistic POC-flux representations on ocean biogeochemistry we compare the fixed double-exponential with the temperature-dependent remineralisation approach using the paleoclimate model GENIE (see Box 2 for more information on the model and experiment set-up). Fig. 2.5 compares global POC, oxygen and nutrient profiles for a modern and a warm Eocene (55.5–33.7 Ma) climate. The global POC flux profile (normalised to export flux) for the static double-exponential just changes slightly in the Eocene experiment, whereas the temperature-dependent profile gets significantly shallower and a smaller POC fraction reaches the sediments due to warmer ocean temperatures (Fig. 2.5A). The global O_2 profile for the temperature-dependent parametrisation in the Eocene also shows this shoaling compared with the modern (Fig. 2.5B). But the temperature dependence of POC remineralisation has also major impacts on the modern ocean as can be inferred from the global O_2 profile,

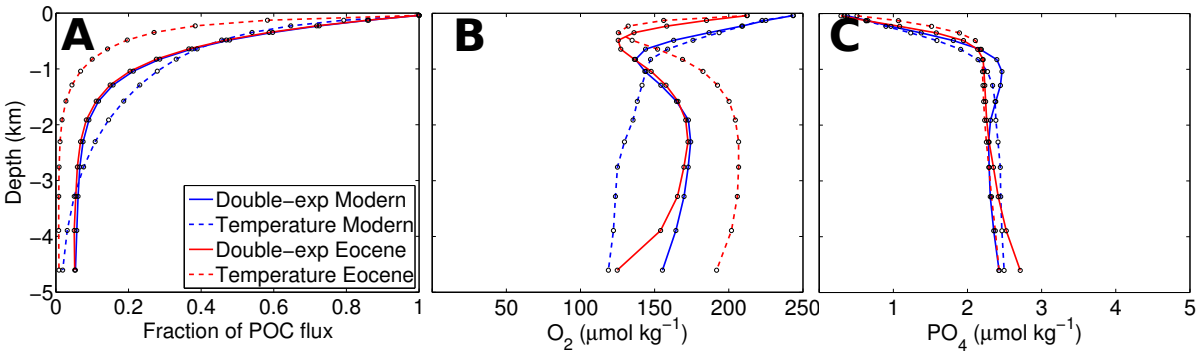

Figure 2.5: Modern and Eocene global profiles for a GENIE set-up using a double-exponential and temperature-dependent POC remineralisation approach. See Box 2 for more information about the experiment set-up.

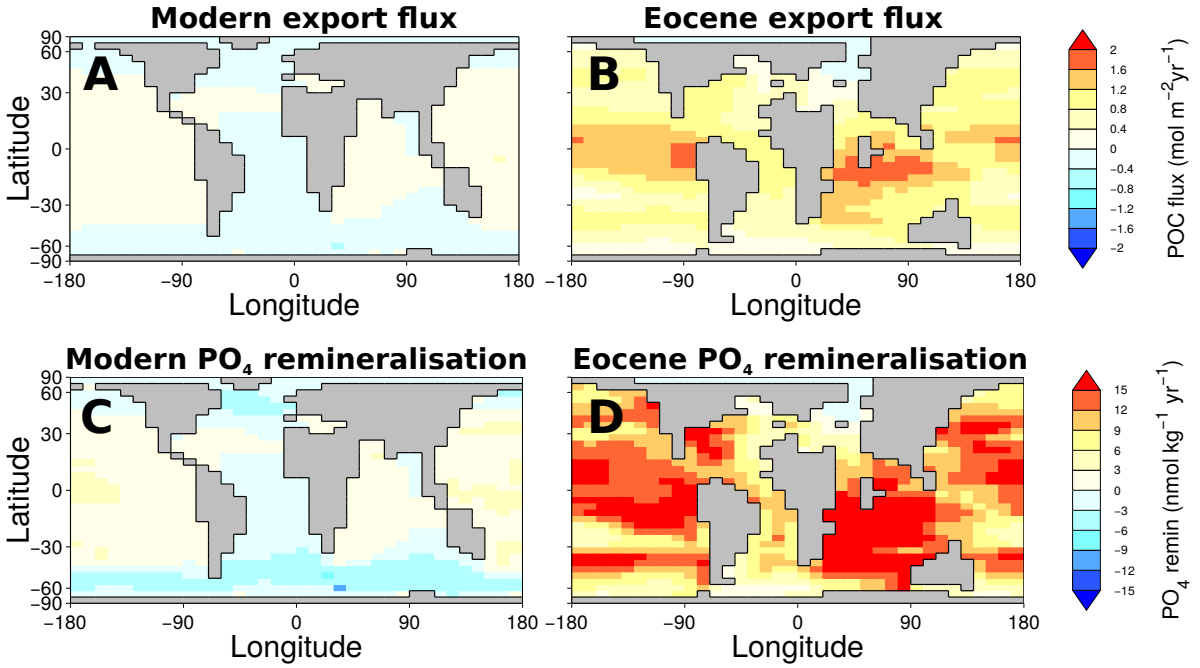

Figure 2.6: Anomaly plots (temperature-dependent minus double-exponential POC remineralisation approach) for the modern (left panel) and the Eocene (right panel). Top: Export production (i.e. POC flux at 40m). Bottom: Depth integrated remineralisation concentration of PO_4.

Box 2: The paleoclimate model GENIE and the experiment set-up

The "Grid ENabled Integrated Earth system model" (GENIE)

The basis GENIE is a 3D-ocean circulation model coupled to a fast energy-moisture balance 2D-atmosphere model ["C-GOLDSTEIN", Edwards and Marsh, 2005]. To help understand the oceanic carbon cycle and its role in regulating atmospheric CO_2 concentrations the model has been extended with a ocean biogeochemistry representation for a variety of elements and isotopes [Ridgwell et al., 2007]. The ocean model is implemented on a 36×36 equal-area horizontal grid and 16 z-coordinate levels in the vertical. Despite its lower resolution, GENIE is able to reproduce the main nutrient and dissolved inorganic carbon $\delta^{13}C$ features of the modern ocean [Holden et al., 2013; Ridgwell et al., 2007]. The same model physics have been applied before to an early Eocene and late Cretaceous bathymetry and continental configuration and successfully modelled various oceanic and sedimentary properties related to the biological carbon pump [John et al., 2014; Kirtland Turner and Ridgwell, 2013; Monteiro et al., 2012; Ridgwell and Schmidt, 2010].

Experiment set-up: Oceanic POC-flux representations (Fig. 2.5, 2.6 and 2.7)

The GENIE set-up for the modern and Eocene experiments is identical to John et al. [2014]. The OAE2 experiments adopt the carbon cycle boundary conditions of Monteiro et al. [2012] using 2 times modern oceanic phosphate concentration (4.5 μmol PO_4 kg^{-1}) and 4 times preindustrial atmospheric CO_2 (1112 ppmv). However, we do not consider nitrogen in our simulations, thus phosphate being the only productivity limiting nutrient. All experiments are run for 10,000 years in order to equilibrate the ocean biogeochemistry. In the reference model set-up, POC-flux throughout the water-column is modelled using the fixed double-exponential approach (equation (4), Fig. 2.3). The temperature-dependent remineralisation uses the formulation as discussed for Fig. 2.4. The free parameters of this approach (i.e. two rate constants (A) and the initial refractory fraction of POC) were calibrated for the modern ocean to find the best fit with the double-exponential approach for the global POC-flux profile. The two approaches are then used under a preindustrial (modern) configuration [Cao et al., 2009], an early Eocene set-up [Ridgwell and Schmidt, 2010] and an OAE2 configuration [Monteiro et al., 2012].

Experiment set-up: Sediment representations (Fig. 2.13 and 2.14)

For this series of experiments GENIE employs the fixed double-exponential POC-flux scheme but is configured with two different sediment boundaries for the modern, Eocene and OAE2 worlds: First, the so-called reflective boundary, where essentially no sediment interactions take place and all particulate species reaching the seafloor are instantaneously remineralised to dissolved carbon and nutrients. The second boundary represents the other end of the spectrum and assumes that the entire deposition flux of POC is buried in the sediments (conservative or semi-reflective boundary). In order to calculate a steady-state situation we configure the model as a "closed" system where the burial loss to the sediments is balanced by an additional weathering input of solutes to the ocean through rivers. Because of the sediment interactions the experiments are run for 20,000 years to reach equilibrium.

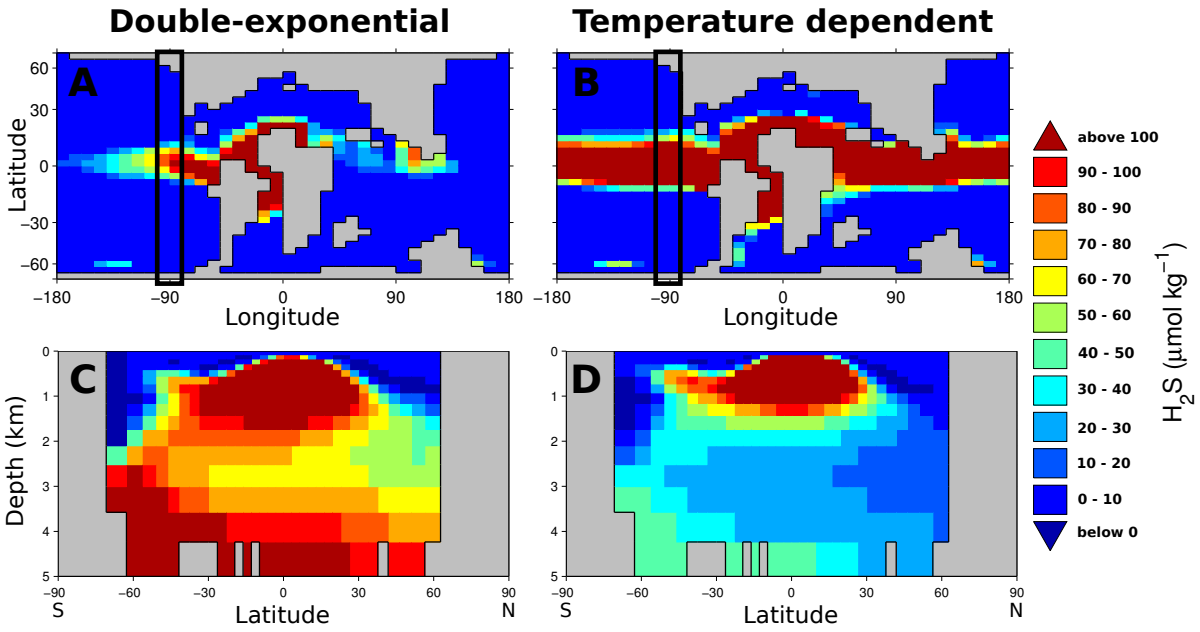

Figure 2.7: Model comparison of H_2S concentration (i.e. euxinia) during OAE2 for a GENIE configuration with double-exponential (left) and temperature-dependent (right) POC remineralisation approach. (A+B): Photic zone euxinia showing modelled H_2S concentration at 80-200 m. (C+D): Vertical profile of H_2S in the East Pacific Ocean (−90° longitude, area indicated by black rectangles in A+B).

showing a different shape compared with the double-exponential scenario. However, in contrast the global profiles for PO_4 do not change significantly (Fig. 2.5C), a result that can be attributed to the fixed initial global phosphate inventory imposed onto the model [compare also, e.g., Kriest and Oschlies, 2013]. The POC remineralisation scheme has not just significant impacts on global mean biogeochemical values but also affects their spatial distribution. Fig. 2.6 shows anomaly plots (temperature-dependent minus double-exponential) for export production (A and B) and depth integrated remineralisation concentrations of PO_4 (C and D). The differences for modern conditions are marginal (Fig. 2.6, A and C) as the temperature-dependent POC flux has been calibrated to the double-exponential flux for these conditions. However, for the Eocene, the temperature-dependent export production increases globally (9.6 Pg C year^{-1} compared to 5.9 Pg C year^{-1} in the double-exponential simulation), in particular in warm equatorial regions (Fig. 2.6B). Also the depth integrated PO_4 remineralisation is significantly higher (Fig. 2.6D). Both can be explained by the shallower, temperature dependent degradation of POC in the warmer Eocene, leading to higher PO_4 availability in the upper ocean and therefore an absolute increase in global productivity.

Fig. 2.7 compares the two remineralisation approaches for another extreme event in Earth history, the Late Cretaceous oceanic anoxic event (OAE2). Shown are modelled H_2S concentrations, another indicator for ocean redox conditions, for the two GENIE configurations for OAE2.

Euxinia is defined by the occurrence of free hydrogen sulphide in the water column, which is characteristic of anoxia as H_2S is produced by sulfate reduction when oxygen is depleted. Fig. 2.7A+B highlights the significant impact the POC-flux representation has on photic zone euxinia, with far more H_2S predicted when the temperature-dependent approach is used, a result that can be explained with warmer ocean temperatures leading to more POC degradation in the upper ocean (POC profile for OAE2 is similar to the Eocene Fig. 2.5, not shown here). However, as the majority of POC is degraded in the upper 500m when using the temperature-dependent approach, less H_2S is produced in the deeper ocean (Fig. 2.7 C+D).

2.3.2.1.4 Summary The different model results highlight that the current lack of a mechanistic theoretical framework to model POC flux seriously compromises the applicability of paleoclimate models to extreme and rapidly changing environmental conditions. A complex process interplay controls organic carbon degradation in the Earth system. It has been shown that the availability of oxygen, variable redox-conditions, euxinic environmental conditions or changing organic carbon sources can exert profound impact on organic matter reactivity and thus degradation and burial [e.g. Arndt et al., 2009; Canfield, 1994; Demaison and Moore, 1980; Meyers, 2007; Sinninghe Damsté et al., 1998]. A robust mechanistic framework is therefore a crucial prerequisite to increase the predictive ability of POC flux models, especially under changing environmental conditions that typically characterise past carbon-cycle perturbations.

2.3.2.2 Dissolved Organic Carbon

2.3.2.2.1 Observations With a size of about 662 Pg C, marine dissolved organic carbon (DOC) is comparable to the amount of carbon in the atmosphere [Hansell and Carlson, 2014]. Recently, various studies have re-emphasized the importance of DOC in the ocean and its contribution to the biological pump [e.g. Hansell et al., 2009; Hansell, 2013; Jiao et al., 2010]. Most marine DOC is produced (together with POC and PIC) by phytoplankton in the surface ocean and accounts for about 30–50% of the primary production [Biddanda and Benner, 1997; Ducklow et al., 1995]. A large part of the produced DOC belongs to the labile or semi-labile DOC pool. The labile fraction is directly recycled in the euphotic zone (lifetime hours to days), whereas the semi-labile DOC mostly consists of carbohydrates that are degraded by heterotrophic processes in the upper 500 m of the ocean (see Table 2.3). Therefore, semi-labile DOC represents an important contributor to the biological carbon pump. Due to short lifetimes the labile and semi-labile DOC fractions account for a mere 1% of the total DOC inventory and have a limited importance for longer carbon sequestration [Hansell, 2013]. The remainder is transported further to deeper waters through the overturning circulation of the ocean or scavenging on sinking aggregates and can be broadly divided into a semi-refractory and refractory pool [Hansell et al., 2012]. Semi-refractory DOC is mainly found at mesopelagic depth of the ocean (< 1000 m) and accounts for about 2% of the DOC inventory [lifetime years to multiple decades, Hansell et al., 2012]. Hansell [2013]

Table 2.3: Characterisation of major DOC fractions [after Hansell, 2013].

Fraction	Inventory (Pg C)	Removal rate (μmol C kg^{-1}year^{-1})	Lifetime	main occurance
Labile	<0.2	~100	hours to days	directly recycled
Semi-labile	6±2	~2–9	months to years	upper mesopelagic zone (< 500 m)
Semi-refractory	14±2	~0.2–0.9	years to decades	mesopelagic zone (< 1000 m)
Refractory	642±32	~0.003	centuries to millennia	everywhere

argues that most of the deep ocean DOC is largely unreactive and degrades on time-scales of several hundreds to thousands of years. This refractory DOC pool thus survives several cycles of ocean overturning and represents the largest fraction of the total marine DOC reservoir (about 97%, Table 2.3). Therefore, it is mostly argued that semi-labile DOC largely dominates the upper ocean (< 500 m), while semi-refractory and refractory DOC represents most of the DOC in the deep ocean [Hansell, 2013]. In contrast, Jannasch [1994] and Arrieta et al. [2015] hypothesise that most of the deep ocean DOC is in fact labile but that its very low concentrations limit their microbial utilisation. This "dilution hypothesis" is supported by the fact that most of the refractory DOC is still unclassified [Kujawinski, 2011] and little evidence exists to proof that it should not be available for microbial degradation.

2.3.2.2.2 Numerical approaches Despite these uncertainties and its unquantified importance for the biological pump, none of the paleoclimate box models integrate an explicit description of DOC (Table 2.4). Most other models describe the heterotrophic degradation of just one single DOC pool by a first order degradation rate law:

$$\frac{\partial \mathrm{DOC}}{\partial t} = k_{\mathrm{DOC}} \cdot \mathrm{DOC}. \tag{2.4}$$

The Bern models, for instance, assume a constant oceanic DOC inventory [Marchal et al., 1998b]. As a consequence, DOC is degraded with a first order degradation rate constant, k_{DOC}, that is dynamically adjusted in a way that DOC production in the euphotic zone is balanced by its degradation in the deep ocean. This approach has been first proposed by Najjar et al. [1992] who argue that the rate constant for DOC degradation cannot be constrained on the basis of data available at that time. The DOC lifetime in MoBidiC has been calibrated to 8.6 years, whereas LOVECLIM applies a degradation rate constant depending on oxygen availability resulting in a DOC lifetime between 20 and 22 years. Both models therefore capture the dynamics of the semi-refractory DOC pool. The standard setup of GENIE accounts for a semi-labile DOC fraction with a lifetime of 0.5 years. GENIE also has the option to represent a second DOC pool which has been used by Ma and Tian [2014] to model a semi-refractory and a refractory DOC pool

Table 2.4: DOC representation in paleoclimate EMICs. Note, none of the reviewed global carbon cycle box models represents a DOC pool.

Model	DOC fraction	Lifetime	Reference
Bern 2.5D	constant inventory	dynamic	Marchal et al. [1998b]
Bern 3D	constant inventory	dynamic	Marchal et al. [1998b]
CLIMBER-2	labile/semi-labile	days to 1 year	Six and Maier-Reimer [1996]
	semi-refractory	40 years	Brovkin et al. [2002a]
GENIE	semi-labile	0.5 years	Ridgwell et al. [2007]
	semi-refractory	20 years	Ma and Tian [2014]
	refractory	10,000 years	Ma and Tian [2014]
GEOCLIM	–	–	–
LOVECLIM	semi-refractory	20–22 years	Goosse et al. [2010]
MESMO	semi-labile	0.5 years	Ridgwell et al. [2007]
MoBidiC	semi-refractory	8.6 years	Crucifix [2005]
UVic	semi-labile/semi-refractory	2–6 years	Schmittner et al. [2005]

(lifetimes of 20 and 10,000 years) for the last glacial maximum. Dissolved organic carbon in the CLIMBER family is simulated with the biological model of Six and Maier-Reimer [1996]. Therefore, the concentration of DOC depends on exudation from phytoplankton, excretion from zooplankton and a nutrient dependent degradation constant (resulting in a lifetime between days and one year). The CLIMBER-2 model also provides the possibility to allocate 10% of the produced detritus to another, semi-refractory DOC pool with a lifetime of 40 years [Brovkin et al., 2002a]. Paleoclimate models thus mainly account for the cycling of, what is operationally classified as, the semi-labile and semi-refractory DOC fractions and generally ignore the largest DOC reservoir and its contribution to the biological carbon pump via carbon sequestration.

2.3.2.2.3 Summary A more realistic representation of DOC in paleoclimate models should include several fractions of DOC with different lifetimes [Kirchman et al., 1993] and the advantages of using a reactive continuum model for DOC should be tested. The lack of a better representation of DOC is often attributed to the limited knowledge about the processes and mechanisms involved in the generation and degradation of this carbon reservoir [e.g. Yamanaka and Tajika, 1997]. Yet, over the recent years, considerable progress has been made in advancing our understanding of the ocean's DOC reservoir [e.g. Hansell and Carlson, 2014]. In addition, a number of authors have recently argued that especially the refractory DOC pool may have played a central role for past carbon isotope excursions and associated climate change [e.g. Sexton et al., 2011; Tziperman et al., 2011]. Sexton et al. [2011] suggested that an anoxic and stratified Eocene deep ocean may have facilitated the accumulation of a large refractory DOC reservoir. Periodic release and oxidation of this surficial carbon pool (about 1,600 Pg C) as a consequence of changes in ocean circulation could explain the observed rapid decline in the δ^{13}C record and associated climate warming. The rapid recovery of the global carbon cycle is for Sexton et al. [2011] an

indicator that CO_2 was sequestered again by the ocean and not by the slower process of silicate rock weathering. However, one problem with this hypothesis is the unknown sensitivity of DOC degradation to ocean oxygenation [compare e.g. Ridgwell and Arndt, 2014]. Elucidating the role of DOC in general and the refractory DOC pool in particular for past carbon cycle and climate perturbations will thus require a better integration of DOC in paleoclimate models.

2.3.2.3 Particulate Inorganic Carbon

2.3.2.3.1 Observations The cycling of particulate inorganic carbon (i.e. $CaCO_3$) in the ocean also affects the biological pump and therefore atmospheric CO_2, but by more indirect mechanisms. Whether carbonates precipitate or dissolve can be directly linked to the saturation state (Ω) of the ocean (readers are referred to Box 1 for a brief primer on carbonate thermodynamics). Compared to the 5% of POC that is exported from the euphotic zone and reaching the sediments, a significantly higher amount of PIC is vertically transported to the bottom of the ocean [about 50% of the PIC export flux, Sarmiento and Gruber, 2006]. The role of sinking particulate inorganic carbon in the biological pump is complex, because the deep dissolution of PIC is largely controlled by the degradation of sinking POC and releases alkalinity, which in turn titrates part of the CO_2 released during POC degradation. In addition its high specific gravity plays a key role for the sinking rates of biogenic aggregates (the ballasting effect) and thus the residence time of particulate carbon in the ocean [e.g., Francois et al., 2002; Klaas and Archer, 2002]. The mechanisms responsible for carbonate dissolution in the ocean are still matter of debate [Morse et al., 2007]. Global observations showing that the depth of the lysocline coincides with the saturation horizon [e.g. Sarmiento and Gruber, 2006] have been used to imply that thermodynamic constraints are a dominant control on calcium carbonate preservation. However, a kinetic control on carbonate dissolution has been highlighted by in-situ experiments in the North Pacific [e.g., Berger, 1967] and laboratory studies reveal that dissolution rates increase in undersaturated waters [Berner and Morse, 1974; Morse and Berner, 1972]. In addition, observational evidence even points to a partial dissolution of sinking carbonate above the saturation horizon [e.g. Milliman, 1993]. Millero [2007] estimates, using global production estimates of $CaCO_3$ and globally averaged deep water sediment trap data, that probably 40–80% of the calcium carbonate produced in the surface ocean dissolves in the upper water column. However, the mechanisms that drive the dissolution of carbonates above the lysocline remain enigmatic. The dissolution of carbonates within acidic micro-environments, such as the digestive system of zooplankton or marine aggregates have been evoked as an explanation for the shallow dissolution [e.g., Alldredge and Cohen, 1987; Fiadeiro, 1980; Jansen et al., 2002; Milliman et al., 1999], but no clear conclusions could be established. Alternative explanations involve more soluble forms of carbonates, such as aragonite or high-magnesium calcites [e.g., Feely et al., 2004; Iglesias-Rodriguez et al., 2002]. In summary, the dissolution of carbonates in the ocean is much more dynamic than our present understanding is able to explain.

Exponential Model

(e.g., Maier-Reimer, 1993):

$$F_{\mathrm{PIC}}(z) = F_{\mathrm{PIC}}(z_{\mathrm{eup}}) \cdot \exp\left(-\frac{(z - z_{\mathrm{eup}})}{L_{\mathrm{PIC}}}\right) \qquad \text{for} \quad z_{\mathrm{eup}} < z \leq z_{max} \tag{1}$$

Thermodynamic Models

Vertically Resolved (e.g., Morse and Berner, 1972, Gehlen et al., 2007):

$$\frac{dF_{\mathrm{PIC}}(z)}{dz} = 0 \qquad \text{if} \quad \Omega \geq 1 \tag{2}$$

$$F_{\mathrm{PIC}}(z) = F_{\mathrm{PIC}}(z_{\mathrm{lys}}) \cdot \exp\left(-\frac{k_{\mathrm{PIC}}(1-\Omega)^n}{w}(z - z_{\mathrm{lys}})\right) \qquad \text{if} \quad \Omega < 1 \tag{3}$$

Simplified (Dissolution solely at the bottom of the ocean):

$$\frac{dF_{\mathrm{PIC}}(z)}{dz} = 0 \qquad \text{for} \quad z_{\mathrm{eup}} < z \leq z_{max} \tag{4}$$

$$F_{diss} = 0 \qquad \text{if} \quad \Omega \geq 1 \text{ at} \quad z = z_{\mathrm{max}} \tag{5}$$

$$F_{diss} = k_{\mathrm{diss}}(\Omega) \cdot F_{\mathrm{PIC}}(z_{\mathrm{max}}) \qquad \text{if} \quad \Omega < 1 \text{ at} \quad z = z_{\mathrm{max}} \tag{6}$$

Glossary

z	Water depth	z_{eup}	Bottom of euphotic zone
z_{max}	Bottom of the ocean	z_{lys}	Depth of lysocline
L_{PIC}	PIC degradation length scale	k_{PIC}	PIC dissolution rate const.
Ω	Saturation state	n	"Order" of the reaction
w	PIC sinking rate	F_{diss}	Dissolution flux at z_{max}
$k_{\mathrm{diss}}(\Omega)$	Carbonate dissolution related to saturation state		

Note: Models considering calcite and aragonite have seperate profiles, the sum of which is equal to the total PIC flux at each depth.

Figure 2.8: Overview of model approaches that are applied in paleoclimate models to calculate the depth profiles of PIC fluxes.

2.3.2.3.2 Numerical approaches This complexity is generally not reflected in the existing paleoclimate models. In fact, the applied approaches reflect much of the uncertainty that exists about the main drivers of calcium carbonate dissolution in the global ocean. In general, two very different approaches for the simulation of PIC depth profiles are applied in paleoclimate models (Fig. 2.8). The majority of paleo-models simply assume an exponential decrease of the PIC flux below the euphotic layer. The applied degradation length scales are typically chosen to be broadly consistent with the PIC flux ratio inferred from observations by Anderson and Sarmiento [1994], as well as Tsunogai and Noriki [1991] and fall within the range between 1000 m and 3000 m. The GENIE model assumes that a fixed fraction of the PIC export production reaches the deep ocean, while only the remaining fraction is subject to an exponential decrease with water depth. The magnitude of the respective fractions as well as the length scale are chosen consistent with the general conclusions of Milliman et al. [1999], and more specifically, with the sediment trap observations of Martin et al. [1993]. In HAMOCC for instance [Maier-Reimer, 1993] the downward flux of $CaCO_3$ is attenuated with a length scale of 2000m. However, for some applications [e.g. Archer et al., 2000a], 30% of the carbonate export production was assumed to reach the sea-floor unchanged. In general, although able to represent calcium carbonate dissolution above the lysocline, the exponential model strongly simplifies calcium carbonate dynamics in the ocean. It is completely decoupled from the saturation state and organic carbon degradation dynamics, the most important drivers of calcium carbonate dissolution. Therefore, the exponential model cannot account for a dynamic response of the PIC flux profile to changing environmental conditions and its applicability to past extreme events is thus questionable. An alternative approach to the exponential model is based on the calcium carbonate reaction kinetics and is commonly used in diagenetic modelling. The overall process of calcium carbonate dissolution is a complex multi-step process. Although, the general rate law, R_{diss}, can be derived from thermodynamic and kinetic considerations [e.g. Lasaga, 1981], the most frequently employed rate law is empirically derived [Morse and Arvidson, 2002; Morse and Berner, 1972]:

$$R_{\mathrm{diss}} = \left(\frac{A}{V}k\right)\cdot(1-\Omega)^n = k_{\mathrm{PIC}}\cdot(1-\Omega)^n \qquad \text{if } \Omega < 1 \tag{2.5}$$

where A is the total surface area of the solid, V is the volume of solution, $k_{(\mathrm{PIC})}$ is the rate constant and n is the apparent order of reaction. A synthesis of dissolution kinetics has shown that the apparent order of reaction varies between 1 and 4.5 [Hales and Emerson, 1997; Keir, 1980; Morse and Arvidson, 2002]. Some paleoclimate models (such as LOVECLIM and GEOCLIM *reloaded*) use a simpler version of the thermodynamic model. Instead of resolving the depth distribution of dissolution rate, they assume that calcium carbonate does not dissolve in the water column but solely at the bottom of the ocean (i.e. mimicking surface sediment dissolution.). The thermodynamic approach accounts for the direct link between the organic and inorganic carbon cycle. In addition, it allows a dynamic response of the simulated PIC flux to changes in ocean chemistry and saturation state. Furthermore, its theoretical framework is based on a mechanistic understanding of the underlying thermodynamic and kinetic drivers which gives

it the potential for feedback with changes in ocean chemistry. However, it does not account for the abundantly observed shallow carbonate dissolution in the modern ocean and might thus underestimate the extent of calcium carbonate dissolution in the water column. What is 'missing' in our understanding and hence models of the full details of the transfer of carbonate from the ocean's surface to underlying sediments is still not clear and hence the importance of this omission is difficult to quantify.

2.3.3 Carbon (re)cycling at the ocean floor and controls on burial

At the seafloor, biogeochemical diagenetic processes are influenced by biogeochemical cycling in the overlying bottom water and the upper ocean. Dissolved species diffuse from the bottom water into the sediments and particulate material (such as organic matter, calcium carbonate or opal) rain down on the sediments and fuel biogeochemical reactions. Diagenesis transforms a substantial part of the deposited material (e.g. via remineralisation and/or dissolution) and the resulting products (e.g., DIC, nutrients) may return to the water column. As such, diagenetic processes are key components in the global carbon cycle as they trigger a delayed response to changes in ocean and atmosphere geochemistry and control the removal of carbon from the ocean reservoir [e.g. Archer and Maier-Reimer, 1994; Arthur et al., 1988; Berner, 1990; Berner et al., 1989; Mackenzie et al., 2004; Ridgwell and Zeebe, 2005].

In marine sediments, carbon is buried as organic carbon or carbonate minerals (Fig. 2.9). Ultimately, only a small fraction of the organic carbon (generally 10–20% of the deposited organic carbon or less than ~0.5% of the gross primary production) escapes remineralisation and is eventually buried in the sediment [e.g. Burdige, 2007; Emerson and Hedges, 1988; Middelburg and Meysman, 2007]. However, organic carbon burial rates have been shown to vary significantly across different environments [e.g., Canfield, 1994] and through geological history [e.g., Arthur et al., 1985]. The relative fraction of the deposited organic carbon that is ultimately buried in marine sediments can range from 0 to 100% [e.g., Canfield, 1994]. A plethora of different mechanisms has been proposed to explain the observed patterns of organic carbon burial in marine sediments but their relative importance remains elusive [Demaison and Moore, 1980; Ibach, 1982; Pedersen and Calvert, 1990; Sageman et al., 2003].

It has been shown that on a global scale, only 10–15% of carbonate produced escapes dissolution and is buried in accumulating sediments [Archer, 1996b; Feely et al., 2004; Milliman and Droxler, 1996]. Carbonate burial strongly depends on the saturation state of bottom- and porewaters. Because oceanic waters become increasingly less saturated at greater depth, deep-sea sediments are typically completely devoid of carbonate minerals. Furthermore, carbonate preservation is strongly influenced by the breakdown of organic matter and the release of metabolic CO_2 [Archer, 1991; Hales, 2003; Jourabchi et al., 2005; Ridgwell and Zeebe, 2005]. Fig. 2.10 illustrates potential differences in carbonate dissolution fluxes as a function of bottom-water saturation (Ω) for two different scenarios. The first considers only bottom-water undersaturation,

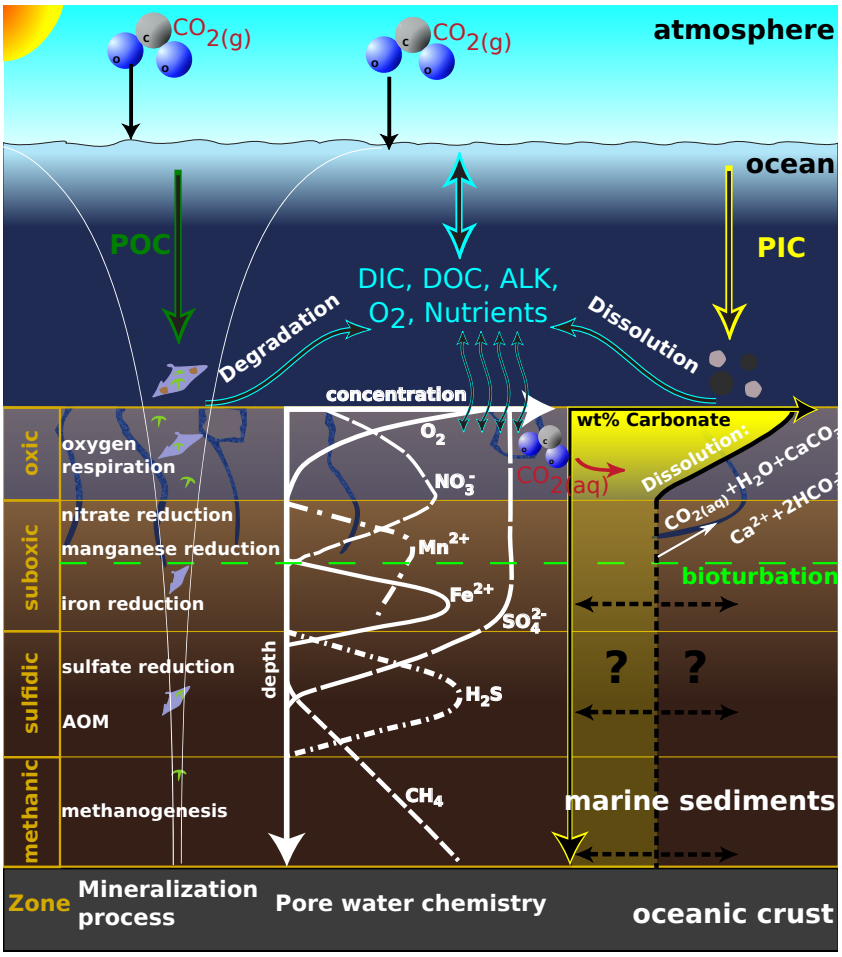

Figure 2.9: Schematic representation of the main early diagenetic processes and redox zonation in marine sediments. Typically sediments consist of several biogeochemical zones [left, as proposed by Berner, 1980a]. Oxygen, and other species, diffuse from the water column into the upper sediment layer (blue arrows, the oxic zone). Deeper layers are suboxic or anoxic (sulfidic, methanic), and are characterised by different reactions in which for instance nitrate, manganese(IV), iron(III) or sulfate ions are reduced (and re-oxidised). Exact depths, however, vary strongly and increase from the shelf to the deep sea. The depth sequence of the dominant remineralisation reaction of organic matter (in white, AOM: Anaerobic Oxidation of Methane) is reflected in the vertical pore water profiles of its reactants and products (white, concentration scales are arbitrary). Carbonate reaching the deep-sea sediments may dissolve during early diagenesis if the bottom water is undersaturated or if porewater metabolic processes (primarily aerobic degradation) cause further undersaturation in the sedimentary porewater (right).

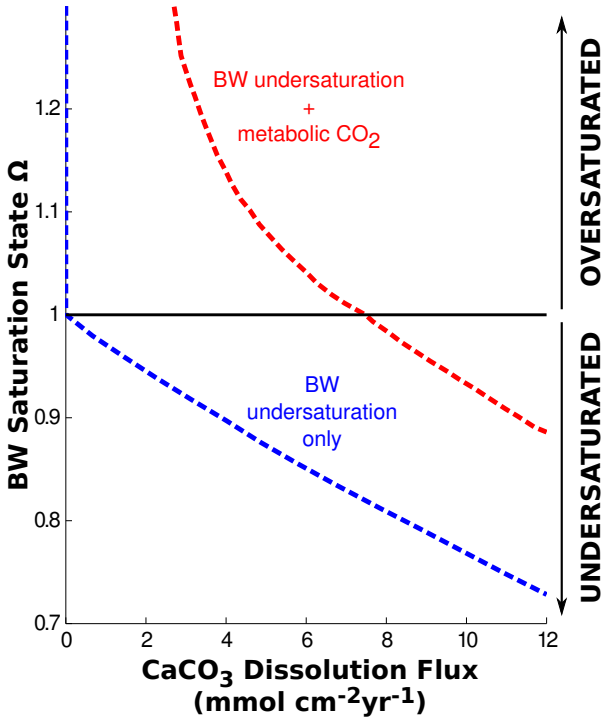

Figure 2.10: Calcite dissolution fluxes as a function of the degree of bottom water saturation, Ω. The blue dashed line represents the dissolution that would occur due to bottom-water undersaturation only, in the absence of any metabolic CO_2 (in analogy to the simplified thermodynamic model, Fig. 2.8). The red dashed line is the total carbonate dissolution (due to bottom-water undersaturation + organic carbon degradation) considering two organic carbon components and an average ocean-basin respiration rate. The two organic carbon component model represents a slower and faster decaying organic carbon pool in the sediments. Note that the scenario including the release of metabolic CO_2 drives more carbonate dissolution for all saturation states. Modified from Hales [2003].

whereas the second takes bottom-water undersaturation and the release of metabolic CO_2 into account. The burial fluxes and efficiencies of carbonates and organic carbon are thus strongly influenced by early diagenetic processes, as well as their feedbacks on ocean biogeochemistry [Archer and Maier-Reimer, 1994; Mackenzie et al., 2004; Ridgwell and Hargreaves, 2007].

In marine sediments, geochemical processes are tightly coupled and geochemical species may undergo several recycling and transformation loops (e.g., authigenic mineral precipitation/dissolution) before they are either buried or diffuse back to the water column. This complex process interplay complicates the interpretation of the sedimentary record, one of the major climate archives on Earth. Coupled paleoclimate models, which include a mechanistic description of all the feedback loops controlling the carbon dynamics, could provide powerful tools to unravel this process interplay, to enable a direct comparison between model results and observations and to test alternative hypotheses concerning the causes and effects of extreme perturbations of the global carbon cycle and climate.

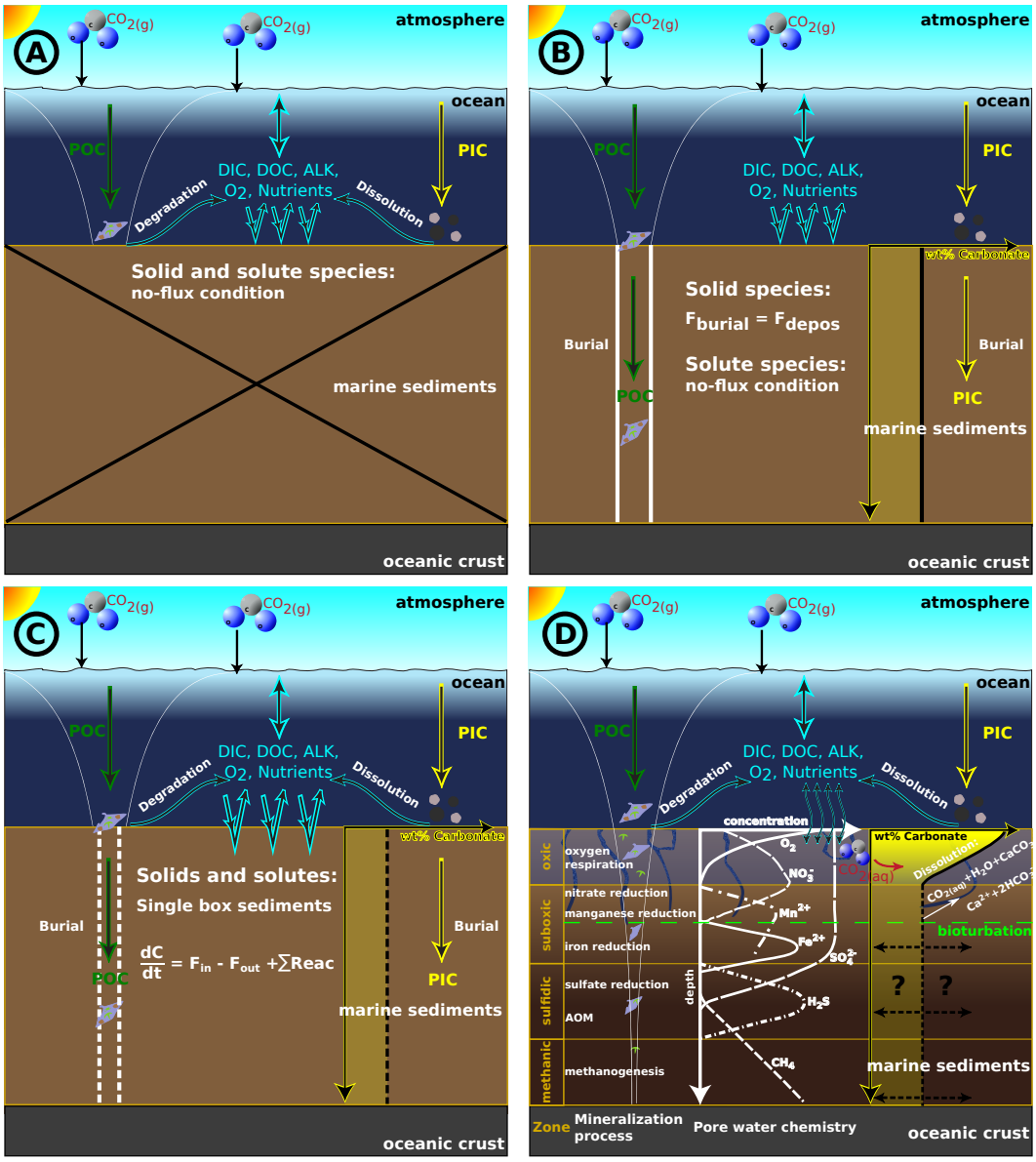

Figure 2.11: Schematic representation of the four different sediment approaches in paleoclimate models. Adapted from Soetaert et al. [2000]. **A**: Reflective Boundary; **B**: Conservative/semi-reflective Boundary; **C**: Vertically-integrated, dynamic model; **D**: Vertically resolved, diagenetic model (same as Fig. 2.9).

However, although state-of-the-art early diagenetic models are sophisticated and comprehensive enough to accurately reproduce observations and predict exchange fluxes [see e.g. Arndt et al., 2013; Boudreau, 1997], most paleoclimate models do not resolve the complexity of diagenetic processes. The primary constraint here is the high computation cost of simulating all of the essential redox and equilibrium reactions within marine sediments that control carbon burial and benthic recycling fluxes: a barrier that is exacerbated if a variety of benthic environments are to be spatially resolved. Instead, most models either neglect or only roughly approximate biogeochemical processes in the sediment and the benthic-pelagic coupling. In the following, we describe model approaches for shallow-water coral reefs and, similar to results of an earlier review of the coupling between benthic and pelagic biogeochemical models [Soetaert et al., 2000], four representations for deep-sea sediments characterised by different levels of complexity (Fig. 2.11 and Fig. 2.12).

2.3.3.1 Shallow-water carbonate sediments

Not all burial of carbonates takes place in the deep-sea; it is currently estimated that approximately an equal amount accumulates in shallow-water (neritic) environments [Milliman and Droxler, 1996; Vecsei, 2004]. Neritic carbonates are primarily the product of seafloor dwelling calcifying organisms such as corals, echinoids, mollusks, benthic foraminifera, bivalves, sea urchins, or coralline algae, whose long-term accumulation can result in the formation of large carbonate banks or reefs [e.g. Perry et al., 2008]. As today the surface ocean is largely oversaturated with respect to aragonite (Ω_{Ar}), most of the global shallow-water carbonate production (about 0.65–0.83 Pg $CaCO_3$ yr^{-1}, Vecsei [2004], i.e., 0.078–0.100 Pg C yr^{-1}) is retained and accumulates in coral-reef sediments. Additionally, particulate organic carbon flux and sedimentation rates are elevated in neritic environments therefore often leading to suboxic and anoxic conditions in the sediments. The current knowledge is that the rate of calcification is controlled by a combination of ambient factors such as aragonite saturation state of the seawater, temperature and light availability [e.g. Jones et al., 2015; Kleypas and Langdon, 2006; Tambutté et al., 2011]. However, more research is needed in order to improve the understanding of the interplay of physico-chemical and biological factors controlling the formation and composition of shallow carbonates [Allemand et al., 2011]. In some paleoclimate models, such as GENIE [Cui et al., 2013], MBM [Munhoven, 2007; Munhoven and François, 1996] and GEOCLIM [Donnadieu et al., 2006a], shallow-water carbonate formation depends on the saturation state of the epicontinental ocean with respect to $CaCO_3$, as well as on the total shelf area available for the formation of carbonate platforms [Goddéris and Joachimski, 2004] and possibly the rate of sea-level change [Munhoven and François, 1996; Walker and Opdyke, 1995]. The majority of paleoclimate models, however, ignore carbonate deposition in shallow-water environments because of resolution issues and the high computational requirements to model the involved suboxic and anoxic redox-reactions.

Conservative/semi-reflective boundary

e.g. in LOVECLIM (Goosse et al., 2010)

$$F_{\mathrm{S,bur}} = F_{\mathrm{S,dep}} \qquad (\text{ or } \alpha \cdot F_{\mathrm{S,dep}}) \tag{1}$$

$$F_{\mathrm{D,rf}} = 0 \qquad (\text{ or } R \cdot (1-\alpha) \cdot F_{\mathrm{S,dep}}) \tag{2}$$

$$\alpha \in (0,1], \text{ (with } \alpha = 1 \text{ for the conservative boundary)}$$

$$C_{\mathrm{D,sed}} = 0 \tag{3}$$

Reflective boundary

e.g., in Bern2.5D (Marchal et al., 1998b) and GENIE (Ridgwell et al., 2007):

$$F_{S,\mathrm{bur}} = 0 \tag{4}$$

$$F_{D,\mathrm{rf}} = g\left(F_{S,\mathrm{dep}}\right) \qquad (\text{ or } R \cdot F_{S,\mathrm{dep}}) \tag{5}$$

$$C_{D,\mathrm{sed}} = 0 \tag{6}$$

Vertically-integrated, dynamic model

e.g., in Bern3D (Tschumi et al., 2011), LOSCAR (Zeebe, 2012) or MBM1996 (Munhoven and François, 1996):

$$F_{S,\mathrm{bur}} = F_{S,\mathrm{dep}} - \sum_j Reac_j \tag{7}$$

$$F_{D,\mathrm{rf}} = \sum_j \beta_j Reac_j \tag{8}$$

$$\frac{dC_{D,\mathrm{sed}}(t)}{dt} = F_{\mathrm{D,in}} - F_{D,\mathrm{out}} + \sum_j (1-\beta_j) Reac_j \tag{9}$$

Vertically resolved, diagenetic model

General steady-state diagenetic equation for solid and dissolved species C_i after Berner (1980).
See e.g. GEOCLIM *reloaded* (Arndt et al., 2011):

$$\begin{aligned} \frac{\partial \xi C_i(t,z)}{\partial t} = 0 &= -\frac{\partial}{\partial z} F + \xi \sum_j Reac_j \\ &= -\frac{\partial}{\partial z}\left(-\xi D_i \frac{\partial C_i}{\partial z} + \xi w C_i\right) + \xi \sum_j Reac_j \end{aligned} \tag{10}$$

Glossary

S	Solid species	D	Dissolved species
$F_{S,\mathrm{bur}}$	Sediment burial flux of solids	$F_{i,\mathrm{dep}}$	Bottom water deposition flux of i
$F_{D,\mathrm{rf}}$	Dissolved return flux due to OM remineralisation	$C_{D,\mathrm{sed}}$	Sediment concentration of D
		$F_{D,\mathrm{in/out}}$	General dissolved in/out-flow
α	Fraction of solids preserved	R	Stoichiometric ratio
$g()$	Steady state return flux	$\beta_j \in [0,1]$	Dissolved fraction returned to ocean
z	Sediment depth	z_{max}	Maximum sediment depth
$\sum_j Reac_j$	Sum of relevant production /consumption processes	ξ	Equals porosity ϕ for solutes and $(1-\phi)$ for solids
F	Transport fluxes	D_i	Diffusion coefficient
w	advection rate		

Figure 2.12: Overview of applied model approaches to calculate burial of solid species (i.e. PIC and POC), return/recycling fluxes of dissolved species resulting from organic matter (OM) remineralisation and sediment concentrations of dissolved species.

2.3.3.2 Deep-sea Sediments

Paleoclimate models use a wide variety of approaches to represent ocean-sediment exchange fluxes. The most simple ones do not include any explicit sediment scheme, but simply assume that particulate fluxes reaching the bottom of the ocean degrade there, and the remineralisation or dissolution products return to the deepest model grid cells or boxes of the ocean. Remineralisation and/or dissolution may be either complete or partial. In the latter case, the non-degraded fraction is returned to the surface ocean, to mimic riverine input, thus avoiding the model drift because of global inventory changes. POC remineralisation rates may be dependent on oxygen concentrations in the grid cells just above the seafloor and PIC dissolution rates on the saturation state with respect to the saturation state of bottom waters. Some models (e.g. BICYCLE) use a restoration scheme, either based upon a prescribed history of the sedimentary lysocline, which is used as a proxy for the calcite saturation horizon [Köhler et al., 2005] or a reference deep-sea CO_3^{2-} concentration [Köhler et al., 2010]. Even models with explicit representations of the surface sediments exhibit a large variety of configurations: Along the vertical in the sediment column, complexity ranges from single-box surface mixed-layers [e.g., Munhoven and François, 1996] to well resolved sediment columns [e.g., 21 grid-points for the surface mixed-layer in MEDUSA, Munhoven, 2007]. Underneath the mixed-layer, some models additionally track the history of preservation in synthetic sediment cores [e.g., Ridgwell and Hargreaves, 2007]. The composition of the model sediments is also highly variable, encompassing the range from a minimalistic calcite-clay mixture [Munhoven and François, 1996; Zeebe, 2012] with an implicit, steady-state porewater [CO_3^{2-}] profile, to a composition that essentially reflects the ocean model tracer (e.g. DIC, O_2, PO_4) in porewaters and material fluxes (e.g. PIC, POC, $CaCO_3$, opal and clay) in the solid fraction [Bern 3D, Tschumi et al., 2011]. Except for MEDUSA in MBM [Munhoven, 2007], no sediment model appears to explicitly consider aragonite as a sediment constituent. In other models, the entire aragonite flux is dissolved close to the sediment-water interface if bottom waters are undersaturated with respect to aragonite, while the flux is entirely preserved in oversaturated bottom waters, possibly "converted" to calcite [e.g. in MBM, Munhoven and François, 1996]. The various adopted approaches may be divided into four major classes, which we review in the following.

2.3.3.2.1 Reflective Boundary The Bern 2.5D model includes the sediment-water interface in form of a reflective boundary [Marchal et al., 1998b] and also the GENIE model provides this as an option [Ridgwell et al., 2007] (Fig. 2.11A). The deposition flux of PIC and POC that would settle onto the sediments is completely consumed in the deepest ocean cell, instantaneously releasing dissolved carbon and nutrients. This approach is, due to its computational efficiency, often used in global biogeochemical models [e.g. Najjar et al., 1992; Sarmiento et al., 1995; Yamanaka and Tajika, 1996]. Usually the partitioning of the return flux (representing benthic transformations) is parameterised by using molar ratios for the particulates but could also be

calculated based on steady-state diagenetic modelling [Regnier et al., 1997; Soetaert and Herman, 1995]. As the reflective boundary approach does not model any benthic PIC and POC burial fluxes it overestimates benthic recycling fluxes and completely neglects the strong coupling between POC and PIC fluxes through the effect of organic matter degradation on carbonate dissolution (Fig. 2.10). In addition, it does not account for the temporal storage of material in the sediment and the time delay between deposition and recycling flux. Therefore, this highly simplified approach cannot resolve the complex benthic-pelagic coupling.

2.3.3.2.2 Conservative/semi-reflective Boundary The conservative boundary approach (Fig. 2.11B) refers to biogeochemical models that impose burial fluxes and sediment-water exchange fluxes. In general, the burial flux of PIC and POC is set equal (or proportional) to their deposition flux. In addition, a no-flux boundary condition is applied for solute species, neglecting any exchange through the sediment-water interface. For instance LOVECLIM incorporates such a sediment model where a constant part of POC and PIC is preserved [Goosse et al., 2010]. The conservative nature of this approach does not violate mass conservation and accounts for the retention capacity of sediments. Nevertheless, it neglects (or oversimplifies) the degradation of POC and the dissolution of PIC in marine sediments and thus overestimates (or crudely approximates) the burial fluxes. In addition, such a simplified approach does not represent the time-delayed recycling of nutrients and dissolved carbon and the impact of these fluxes on the biogeochemical functioning of the ocean-atmosphere system. Another important caveat of this approach is that it cannot account for a change in speciation. Generally, the composition of the benthic return fluxes is fundamentally different from the composition of the deposition flux [e.g. Soetaert et al., 2000]. In marine sediments, the coupled redox-reactions, mineral precipitation/dissolution or equilibrium reactions control the speciation. The exact composition of the total dissolved carbon flux, for instance, strongly depends on the vertical distribution of biogeochemical reaction rates and their combined influence on the ambient pH. The conservative boundary approach does not capture this biogeochemical complexity and thus does not appropriately represent the sedimentary response.

In order to illustrate how different sediment boundary conditions affect biogeochemistry in the ocean we compare a GENIE set-up using the reflective boundary with the conservative boundary for two climate scenarios (see Box 2 for more information). The impact of including organic carbon burial on global mean water-column O_2 and PO_4 concentration during the Eocene is shown in Fig. 2.13 (A+B). Global deep water O_2 concentration increases as POC reaching the seafloor is buried and not remineralised. In contrast, nutrient concentration in the deep ocean is decreasing as less PO_4 is released to the ocean. But not just the global O_2 concentration changes, also the spatial difference of bottom water oxygenation for the two sediment schemes varies significantly for the modern and the Eocene (Fig. 2.13C+D). Ocean redox differences are even more pronounced when applying the two sediment representations for the Late Cretaceous. Fig. 2.14 (A) highlights the problem of the reflective lower boundary by showing an unrealistically high concentration of

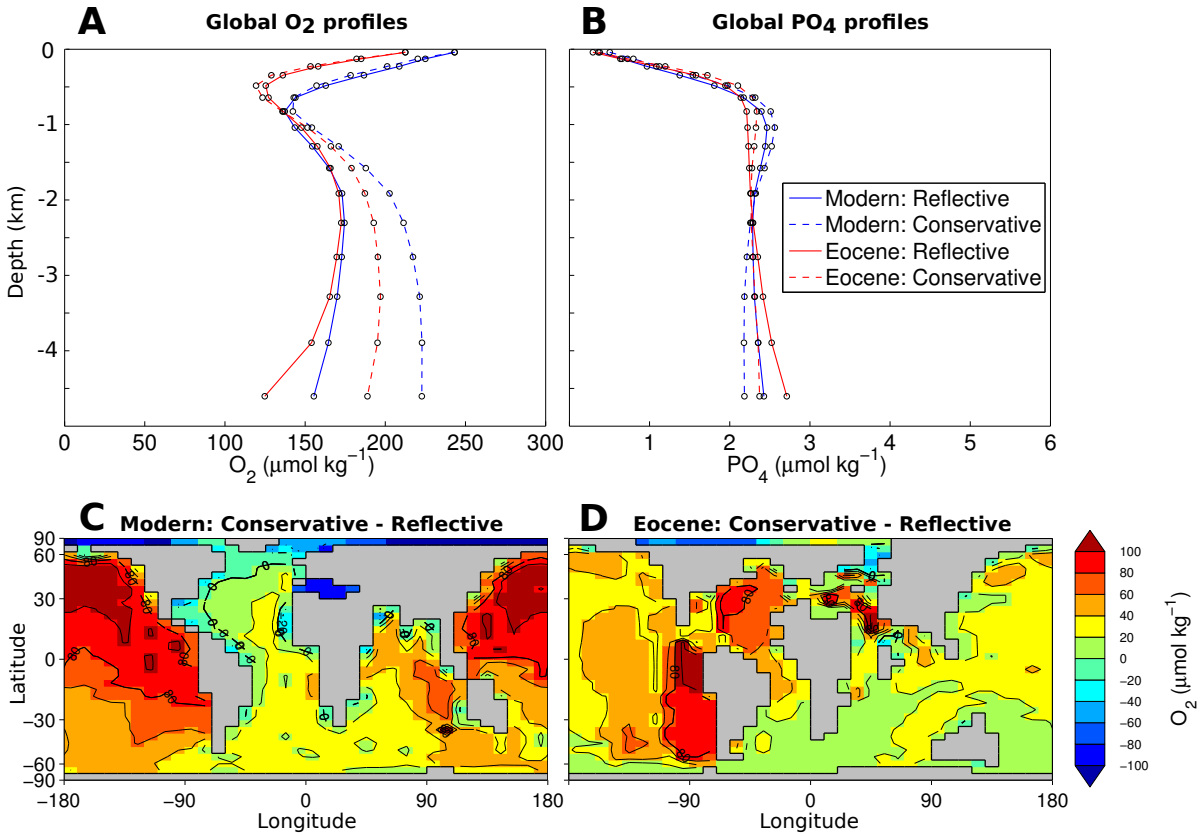

Figure 2.13: Model comparison of marine biogeochemistry with GENIE configurations using the Conservative and Reflective sediment approach for the modern and Eocene world. Modelled global oxygen (A) and phosphate (B) profiles. (C+D): Anomaly plots (Conservative minus Reflective) of bottom water oxygen concentration for modern (C) and Eocene (D) world.

H_2S at the seafloor. This result is an artifact of the lower boundary condition as all POC gets instantaneously remineralised at the seafloor. On the other hand, the conservative boundary (Fig. 2.14B) shows very little H_2S in the deeper ocean as it neglects completely the degradation of POC at the seafloor. However, the employed lower boundary condition does not only have implications on redox conditions at the bottom of the ocean but can also be seen in the photic zone (Fig. 2.14C).

2.3.3.2.3 Vertically-integrated dynamic model In the vertically-integrated approach, the sediment is represented as a single box (Fig. 2.11C). The average concentration of the represented species in this box is calculated as the balance between the deposition and burial flux, as well as the sum of consumption processes. The diffusive flux of dissolved species through the sediment-water interface in turn equals the sum of consumption/production processes that are usually tightly linked to the transformation of particulate material [e.g. Maier-Reimer, 1993]. The model thus neglects temporary storage of dissolved species and fluxes in porewaters. However, this approach is clearly superior to the two simpler approaches. It has the merit of simplicity and

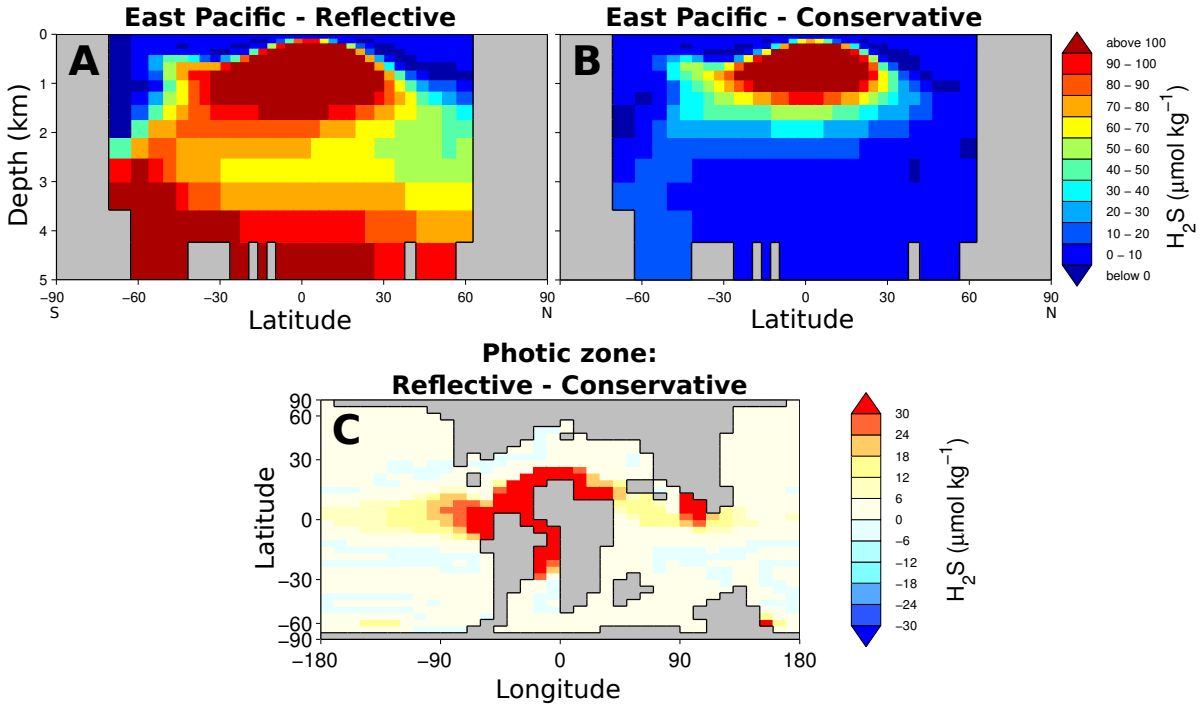

Figure 2.14: Model comparison of H_2S concentration during OAE2 with GENIE configurations using the Conservative and Reflective sediment approach. (A+B): Vertical profile of H_2S in the East Pacific Ocean ($-90°$ longitude). (C): Anomaly plots (Reflective minus Conservative) of photic zone euxina (i.e. H_2S concentration for 80-200m depth).

is computationally efficient. In addition, it also reproduces some of the complexity associated with the short- and long-term evolution of benthic recycling fluxes. Such an approach also allows differentiating between various fractions of organic matter (if POC is represented) and therefore is able to resolve some of the biogeochemical complexity associated with the decrease of organic matter reactivity with sediment depth. Most paleo-EMICs incorporate a vertically-integrated sediment model for PIC only, sometimes considering oxic-only sediment respiration of organic carbon (compare Tab. 2.1). Bern 3D being a notable exception, as it includes a vertically-integrated dynamic model also considering oxic degradation and denitrification of organic carbon [Tschumi et al., 2011],

2.3.3.2.4 Vertically resolved diagenetic model So-called diagenetic models provide the most robust description of the benthic-pelagic coupling (Fig. 2.11D). Those models solve the one-dimensional, fully coupled reaction-transport equation for solid and dissolved species [e.g. Berner, 1980a; Boudreau, 1997]. This approach thus accounts for all important transport processes, such as burial, compaction, bioturbation, molecular diffusion and bioirrigation. In addition it resolves the fully coupled biogeochemical dynamics of the carbon, oxygen and nutrient cycles and the resulting characteristic redox-zonation of marine sediments (also compare Fig. 2.9). However,

controversy still revolves around the formulations of organic matter degradation [e.g. Arndt et al., 2013] and calcite dissolution [e.g. Jourabchi et al., 2005]. In addition, the parametrisation of diagenetic models requires a good understanding of diagenetic dynamics and careful consideration of the environmental conditions. For instance, rate constants that are typically used in state-of-the art diagenetic models may predict the benthic response in the modern-day, well ventilated ocean, but might not be applicable under extreme environmental conditions such as OAEs or the PETM. The major drawback of those models is the computational cost associated with the computation of vertically-resolved reaction-transport equations for a number of interacting species. Therefore, paleoclimate models that include a diagenetic model generally reveal a very low spatial resolution of the benthic environment [e.g. GEOCLIM *reloaded* only resolves three sediment columns; Arndt et al., 2011] or use other methods to reduce computational demands: DCESS for instance uses a semi-analytical, iterative approach considering $CaCO_3$ dissolution and (oxic and anoxic) organic matter remineralisation [Shaffer et al., 2008]. One exception here is the early diagenesis model MEDUSA which is coupled to the multi-box model MBM [Munhoven, 2007]. MEDUSA operates in a fully transient way at 100 m depth intervals over the whole model sea-floor, in five regions, totalling 304 columns.

2.3.3.3 Conclusion

Marine sediments represent the largest reservoir of carbon among the exogenic reservoirs [Mackenzie et al., 2004]. The assessment of the response of the ocean to variabilities in atmospheric CO_2 concentrations requires a robust quantification of the benthic-pelagic coupling and the sedimentary carbon sink [Archer et al., 1998; Archer and Maier-Reimer, 1994; Heinze et al., 1999; Sigman et al., 1998]. However, it appears that convenience rather than a careful mechanistic representation and the ability of the approach to provide an answer to the problem guides the choice of the lower boundary condition for the ocean model. Paleoclimate modelling has developed to a stage where increasingly complex and multi-dimensional ocean, atmosphere and continental vegetation models are coupled [e.g. McGuffie and Henderson-Sellers, 2005; Randall et al., 2007]. Yet, compared to these developments, considerably less effort has been devoted to the coupling between ocean and sediment models. However, sophisticated, comprehensive and carefully calibrated and tested diagenetic models [e.g. Aguilera et al., 2005; Archer et al., 1998; Cappellen and Wang, 1996; Soetaert et al., 1996], as well as computationally efficient pseudo dynamic approaches [e.g. Arndt and Regnier, 2007; Ruardij and Van Raaphorst, 1995] are now available and could be incorporated into paleoclimate models in numerically efficient ways, such as for instance look-up tables [see e.g. Ridgwell and Hargreaves, 2007] or neural networks (see Section 2.4.3). Ultimately, our ability to understand past climate change critically depends on a better quantification of the sedimentary carbon sink and its response to extreme environmental conditions [Archer and Maier-Reimer, 1994; Berner et al., 1989; Mackenzie et al., 2004; Ridgwell and Zeebe, 2005].

2.4 Discussion and Conclusions

The biological pump in the ocean involves a complex interaction between biology, chemistry, and physics and represents a dynamic system that exhibits feedback with changing climate. Mechanistic understanding of the processes involved continue to improve and an increasing number of paleoclimate models incorporating marine carbon cycle dynamics are becoming available. However, the organic and inorganic carbon cycling in the ocean and the benthic-pelagic coupling are still widely represented by highly simplified approaches and are therefore of limited transferability across time and space. Progress in understanding past climate variations will crucially depend on the combined use of different representations (e.g. conceptual and mechanistic) of the surficial carbon cycle and the quantification of related model uncertainties.

In this final section we highlight the importance of using models of different complexities (2.4.1), provide suggestions how these models can be applied to explore and quantify different model uncertainties (2.4.2), and identify two major challenges to help direct future research for the paleoclimate (modelling) community (2.4.3).

2.4.1 The importance of different models

Fundamentally, numerical models are always approximations of the complex, real Earth system and all assumptions are erroneous on some level [Oreskes et al., 1994]. For instance, assuming a reflective sediment-water interface is appropriate when investigating carbon cycle processes on time scales shorter than 1000 years but is misleading when studying longer time scales. A box model approach is helpful when trying to isolate the dominant process in an observed global or large-scale output but not very helpful if one is interested in a more detailed (spatial) analysis of a problem (e.g. modelling marine ecology which is dependent on local transport and mixing processes and the spatial resolution of the ocean) or contrasting with regionally-specific observations.

Both model types (i.e. structurally simple or conceptual models and more coupled or mechanistic models) have their advantages and disadvantages [compare e.g. Nihoul, 1994]. The structural simplicity of box models considerably reduces the models dependency on initial and boundary conditions and the model is easier to constrain as it includes fewer parameters and variables. Due to their lower computational demand box models can be used for large-ensemble experiments needed to address important questions regarding uncertainty quantification (see Section 2.4.2). Also, the output is less complex, easier to interpret and therefore may provide a clearer understanding of the dominant process. However, there is a higher possibility of misinterpreting the *real* process if it is actually the product of several interacting processes not represented in the model. Furthermore, the simplicity of the model (in terms of resolution and represented processes) usually restricts the development of emergent behaviours and in the case of ocean circulation and prescribed water mass exchanges between boxes, there can be no emergent

behaviour (in circulation). More coupled or mechanistic models provide a slightly more complete view of the real system and have a greater degree of freedom in their dynamical properties. However, simply including more and more complexity (in the sense of additional mechanisms) does not guarantee an improvement of the predictive ability of the model. It may even reduce it, if the new representation is based on over fitting imprecisely known free parameters to limited observations [Davies, 1994]. Thus, a crucial step is to show that the representation of the new mechanism has an acceptable level of accuracy over a range of conditions.

Improving mechanistic parametrisation of key processes is one of the main challenges that hinder better understanding in Earth sciences. That does not, however, undermine the value of non-mechanistic models (e.g. conceptual, mathematical, statistical or numerical). Starting an investigation with a simple model and gradually increasing its complexity can reveal emerging model and system behaviours which might have been overlooked when employing the most complex model alone [compare Marinov et al., 2008, for an example]. Also, how processes are represented even within the same model structure can vary and testing different assumptions can lead to improved understanding of the system, as has been demonstrated in this review. Hence, one way forward is rather than solely using existing, static numerical representations for the biological pump and trying to reproduce certain paleo-observations as perfectly as possible (which is in essence often just a fitting exercise), paleoclimate models can be used to explore alternative methodologies and biogeochemical mechanisms and hence map out the range of dynamical behaviour of the biological carbon pump that is possible. Whilst not then necessarily fitting the observations of any one particular geologic event, assessing the behaviours of different incarnations (of the same model) may provide insight into other events or potentially, future responses (for which there is no data constraints). The resulting range of states or responses to perturbation, can also provide insight into model (structural) uncertainty, which we discuss next.

2.4.2 Quantifying uncertainty

Beside being ideal tools for testing our understanding of the biological carbon pump and for exploring the long-term carbon cycle evolution, paleoclimate models should further be used to investigate uncertainties related to modelling climate and marine carbon cycle feedbacks and to identify which processes have the greatest influence upon model predictions. Currently uncertainty estimates for the climate-carbon cycle response are primarily done using different future emission scenarios [e.g. Eby et al., 2009; Plattner et al., 2008; Zickfeld et al., 2013] or, where possible, by comparing model results with observational uncertainty estimates [e.g. Eby et al., 2013; Najjar et al., 2007]. In the case of model intercomparison projects mainly simplified characteristics such as the ensemble standard deviation or range are used [e.g. Najjar et al., 2007; Plattner et al., 2008; Zickfeld et al., 2013] or EMIC results are compared with results obtained from GCMs [e.g. Friedlingstein et al., 2006; Petoukhov et al., 2005; Plattner et al., 2008].

Uncertainty in (Earth system) modelling can generally be considered as a lack of knowledge or

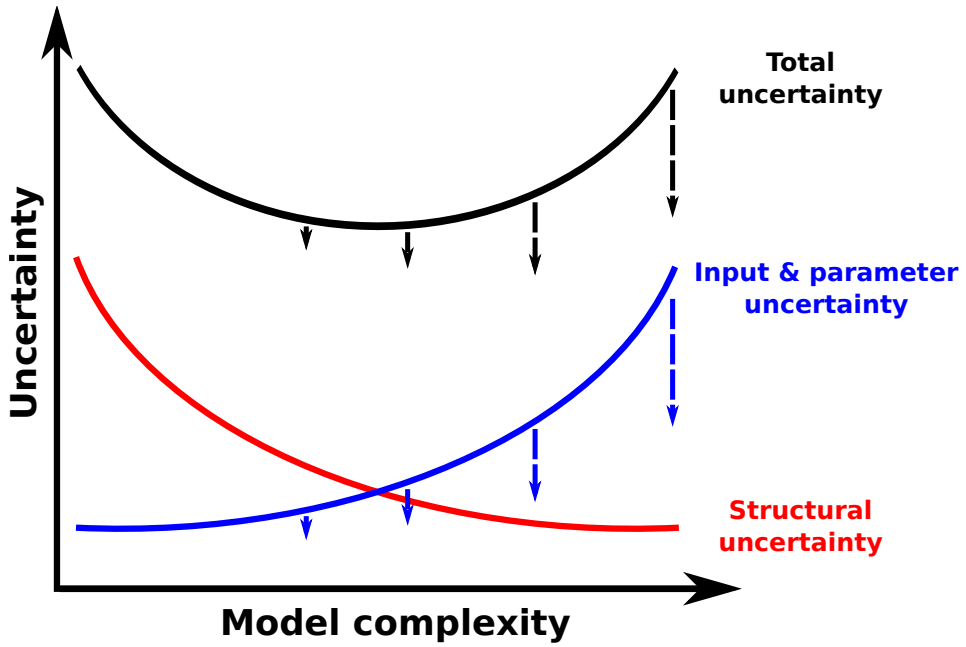

Figure 2.15: Idealised dependency of various sources of uncertainty on model complexity (i.e. components, resolution and represented processes). Blue arrows depict an improvement of input or parameter uncertainty using SA and empirical methods (see text) which results in a decrease in total model uncertainty (black arrows). Adapted from Solomatine and Wagener [2011].

information concerning the processes involved and comes from a variety of sources [Beven et al., view; Solomatine and Wagener, 2011]. First, there is input uncertainty, that is the uncertainty caused by errors in the boundary conditions, such as continental configuration, bathymetry, oceanic nutrient concentration or atmospheric CO_2 forcing. Second, there is parameter uncertainty, introduced through uncertain estimates of model parameters or because the optimal parameter set is ambiguous. And third, model structural uncertainty, resulting from simplifications, discretisations, inadequacies or ambiguities in the numerical representation of the real process. The different sources of uncertainty generally vary with model complexity (Fig. 2.15). Ideally, as more processes are described in the model (i.e. an increase in model complexity) the structural uncertainty of the model decreases. However, at the same time more parameters and inputs are needed to describe and/or constrain these processes, therefore increasing input and parameter uncertainty. Due to this trade-off between different complexities there is theoretically an optimal model for every given real world problem characterised by minimal total uncertainty. Obviously, this is an idealised example and in reality it is not possible to decide which model is the optimal one, especially in the case of paleoclimate modelling where validation against observations is limited.

One strategy to explore and quantify model uncertainty that can always be applied is sensitivity analysis (SA). Pianosi et al. [2014] deliver a comprehensive review of SA methods most

widely used in other environmental modelling fields. They also provide practical guidelines for choosing the most appropriate SA method for a specific problem, depending on the purpose of the analysis and the computational complexity of the method. Sensitivity analysis in combination with empirical approaches can also be used to iteratively reduce the uncertainty for a given numerical model [compare e.g. Bradley et al., 2016]. For instance in the case of parameter uncertainty, SA can identify which parameters have the greatest influence upon model output and how constrained their values are. Mechanistic parameters with explicit relevance to biology or physics (such as degradation rate constants, activation energies and temperature dependencies) may then be better constrained empirically using laboratory experiments or more observations, thus decreasing parameter uncertainty (compare Fig. 2.15). However, more conceptual parameters (e.g. Martin's b-value), that implicitly account for various processes, are more specific to individual model formulations and have to be determined by fitting each model to observations. The lack of correlation between these abstract parameters and real biogeochemical processes leads to an increase in parameter uncertainty (i.e. decrease in predictive ability) if the numerical model is applied under different environmental conditions. SA should be applied here to quantify this uncertainty.

Currently most studies treat only parameter uncertainty as source of uncertainty. However, research in hydrological modelling has shown that input or structural uncertainty can be even more important [Solomatine and Wagener, 2011; Wagener and Gupta, 2005]. Therefore, other questions concerning input and structural uncertainty should be explored more often using SA: How much does it matter if we change boundary conditions or forcings? What is the uncertainty in model results due to missing or oversimplified biogeochemistry? The computational efficiency of paleoclimate models (especially of box models) facilitates large simulation ensembles and systematic sensitivity studies thus allowing the estimation of these uncertainties using objective statistical methods. Kriest et al. [2010] and Kriest et al. [2012] for example present extensive sensitivity experiments to assess the skill of different global marine biogeochemical models for the modern ocean.

2.4.3 Outstanding modelling issues

As shown in this study, a major problem is the lack of the existence of a fundamental theoretical framework for describing the biological pump and hence the ability to directly derive a parameterisation for the particulate organic carbon flux under changing environmental conditions. (A universal single representation would not be possible anyway, as illustrated by how in physical ocean circulation modelling where although the fundamental fluid dynamics on a rotating sphere is known, practical constraints of model resolution and time-step lead to different e.g. approximations and parameterisations.) Different generic algorithms for this parametrisation, based on current process understanding, are needed to resolve changes in the efficiency of the biological pump which is observed over time [e.g., John et al., 2014; Kohfeld et al., 2005; Sigman and Boyle,

2000] and in space [e.g., Weber et al., 2016]. Although the basic power-law or double-exponential decrease in POC flux with depth has been widely used and characterized, there is a strong need to link changes in downward particulate flux to the mechanistic understanding of the underlying processes. The results of different representations should be compared against each other as discussed above.

Another outstanding issue are the current oversimplified sediment representations in paleoclimate models, which are often not able to model the properties needed for a comparison to proxy-observations. To overcome comparable problems, offline coupling approaches are often used. For instance, sophisticated atmospheric models such as FOAM are often run for a wide range of different atmospheric CO_2 concentrations. Based on these stand-alone simulations, look-up tables are created that link the modelled climatic conditions (e.g. precipitation, temperature) to atmospheric CO_2 [e.g., Donnadieu et al., 2006a]. These look-up tables are numerically efficient representations of the full model that can subsequently be used in EMIC simulations to simulate the climatic response to changing atmospheric CO_2 concentrations. Artifical neural networks (which represent more sophisticated look-up tables or transfer functions that allow linking a number of input parameters to a number of output parameters) can be used to encapsulate a numerically cost intensive model in a similar way. A neural network encapsulation of sediment dynamics has to be trained using a large set of simulated bottom water conditions and related burial and benthic recycling fluxes calculated by a full diagenetic model. Instead of following static, human prescribed rules, neural networks have the ability to learn automatically the underlying relationship from the training set and are practically able to approximate any relationship between input and output properties [Bernhardt, 2008; Melesse and Hanley, 2005]. These approaches thus allow a full, dynamic coupling of both models at a significantly reduced computational cost. While a neural network in effect becomes a 'black box' and loses the ability to be able to ascribe causes to consequences, it should be noted that the existence of the underlying mechanistic model on which a neural network has been trained allows for the dynamics of the system as a whole to still be picked apart/understood; i.e. unlike training a neural network on data when nothing per se can then be learned about processes, the underlying mechanistic model can be employed alongside (or in limited cases, in lieu of) the neural network to ensure that a mechanistic interpretation can always be made.

CHAPTER 3

OMEN-SED 1.0: A NOVEL, NUMERICALLY EFFICIENT ORGANIC MATTER SEDIMENT DIAGENESIS MODULE FOR COUPLING TO EARTH SYSTEM MODELS

Contributions and acknowledgements
This chapter is adapted from a research article ready for submission for publication in Geoscientific Model Development. All co-authors (S. Arndt, S. Daines, P. Regnier and A. Ridgwell) provided assistance with editing and advised on aspects of this work. S. Daines helped with the development of the Generic Boundary Condition Matching algorithm. All work presented in this chapter is my own.

3.1 Introduction

Marine surface sediments are key components in the Earth system. They host the largest carbon reservoir within the surficial Earth system, provide the primary long term sink for atmospheric CO_2, recycle nutrients, and represent the most important geochemical archive used for deciphering past changes of biogeochemical cycles and climate [e.g. Archer and Maier-Reimer, 1994; Arndt et al., 2013; Berner, 1991; Ridgwell and Zeebe, 2005]. Physical and chemical processes in sediments (i.e. diagenetic processes) depend on the water column and vice versa: Diagenesis is controlled by the external supply of solid material (e.g. organic matter, calcium carbonate, opal) from the water column and is affected by overlying bottom water concentrations of solutes. At the same time, sediments impact the water column directly either by short- and long-term storage of deposited material or diagenetic processing of deposited material and transport of

terminal electron acceptors (e.g. O_2, SO_4) into the sediments, as well as metabolic products (e.g. nutrients, DIC) to the overlying bottom waters. This so-called benthic-pelagic coupling is essential for understanding global biogeochemical cycles and climate [e.g. Archer and Maier-Reimer, 1994; Archer et al., 2000a; Mackenzie, 2005; Soetaert et al., 2000].

Biological primary production of organic matter (OM, generally represented in its simple form CH_2O in equation 3.1) and the reverse process of degradation can be written in a greatly simplified reaction as:

$$CO_2 + H_2O \rightleftharpoons CH_2O + O_2. \tag{3.1}$$

On geological timescales, production of OM is generally greater than degradation, which results in some organic matter being buried in marine sediments and oxygen accumulating in the atmosphere. Thus, burial of OM deep into the sediment leads to net oxygen input to, and CO_2 removal from the atmosphere [Berner, 2004]. On shorter timescales, the upper few meters of the sediments, where early diagenesis occurs are specifically important, as this zone controls whether a substance is recycled to the water column or buried for a longer period of time in the deeper sediments [Hensen et al., 2006]. Most biogeochemical cycles and reactions in this part of marine sediments can be related either directly or indirectly to the degradation of organic matter [Arndt et al., 2013; Middelburg et al., 1993]. Oxygen and nitrate for instance, the highest energy yielding electron acceptors, are preferentially consumed in the course of the degradation of organic matter, resulting in the release of ammonium and phosphorus to the pore water. As such, degradation of OM in the sediments can profoundly affect the oxygen and nutrient inventory of the ocean and thus primary productivity [Lenton and Watson, 2000; Van Cappellen and Ingall, 1994]. Furthermore, organic matter degradation releases metabolic CO_2 to the pore water, causing it to have a lower pH and carbonate ion concentration, thus provoking the dissolution of calcium carbonate $CaCO_3$ [Emerson and Bender, 1981].

Benthic nutrient recycling from marine sediments has been suggested to play a key role for climate and ocean biogeochemistry throughout Earth history. For example, feedbacks between phosphorus storage and erosion from shelf sediments and marine productivity have been hypothesised to play an important role for glacial/interglacial atmospheric CO_2 changes [Broecker, 1982; Ruttenberg, 1993]. Furthermore, benthic nutrient recycling from anoxic sediments has been invoked to explain the occurrence of more extreme events in Earth history, for instance Oceanic Anoxic Events [OAEs, e.g. Mort et al., 2007; Tsandev and Slomp, 2009; Van Cappellen and Ingall, 1994]. OAEs represent severe disturbances of the global carbon, oxygen and nutrient cycles of the ocean and are usually characterized by widespread bottom water anoxia and photic zone euxinia [Jenkyns, 2010]. One way to explain the genesis and persistence of OAEs is increased oxygen demand due to enhanced primary productivity. Increased nutrient inputs to fuel primary productivity may in turn have come from marine sediments as the burial efficiency of phosphorus declines when bottom waters become anoxic [Ingall and Jahnke, 1994; Van Cappellen and Ingall, 1994]. The recovery from OAE like conditions is thought to involve the permanent removal of

excess CO_2 from the atmosphere and ocean by burying carbon in the form of organic matter in marine sediments [e.g. Arthur et al., 1988; Jarvis et al., 2011], which is consistent with the geological record of widespread black shale formation [Stein et al., 1986]. Models capable of simulating not only the expansion and intensification of oxygen minimum zones, but also of predicting how the underlying sediments interact are hence needed.

Quantifications of diagenetic processes in the sediments are possible through the application of idealised mathematical representations, or so-called diagenetic models [see e.g. Berner, 1980a; Boudreau, 1997]. A plethora of different approaches have been developed, mainly following two distinct directions [see Arndt et al., 2013, for an overview]. First, state-of-the art vertically resolved numerical models simulating the entire suite of essential coupled redox and equilibrium reactions within marine sediments (e.g. BRNS, Aguilera et al., 2005; CANDI, Boudreau, 1996; MEDIA, Meysman et al., 2003; MUDS, Archer et al., 2002; STEADYSED, Cappellen and Wang, 1996). These "complete", multi-component steady-state or non-steady-state models, thus resolve the resulting characteristic redox-zonation of marine sediments through explicitly accounting for oxic OM degradation, denitrification, oxidation by manganese and iron (hydr)oxides, sulfate reduction and methanogenesis as well as the reoxidation of reduced byproducts [i.e. NH_4, Mn^{2+}, Fe^{2+}, H_2S, CH_4, see e.g. Regnier et al., 2011]. Furthermore, they incorporate various mineral dissolution and precipitation reactions, as well as fast equilibrium sorption processes for example of NH_4, PO_4 and metal ions [i.e. Mn^{2+}, Fe^{2+} and Mg^{2+}, compare Cappellen and Wang, 1996; Meysman et al., 2003]. Modelled, depth-dependent, transport processes usually comprise advection, diffusion, bioturbation and bio-irrigation. This group of diagenetic models generally describes OM degradation via a so-called multi-G approach [Berner, 1980a; Jørgensen, 1978], thus dividing the bulk organic matter pool into a number of compound classes that are characterised by different degradabilities k_i. Alternative approaches, so-called continuum models [Boudreau and Ruddick, 1991; Middelburg, 1989], assume a continuous distribution of reactive types but, although conceptually superior, are much less popular [Arndt et al., 2013]. These complex, multi-component models have a great potential for quantifying diagentic dynamics at sites where comprehensive observational data sets are available to constrain its model parameters [see e.g. Boudreau et al., 1998; Thullner et al., 2009; Wang and Van Cappellen, 1996, for applications]. However, due to the high degree of coupled processes and depth-varying parameters, the diagenetic equation needs to be solved numerically, thus resulting in a very high computational demand and consequently rendering their application in an Earth system model (ESM) framework with a large number of grid points prohibitive. Additionally, their global applicability is seriously compromised by the restricted transferability of model parameters from one site to the global scale [Arndt et al., 2013].

The second group of diagenetic models emerged during the early days of diagenetic modelling when computing power was severely restricted [e.g. Berner, 1964b]. These models solve the diagenetic equation analytically, thus providing an alternative and computationally more efficient

approach. Finding an analytical solution, especially when complex reaction networks are to be considered, is not straightforward and analytical models are thus usually less sophisticated and comprehensive than numerical models and generally require the assumption of steady state conditions. It has been shown that the complexity of the reaction network can be reduced by dividing the sediment column into distinct zones and accounting for the most pertinent biogeochemical processes within each zone, thus increasing the likelihood of finding an analytical solution without oversimplifying the problem. Analytical approaches with distinct biogeochemical zones were implemented and used in the seventies and eighties to describe observed pore water profiles [e.g. Billen, 1982; Boudreau and Westrich, 1984; Goloway and Bender, 1982; Vanderborght and Billen, 1975; Vanderborght et al., 1977] and later for inclusion into multi-box ecosystem models [e.g. Gypens et al., 2008; Ruardij and Van Raaphorst, 1995] and global Earth system models [Tromp et al., 1995]. However, in addition to the oxic zone these models generally only describe one anoxic zone explicitly, either a denitrification [Billen, 1982; Goloway and Bender, 1982; Gypens et al., 2008; Ruardij and Van Raaphorst, 1995; Vanderborght and Billen, 1975] or a sulfate reduction zone [Boudreau and Westrich, 1984; Tromp et al., 1995]. Furthermore, the approaches of Vanderborght and Billen [1975], Goloway and Bender [1982] and Tromp et al. [1995] do not explicitly account for reduced species (i.e. NH_4 and H_2S, respectively).

In most current ESMs sediment-water dynamics are either neglected or treated in a very simplistic way [Hülse et al., 2017; Soetaert et al., 2000]. Most Earth system Models of Intermediate Complexity (EMICs) and also some of the higher resolution Earth system/climate models represent the sediment-water interface either as a reflective or a conservative/semi-reflective boundary [Hülse et al., 2017]. Thus, all particulate material deposited on the seafloor is either instantaneously consumed (reflective boundary), or a fixed fraction is buried in the sediments (conservative/semi-reflective boundary). Both highly simplified approaches furthermore completely neglect the exchange of solute species through the sediment-water interface and, therefore, cannot resolve the complex benthic-pelagic coupling. However, due to their computational efficiency, both representations are often used in global biogeochemical models [e.g. Goosse et al., 2010; Najjar et al., 2007; Ridgwell et al., 2007]. Analytical diagenetic model represent the most complex description of diagenetic dynamics in Earth system models. Examples of global ESMs employing a vertically resolved diagenetic model are NorESM [Tjiputra et al., 2013] and HAMOCC [Ilyina et al., 2013; Palastanga et al., 2011], both using a version of Heinze et al. [1999]. None of the EMICs reviewed by Hülse et al. [2017] use such a sediment representation. DCESS [Shaffer et al., 2008] and MBM [Munhoven, 2007] are box models employing a vertically resolved diagenetic model. These analytic models account for the most important transport processes (i.e advection, bioturbation and molecular diffusion) through basic parametrizations and include fewer biogeochemical reactions which are generally restricted to the upper, bioturbated 10 cm of the sediments. Pore water species explicitly represented in DCESS [Shaffer et al., 2008] and the HAMOCC model of Heinze et al. [1999] and Palastanga et al. [2011] are restricted to DIC, TA,

PO_4 and O_2. The MEDUSA model [Munhoven, 2007] considers CO_2, HCO_3^-, CO_3^{2-} and O_2. Other species produced or consumed during OM degradation are neglected. Thus, with oxygen being the only TEA explicitly modelled, the influence of reduced species is only implicitly included in the boundary conditions for O_2. A newer versions of the HAMOCC model is a notable exception, as Ilyina et al. [2013] include NO_3 and denitrification explicitly. Furthermore, the version of Palastanga et al. [2011] represents an redox-dependent explicit sedimentary phosphorus cycle. Yet, reoxidation of reduced byproducts, so-called secondary redox reactions (e.g. oxidation of NH_4, H_2S or CH_4), or sorption processes are not included in any of the discussed models. Furthermore, these global models assume that the sedimentary organic matter pool is composed of just a single compound class which is either degraded with a globally invariant degradation rate constant [Munhoven, 2007] or a fixed rate constant depending on local oxygen concentrations [Palastanga et al., 2011; Shaffer et al., 2008].

Obviously, such a simplification of the OM pool can neither account for the observed vast structural complexity in natural organic matter and its resulting different degradation rates nor for the rapid decrease in OM degradability in the uppermost centimetres of the sediments [Arndt et al., 2013]. It has been suggested that at least a 3G approach is necessary to accurately represent organic matter dynamics in this part of the sediments where most OM is degraded [e.g. Soetaert et al., 1996]. Even more restrictive is the use of O_2 as the only TEA and the complete absence of reduced substances and related secondary redox reactions. For the majority of the modern sediments (i.e. in the deep-ocean) O_2 is the primary electron acceptor, however, recent model and data studies have reported that sulfate reduction is the dominant degradation pathway on a global average [with contributions of 55-76% Canfield et al., 2005; Jørgensen and Kasten, 2006; Thullner et al., 2009]. Oxygen becomes progressively less important as TEA with decreasing seafloor depth and sulfate reduction has been shown to account for 83% of OM degradation in coastal sediments [Krumins et al., 2013]. In these environments most O_2 is used to reoxidise reduced substances produced during anaerobic degradation [Canfield et al., 2005; Thullner et al., 2009]. Thus, the in situ production of e.g. NO_3 and SO_4 through oxidation of NH_4 and H_2S forms an important sink for O_2 which is entirely neglected in current sediment representations in global models. In addition, the lack of anoxic degradation pathways in these models limits their application to oxic oceans. Currently no analytical sediment model exists that can be used under anoxic conditions. Due to the lack of an appropriate sedimentary P cycle [with the exception of the HAMOCC version of Palastanga et al., 2011], no current global ESM is able to model the redox dependent P release from marine sediments and its implications for primary productivity, global biogeochemical cycles and climate. A sediment model suitable for the coupling to an ESM and enabling a wide range of paleo questions to be addressed has to provide a robust quantification of organic (and inorganic) carbon burial fluxes, benthic uptake/return fluxes of oxygen, growth-limiting nutrients and reduced species, as well as anoxic degradation pathways. As a consequence, the reaction network must account for the most important primary

and secondary redox reactions, equilibrium reactions, mineral precipitation/dissolution and adsorption/desorption, resulting in a complex set of coupled reaction-transport equations.

Therefore, we developed the OrganicMatter ENabled SEDiment model (OMEN-SED), a new, one-dimensional, numerically efficient diagenetic model. OMEN-SED builds upon and stands in the tradition of earlier stand-alone, analytical diagenetic models [Billen, 1982; Boudreau, 1991; Goloway and Bender, 1982; Vanderborght et al., 1977], as well as of analytical diagenetic models developed for the coupling to regional scale ecosystem or global Earth system models [Gypens et al., 2008; Heinze et al., 1999; Ruardij and Van Raaphorst, 1995; Tromp et al., 1995]. However, unique features of OMEN-SED are the more comprehensive reaction network, the explicit rerpesentation of reduced species and the redox-dependent P cycle. OMEN-SED is the first analytical model to explicitly describe OM cycling as well as associated dynamics of the most important TEAs (i.e. O_2, NO_3, SO_4), related reduced substances (NH_4, H_2S), the full suite of secondary-redox reactions, macronutrients (PO_4) and associated pore water quantities (ALK, DIC). In order to simplify the reaction network the solid phase iron and manganese oxidants and its reductants are not considered. To represent a redox-dependent sedimentary P cycle we consider the formation and burial of Fe-bound P and authigenic Ca-P minerals. In order to find a computationally efficient analytical solution of the model equations, OMEN-SED assumes steady state, divides the sediment column into a number of functional biogeochemical zones and assumes that the oxidation of upward-diffusing reduced species mainly happens at the oxic-anoxic boundary layer (i.e. represented as a flux to the boundary condition for oxygen). Thus, while OMEN-SED captures most of the features of a complex, numerical diagenetic model, its computational efficiency allows the coupling to global Earth system models and therefore the investigation of coupled global biogeochemical dynamics over different timescales. Here, the model is presented as a 2G-approach, however, OMEN-SED can be easily extended to a Multi-G approach. The first part of the paper provides a detailed description of OMEN-SED (Section 3.2). This includes descriptions of the general model approach (Section 3.2.1), of the conservation equations for all explicitly represented biogeochemical tracers (Section 3.2.2), as well as a summary of global relationships used to constrain reaction and transport parameters in OMEN-SED (Section 3.2.4). In addition, a generic algorithm is described which is used to match internal boundary conditions and to determine the integration constants for the analytical solutions (Section 3.2.3). In order to validate the stand-alone version of OMEN-SED, the second part of the paper performs an extensive sensitivity analysis for the most important model parameters and resulting sediment-water interface fluxes are compared with a global database (Section 3.3.1). In addition, results of the stand-alone model are compared with observed pore water profiles from different ocean depths (Section 3.3.2) and OMEN-SED simulations of TEA-fluxes along a typical ocean transect are compared with observations and results from a complete, numerical diagenetic model (Section 3.3.3). We finally discuss potential applicabilities of OMEN-SED and critically analyse model limitations (Section 3.4).

3.2 Model Description

OMEN-SED is implemented as a FORTRAN version that can be easily coupled to any pelagic, biogeochemical model via the coupling routine OMEN_SED_main. In addition, OMEN-SED exists as a stand-alone version implemented in MATLAB and the entire model can be executed on a standard personal computer in less than 0.1 seconds. The source code of both, the Fortran and the MATLAB stand-alone version, as well as instructions for executing OMEN-SED and for plotting model results are available as a supplement to this paper.

The following section provides a detailed description of OMEN-SED and the fundamental equations underlying the model are highlighted. Tables 3.1 and B.1 summarise the biogeochemical reaction network and Tables 3.9 and 3.10 provide a glossary of model parameters along with their respective units.

3.2.1 General Model Approach

In OMEN-SED, the calculation of benthic uptake, recycling and burial fluxes is based on the vertically resolved conservation equation for solid and dissolved species in porous media [e.g. Berner, 1980a; Boudreau, 1997]:

$$\frac{\partial \xi C_i}{\partial t} = -\frac{\partial}{\partial z}\left(-\xi D_i \frac{\partial C_i}{\partial z} + \xi w C_i\right) + \xi \sum_j R_i^j \tag{3.2}$$

where C_i is the concentration of biogeochemical species i, ξ equals the porosity ϕ for solute species (which is defined as $\phi = \frac{\text{volume porewater}}{\text{volume porewater + solid sediment}}$) and $(1-\phi)$ for solid species. The term z is the sediment depth, t denotes the time, D_i is the apparent diffusion coefficient of species i, w is the burial rate and $\sum_j R_i^j$ represents the sum of all biogeochemical rates j affecting species i.

OMEN-SED accounts for both the advective, as well as the diffusive transport of solid and dissolved species. They are buried in the sediment according to a constant burial rate w, thus neglecting the effect of sediment compaction (i.e. $\frac{\partial \phi}{\partial z} = 0$) due to mathematical constraints. The molecular diffusion of dissolved species is described by Fick's law applying a species-specific apparent diffusion coefficient, $D_{\text{mol},i}$. In addition, the activity of infaunal organisms in the bioturbated zone is simulated using a diffusive term [e.g. Boudreau, 1986], with a constant bioturbation coefficient D_{bio} in the bioturbated zone, while D_{bio} is set to zero below the maximum bioturbation depth, z_{bio}. The pumping activity by burrow-dwelling animals and the resulting ventilation of tubes, the so-called bioirrigation, is encapsulated in a factor f_{ir} that enhances the molecular diffusion coefficient [hence, $D_{i,0} = D_{\text{mol},i} \cdot f_{ir}$, Soetaert et al., 1996]. The reaction network of OMEN-SED accounts for the most important primary and secondary redox reactions, equilibrium reactions, mineral dissolution and precipitation, as well as adsorption and desorption processes associated with OM dynamics that affect the dissolved and solid species explicitly resolved in the model. Tables 3.1 and B.1 provide a summary of the reactions and biogeochemical tracers considered in OMEN-SED together with their respective reaction stoichiometries.

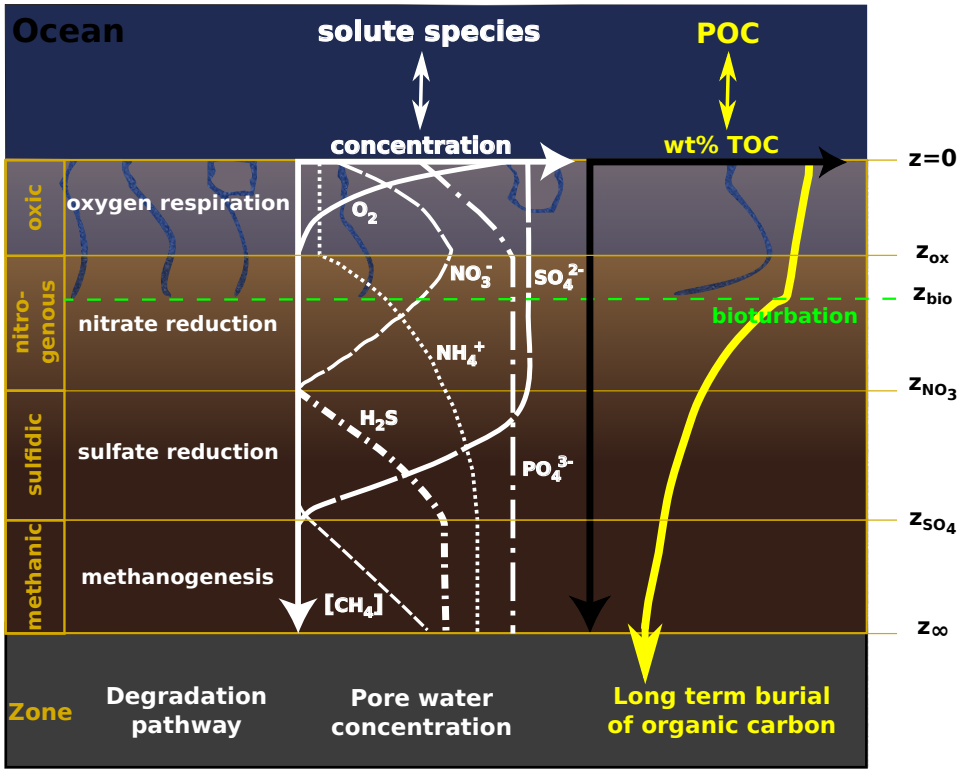

Figure 3.1: Schematic of the different modelled species and zones in OMEN-SED. Here showing the case $z_{\mathrm{ox}} < z_{\mathrm{bio}} < z_{\mathrm{NO_3}} < z_{\mathrm{SO_4}}$.

Table 3.1: Reactions and biogeochemical tracers implemented in the reaction network of OMEN-SED. The primary and secondary redox reactions are listed in the sequence they occur with increasing sediment depth.

	Description
Primary redox reactions	Degradation of organic matter via aerobic degradation, denitrification, sulfate reduction, methanogenesis (implicit)
Secondary redox reactions	Oxidation of ammonium and sulfide by oxygen, anaerobic oxidation of methane by sulfate
Adsorption/Desorption	Ad-/Desorption of P on/from $Fe(OH)_3$, NH_4 and PO_4 adsorption
Mineral precipitation	Formation of authigenic P
Biogeochemical tracers	Organic matter (2-G or pseudo 3-G), oxygen, nitrate, ammonium, sulfate, hydrogen sulfide, phosphate, Fe-bound P, DIC, ALK

All parameters in Eq. (3.2) may vary with depth and many reaction rate expressions depend on the concentration of other species. Expressing Eq. (3.2) for a set of chemical species thus results in a non-linear, coupled set of equations that can only be solved numerically. However, OMEN-SED is designed for the coupling to Earth system models and, therefore, cannot afford a computationally expensive numerical solution. Instead, similar to early, analytical diagenetic models, a computationally efficient analytical solution of Eq. (3.2) can be derived by 1) assuming steady state conditions (i.e. $\frac{\partial C_i}{\partial t} = 0$) and 2) reducing the vertical variability in parameters and reaction rate expressions by dividing the sediment column into a number of functional biogeochemical zones [Fig. 3.1, compare e.g. Billen, 1982; Goloway and Bender, 1982; Gypens et al., 2008; Ruardij and Van Raaphorst, 1995; Tromp et al., 1995, for similar solutions]. More specifically, OMEN-SED follows Berner [1980a] by dividing the sediment column into: I) a bioturbated and II) a non-bioturbated zone defined by an imposed, constant bioturbation depth z_{bio} (Fig. 3.1). Furthermore, it resolves the dynamic redox stratification of marine sediments by dividing the sediment into 1) an oxic zone delineated by the oxygen penetration depth z_{ox}; 2) a denitrification (or nitrogenous) zone situated between z_{ox} and the nitrate penetration depth $z_{\mathrm{NO_3}}$; 3) a sulfate reduction zone situated between $z_{\mathrm{NO_3}}$ and the sulfate penetration depth $z_{\mathrm{SO_4}}$; and 4) a methanogenic zone situated below $z_{\mathrm{SO_4}}$ (Fig. 3.1). Although in each of these zones Eq. (3.2) is applied with depth invariant parameters, parameter values may differ across zones. The biogeochemical zones are linked by stating continuity in both concentrations and fluxes at the dynamic, internal boundaries [$z_b \in \{z_{\mathrm{bio}}, z_{\mathrm{ox}}, z_{\mathrm{NO_3}}, z_{\mathrm{SO_4}}\}$, compare e.g. Billen, 1982; Ruardij and Van Raaphorst, 1995]. Note that these boundaries are dynamic because their depth varies in response to changing ocean boundary conditions and forcings (see Section 3.2.3.1 for details). Furthermore, the maximum bioturbation depth is not restricted to a specific biogeochemical zone, hence OMEN-SED allows bioturbation to occur in the anoxic zones of the sediment (here all zones $z > z_{\mathrm{ox}}$ combined).

The formulation of the reaction term in Eq. (3.2) varies between zones and encapsulates the most pertinent reaction processes within the respective zone (see Section 3.2.2), thus simplifying the mathematical description of the reaction network while retaining most of its biogeochemical complexity. One such simplification is that the solid phase iron and manganese oxidants and its reductants are not considered in the reaction network. All consumption or production processes of dissolved species related to the degradation of organic matter are a function of the organic matter concentration. Because organic matter degradation is described as a first-order degradation, these processes can be expressed as a series of exponential terms ($\sum_j \alpha_j \exp(-\beta_j z)$, see Eq. (3.3)). In addition, slow adsorption/desorption and mineral precipitation processes can be expressed as zero or first order (reversible) reaction (Q_m or $k_l \cdot C_i$), in Eq. (3.3)). Fast adsorption of NH_4 and PO_4 to the sediment matrix is described as an instantaneous equilibrium reaction using constant adsorption coefficients K_i. The partial reoxidation of reduced substances ($\gamma_{\mathrm{NH_4}}$, $\gamma_{\mathrm{H_2S}}$, $\gamma_{\mathrm{CH_4}}$) is accounted for implicitly by adding a (consumption/production) flux to the internal boundary

conditions (see Sections 3.2.2.2, 3.2.2.3 and 3.2.2.4). This simplification has been used previously by Gypens et al. [2008] for nitrate and ammonium and can be justified as it has been shown that the reoxidation mainly occurs within a thin layer at the oxic/anoxic interface [Soetaert et al., 1996]. The general reaction-transport equation underlying OMEN-SED is thus given by:

$$\frac{\partial C_i}{\partial t} = 0 = \frac{D_i}{1+K_i}\frac{\partial^2 C_i}{\partial z^2} - w\frac{\partial C_i}{\partial z} - \frac{1}{1+K_i}\left(\sum_j \alpha_j \exp(-\beta_j z) + \sum_l k_l \cdot C_i - \sum_m Q_m\right) \tag{3.3}$$

where $1/\beta_j$ can be interpreted as the length scale and α_j as the relative importance (or the magnitude at $z = 0$) of reaction j [Boudreau, 1997], k_l are generic first order reaction rate constants and Q_m are zero-order (or constant) reaction rates.

The analytical solution of Eq. (3.3) is of the general form:

$$C_i(z) = A \cdot \exp(az) + B \cdot \exp(bz) + \sum_j \frac{\alpha_j}{D\beta_j^2 - w\beta_j - \sum_l k_l} \cdot \exp(-\beta_j z) + \frac{\sum_m Q_m}{\sum_l k_l} \tag{3.4}$$

with

$$a = \frac{w - \sqrt{w^2 + 4 \cdot D \cdot \sum_l k_l}}{2 \cdot D}, \quad b = \frac{w + \sqrt{w^2 + 4 \cdot D \cdot \sum_l k_l}}{2 \cdot D} \tag{3.5}$$

where A and B are integration constants that can be determined by applying a set of internal boundary conditions (see Section 3.2.3) and $D = \frac{D_i}{1+K_i}$.

Based on Eq. (3.3) and its analytical solution Eq. (3.4), OMEN-SED returns the fraction of particulate organic carbon (POC) buried in the sediment, f_{POC}, as well as the benthic uptake/return fluxes F_{C_i} of dissolved species C_i (in mol cm^{-2} year^{-1}) in response to the dynamic interplay of transport and reaction processes under changing boundary conditions and forcings:

$$f_{\mathrm{POC}} = \frac{\mathrm{POC}(z_\infty)}{\mathrm{POC}(0)} \tag{3.6}$$

$$F_{C_i} = \phi(0)\left(D_i \frac{\partial C_i(z)}{\partial z}\Big|_{z=0} - w \cdot C_i(0)\right) \tag{3.7}$$

where w is the deposition rate, D_i is the diffusion coefficient and POC(0), POC(z_∞), $C_i(0)$ denote the concentration of POC and dissolved species i at the SWI and at the lower sediment boundary, respectively.

3.2.2 Conservation Equations and Analytical Solution

The following sections provide a detailed description of the conservation equations and analytical solutions for each chemical species that is resolved in this version of OMEN-SED.

3.2.2.1 Organic Matter or Particulate Organic Carbon (POC)

In marine sediments, organic matter (or in the following called particulate organic carbon, POC) is degraded by heterotrophic activity coupled to the sequential utilisation of terminal electron acceptors (TEAs) according to the free energy gain of the half-reaction [$O_2 > NO_3^- > MnO_2 > Fe(OH)_3 > SO_4^{2-}$, e.g. Stumm and Morgan, 2012]. Once all TEAs are depleted, organic matter is degraded via methanogenesis. Here, organic matter degradation is described via a multi G-model approach [Jørgensen, 1978], dividing the bulk OM into a number i of discrete compound classes POC_i characterised by class-specific first-order degradation rate constants k_i. The conservation equation for organic matter dynamics is thus given by:

$$\frac{\partial \mathrm{POC}_i}{\partial t} = 0 = D_{\mathrm{POC}_i} \frac{\partial^2 \mathrm{POC}_i}{\partial z^2} - w \frac{\partial \mathrm{POC}_i}{\partial z} - k_i \cdot \mathrm{POC}_i \tag{3.8}$$

with $D_{\mathrm{POC}_i} = D_{\mathrm{bio}}$ for $z \leq z_{\mathrm{bio}}$ and $D_{\mathrm{POC}_i} = 0$ for $z > z_{\mathrm{bio}}$. Integration of equations (3.8) yields the following general solutions for the bioturbated and non-bioturbated layers:

I. Bioturbated zone ($z \leq z_{bio}$)

$$\mathrm{POC}_i^I(z) = A_{1i} \cdot exp(a_{1i} z) + B_{1i} \cdot exp(b_{1i} z) \tag{3.9}$$

II. Non-bioturbated zone ($z_{bio} < z$)

$$\mathrm{POC}_i^{II}(z) = A_{2i} \cdot exp(a_{2i} z) \tag{3.10}$$

where

$$a_{1i} = \frac{w - \sqrt{w^2 + 4 \cdot D_{\mathrm{POC}_i} \cdot k_i}}{2 \cdot D_{\mathrm{POC}_i}}, \quad b_{1i} = \frac{w + \sqrt{w^2 + 4 \cdot D_{\mathrm{POC}_i} \cdot k_i}}{\cdot 2 D_{\mathrm{POC}_i}}, \quad a_{2i} = -\frac{k_i}{w} \tag{3.11}$$

Determining the integration constants ($A_{1,i}$, $B_{1,i}$, $A_{2,i}$) requires the definition of a set of boundary conditions (Table 3.2). For organic matter, OMEN-SED applies a known concentration/flux at the sediment-water interface and assumes continuity across the bottom of the bioturbated zone, z_{bio}. The integration constants ($A_{1,i}$, $B_{1,i}$, $A_{2,i}$) are thus given by:

$$\begin{aligned} B_{1i} &\overset{\mathrm{BC1)}}{=} \mathrm{POC}_{0i} - A_{1i} \\ A_{2i} &\overset{\mathrm{BC2)}}{=} \frac{A_{1i} \cdot exp(a_{1i} z_{bio}^-) + B_{1i} \cdot exp(b_{1i} z_{bio}^-)}{exp(a_{2i} z_{bio}^+)} \\ A_{1i} &\overset{\mathrm{BC3)}}{=} -\frac{B_{1i} b_{1i} \cdot exp(b_{1i} z_{bio}^-)}{a_{1i} \cdot exp(a_{1i} z_{bio}^-)} \end{aligned} \tag{3.12}$$

See Section 3.2.3.1 for further details on how to find the analytical solution.

Table 3.2: OM Boundary conditions applied in OMEN-SED. For the boundaries we define: $z^-_{\mathrm{bio}} := \lim_{h\to 0}(z_{\mathrm{bio}} - h)$ and $z^+_{\mathrm{bio}} := \lim_{h\to 0}(z_{\mathrm{bio}} + h)$.

Boundary	**Condition**	
$z = 0$	known concentration	1) $\mathrm{POC}_i(0) = \mathrm{POC}_{0i}$
$z = z_{\mathrm{bio}}$	continuity	2) $\mathrm{POC}_i(z^-_{\mathrm{bio}}) = \mathrm{POC}_i(z^+_{\mathrm{bio}})$
		3) $-D_{\mathrm{bio}} \cdot \frac{\partial \mathrm{POC}_i}{\partial z}\vert_{z^-_{\mathrm{bio}}} = 0$

3.2.2.2 Oxygen

OMEN-SED explicitly accounts for oxygen consumption by the aerobic degradation of organic matter within the oxic zone, as well as the oxidation of reduced species (i.e. NH_4, H_2S) produced in the anoxic zones of the sediment. In the oxic zone ($z < z_{ox}$), the aerobic degradation consumes oxygen with a fixed $O_2 : C$ ratio (O_2C, Tab. 3.10). A predefined fraction, γ_{NH_4}, of the ammonium produced during the aerobic degradation of OM is nitrified to nitrate, consuming two moles of oxygen per mole of ammonium produced. In addition, OMEN-SED implicitly accounts for the oxygen consumption due to oxidation of reduced species (NH_4, H_2S) produced below the oxic zone through the flux boundary condition at the dynamically calculated (see section 3.2.4.2 for details) oxygen penetration depth z_{ox}. All oxygen consumption processes can thus be formulated as a function of organic matter degradation. The conservation equation for oxygen is given by:

(3.13)
$$\frac{\partial \mathrm{O_2}}{\partial t} = 0 = D_{\mathrm{O_2}} \frac{\partial^2 \mathrm{O_2}}{\partial z^2} - w \frac{\partial \mathrm{O_2}}{\partial z} - \frac{1-\phi}{\phi} \sum_i k_i \cdot [\mathrm{O_2C} + 2\gamma_{\mathrm{NH_4}} \mathrm{NC_i}] \cdot \mathrm{POC}_i(z)$$

For illustrative purposes, we here substitute the analytical solution for the POC depth profile and provide the analytical solution. The remaining paragraphs only outline the general equation, whose analytical solution can be derived in an identical manner. Substituting Eq. (3.9) and (3.10) for $\mathrm{POC_i(z)}$ and Eq. (3.12) for B_{1i} gives:

I Bioturbated zone ($z \le z_{\mathrm{bio}}$)

$$\begin{aligned}\frac{\partial \mathrm{O_2^I}}{\partial t} &= 0 \overset{3.9\&3.12}{=} D^I_{\mathrm{O_2}} \frac{\partial^2 \mathrm{O_2}}{\partial z^2} - w \frac{\partial \mathrm{O_2}}{\partial z} \\ &\quad - \frac{1-\phi}{\phi} \sum_i k_i \cdot [\mathrm{O_2C} + 2\gamma_{\mathrm{NH_4}} \mathrm{NC_i}] \cdot \left(A_{1i} \cdot [exp(a_{1i} z) - exp(b_{1i} z)] + \mathrm{POC}_{0i} \cdot exp(b_{1i} z) \right)\end{aligned}$$

II Non-bioturbated zone ($z_{\mathrm{bio}} < z < z_{\mathrm{ox}}$)

$$\frac{\partial \mathrm{O_2}^{II}}{\partial t} = 0 \overset{3.10}{=} D^{II}_{\mathrm{O_2}} \frac{\partial^2 \mathrm{O_2}}{\partial z^2} - w \frac{\partial \mathrm{O_2}}{\partial z} - \frac{1-\phi}{\phi} \sum_i k_i \cdot [\mathrm{O_2C} + 2\gamma_{\mathrm{NH_4}} \mathrm{NC_i}] \cdot \left(A_{2i} \cdot exp(a_{2i} z) \right)$$

where $D^I_{\mathrm{O_2}}$ and $D^{II}_{\mathrm{O_2}}$ denote the O_2 diffusion coefficient for the bioturbated and non-bioturbated zone, respectively. The term $\frac{1-\phi}{\phi}$ accounts for the volume conversion from solid to dissolved

phase and NC_i is the nitrogen to carbon ratio in POC. Integration yields the following analytical solution for each zone:

I Bioturbated zone ($z \leq z_{bio}$):

$$O_2{}^I(z) = A^1_{O_2} + B^1_{O_2} \cdot \exp(b^1_{O_2} z) + \sum_i \Phi^I_{1,i} \cdot \exp(a_{1i} z) + \sum_i \Phi^{II}_{1,i} \cdot \exp(b_{1i} z) + \sum_i \Phi^{III}_{1,i} \cdot \exp(b_{1i} z) \tag{3.14}$$

II Non-bioturbated zone ($z_{bio} < z < z_{ox}$)

$$O_2{}^{II}(z) = A^2_{O_2} + B^2_{O_2} \cdot \exp(b^2_{O_2} z) + \sum_i \Phi^I_{i,2} \cdot \exp(a_{2i} z) \tag{3.15}$$

with

$$b^1_{O_2} = \frac{w}{D^I_{O_2}}, \quad b^2_{O_2} = \frac{w}{D^{II}_{O_2}}$$

$$\Phi^I_{1,i} = \frac{1-\phi}{\phi} \cdot \frac{k_i \cdot (O_2C + 2\gamma_{NH_4} NC_i) \cdot A_{1i}}{D^I_{O_2}(-a_{1i})^2 - w \cdot (-a_{1i})}, \qquad \Phi^{II}_{1,i} = -\frac{1-\phi}{\phi} \cdot \frac{k_i \cdot (O_2C + 2\gamma_{NH_4} NC_i) \cdot A_{1i}}{D^I_{O_2}(-b_{1i})^2 - w \cdot (-b_{1i})}$$

$$\Phi^{III}_{1,i} = \frac{1-\phi}{\phi} \cdot \frac{k_i \cdot (O_2C + 2\gamma_{NH_4} NC_i) \cdot POC_{0i}}{D^I_{O_2}(-b_{1i})^2 - w \cdot (-b_{1i})}$$

$$\Phi^I_{i,2} := \frac{1-\phi}{\phi} \cdot \frac{k_i \cdot (O_2C + 2\gamma_{NH_4} NC_i) \cdot A_{2i}}{D^{II}_{O_2}(-a_{2i})^2 - w \cdot (-a_{2i})}$$

Determining the four integration constants ($A^1_{O_2}, B^1_{O_2}, A^2_{O_2}, B^2_{O_2}$, see Section 3.2.3 for details), as well as the *a priori* unknown oxygen penetration depth requires the definition of five boundary conditions (see Table 3.3). At the sediment-water interface, OMEN-SED applies a Dirichlet condition (i.e. known concentration) and assumes concentration and flux continuity across the bottom of the bioturbated zone, z_{bio}. The oxygen penetration depth z_{ox} marks the lower boundary and is dynamically calculated as the depth at which $O_2(z) = 0$. Therefore, OMEN-SED applies a Dirichlet boundary condition $O_2(z_{ox}) = 0$. In addition, a flux boundary is applied that implicitly accounts for the oxygen consumption by the partial oxidation of NH_4 and H_2S diffusing into the oxic zone from below (BC 4.2, Table 3.3). It is assumed that respective fractions (γ_{NH_4} and γ_{H_2S}) are directly reoxidised at the oxic/anoxic interface and the remaining fraction escapes reoxidation. OMEN-SED iteratively solves for z_{ox} by first testing if there is oxygen left at z_∞ (i.e. $O_2(z_\infty) > 0$). If that is not the case, it determines the root for the flux boundary condition 4.2 (Table 3.3). If $z_{ox} = z_\infty$, a zero diffusive flux boundary condition is applied as lower boundary condition.

3.2.2.3 Nitrate and Ammonium

Nitrogen dynamics in OMEN-SED are controlled by the metabolic production of ammonium, nitrification, denitrification as well as ammonium adsorption. Ammonium is produced by organic matter degradation in both the oxic and anoxic zones, while denitrification consumes nitrate in the denitrification zone with a fixed $NO_3 : C$ ratio (NO_3C, Tab. 3.10).

Table 3.3: Boundary conditions for oxygen. For the boundaries we define: $z^-_{\mathrm{bio}} := \lim_{h\to 0}(z_{\mathrm{bio}} - h)$ and $z^+_{\mathrm{bio}} := \lim_{h\to 0}(z_{\mathrm{bio}} + h)$.

Boundary	**Condition**		
$z = 0$	known concentration	1)	$\mathrm{O_2}(0) = O_{20}$
$z = z_{\mathrm{bio}}$	continuity	2)	$\mathrm{O_2}(z^-_{\mathrm{bio}})$=$\mathrm{O_2}(z^+_{\mathrm{bio}})$
		3)	$-\left(D_{\mathrm{O_2},0} + D_{\mathrm{bio}}\right) \cdot \frac{\partial \mathrm{O_2}}{\partial z}\vert_{z^-_{\mathrm{bio}}} = -D_{\mathrm{O_2},0} \cdot \frac{\partial \mathrm{O_2}}{\partial z}\vert_{z^+_{\mathrm{bio}}}$
$z = z_{\mathrm{ox}}$	$\mathrm{O_2}$ consumption	4)	**IF** $(\mathrm{O_2}(z_\infty) > 0)$
	$(z_{\mathrm{ox}} = z_\infty)$	4.1)	$\frac{\partial \mathrm{O_2}}{\partial z}\vert_{z_{\mathrm{ox}}} = 0$
			ELSE
	$(z_{\mathrm{ox}} < z_\infty)$	4.2)	$\mathrm{O_2}(z_{\mathrm{ox}}) = 0 \quad \text{and} \quad -D_{\mathrm{O_2}} \cdot \frac{\partial \mathrm{O_2}}{\partial z}\vert_{z_{\mathrm{ox}}} = F_{red}(z_{\mathrm{ox}})$
	with		$F_{red}(z_{\mathrm{ox}}) = \frac{1-\phi}{\phi} \cdot \int_{\tilde{z}_{\mathrm{NO_3}}}^{\infty} \sum_i \left(2\gamma_{\mathrm{NH_4}}\mathrm{NC_i} + 2\gamma_{\mathrm{H_2S}}\mathrm{SO_4C}\right) \cdot k_i \mathrm{POC}_i \, dz$

Note: $\tilde{z}_{\mathrm{NO_3}} = z_{\mathrm{ox}}$ as upper boundary here, as $z_{\mathrm{NO_3}}$ is not known at this point.

The adsorption of ammonium to sediment particles is formulated as an equilibrium process with constant equilibrium adsorption coefficient $K_{\mathrm{NH_4}}$, thus assuming that the adsorption is fast compared to the characteristic time scales of transport processes [Wang and Van Cappellen, 1996]. In addition, a defined fraction, $\gamma_{\mathrm{NH_4}}$, of metabolically produced ammonium is directly nitrified to nitrate in the oxic zone, while the nitrification of upward diffusing ammonium produced in the sulfidic and methanic zones is implicitly accounted for in the boundary conditions. The conservation equations for ammonium and nitrate are thus given by:

1. Oxic zone ($z \le z_{\mathrm{ox}}$)

$$\frac{\partial \mathrm{NO_3}^I}{\partial t} = 0 = D_{\mathrm{NO_3}} \frac{\partial^2 \mathrm{NO_3}^I}{\partial z^2} - w \frac{\partial \mathrm{NO_3}^I}{\partial z} + \gamma_{\mathrm{NH_4}} \frac{1-\phi}{\phi} \cdot \sum_i \mathrm{NC_i} \cdot k_i \cdot \mathrm{POC}_i(z) \tag{3.16}$$

$$\frac{\partial \mathrm{NH_4}^I}{\partial t} = 0 = \frac{D_{\mathrm{NH_4}}}{1+K_{\mathrm{NH_4}}} \frac{\partial^2 \mathrm{NH_4}^I}{\partial z^2} - w \frac{\partial \mathrm{NH_4}^I}{\partial z} + \frac{1-\gamma_{\mathrm{NH_4}}}{1+K_{\mathrm{NH_4}}} \cdot \frac{1-\phi}{\phi} \cdot \sum_i \mathrm{NC_i} \cdot k_i \cdot \mathrm{POC}_i(z) \tag{3.17}$$

2. Denitrification (or nitrogenous) zone ($z_{\mathrm{ox}} < z \le z_{\mathrm{NO_3}}$)

$$\frac{\partial \mathrm{NO_3}^{II}}{\partial t} = 0 = D_{\mathrm{NO_3}} \frac{\partial^2 \mathrm{NO_3}^{II}}{\partial z^2} - w \frac{\partial \mathrm{NO_3}^{II}}{\partial z} - \frac{1-\phi}{\phi} \mathrm{NO_3C} \cdot \sum_i k_i \cdot \mathrm{POC}_i(z) \tag{3.18}$$

$$\frac{\partial \mathrm{NH_4}^{II}}{\partial t} = 0 = \frac{D_{\mathrm{NH_4}}}{1+K_{\mathrm{NH_4}}} \frac{\partial^2 \mathrm{NH_4}^{II}}{\partial z^2} - w \frac{\partial \mathrm{NH_4}^{II}}{\partial z} \tag{3.19}$$

3. Sulfidic and methanic zone ($z_{\mathrm{NO_3}} < z \le z_\infty$)

$$\frac{\partial \mathrm{NH_4}^{III}}{\partial t} = 0 = \frac{D_{\mathrm{NH_4}}}{1+K_{\mathrm{NH_4}}} \frac{\partial^2 \mathrm{NH_4}^{III}}{\partial z^2} - w \frac{\partial \mathrm{NH_4}^{III}}{\partial z} + \frac{1}{1+K_{\mathrm{NH_4}}} \cdot \frac{1-\phi}{\phi} \cdot \sum_i \mathrm{NC_i} \cdot k_i \cdot \mathrm{POC}_i(z) \tag{3.20}$$

where $D_{\mathrm{NO_3}}$ and $D_{\mathrm{NH_4}}$ denote the diffusion coefficients for $\mathrm{NO_3}$ and $\mathrm{NH_4}$ which depend on the bioturbation status of the respective geochemical zone (compare Section 3.2.3.1). Integration of

Table 3.4: Boundary conditions for nitrate and ammonium. For the boundaries we define: $z_{\_}^{-} := \lim_{h\to 0}(z_{\_} - h)$ and $z_{\_}^{+} := \lim_{h\to 0}(z_{\_} + h)$.

Boundary	**Condition**		
$z = 0$	known concentration	1)	$NO_3(0) = NO_{30}$
$z = z_{bio}$	continuity	2)	$NO_3(z_{bio}^{-})$=$NO_3(z_{bio}^{+})$
		3)	$-\left(D_{NO_3,0} + D_{bio}\right) \cdot \frac{\partial NO_3}{\partial z}\vert_{z_{bio}^{-}} = -D_{NO_3,0} \cdot \frac{\partial NO_3}{\partial z}\vert_{z_{bio}^{+}}$
$z = z_{ox}$	continuity	4)	$NO_3(z_{ox}^{-})$=$NO_3(z_{ox}^{+})$
		5)	$-D_{NO_3} \cdot \frac{\partial NO_3}{\partial z}\vert_{z_{ox}^{-}} + \gamma_{NH_4} \cdot F_{NH_4}(z_{ox}) = -D_{NO_3} \cdot \frac{\partial NO_3}{\partial z}\vert_{z_{ox}^{+}}$
	where:		$F_{NH_4}(z_{ox}) = \frac{1}{1+K_{NH_4}} \cdot \frac{1-\phi}{\phi} \cdot \int_{z_{NO_3}}^{\infty} \sum_i NC_i \cdot k_i \cdot POC_i \; dz$
$z = z_{NO_3}$	NO_3 consumption	6)	**IF** $(NO_3(z_\infty) > 0)$
	$(z_{NO_3} = z_\infty)$	6.1)	$\frac{\partial NO_3}{\partial z}\vert_{z_{NO_3}} = 0$
			ELSE
	$(z_{NO_3} < z_\infty)$	6.2)	$NO_3(z_{NO_3}) = 0$ and $\frac{\partial NO_3}{\partial z}\vert_{z_{NO_3}} = 0$
$z = 0$	known concentration	1)	$NH_4(0) = NH_{40}$
$z = z_{bio}$	continuity	2)	$NH_4(z_{bio}^{-})$=$NH_4(z_{bio}^{+})$
		3)	$-\frac{D_{NH_4,0}+D_{bio}}{1+K_{NH_4}} \cdot \frac{\partial NH_4}{\partial z}\vert_{z_{bio}^{-}} = -\frac{D_{NH_4,0}}{1+K_{NH_4}} \cdot \frac{\partial NH_4}{\partial z}\vert_{z_{bio}^{+}}$
$z = z_{ox}$	continuity	4)	$NH_4(z_{ox}^{-})$=$NH_4(z_{ox}^{+})$
		5)	$-\frac{D_{NH_4}}{1+K_{NH_4}} \cdot \frac{\partial NH_4}{\partial z}\vert_{z_{ox}^{-}} - \gamma_{NH_4} \cdot F_{NH_4}(z_{ox}) = -\frac{D_{NH_4}}{1+K_{NH_4}} \cdot \frac{\partial NH_4}{\partial z}\vert_{z_{ox}^{+}}$
	where:		$F_{NH_4}(z_{ox}) = \frac{1}{1+K_{NH_4}} \cdot \frac{1-\phi}{\phi} \cdot \int_{z_{NO_3}}^{\infty} \sum_i NC_i \cdot k_i \cdot POC_i \; dz$
$z = z_{NO_3}$	continuity	6)	$NH_4(z_{NO_3}^{-})$=$NH_4(z_{NO_3}^{+})$
	flux	7)	$-\frac{D_{NH_4}}{1+K_{NH_4}} \cdot \frac{\partial NH_4}{\partial z}\vert_{z_{NO_3}^{-}} = -\frac{D_{NH_4}}{1+K_{NH_4}} \cdot \frac{\partial NH_4}{\partial z}\vert_{z_{NO_3}^{+}}$
$z = z_\infty$	zero NH_4 flux	8)	$\frac{\partial NH_4}{\partial z}\vert_{z_\infty} = 0$

Eq. (3.16) - (3.20) yields the analytical solutions, which are not further developed here but follow the procedure outlined in Section 3.2.2.2 for oxygen (also see Section 3.2.3.1 for more details on how to find the analytical solution). Table 3.4 summarises the boundary conditions applied in OMEN-SED to solve Eq. (3.16) - (3.20) and to find the *a priori* unknown nitrate penetration depth, z_{NO_3}. The model assumes known bottom water concentrations for both NO_3 and NH_4, the complete consumption of nitrate at the nitrate penetration depth (in case $z_{NO_3} < z_\infty$) and no change in ammonium flux at z_∞. In addition, concentration and diffusive flux continuity across z_{bio} and z_{ox} is considered for NO_3 and NH_4. Furthermore, the reoxidation of upward-diffusing reduced ammonium is accounted for in the oxic-anoxic boundary condition for nitrate and ammonium. OMEN-SED iteratively solves for z_{NO_3} by first testing if there is nitrate left at z_∞ (i.e. $NO_3(z_\infty) > 0$) and, otherwise, by finding the root for the flux boundary condition 6.2 (Table 3.4).

3.2.2.4 Sulfate and Sulfide

Below the denitrification zone ($z > z_{NO_3}$), organic matter degradation is coupled to sulfate reduction, consuming sulfate and producing hydrogen sulfide with a fixed $SO_4 : C$ ratio (SO_4C,

Tab. 3.10). In addition, the anaerobic oxidation of upward diffusing methane (AOM) produced below the sulfate penetration and the associated consumption of sulfate and production of sulfide; as well as the production of sulfate and consumption of sulfide through sulfide oxidation are implicitly accounted for through the boundary conditions (Table 3.5). The conservation equations for sulfate and sulfide are thus given by:

1. Oxic and nitrogenous zone ($z \leq z_{NO_3}$)

$$\frac{\partial SO_4{}^I}{\partial t} = 0 = D_{SO_4} \frac{\partial^2 SO_4{}^I}{\partial z^2} - w \frac{\partial SO_4{}^I}{\partial z} \tag{3.21}$$

$$\frac{\partial H_2S^I}{\partial t} = 0 = D_{H_2S} \frac{\partial^2 H_2S^I}{\partial z^2} - w \frac{\partial H_2S^I}{\partial z} \tag{3.22}$$

2.Sulfidic zone ($z_{NO_3} < z \leq z_{SO_4}$)

$$\frac{\partial SO_4{}^{II}}{\partial t} = 0 = D_{SO_4} \frac{\partial^2 SO_4{}^{II}}{\partial z^2} - w \frac{\partial SO_4{}^{II}}{\partial z} - \frac{1-\phi}{\phi} \cdot \sum_i SO_4C \cdot k_i \cdot POC_i(z) \tag{3.23}$$

$$\frac{\partial H_2S^{II}}{\partial t} = 0 = D_{H_2S} \frac{\partial^2 H_2S^{II}}{\partial z^2} - w \frac{\partial H_2S^{II}}{\partial z} + \frac{1-\phi}{\phi} \cdot \sum_i SO_4C \cdot k_i \cdot POC_i(z) \tag{3.24}$$

3. Methanic zone ($z_{SO_4} < z \leq z_\infty$)

$$\frac{\partial H_2S^{III}}{\partial t} = 0 = D_{H_2S} \frac{\partial^2 H_2S^{III}}{\partial z^2} - w \frac{\partial H_2S^{III}}{\partial z} \tag{3.25}$$

where D_{SO_4} and D_{H_2S} denote the diffusion coefficients for SO_4 and H_2S which depend on the bioturbation status of the respective geochemical zone (compare Section 3.2.3.1). Integration of Eq. (3.21) - (3.25) yields the analytical solution and Table 3.5 summarises the boundary conditions applied. OMEN-SED assumes known concentrations at the sediment-water interface and continuity across the bioturbation depth and the nitrate penetration depth. The reoxidation of reduced H_2S to SO_4 is accounted for implicitly via the oxic-anoxic boundary condition for both species, while reduction of SO_4 and the associated production of H_2S via AOM is accounted for through the respective boundary conditions at z_{SO_4}. In case $z_{SO_4} < z_\infty$, OMEN-SED assumes zero sulfate concentration at z_{SO_4} and its diffusive flux must equal the amount of methane produced below (with a methane to carbon ratio of MC); or, in case $z_{SO_4} = z_\infty$, a zero diffusive flux condition for sulfate is considered. OMEN-SED iteratively solves for z_{SO_4} by first testing if there is sulfate left at z_∞ (i.e. $SO_4(z_\infty) > 0$) and, otherwise, by finding the root for the flux boundary condition 8.2 (Table 3.5). At the lower boundary z_∞ zero diffusive flux of H_2S is considered.

3.2.2.5 Phosphate

The biogeochemical description of phosphorus (P) dynamics builds on earlier models developed by Slomp et al. [1996] and accounts for phosphorus recycling through organic matter degradation,

Table 3.5: Boundary conditions for sulfate and sulfide. For the boundaries we define: $z_{\_\_}^{-} := \lim_{h\to 0}(z_{\_\_} - h)$ and $z_{\_}^{+} := \lim_{h\to 0}(z_{\_} + h)$.

Boundary	**Condition**		
$z = 0$	known concentration	1)	$SO_4(0)$=SO_{40}
$z = z_{\text{bio}}$	continuity	2)	$SO_4(z_{\text{bio}}^{-})$=$SO_4(z_{\text{bio}}^{+})$
	flux	3)	$-\left(D_{SO_4,0} + D_{\text{bio}}\right) \cdot \frac{\partial SO_4}{\partial z}\vert_{z_{\text{bio}}^{-}} = -D_{SO_4,0} \cdot \frac{\partial SO_4}{\partial z}\vert_{z_{\text{bio}}^{+}}$
$z = z_{\text{ox}}$	continuity	4)	$SO_4(z_{\text{ox}}^{-})$=$SO_4(z_{\text{ox}}^{+})$
	flux	5)	$-D_{SO_4} \cdot \frac{\partial SO_4}{\partial z}\vert_{z_{\text{ox}}^{-}} + \gamma_{H_2S} \cdot F_{H_2S}(z_{\text{ox}}) = -D_{SO_4} \cdot \frac{\partial SO_4}{\partial z}\vert_{z_{\text{ox}}^{+}}$
	where:		$F_{H_2S}(z_{\text{ox}}) = \frac{1-\phi}{\phi} \cdot \left(\int_{z_{NO_3}}^{SO_4} \sum_i SO_4C \cdot k_i \cdot POC_i \; dz + \gamma_{CH_4} \cdot \int_{z_{SO_4}}^{\infty} \sum_i MC \cdot k_i \cdot POC_i \; dz\right)$
$z = z_{NO_3}$	continuity	6)	$SO_4(z_{NO_3}^{-})$=$SO_4(z_{NO_3}^{+})$
	flux	7)	$-D_{SO_4} \cdot \frac{\partial SO_4}{\partial z}\vert_{z_{NO_3}^{-}} = -D_{SO_4} \cdot \frac{\partial SO_4}{\partial z}\vert_{z_{NO_3}^{+}}$
$z = z_{SO_4}$	SO_4 consumption	8)	**IF** $(SO_4(z_\infty) > 0)$
	$(z_{SO_4} = z_\infty)$	8.1)	$\frac{\partial SO_4}{\partial z}\vert_{z_{SO_4}} = 0$
			ELSE
	$(z_{SO_4} < z_\infty)$	8.2)	$SO_4(z_{SO_4}) = 0 \quad \text{and} \quad -D_{SO_4} \cdot \frac{\partial SO_4}{\partial z}\vert_{z_{SO_4}} = \gamma_{CH_4} \cdot F_{CH_4}(z_{SO_4})$
	with		$F_{CH_4}(z_{SO_4}) = \frac{1-\phi}{\phi} \cdot \int_{z_{SO_4}}^{\infty} \sum_i MC \cdot k_i \cdot POC_i \; dz$
$z = 0$	known concentration	1)	$H_2S(0) = H_2S_0$
$z = z_{\text{bio}}$	continuity	2)	$H_2S(z_{\text{bio}}^{-})$=$H_2S(z_{\text{bio}}^{+})$
	flux	3)	$-\left(D_{H_2S,0} + D_{\text{bio}}\right) \cdot \frac{\partial H_2S}{\partial z}\vert_{z_{\text{bio}}^{-}} = -D_{H_2S,0} \cdot \frac{\partial H_2S}{\partial z}\vert_{z_{\text{bio}}^{+}}$
$z = z_{\text{ox}}$	continuity	4)	$H_2S(z_{\text{ox}}^{-})$=$H_2S(z_{\text{ox}}^{+})$
	flux	5)	$-D_{H_2S} \cdot \frac{\partial H_2S}{\partial z}\vert_{z_{\text{ox}}^{-}} - \gamma_{H_2S} F_{H_2S}(z_{\text{ox}}) = -D_{H_2S} \cdot \frac{\partial H_2S}{\partial z}\vert_{z_{\text{ox}}^{+}}$
	where:		$F_{H_2S}(z_{\text{ox}}) = \frac{1-\phi}{\phi} \cdot \left(\int_{z_{NO_3}}^{SO_4} \sum_i SO_4C \cdot k_i \cdot POC_i \; dz + \gamma_{CH_4} \cdot \int_{z_{SO_4}}^{\infty} \sum_i MC \cdot k_i \cdot POC_i \; dz\right)$
$z = z_{NO_3}$	continuity	6)	$H_2S(z_{NO_3}^{-})$=$H_2S(z_{NO_3}^{+})$
	flux	7)	$-D_{H_2S} \cdot \frac{\partial H_2S}{\partial z}\vert_{z_{NO_3}^{-}} = -D_{H_2S} \cdot \frac{\partial H_2S}{\partial z}\vert_{z_{NO_3}^{+}}$
$z = z_{SO_4}$	continuity	8)	$H_2S(z_{SO_4}^{-})$=$H_2S(z_{SO_4}^{+})$
	flux (with AOM)	9)	$-D_{H_2S} \cdot \frac{\partial H_2S}{\partial z}\vert_{z_{SO_4}^{-}} + \gamma_{CH_4} \cdot F_{CH_4}(z_{SO_4}) = -D_{H_2S} \cdot \frac{\partial H_2S}{\partial z}\vert_{z_{SO_4}^{+}}$
	where:		$F_{CH_4}(z_{SO_4}) = \frac{1-\phi}{\phi} \cdot \int_{z_{SO_4}}^{\infty} \sum_i MC \cdot k_i \cdot POC_i \; dz$
$z = z_\infty$	zero H_2S flux	10)	$\frac{\partial H_2S}{\partial z}\vert_{z_\infty} = 0$

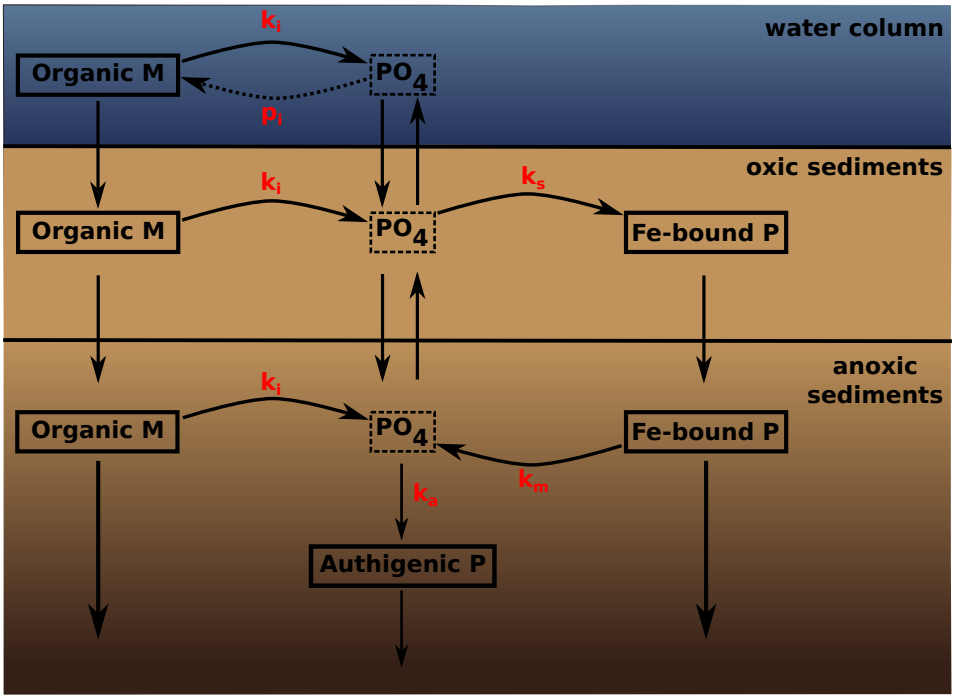

Figure 3.2: A schematic of the sedimentary P cycle in OMEN-SED. Red numbers represent kinetic rate constants for phosphorus dynamics (compare Table 3.10; p_i represents uptake rate of PO_4 via primary production in shallow environments). Adapted from Slomp et al. [1996].

adsorption onto sediments and iron(III) hydroxides (Fe-bound P), as well as carbonate fluorapatite (CFA or authigenic P) formation (see Figure 3.2 for a schematic overview of the sedimentary P cycle). In the oxic zone of the sediment, PO_4 liberated through organic matter degradation can adsorb to iron(III) hydroxides forming Fe-bound P [or FeP, Slomp et al., 1998]. Below the oxic zone, PO_4 is not only produced via organic matter degradation but can also be released from the Fe-bound P pool due to the reduction of iron(III) hydroxides under anoxic conditions. Furthermore, in these zones phosphate concentrations build up and pore waters can thus become supersaturated with respect to carbonate fluorapatite, thus triggering the authigenic formation of CFA [Van Cappellen and Berner, 1988]. Phosphorus bound in these authigenic minerals represents a permanent sink for reactive phosphorus [Slomp et al., 1996]. As for ammonium, the adsorption of P to the sediment matrix is treated as an equilibrium processes, parameterised with dimensionless adsorption coefficients for the oxic and anoxic zone, respectively [$K^{\mathrm{ox}}_{\mathrm{PO_4}}$, $K^{\mathrm{anox}}_{\mathrm{PO_4}}$ Slomp et al., 1998]. The sorption and desorption of P to iron(III) hydroxides as well as the authigenic fluorapatite formation are described as first-order reactions with rate constants k_s, k_m and k_a, respectively (Table 3.10). The rate of the respective process is calculated as the product of the rate constant and the difference between the current concentration (of PO_4 and FeP) and an equilibrium or asymptotic concentration Slomp et al. [1996]. The asymptotic Fe-

bound P concentration is FeP^{∞} and the equilibrium concentration for P sorption and authigenic fluorapatite formation are ${PO_4}^s$ and ${PO_4}^a$, respectively (Table 3.10). The last term in Eq. (3.26) and (3.27) represents sorption of PO_4 to FeP in the oxic zone, the last term in Eq. (3.28) and (3.29) is the release of PO_4 from the FeP pool and the 4th term in Eq. (3.29) represents the permanent loss of PO_4 to authigenic fluorapatite formation. The conservation equations for phosphate and Fe-bound P are thus given by:

1. Oxic zone ($z \leq z_{ox}$)

$$\frac{\partial {PO_4}^I}{\partial t} = \frac{D_{PO_4}}{1+K^{ox}_{PO_4}} \frac{\partial^2 {PO_4}^I}{\partial z^2} - w\frac{\partial {PO_4}^I}{\partial z} + \frac{1-\phi}{\phi}\frac{1}{1+K^{ox}_{PO_4}} \sum_i (PC_i \cdot k_i \cdot POC_i(z))$$

$$- \frac{k_s}{1+K^{ox}_{PO_4}} ({PO_4}^I - {PO_4}^s) \tag{3.26}$$

$$\frac{\partial FeP^I}{\partial t} = D_{FeP}\frac{\partial^2 FeP^I}{\partial z^2} - w\frac{\partial FeP^I}{\partial z} + \frac{\phi}{1-\phi} k_s ({PO_4}^I - {PO_4}^s) \tag{3.27}$$

2. Anoxic zones ($z_{ox} < z \leq z_{\infty}$)

$$\frac{\partial FeP^{II}}{\partial t} = D_{FeP}\frac{\partial^2 FeP^{II}}{\partial z^2} - w\frac{\partial FeP^{II}}{\partial z} - k_m (FeP^{II} - FeP^{\infty}) \tag{3.28}$$

$$\frac{\partial {PO_4}^{II}}{\partial t} = \frac{D_{PO_4}}{1+K^{anox}_{PO_4}} \frac{\partial^2 {PO_4}^{II}}{\partial z^2} - w\frac{\partial {PO_4}^{II}}{\partial z} + \frac{1-\phi}{\phi}\frac{1}{1+K^{anox}_{PO_4}} \sum_i (PC_i \cdot k_i \cdot POC_i(z))$$

$$- \frac{k_a}{1+K^{anox}_{PO_4}} ({PO_4}^{II} - {PO_4}^a) + \frac{(1-\phi)}{\phi}\frac{k_m}{1+K^{anox}_{PO_4}} (FeP^{II} - FeP^{\infty}) \tag{3.29}$$

where D_{PO_4} denotes the diffusion coefficient for PO_4 which depends on the bioturbation status of the respective geochemical zone and $D_{FeP} = D_{bio}$ for $z \leq z_{bio}$ and $D_{FeP} = 0$ for $z > z_{bio}$ (compare Section 3.2.3.1). Integration of Eq. (3.26) - (3.29) yields the analytical solution and Table 3.6 summarises the boundary conditions applied in OMEN-SED. The model assumes known bottom water concentrations and equal concentrations and diffusive fluxes at z_{bio} and z_{ox} for both species. Additionally OMEN-SED considers no change in phosphate flux and an asymptotic Fe-bound P concentration at z_{∞}.

3.2.2.6 Dissolved Inorganic Carbon (DIC)

OMEN-SED accounts for the production of dissolved inorganic carbon (DIC) through organic matter degradation, as well as methane oxidation. Organic matter degradation produces dissolved inorganic carbon with a stoichiometric DIC : C ratio of 1:2 in the methanic zone and 1:1 in the rest of the sediment column ($DICC^{II}$ and $DICC^{I}$ respectively). DIC production through methane oxidation is implicitly taken into account through the boundary condition at z_{SO_4}. A mechanistic description of DIC production from $CaCO_3$ dissolution would lead to significant mathematical problems and is therefore not included in the current version of OMEN-SED. The conservation equations for DIC are thus given by:

Table 3.6: Boundary conditions for phosphate and Fe-bound P (FeP). For the boundaries we define: $z^-_{\_} := \lim_{h\to 0}(z_{\_} - h)$ and $z^+_{\_} := \lim_{h\to 0}(z_{\_} + h)$.

Boundary	**Condition**	
$z = 0$	known concentration	1) $PO_4(0)=PO_{40}$
$z = z_{\text{bio}}$	continuity	2) $PO_4(z^-_{\text{bio}})=PO_4(z^+_{\text{bio}})$
	flux	3) $\left(D_{PO_4,0} + D_{\text{bio}}\right) \cdot \frac{\partial PO_4}{\partial z}\vert_{z^-_{\text{bio}}} = D_{PO_4,0} \cdot \frac{\partial PO_4}{\partial z}\vert_{z^+_{\text{bio}}}$
$z = z_{\text{ox}}$	continuity	4) $PO_4(z^-_{\text{ox}})=PO_4(z^+_{\text{ox}})$
	flux	5) $-\frac{D_{PO_4}}{1+K^{ox}_{PO_4}} \cdot \frac{\partial PO_4}{\partial z}\vert_{z^-_{\text{ox}}} = -\frac{D_{PO_4}}{1+K^{anox}_{PO_4}} \cdot \frac{\partial PO_4}{\partial z}\vert_{z^+_{\text{ox}}}$
$z = z_\infty$	flux	10) $\frac{\partial PO_4}{\partial z}\vert_{z_\infty} = 0$
$z = 0$	known concentration	1) $FeP(0) = FeP_0$
$z = z_{\text{bio}}$	continuity	2) $FeP(z^-_{\text{bio}})=FeP(z^+_{\text{bio}})$
	flux	3) $\frac{\partial FeP}{\partial z}\vert_{z^-_{\text{bio}}} = \frac{\partial FeP}{\partial z}\vert_{z^+_{\text{bio}}}$
$z = z_{\text{ox}}$	continuity	4) $FeP(z^-_{\text{ox}})=FeP(z^+_{\text{ox}})$
	flux	5) $\frac{\partial FeP}{\partial z}\vert_{z^-_{\text{ox}}} = \frac{\partial FeP}{\partial z}\vert_{z^+_{\text{ox}}}$
$z = z_\infty$	asymptotic concentration	10) $FeP(z_\infty) = FeP_\infty$

1. Oxic, nitrogenous and sulfidic zone ($z \le z_{SO_4}$)

$$\frac{\partial \text{DIC}^I}{\partial t} = 0 = D_{\text{DIC}} \frac{\partial^2 \text{DIC}^I}{\partial z^2} - w \frac{\partial \text{DIC}^I}{\partial z} + \frac{1-\phi}{\phi} \cdot \sum_i \text{DICC}^{\text{I}} \cdot k_i \cdot \text{POC}_i(z) \tag{3.30}$$

2. Methanic zone ($z_{SO_4} < z \le z_\infty$)

$$\frac{\partial \text{DIC}^{II}}{\partial t} = 0 = D_{\text{DIC}} \frac{\partial^2 \text{DIC}^{II}}{\partial z^2} - w \frac{\partial \text{DIC}^{II}}{\partial z} + \frac{1-\phi}{\phi} \cdot \sum_i \text{DICC}^{\text{II}} \cdot k_i \cdot \text{POC}_i(z) \tag{3.31}$$

where D_{DIC} denotes the diffusion coefficient for DIC (taking the values for HCO_3^- from Schulz [2006]) which depends on the bioturbation status of the respective geochemical zone. Integration of Eq. (3.30) and (3.31) yields the analytical solution and Table 3.7 summarises the boundary conditions applied in OMEN-SED. A Dirichlet condition is applied at the sediment-water interface. In addition, the model assumes a zero diffusive flux through the lower boundary z_∞ and continuity across the bottom of the bioturbated zone, as well as the sulfate penetration depth. An additional flux boundary condition at z_{SO_4}, implicitly accounts for DIC production through anaerobic oxidation of methane (Table 3.7 Eq. 5).

3.2.2.7 Alkalinity

Organic matter degradation and secondary redox reactions exert a complex influence on alkalinity [e.g. Jourabchi et al., 2005; Krumins et al., 2013; Wolf-Gladrow et al., 2007]. To model alkalinity, OMEN-SED divides the sediment column is into four geochemical zones, where different equations describe the biogeochemical processes using variable stoichiometric coefficients (compare values in Table 3.10). Above z_{ox}, the combined effects of NH_4 and P release due to aerobic OM degradation increases alkalinity according to ALK^{OX} whereas nitrification decreases

Table 3.7: Boundary conditions for DIC. For the boundaries we define: $z^-_{\_} := \lim_{h\to 0}(z_{\_} - h)$ and $z^+_{\_} := \lim_{h\to 0}(z_{\_} + h)$.

Boundary	**Condition**	
$z = 0$	known concentration	1) $\mathrm{DIC}(0) = \mathrm{DIC}_0$
$z = z_{\mathrm{bio}}$	continuity	2) $\mathrm{DIC}(z^-_{\mathrm{bio}})$=$\mathrm{DIC}(z^+_{\mathrm{bio}})$
	flux	3) $-\left(D_{\mathrm{DIC},0} + D_{\mathrm{bio}}\right) \cdot \frac{\partial \mathrm{DIC}}{\partial z}\vert_{z^-_{\mathrm{bio}}} = -D_{\mathrm{DIC},0} \cdot \frac{\partial \mathrm{DIC}}{\partial z}\vert_{z^+_{\mathrm{bio}}}$
$z = z_{\mathrm{SO_4}}$	continuity	4) $\mathrm{DIC}(z^-_{\mathrm{SO_4}})$=$\mathrm{DIC}(z^+_{\mathrm{SO_4}})$
	flux (with AOM)	5) $-D_{\mathrm{DIC}} \cdot \frac{\partial \mathrm{DIC}}{\partial z}\vert_{z^-_{\mathrm{SO_4}}} + \gamma_{\mathrm{CH_4}} \cdot F_{\mathrm{CH_4}}(z_{\mathrm{SO_4}}) = -D_{\mathrm{DIC}} \cdot \frac{\partial \mathrm{DIC}}{\partial z}\vert_{z^+_{\mathrm{SO_4}}}$
	where:	$F_{\mathrm{CH_4}}(z_{\mathrm{SO_4}}) = \frac{1-\phi}{\phi} \cdot \int_{z_{\mathrm{SO_4}}}^{\infty} \sum_i \mathrm{MC} \cdot k_i \cdot \mathrm{POC}_i \, dz$
$z = z_\infty$	zero DIC flux	6) $\frac{\partial \mathrm{DIC}}{\partial z}\vert_{z_\infty} = 0$

alkalinity with stoichiometry $\mathrm{ALK^{NIT}}$. In the remaining three zones anaerobic OM degradation generally results in an increase in alkalinity, with the exact magnitude depending on the nature of the terminal electron acceptor used (i.e. $\mathrm{ALK^{DEN}}$, $\mathrm{ALK^{SUL}}$, $\mathrm{ALK^{MET}}$). In addition, the effect of secondary redox reactions, such as nitrification, sulfide and methane oxidation are implicitly accounted for in the boundary conditions. Note that the alkalinity description in the current version of OMEN-SED does not account for $CaCO_3$ dissolution/precipitation due to the mathematical complexity of the problem. In OMEN-SED, the conservation equations for alkalinity are thus given by:

1. Oxic zone ($z \le z_{\mathrm{ox}}$)

$$\begin{aligned} \frac{\partial \mathrm{ALK}^I}{\partial t} = 0 = D_{\mathrm{ALK}} \frac{\partial^2 \mathrm{ALK}^I}{\partial z^2} - w \frac{\partial \mathrm{ALK}^I}{\partial z} \\ + \frac{1-\phi}{\phi} \cdot \sum_i \left(\mathrm{ALK^{NIT}} \cdot \frac{\gamma_{\mathrm{NH_4}}}{1 + K_{\mathrm{NH_4}}} \mathrm{NC_i} + \mathrm{ALK^{OX}} \right) \cdot k_i \cdot \mathrm{POC}_i(z) \end{aligned} \tag{3.32}$$

2. Dentrification or nitrogenous zone ($z_{\mathrm{ox}} < z \le z_{\mathrm{NO_3}}$)

$$\frac{\partial \mathrm{ALK}^{II}}{\partial t} = 0 = D_{\mathrm{ALK}} \frac{\partial^2 \mathrm{ALK}^{II}}{\partial z^2} - w \frac{\partial \mathrm{ALK}^{II}}{\partial z} + \frac{1-\phi}{\phi} \cdot \sum_i \mathrm{ALK^{DEN}} \cdot k_i \cdot \mathrm{POC}_i(z) \tag{3.33}$$

3. Sulfidic zone ($z_{\mathrm{NO_3}} < z \le z_{\mathrm{SO_4}}$)

$$\frac{\partial \mathrm{ALK}^{III}}{\partial t} = 0 = D_{\mathrm{ALK}} \frac{\partial^2 \mathrm{ALK}^{III}}{\partial z^2} - w \frac{\partial \mathrm{ALK}^{III}}{\partial z} + \frac{1-\phi}{\phi} \cdot \sum_i \mathrm{ALK^{SUL}} \cdot k_i \cdot \mathrm{POC}_i(z) \tag{3.34}$$

4. Methanic zone ($z_{\mathrm{SO_4}} < z \le z_\infty$)

$$\frac{\partial \mathrm{ALK}^{IV}}{\partial t} = 0 = D_{\mathrm{ALK}} \frac{\partial^2 \mathrm{ALK}^{IV}}{\partial z^2} - w \frac{\partial \mathrm{ALK}^{IV}}{\partial z} + \frac{1-\phi}{\phi} \cdot \sum_i \mathrm{ALK^{MET}} \cdot k_i \cdot \mathrm{POC}_i(z) \tag{3.35}$$

where D_{ALK} denotes the diffusion coefficient for alkalinity (taking the values for HCO_3^- from Schulz [2006]) which depends on the bioturbation status of the respective geochemical zone.

Integration of Eq. (3.32) - (3.35) yields the analytical solution and Table 3.8 summarises the boundary conditions applied in OMEN-SED. A Dirichlet boundary condition is applied at the sediment-water interface. The decrease of alkalinity due to oxidation of reduced species produced in the anoxic zones (with stoichiometry $\mathrm{ALK}^{\mathrm{NIT}}$ and $\mathrm{ALK}^{\mathrm{H_2S}}$) is implicitly taken into account through the flux boundary condition at z_{ox} (Table 3.8 Eq. 5). Furthermore, the oxidation of methane by sulfate reduction increases alkalinity with stoichiometry $\mathrm{ALK}^{\mathrm{AOM}}$ which is accounted for through the flux boundary condition at $z_{\mathrm{SO_4}}$ (Table 3.8 Eq. 9). At the lower boundary z_∞ a zero diffusive flux condition is applied.

3.2.3 Determination of Integration Constants

The integration constants of all general analytical solutions derived above change in response to changing boundary conditions. Thus, OMEN-SED has to re-determine integration constants for each dynamic zone (i.e. $z_{\mathrm{ox}}, z_{\mathrm{bio}}, z_{\mathrm{NO_3}}$ and $z_{\mathrm{SO_4}}$) at every time step for all biogeochemnical species. The bioturbation boundary poses a particular challenge as it can theoretically occur in any of the dynamic geochemical zones (Fig. 3.3). Therefore, in order to generalise and simplify this recurring boundary matching problem, an independent, generic algorithm (Generic Boundary Condition Matching) is implemented (rather than using multiple fully-worked-out algebraic solutions for each possible case and every biogeochemical species). As a consequence, the algorithm only has to solve a two-simultaneous-equation problem.

3.2.3.1 Generic Boundary Condition Matching (GBCM)

As discussed in Section 3.2.1, the solution of the general steady-state transport-reaction equation (Eq. (3.3)) for a generic species C is of the general form:

$$C(z) = A\exp(az) + B\exp(bz) + \sum_j \frac{\alpha_j}{D\beta_j^2 - w\beta_j - k} \cdot \exp(-\beta_j z) + \frac{Q}{k} \tag{3.36}$$

and can therefore be expressed as:

$$C(z) = A \cdot E(z) + B \cdot F(z) + G(z) \tag{3.37}$$

where $E(z)$, $F(z)$ are the homogeneous solutions of the ODE, G(z) the particular integral (collectively called the basis functions), and A, B are the integration constants that must be determined using the boundary conditions (shown in Fig. 3.3 for the whole sediment column).

Each internal boundary matching problem (i.e. excluding $z = 0$ and $z = z_\infty$) involves matching continuity and flux for the two solutions of the respective reaction-transport equation above, $C_U(z)$ (= 'upper'), and below, $C_L(z)$ (= 'lower'), the dynamic boundary at $z = z_b$:

$$C_U(z) = A_U \cdot E_U(z) + B_U \cdot F_U(z) + G_U(z) \tag{3.38}$$

$$C_L(z) = A_L \cdot E_L(z) + B_L \cdot F_L(z) + G_L(z). \tag{3.39}$$

Table 3.8: Boundary conditions for alkalinity. For the boundaries we define: $z_{\_}^{-} := \lim_{h\to 0}(z_{\_} - h)$ and $z_{\_}^{+} := \lim_{h\to 0}(z_{\_} + h)$.

Boundary	**Condition**		
$z = 0$	known concentration	1)	$\mathrm{ALK}(0) = \mathrm{ALK}_0$
$z = z_{\mathrm{bio}}$	continuity	2)	$\mathrm{ALK}(z_{\mathrm{bio}}^{-}) = \mathrm{ALK}(z_{\mathrm{bio}}^{+})$
	flux	3)	$-\left(D_{\mathrm{ALK},0} + D_{\mathrm{bio}}\right) \cdot \frac{\partial \mathrm{ALK}}{\partial z}\big\vert_{z_{\mathrm{bio}}^{-}} = -D_{\mathrm{ALK},0} \cdot \frac{\partial \mathrm{ALK}}{\partial z}\big\vert_{z_{\mathrm{bio}}^{+}}$
$z = z_{\mathrm{ox}}$	continuity	4)	$\mathrm{ALK}(z_{\mathrm{ox}}^{-}) = \mathrm{ALK}(z_{\mathrm{ox}}^{+})$
	flux	5)	$-D_{\mathrm{ALK}} \cdot \frac{\partial \mathrm{ALK}}{\partial z}\big\vert_{z_{\mathrm{ox}}^{-}} + F_{\mathrm{ALK}}(z_{\mathrm{ox}}) = -D_{\mathrm{ALK}} \cdot \frac{\partial \mathrm{ALK}}{\partial z}\big\vert_{z_{\mathrm{ox}}^{+}}$
	where:		$F_{\mathrm{ALK}}(z_{\mathrm{ox}}) = \frac{1-\phi}{\phi} \cdot \left(\mathrm{ALK}^{\mathrm{H_2S}} \cdot \gamma_{\mathrm{H_2S}} \int_{z_{\mathrm{NO_3}}}^{\mathrm{SO_4}} \sum_i \mathrm{SO_4C} \cdot k_i \cdot \mathrm{POC}_i \, dz\right)$ $+ \frac{1-\phi}{\phi} \cdot \left(\mathrm{ALK}^{\mathrm{NIT}} \frac{\gamma_{\mathrm{NH_4}}}{1+k_{\mathrm{NH_4}}} \int_{z_{\mathrm{NO_3}}}^{\infty} \sum_i \mathrm{NC}_i \cdot k_i \cdot \mathrm{POC}_i \, dz\right)$
$z = z_{\mathrm{NO_3}}$	continuity	6)	$\mathrm{ALK}(z_{\mathrm{NO_3}}^{-}) = \mathrm{ALK}(z_{\mathrm{NO_3}}^{+})$
	flux	7)	$-D_{\mathrm{ALK}} \cdot \frac{\partial \mathrm{ALK}}{\partial z}\big\vert_{z_{\mathrm{NO_3}}^{-}} = -D_{\mathrm{ALK}} \cdot \frac{\partial \mathrm{ALK}}{\partial z}\big\vert_{z_{\mathrm{NO_3}}^{+}}$
$z = z_{\mathrm{SO_4}}$	continuity	8)	$\mathrm{ALK}(z_{\mathrm{SO_4}}^{-}) = \mathrm{ALK}(z_{\mathrm{SO_4}}^{+})$
	flux (with AOM)	9)	$-D_{\mathrm{ALK}} \cdot \frac{\partial \mathrm{ALK}}{\partial z}\big\vert_{z_{\mathrm{SO_4}}^{-}} + F_{\mathrm{ALK}}(z_{\mathrm{SO_4}}) = -D_{\mathrm{ALK}} \cdot \frac{\partial \mathrm{ALK}}{\partial z}\big\vert_{z_{\mathrm{SO_4}}^{+}}$
	where:		$F_{\mathrm{ALK}}(z_{\mathrm{SO_4}}) = \frac{1-\phi}{\phi} \cdot \left(\mathrm{ALK}^{\mathrm{AOM}} \gamma_{\mathrm{CH_4}} \cdot \int_{z_{\mathrm{SO_4}}}^{\infty} \sum_i k_i \cdot \mathrm{POC}_i \, dz\right)$
$z = z_{\infty}$	zero ALK flux	10)	$\frac{\partial \mathrm{ALK}}{\partial z}\big\vert_{z_{\infty}} = 0$

OMEN-SED generally applies concentration continuity and flux boundary conditions at its internal, dynamic boundaries:
Continuity (where for generality we allow a discontinuity V_b)

$$C_U(z_b) = C_L(z_b) + V_b \tag{3.40}$$

Flux

$$D_U C'_U(z_b) + wC_U(z_b) = D_L C'_L(z_b) + wC_L(z_b) + F_b \tag{3.41}$$

where w is advection, D are the diffusion coefficients and F_b is any flux discontinuity (e.g. resulting from secondary redox reactions).

Considering that the advective flux above and below the boundary is equal (i.e. $wC_U(z_b) = wC_L(z_b)$) and substituting the general ODE solutions (3.38), (3.39), the boundary conditions can be represented as two equations connecting the four integration constants:

$$\begin{pmatrix} E_U & F_U \\ D_U E'_U & D_U F'_U \end{pmatrix} \begin{pmatrix} A_U \\ B_U \end{pmatrix} = \begin{pmatrix} E_L & F_L \\ D_L E'_L & D_L F'_L \end{pmatrix} \begin{pmatrix} A_L \\ B_L \end{pmatrix} + \begin{pmatrix} G_L - G_U + V_b \\ D_L G'_L - D_U G'_U + F_b - wV_b \end{pmatrix} \tag{3.42}$$

where the ODE solutions E, F, G are all evaluated at z_b.

Equation (3.42) can now be solved to give A_U and B_U as a function of the integration constants from the layer below (A_L and B_L), thereby constructing a piecewise solution for both layers, with just two integration constants (this is implemented in the function benthic_utils.matchsoln of OMEN-SED):

$$\begin{pmatrix} A_U \\ B_U \end{pmatrix} = \begin{pmatrix} c_1 & c_2 \\ c_3 & c_4 \end{pmatrix} \begin{pmatrix} A_L \\ B_L \end{pmatrix} + \begin{pmatrix} d_1 \\ d_2 \end{pmatrix}. \tag{3.43}$$

Using Eq. (3.43), $C_U(z)$ in (3.38) can now be rewritten as a function of A_L and B_L (implemented in benthic_utils.xformsoln)):

$$C_U(z) = (c_1 A_L + c_2 B_L + d_1) \cdot E_U(z) + (c_3 A_L + c_4 B_L + d_2) \cdot F_U(z) + G_U(z) \tag{3.44}$$

and hence define the "transformed" basis functions $E^*_U(z)$, $F^*_U(z)$, $G^*_U(z)$ such that:

$$C_U(z) = A_L \cdot E^*_U(z) + B_L \cdot F^*_U(z) + G^*_U(z) \tag{3.45}$$

where

$$\begin{aligned} E^*_U(z) &= c_1 E_U(z) + c_3 F_U(z) \\ F^*_U(z) &= c_2 E_U(z) + c_4 F_U(z) \\ G^*_U(z) &= G_U(z) + d_1 E_U(z) + d_2 F_U(z) \end{aligned} \tag{3.46}$$

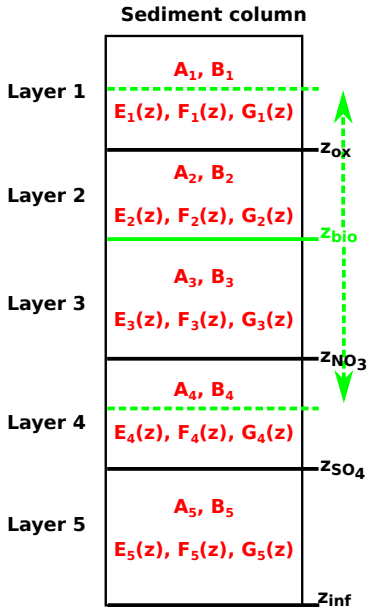

Figure 3.3: Schematic of the generic boundary condition matching (GBCM) problem. Showing the resulting integration constants (A_i, B_i) and ODE solutions (E_i, F_i, G_i) for the different sediment layers and the variable bioturbation boundary.

Equations (3.43), (3.45) and (3.46) can now be consecutively applied for each of the dynamic biogeochemical zone boundaries (Fig. 3.3), starting at the bottom of the sediment column. The net result is a piecewise solution of the whole sediment column with just two integration constants (coming from the lowest layer), which can then be solved for by applying the boundary conditions at the sediment-water interface and the bottom of the sediments.

3.2.3.2 Abstracting out the bioturbation boundary

The bioturbation boundary affects the diffusion coefficient of the modelled solutes, as well as the conservation equation of organic matter (and thereby the exact form of each reaction-transport equation). This boundary is particularly inconvenient as it can, in principle, occur in the middle of any of the dynamically shifting biogeochemical zones and therefore generate multiple cases (Fig. 3.3). The GBCM algorithm described above is thus not only used to construct a piecewise solution of the whole sediment column, but also to abstract out the bioturbation boundary. For each biogeochemical zone the "bioturbation-status" is initially tested (i.e. fully bioturbated, fully non-bioturbated, or crossing the bioturbation boundary). Therefore, the upper and lower boundaries for the different zones (e.g. for the nitrogenous zone: $z_U = z\text{ox}$, $z_L = z_{\text{NO}_3}$), as well as the respective reactive terms and diffusion coefficients (bioturbated and non-bioturbated) are passed over to the routine zTOC.prepfg_l12 where the bioturbation-status is determined. In case the bioturbation depth is located within this zone (i.e. $z_U < z_{\text{bio}} < z_L$) a piecewise solu-

tion for this layer is constructed. Therefore, the reactive terms and diffusion coefficients are handed over to the routines zTOC.calcfg_l1 and zTOC.calcfg_l2 which calculate the basis functions (E_U,F_U,G_U and E_L,F_L,G_L) and their derivatives for the bioturbated and the non-bioturbated part of this specific geochemical zone. The concentration and flux for both solutions at z_{bio} are matched and the coefficients $c_1, c_2, c_3, c_4, d_1, d_2$ (as in Eq. (3.43)) are calculated by the routine benthic_utils.matchsoln. These coefficients and the "bioturbation-status" of the layer are passed back to the main GBCM algorithm where they can be used by the routine benthic_utils.xformsoln to calculate the "transformed" basis functions ($E_U^*(z)$, $F_U^*(z)$, $G_U^*(z)$) such that both layers are expressed in the same basis (compare Eq. (3.44 - 3.46).

For instance, in the case of sulfate, zTOC.prepfg_l12 is called three times before the actual profile is calculated (once per zone: oxic, nitrogenous, sulfidic) and hands back the information about the "bioturbation-status" of the three layers and the coefficients $c_1, c_2, c_3, c_4, d_1, d_2$ for the biogeochemical zone including the bioturbation depth. When calculating the complete piecewise solution for the sediment column, this information is passed to the function zTOC.calcfg_l12 which sorts out the correct solution type to use. The main GBCM algorithm therefore never needs to know whether it is dealing with a piecewise solution (i.e. matched across the bioturbation boundary) or a "simple" solution (i.e. the layer is fully bioturbated or fully non-bioturbated).

3.2.4 Model Parameters

The following section provides a summary of global relationships used to constrain reaction and transport parameters in OMEN-SED. Table 3.9 synthesises sediment and transport parameters, while Tab. 3.10 provides an overview of all biogeochemical parameters used in OMEN-SED.

3.2.4.1 Transport Parameters

The burial of sediments and pore water is directly related to the accumulation of new material on the seafloor [i.e. sedimentation, Burdige, 2006]. This results in a downward advective flux of older sediment material and pore water in relation to the sediment-water interface. When coupled to an ocean model, its sedimentation flux can be readily used in OMEN-SED. The stand-alone version of OMEN-SED uses the empirical global relationship between sediment accumulation rate (w in cm yr^{-1}) and seafloor depth (z in m) of Middelburg et al. [1997]:

$$w = 3.3 \cdot 10^{-0.87478367 - 0.00043512 \cdot z}. \tag{3.47}$$

As an option we include the parameterisation of Burwicz et al. [2011]

$$w = \frac{w_1}{1 + (\frac{z}{z1})^{c1}} + \frac{w_2}{1 + (\frac{z}{z2})^{c2}} \tag{3.48}$$

with parameter values as found in the original study (i.e. $w_1 = 0.117$ cm yr^{-1}, $w_2 = 0.006$ cm yr^{-1}, $z1 = 200$ m, $z2 = 4000$ m, $c1 = 3$, $c2 = 10$). As mentioned before (Section 3.2.1), the diffusion

coefficient of species i is calculated as $D_i = D_{i,0} + D_{\text{bio}} = D_{\text{mol},i} \cdot f_{ir} + D_{\text{bio}}$ for dissolved species and $D_i = D_{\text{bio}}$ for solid species. The bioturbation coefficient D_{bio} (cm^2 yr^-1) is constant in the bioturbated zone and also follows the empirical relationship by Middelburg et al. [1997]:

$$D_{\text{bio}} = 5.2 \cdot 10^{0.76241122 - 0.00039724 \cdot z} \tag{3.49}$$

Observations indicate that bioturbation is largely restricted to the upper 10 cm of the sediments and is only marginally related to seafloor depth [e.g. Boudreau, 1998; Teal et al., 2010]. Therefore, OMEN-SED imposes a globally invariant bioturbation depth z_{bio} of 10 cm. In case the bottom water oxygen concentration is below 5 nmol cm^{-3} infaunnal activity is assumed to cease and $z_{\text{bio}} = 0.01$ cm. We choose a low value unequal to zero in order to simplify the implementation of the model. This approach ensures that the sediment column always consists of a bioturbated (even though very small for the low oxygen condition) and a non-bioturbated zone, thus the same GBCM algorithm can be used to solve the conservation equations. Furthermore, when OMEN-SED is coupled to an Earth system model the same method can be used to convert the POC depositional flux into a SWI concentration (i.e. the flux needs to be converted assuming bioturbation, see Section 4.2).

Bioirrigation (i.e the pumping activity by burrow-dwelling animals) exchanges burrow water with overlying water and may enhance the SWI-flux of solutes [Aller, 1984, 1988]. Several approaches exist to incorporate this into a 1-D diagenetic model, for instance as a non-local transport/exchange process [Boudreau, 1984; Emerson et al., 1984] or as an enhancement factor of the molecular diffusion coefficient [Devol and Christensen, 1993; Soetaert et al., 1996]. In OMEN-SED the latter approach is applied and the apparent "bio-diffusion" coefficient is calculated as $D_{i,0} = D_{\text{mol},i} \cdot f_{ir}$. Soetaert et al. [1996] derived an empirical relationship between f_{ir} and seafloor depth ($f_{ir} = \text{Min}\{1; 15.9 \cdot z^{-0.43}\}$) based on observations from Archer and Devol [1992] and Devol and Christensen [1993]. As this relationship just varies for depth above ~623 m (with a maximum value of 3 at ~50 m) a constant value of $f_{ir} = 1$ is used in the default OMEN-SED configuration. The specific molecular diffusion coefficients $D_{\text{mol},i}$ are corrected for sediment porosity ϕ, tortuosity F and are linearly interpolated for an ambient temperature T using zero-degree coefficients D_i^0 and temperature-dependent diffusion coefficients D_i^T [Soetaert et al., 1996]:

$$D_{\text{mol},i} = (D_i^0 + D_i^T \cdot T) \cdot \frac{1}{\phi \cdot F}.$$

Tortuosity can be expressed in terms of porosity as $F = \frac{1}{\phi^m}$ [Ullman and Aller, 1982] with the exponent m varying according to the type of sediment (here $m = 3$ is used representing muddy sediments with high porosity). Values for D_i^T and D_i^0 are summarised in Table 3.9 and are adapted from Li and Gregory [1974], Schulz [2006] and Gypens et al. [2008].

Table 3.9: Sediment characteristics and transport parameters.

Parameter	Unit	Value	Description/Source
ρ_{sed}	$\text{g}\,\text{cm}^{-3}$	2.6	Sediment density
w	$\text{cm}\,\text{yr}^{-1}$	Fct. of seafloor depth or from ESM	Advection/Sediment accumulation rate [Middelburg et al., 1997]
z_{bio}	cm	10 or 0.01	Bioturbation depth [Boudreau, 1998; Teal et al., 2010]
D_{bio}	$\text{cm}^2\,\text{yr}^{-1}$	Fct. of seafloor depth	Bioturbation coefficient [Middelburg et al., 1997]
ϕ	-	0.85	Porosity
F	-	$\frac{1}{\phi^m}$	Tortuosity, here m=3
f_{ir}	-	1	Irrigation factor
Diffusion coefficients [Gypens et al., 2008; Li and Gregory, 1974; Schulz, 2006]			
$D^0_{\text{O}_2}$	$\text{cm}^2\,\text{yr}^{-1}$	348.62	Molecular diffusion coefficient of oxygen at 0°C
$D^T_{\text{O}_2}$	$\text{cm}^2\,\text{yr}^{-1}\,^\circ\text{C}^{-1}$	14.09	Diffusion coefficient for linear temp. dependence of oxygen
$D^0_{\text{NO}_3}$	$\text{cm}^2\,\text{yr}^{-1}$	308.42	Molecular diffusion coefficient of nitrate at 0°C
$D^T_{\text{NO}_3}$	$\text{cm}^2\,\text{yr}^{-1}\,^\circ\text{C}^{-1}$	12.26	Diffusion coefficient for linear temp. dependence of nitrate
$D^0_{\text{NH}_4}$	$\text{cm}^2\,\text{yr}^{-1}$	309.05	Molecular diffusion coefficient of ammonium at 0°C
$D^T_{\text{NH}_4}$	$\text{cm}^2\,\text{yr}^{-1}\,^\circ\text{C}^{-1}$	12.26	Diffusion coefficient for linear temp. dependence of ammonium
$D^0_{\text{SO}_4}$	$\text{cm}^2\,\text{yr}^{-1}$	157.68	Molecular diffusion coefficient of sulfate at 0°C
$D^T_{\text{SO}_4}$	$\text{cm}^2\,\text{yr}^{-1}\,^\circ\text{C}^{-1}$	7.88	Diffusion coefficient for linear temp. dependence of sulfate
$D^0_{\text{H}_2\text{S}}$	$\text{cm}^2\,\text{yr}^{-1}$	307.48	Molecular diffusion coefficient of sulfide at 0°C
$D^T_{\text{H}_2\text{S}}$	$\text{cm}^2\,\text{yr}^{-1}\,^\circ\text{C}^{-1}$	9.64	Diffusion coefficient for linear temp. dependence of sulfide
$D^0_{\text{PO}_4}$	$\text{cm}^2\,\text{yr}^{-1}$	112.91	Molecular diffusion coefficient of phosphate at 0°C
$D^T_{\text{PO}_4}$	$\text{cm}^2\,\text{yr}^{-1}\,^\circ\text{C}^{-1}$	5.59	Diffusion coefficient for linear temp. dependence of phosphate
D^0_{DIC}	$\text{cm}^2\,\text{yr}^{-1}$	151.69	Molecular diffusion coefficient of DIC at 0°C
D^T_{DIC}	$\text{cm}^2\,\text{yr}^{-1}\,^\circ\text{C}^{-1}$	7.93	Diffusion coefficient for linear temp. dependence of DIC
D^0_{ALK}	$\text{cm}^2\,\text{yr}^{-1}$	151.69	Molecular diffusion coefficient of ALK at 0°C
D^T_{ALK}	$\text{cm}^2\,\text{yr}^{-1}\,^\circ\text{C}^{-1}$	7.93	Diffusion coefficient for linear temp. dependence of ALK
Note: DIC and ALK coefficients are the values of HCO_3^- from Schulz [2006].			

3.2.4.2 Stoichiometries and reaction parameters

The first-order organic matter degradation constants of compound class i, k_i (yr^{-1}), are assumed invariant along the sediment column and therefore independent of the nature of the terminal electron acceptor. The rate constants can be altered manually to fit observed sediment profiles (compare modelled profiles in Section 3.3.2) or related to a master variable provided by a coupled Earth system model (e.g. sedimentation rate, see Section 4.3). The partitioning of the bulk OM pool into reactivity classes (f_i) needs to be specified manually in the stand-alone version or can be provided by the ESM. Organic matter degradation releases N, P and DIC to the pore water using Redfield molar ratios [Redfield, 1963] and consumes TEA with specific stoichiometries (O_2C, NO_3C, SO_4C) as summarised in Table 3.10. Table B.1 in the appendix provides a list of reactions and their stoichiometries as implemented in OMEN-SED. The effect of OM degradation and secondary redox reactions on total alkalinity is also accounted for via reaction specific stoichiometries representing the release of NH_4, H_2S and P and is based on Jourabchi et al. [2005]. In reality, the reoxidation of reduced substances produced during OM degradation may be incomplete. Yet, in OMEN-SED we have to assume their complete, instantaneous reoxidation at z_{ox} to allow for an analytical solution. In order to relax this assumption, for cases where it can be justified, we include a "switch" to allow part of the NH_4, H_2S and CH_4 flux to escape reoxidation. The secondary redox parameters (i.e. γ_{NH_4}, γ_{H_2S}, γ_{CH_4}) therefore account for the fraction of reduced substances that are reoxidised and would be ideally parameterised for instance in relation to bottom water oxygen concentration or oxygen penetration depth (z_{ox}). Gypens et al. [2008] for example expressed γ_{NH_4} as a function of oxygen penetration depth ($\gamma_{NH_4} = 0.243 \cdot \ln(z_{ox}) + 1.8479$) based on a fitting exercises to a numerical model and showed that the fraction varies between 0.2 for $z_{ox} = 0.1$cm and 1.0 for $z_{ox} > 3$cm. Due to mathematical constraints in OMEN-SED for finding an analytical solution to the model equations these fractions take constant values generally representing oxygenated deep sea conditions. The instantaneous equilibrium adsorption coefficients of NH_4 and PO_4 (K_{NH_4}, $K^{ox}_{PO_4}$, $K^{anox}_{PO_4}$) are based on Wang and Van Cappellen [1996] and Slomp et al. [1998], respectively. The first order rate constants for sorption of PO_4 to Fe oxides (k_s), release of PO_4 from Fe-bound P due to Fe-oxide reduction (k_m) and authigenic CFA precipitation (k_a), as well as the pore water equilibrium concentrations for P sorption and CFA precipitation ($PO_4{}^s$, $PO_4{}^a$) and the asymptotic concentration for Fe-bound P (FeP^∞) are taken from Slomp et al. [1996]. See Table 3.10 for a complete summary of the parameters and their values.

Table 3.10: Values for biogeochemical parameters used in OMEN-SED. The variables x, y and z denote the elemental ratio of carbon, nitrogen and phosphorus of the degrading organic matter (here set to $C:N:P = 106:16:1$).

Parameter/Variable	Unit	Value	Description
Stoichiometric factors and molecular ratios			
NC_i	mol/mol	$\frac{y}{x} = \frac{16}{106}$	Nitrogen to carbon ratio
PC_i	mol/mol	$\frac{z}{x} = \frac{1}{106}$	Phosphorus to carbon ratio
MC	mol/mol	0.5	Methane to carbon ratio produced during methanogenesis
$DICC^I$	mol/mol	1.0	DIC to carbon ratio until z_{SO_4}
$DICC^{II}$	mol/mol	0.5	DIC to carbon ratio below z_{SO_4}
O_2C	mol/mol	$\frac{x+2y}{x} = \frac{138}{106}$	Oxygen to carbon ratio
NO_3C	mol/mol	$\frac{4x+3y}{5x} = \frac{94.4}{106}$	Nitrate to carbon ratio
SO_4C	mol/mol	$\frac{106}{212}$	Sulfate to carbon ratio
ALK^{OX}	mol/mol	$\frac{y-2z}{x} = \frac{14}{106}$	ALK from aerobic degradation
ALK^{NIT}	mol/mol	-2	ALK from nitrification
ALK^{DEN}	mol/mol	$\frac{4x+3y-10z}{5x} = \frac{92.4}{106}$	ALK from denitrification
ALK^{SUL}	mol/mol	$\frac{x+y-2z}{x} = \frac{120}{106}$	ALK from sulfate reduction
ALK^{MET}	mol/mol	$\frac{y-2z}{x} = \frac{14}{106}$	ALK from methanogenesis
ALK^{H_2S}	mol/mol	-2	ALK from H_2S oxidation
ALK^{AOM}	mol/mol	2	ALK from AOM
Secondary reaction parameters			
γ_{NH_4}	-	0.9	Fraction of NH_4 that is nitrified
γ_{H_2S}	-	0.95	Fraction of H_2S that is oxidised
γ_{CH_4}	-	0.99	Fraction of CH_4 that is oxidised
Adsorption coefficients [Slomp et al., 1998; Wang and Van Cappellen, 1996]			
K_{NH_4}	-	1.4	NH_4 adsorption coefficient
$K^{ox}_{PO_4}$, $K^{anox}_{PO_4}$	-	200.0, 2.0	PO_4 adsorption coefficient (oxic, anoxic)
P related parameters [Slomp et al., 1996]			
k_s	yr^{-1}	94.9	Rate constant for PO_4 sorption
k_m	yr^{-1}	0.193	Rate constant for Fe-bound P release
k_a	yr^{-1}	0.365	Rate constant for authigenic CFA precip.
${PO_4}^s$	$mol\,cm^{-3}$	$1 \cdot 10^{-9}$	Equilibrium conc. for P sorption
FeP^{∞}	$mol\,cm^{-3}$	$1.99 \cdot 10^{-10}$	Asymptotic concentration for Fe-bound P
${PO_4}^a$	$mol\,cm^{-3}$	$3.7 \cdot 10^{-9}$	Equilibrium conc. for authigenic P precip.

3.3 Stand-alone sensitivity analysis and case studies

3.3.1 Sensitivity Analysis

3.3.1.1 Methodology

Model parameters implicitly account for processes that are not explicitly resolved. They are notoriously difficult to constrain and thus a primary source of uncertainty for numerical and analytical models - in particular on the global scale and/or in data-poor areas. A comprehensive sensitivity analysis can help quantify this uncertainty and identify the most sensitive parameters. More specifically, sensitivity analysis is used to investigate how the variations in the outputs (y_1, ..., y_N) of a model can be attributed to variations in the different input parameters [x_1, ..., x_M, Pianosi et al., 2016]. Different types of sensitivity indices, which quantify the relative influence of parameter x_i on output y_j with a scalar $S_{i,j}$ (for $i \in \{1, ..., M\}$ and $j \in \{1, ..., N\}$), can be calculated, ranging from simple one-at-a-time methods to statistical evaluations of the output distribution [e.g. variance-based or density-based approaches Pianosi et al., 2016]. The latter indices take values between zero and one ($S_{i,j} \in [0,1]$), where zero indicates a non-influential parameter and a higher value a more influential parameter. Here, sensitivity analysis is used mainly to identify which parameters have the largest impact on the different model outputs and therefore require more careful calibration. As the probability density functions of our model outputs (i.e. the resulting SWI-fluxes) are generally highly-skewed towards extreme organic matter degradation rates (not shown) variance-based sensitivity indices may not be a suitable proxy for output uncertainty [Pianosi et al., 2016]. Hence, instead the density-based PAWN method by Pianosi and Wagener [2015] is employed which considers the entire conditional and unconditional Cumulative Distribution Function (CDF) of the model output rather than its variance only. The unconditional CDF, $F_y(y)$, of output y is obtained when all uncertain parameters (x_1, ..., x_M) are varied simultaneously, and the conditional CDFs, $F_{y|x_i}(y)$, are obtained when all inputs but the i-th parameter are varied (i.e. x_i is fixed to a so-called conditioning value). The sensitivity index of parameter i is measured by the distance between the two CDFs using the Kolmogorov-Smirnov statistic [Kolmogorov, 1933; Smirnov, 1939], i.e.:

$$S_i = \max_{x_i} \max_{y} |F_y(y) - F_{y|x_i}(y)|. \tag{3.50}$$

Since $F_{y|x_i}(y)$ accounts for what happens when the variability due to x_i is removed, the distance between the two CDFs provides a measure of the effects of x_i on the output y. Due to the model complexity it is impossible to compute the sensitivity indices analytically. Therefore, they are approximated from a Latin-Hypercube sampling of parameter inputs and calculated outputs. For a brief description of the methodology, see Fig. 3.4. For more details, we refer the interested reader to Pianosi and Wagener [2015].

The PAWN method, as implemented within the Sensitivity Analysis for Everyone (SAFE) matlab toolbox [Pianosi et al., 2015], is used to investigate M = 11 model parameters for ranges as

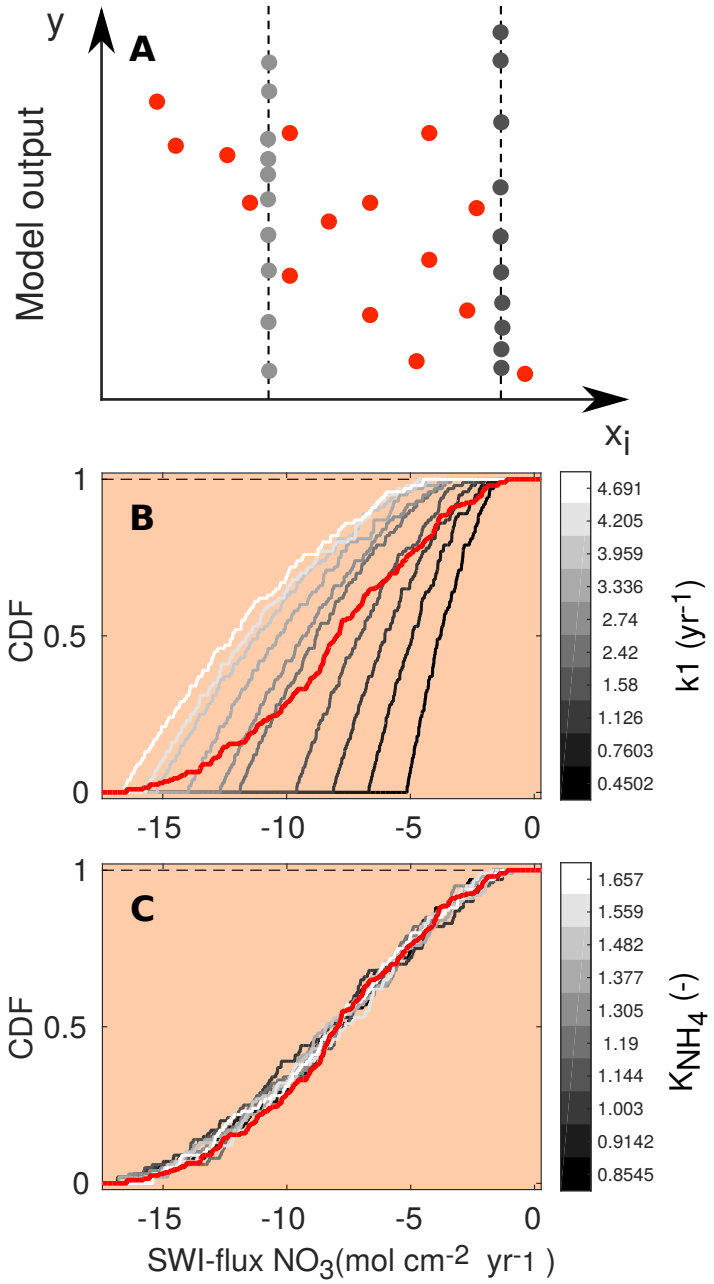

Figure 3.4: A: Schematic of the PAWN method, plotting an uncertain parameter (x_i) against a generic model output (y). Red dots represent points for calculating the unconditional CDF (NU, here 15), grey dots are points for calculating each conditional CDF (NC, here 10) with n = 2 conditioning points as an example. The user can change the values of NU, NC and n. The number of model evaluations equals N_{eval} =NU + n·NC·M, where M is the number of uncertain input parameters. B + C: Two examples of CDFs of the model calculated SWI-flux of NO_3 using NU = 200, NC = 100 and n = 10. The red lines are the unconditional distribution functions $F_y(NO_3)$ and the grey lines are the conditional distribution functions $F_{y|x_i}(NO_3)$ at different fixed values of the input parameters k_1 (B) and K_{NH_4} (C). As the maximal distance between conditional CDFs and unconditional CDF is greater for k_1, this parameter is more influential for the model output (here SWI-flux of NO_3, compare Fig. 3.5).

Table 3.11: Range of model parameters used for sensitivity analysis of model predicted output.

Parameter	Description	Units	Minimum	Maximum	Source
k_1	labile OM degradation constant	yr^{-1}	$1e^{-4}$	5.0	(1)
$\widetilde{k_2}$	order of refractory OM degradation constant ($k_2 = \widetilde{k_2} \cdot k_1$)	-	$1e^{-4}$	$1e^{-1}$	(1)
f_1	fraction of labile OM	-	0.02	0.98	-
K_{NH_4}	Adsorption coefficient	-	0.8	1.7	(2)
γ_{NH_4}	NH_4 fraction oxidised		0.5	1.0	-
γ_{H_2S}	H_2S fraction oxidised		0.5	1.0	-
$K^{ox}_{PO_4}$	Adsorption coeff. oxic	-	100.0	400.0	(3)
$K^{anox}_{PO_4}$	Adsorption coeff. anoxic	-	1.3	2.0	(3)
k_s	kinetic P sorption	yr^{-1}	0.1	100.0	(4, 5)
k_m	Fe-bound P release	yr^{-1}	0.015	0.02	(4, 5)
k_a	authigenic P formation	yr^{-1}	0.001	10.0	(4, 6)
Sources:	(1) Arndt et al. [2013]; (2): Cappellen and Wang [1996]; (3): Krom and Berner [1980] (4): Gypens et al. [2008]; (5): Slomp et al. [1996]; (6): Van Cappellen and Berner [1988]				

Table 3.12: Model boundary conditions for the two idealised sediment conditions used for the sensitivity analysis (Fig. 3.5 and 3.6). All solute concentrations are in nmol cm^{-3}.

Depth (m)	Temp. (°C)	OC (wt%)	O_2	NO_3	SO_4	PO_4	z_{bio} (cm)
400	8.0	2.0	0.0	40.0	28,000	40.0	0.001
4000	1.5	1.0	300.0	20.0	28,000	40.0	10.0

specified in Table 3.11. Sensitivity indices for all resulting SWI-fluxes for two idealised sediment conditions (i.e. anoxic at 400 m and oxic at 4000 m, see Table 3.12) are calculated. We use NU = 200 samples to estimate the unconditional CDF, NC = 100 samples to estimate the conditional CDFs and n = 10 conditioning points. Thus as $N_{eval} = 200 + 100 \cdot 10 \cdot 11$, 11200 model evaluations are performed for each sediment condition. The resulting indices are then translated into a color code and summarised in a pattern plot to simplify comparison (Fig. 3.5).

3.3.1.2 Results

Fig. 3.5 summarises results of the sensitivity analysis as a colour map. Results indicate that generally the most significant parameters for all model outputs are the degradation rate constant for the labile OM pool (k_1) and the fraction of this pool to the total OM stock (f_1). Other parameters play a minor role for the SWI-fluxes, with the exception of the secondary redox parameters (i.e. γ_{NH_4}, γ_{H_2S}) in the oxic scenario. Here, NH_4, SO_4 and H_2S are very sensitive to changes in γ_{NH_4} and γ_{H_2S}, as these parameters determine how much of the respective TEA is produced in situ via reoxidation, thus affecting the resulting SWI-fluxes. For the oxic scenario, the reoxidation of H_2S produced in the sulfidic layer also has a strong influence on alkalinity (γ_{H_2S}, Table 3.8 Eq. 5) as it decreases alkalinity by 2 moles per mole of S oxidized (ALK^{H_2S}, Table 3.10).

However, these high sensitivities are partially caused by the wide range of allowed values (γ_{NH_4}, $\gamma_{NH_4} \in [0.5; 1.0]$). Yet, for oxic deep sea conditions it is more likely that reduced substances are almost completely reoxidised [e.g. Hensen et al., 2006]. For the anoxic scenario the secondary redox parameters are essentially non-influential as no O_2 is available for the reoxidation of reduced substances. Especially for the oxic condition the PO_4 SWI-flux appears to be insensitive to P-related parameters (i.e. $K^{ox}_{PO_4}$, $K^{anox}_{PO_4}$, k_s, k_m, k_a) as the majority is absorbed to Fe-oxides. The sensitivities change if other PO_4 related equilibrium concentrations ${PO_4}^s$, ${PO_4}^a$ and FeP^{∞} are used (not shown). Overall the results of the sensitivity analysis are in line with what one would expect from a diagenetic model and thus provide ground to confirm that OMEN-SED provides sensible results. The parameterisation of the organic matter pools (f_1) and their degradation rate constants (k_1, k_2) is critical especially when the model is used in a global Earth system model framework, as these parameters, as well as the γ-parameters, can have a very important influence on the flux of dissolved species through the SWI. At the same time these are the weakest constrained parameters. Thus, one should rather choose γ-values close to 1 and consider carefully where a relaxation of the "all reoxidised" assumption is appropriate. In contrast, the importance of the OM degradation rate constants can not be overemphasised. Therefore, much care should be given to how these are parameterised in coupled simulations and a range of different plausible scenarios should be tested to quantify uncertainty.

Because of the strong sensitivity of model results on OM degradation rate parameters, we further explore the sensitivity of simulated sediment-water exchange fluxes to variations in organic matter degradation parameters by varying k_1, f_1 and $\widetilde{k_2}$ while all other model parameters are set to their default values (Tables 3.9 and 3.10). Minimum and maximum values for k_1, $\widetilde{k_2}$ and f_1 in the shallow ocean are as in Table 3.11. For the deep sea condition we account for the presence of more refractory OM by sampling $f_1 \in [0.02, 0.3]$, whereas the variation of k_1 and $\widetilde{k_2}$ is as in the shallow ocean. The parameter space is sampled using another Latin-Hypercube approach with sample sizes of $N = 3500$ for each idealised sediment condition. Figure 3.6 summarises the results of the sensitivity study and the ranges of observed O_2 and NO_3 sediment-water interface fluxes extracted from a global database [Stolpovsky et al., 2015] are indicated on the colour scale. The colour patterns in Figure 3.6 A and B reveal the complex interplay between the amount of labile OM f_1 and its degradation rate k_1 for the resulting SWI-fluxes of NO_3 in anoxic sediments and O_2 in aerobic sediments. In general, a higher degradation rate in combination with more labile OM available leads to a higher SWI-flux. However, higher fluxes extend over a larger range of k_1-values when the amount of labile OM f_1 is high. The absence of a colour pattern in Figure 3.6 C highlights the limited interaction of the two model parameters for NO_3 SWI-fluxes under oxic conditions. Figure 3.6 shows that SWI-fluxes can vary widely over the range of plausible organic matter degradation parameters and that simulated fluxes generally fall within the range of observed SWI-fluxes. However, a large number of different k-f combinations can result in SWI-fluxes that fall within the observed ranges reported by Stolpovsky et al. [2015] further

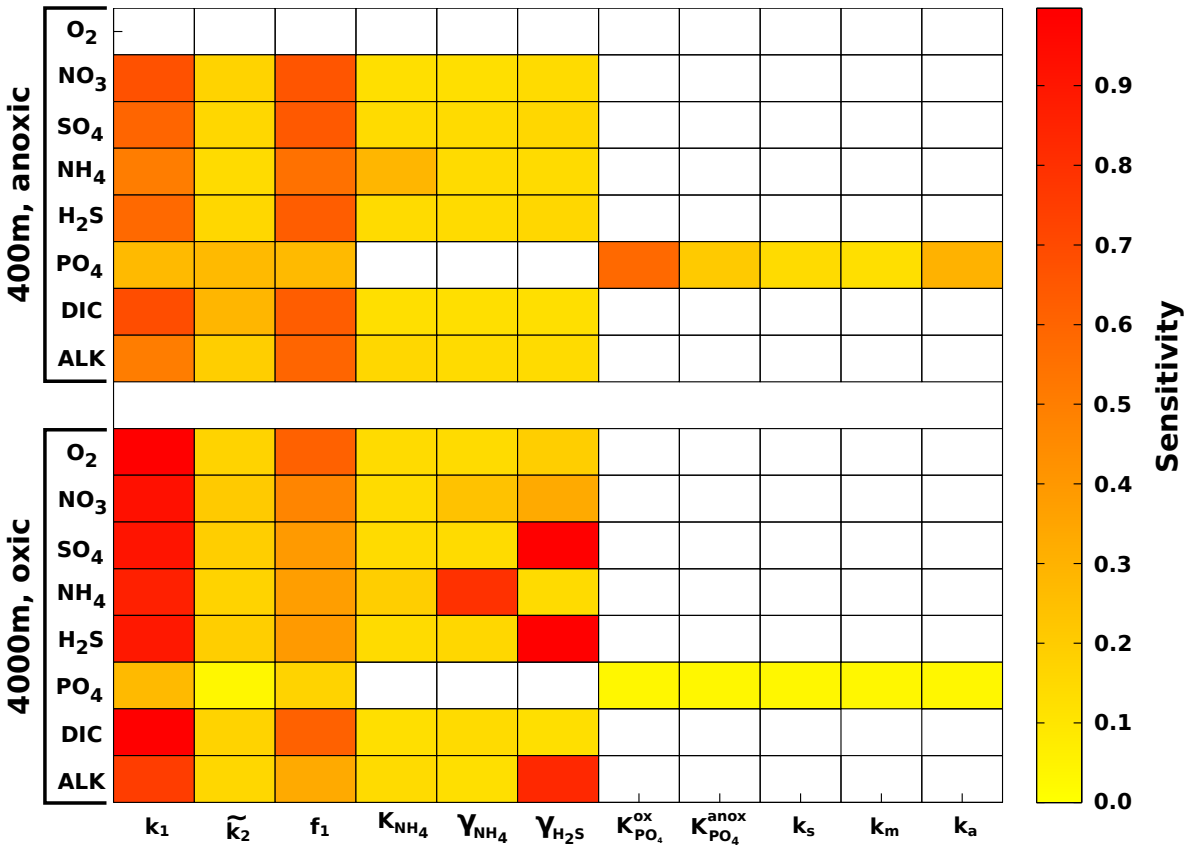

Figure 3.5: Pattern plot, showing the output sensitivity for each SWI flux (i.e. the chemical compounds on the vertical axis) and each input factor (i.e. the model parameters on the horizontal axis) for two idealised sediment cores. White patterns are assigned where the SWI flux is independent of the specific parameter.

emphasising the care that should be devoted to constraining OM degradation parameters.

3.3.2 Case study: Simulations of sediment cores

3.3.2.1 Methodology

In order to illustrate the capabilities of OMEN-SED, comprehensive datasets from the Santa Barbara Basin [Reimers et al., 1996], as well as from the Iberian margin and the Nazaré Canyon [Epping et al., 2002] are modelled. Modelled profiles are compared with measured pore water data from different depths including the continental shelf (108 m) and the lower slope (2213 m) located at the Iberian margin, the upper slope (585 m) from the Santa Barbara Basin, and a deep sea site (4298 m) in the Nazaré Canyon. The Santa Barbara Basin is characterised by anoxic bottom waters, high POC concentrations and varved sediments [Reimers et al., 1990], therefore

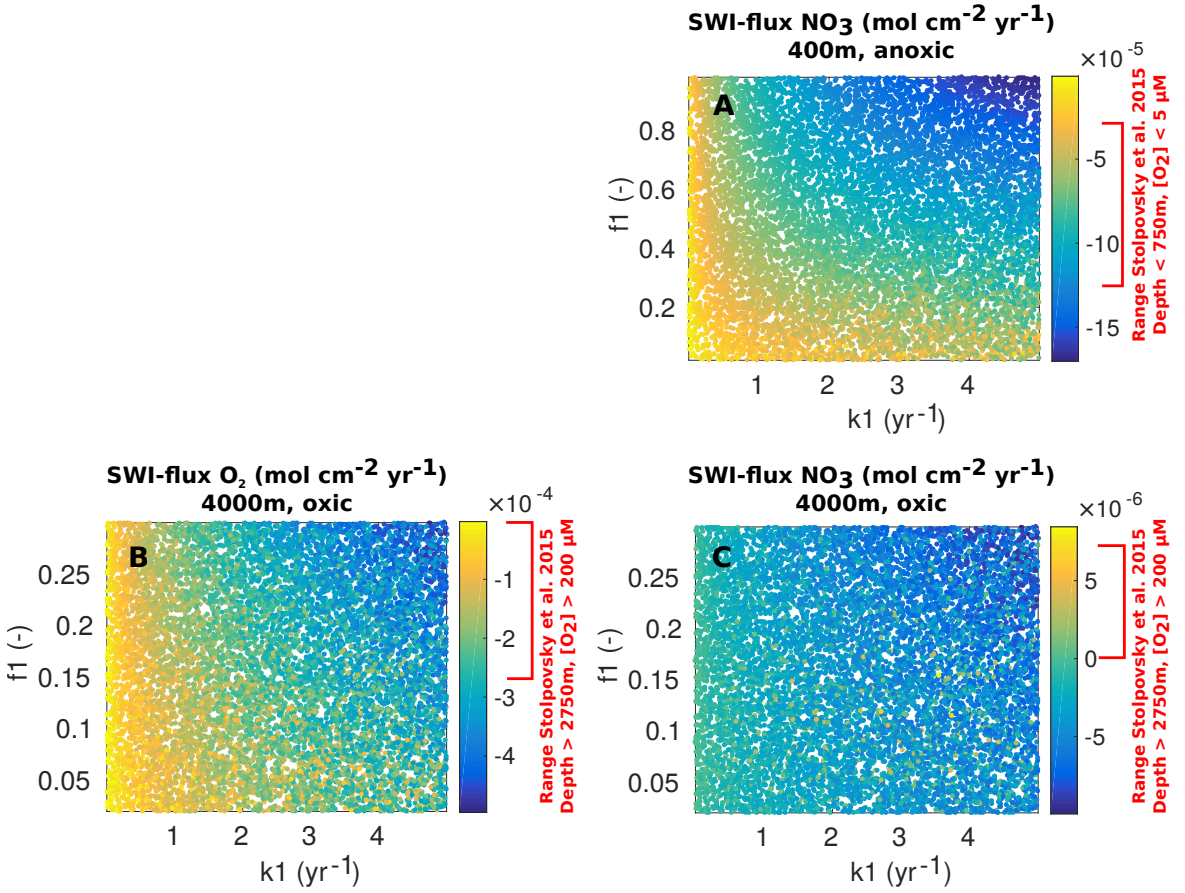

Figure 3.6: Scatter plots (k_1 vs f_1) of resulting OMEN-SED SWI-fluxes for the 400m anoxic (A: NO_3) and 4000m oxic (B: O_2, C: NO_3) scenario. Negative values represent a flux from the water column into the sediments. Ranges indicated in red on the colour scale correspond to observed benthic fluxes as reported in the global database of Stolpovsky et al. [2015].

the depth of bioturbation in OMEN-SED is restricted to the upper 0.01 cm. In the uppermost sediments iron(III) hydroxides are reduced, releasing Fe^{2+} which reacts with sulfide to form iron sulfides. Thus, the Fe cycle exerts a strong control on sulfide concentrations in the sediments of this basin [Reimers et al., 1996]. In addition, the sediments are generally supersaturated with respect to carbonate fluorapatite by and below 2 cm [Reimers et al., 1996]. The Iberian margin, situated in the northeastern Atlantic, generally belongs to the more productive regions of the global ocean [Longhurst et al., 1995], however, seasonal changes in upwelling creates a strong temporal variability in primary productivity and organic carbon deposition. Submarine canyons in this area (like the Nazaré Canyon) may deliver organic carbon from the shelf to the ocean interior [Epping et al., 2002; van Weering et al., 2002]. For a more detailed description of the study areas and the experimental work, the interested reader is referred to the publications by Reimers et al. [1996] and Epping et al. [2002].

Table 3.13: Model boundary conditions for the simulated sediment profiles in the Santa Barbara basin (108 and 2213 m) and Iberian margin (585 and 4298 m) reported in Figure 3.7. For all sites a DIC bottom water concentration of 2,400 nmols cm^{-3} is assumed.

Sediment characteristics:								
Depth (m)	Temp. (°C)	z_{bio} (cm)	D_{bio} ($cm^2 yr^{-1}$)	POC_1 (wt%)	POC_2 (wt%)	k_1 (yr^{-1})	k_2 (yr^{-1})	PO_4^a (nmol cm^{-3})
108	12.50	1.00	0.02	2.64	1.8	0.650	$1.0e^{-5}$	15.0
585	5.85	0.01	0.02	2.00	3.5	0.200	$8.0e^{-4}$	90.0
2213	3.20	10.00	0.17	0.45	0.5	0.100	$4.0e^{-4}$	5.0
4298	2.50	4.20	0.18	0.83	1.2	0.052	$1.0e^{-5}$	5.0
Bottom water concentrations of solutes (all in nmol cm^{-3}):								
Depth	O_2	NO_3	SO_4	NH_4	H_2S	PO_4	Alkalinity	
108	210.0	9.6	28,000	0.40	0.0	0.0	2,400	
585	10.0	25.0	28,000	0.00	0.0	50.0	2,480	
2213	250.0	25.0	28,000	0.60	0.0	0.0	2,400	
4298	243.0	30.1	28,000	0.22	0.0	0.0	2,400	

In OMEN-SED sediment characteristics and boundary conditions are set to the observed values where available (Table 3.13). Other sediment characteristics (e.g. sedimentation rate, porosity, density), stoichiometric factors and secondary reaction parameters are set to the default value (see Tables 3.9 and 3.10). Organic matter is modelled as two fractions, with different first-order degradation rate constants. The POC and pore water profiles were manually fitted by optimizing the POC partitioning into the fast and slow degrading pool and their respective first-order degradation rate constants (priority is given to reproduce the POC and O_2 profiles). For phosphorus the equilibrium concentration for authigenic P formation (PO_4^a) was adjusted to fit the PO_4 concentration at z_∞.

3.3.2.2 Results

Fig. 3.7 compares modelled and observed sediment profiles for the Santa Barbara Basin and the Iberian margin. Results show that OMEN-SED is able to capture the main diagenetic features across a range of different environments without changing model parameters (other than the 4 we tuned, i.e. k_1, k_2, f_1 and PO_4^a) to site specific conditions. For the two open Iberian margin stations (108 and 2213 m) OMEN-SED fits all observations well. OMEN-SED does especially well at seafloor depth (SFD) 2213 m by reproducing the deep O_2 penetration and the subsurface maximum in NO_3 concentration due to the nitrification of NH_4 (note, that NH_4 is overestimated at this SFD). For the anoxic Santa Barbara Basin (585 m) the decrease in SO_4 and the increase in ALK concentration with sediment depth is well represented, indicating the importance of sulfate reduction as the primary pathway of OM degradation at this site [compare with Meysman et al., 2003]. However, a misfit is observed for H_2S and PO_4 in the upper 20 cm of this sediment core. The discrepancy for H_2S can be explained by high iron(III) hydroxide concentrations, which is

reduced to degrade organic matter (especially in the $2-4$ cm depth interval), therefore placing the beginning of the sulfate reduction zone and the production of H_2S to the deeper sediments [Reimers et al., 1996]. Iron processes are currently not dynamically represented in OMEN-SED. In addition, produced dissolved Fe reacts with H_2S to form iron sulfides (e.g. pyrite, FeS_2) and thus further inhibits the rise of H_2S [Reimers et al., 1990]. The iron cycle also plays a critical role for phosphorus, as the reduction of iron(III) hydroxides in the surface sediments releases sorbed phosphate, leading to pore waters around and below 2 cm which are supersaturated with respect to fluorapatite, thus initiating CFA precipitation. Reimers et al. [1996] could even show that the accumulation of CFA is mainly restricted to the near-surface sediments (~ 5 cm) instead of throughout the sediment column. As OMEN-SED currently does not include an iron-cyle, and Fe-bound P and CFA processes are highly parameterised, the model is not able to capture these complex, non-steady state phosphorus dynamics at this specific site.

For the Nazaré Canyon station (4298 m) satisfactory fits could be realised apart from NH_4. However, also Epping et al. [2002] could not obtain a better fit using the diagenetic model OMEX-DIA. They suggested non-local solute exchange resulting from bioirrigation being responsible for the higher NH_4 concentrations at this site which is neglected in their model, as well as in OMEN-SED. Furthermore, the fractured POC profile (indicating episodic depositional events through the canyon) could have been approximated using a different partitioning of the bulk POC into labile and refractory pool with different degradation rate constants, thus potentially leading to a better fit of the NH_4 profile. In general, better approximations of the data could have potentially been acquired by applying a sensitivity study using different NC-ratios [e.g. Epping et al., 2002, report different ratios from Redfield stoichiometry] and exploring the parameter space for the secondary reaction parameters (γ_{NH_4}, γ_{H_2S}). However, considering these generalisations and our assumption of steady-state, which might not be valid, particularly for the complex Santa Barbara basin, the shallow core and the Nazaré Canyon, which are affected by seasonality and biology, OMEN-SED generally reproduces the observed pore water trends and hence captures the main diagenetic processes.

3.3.3 Case study: Stand-alone simulations of global ocean transect

3.3.3.1 Methodology

In this section we explore to what degree OMEN-SED is capable of capturing the dynamics of organic matter degradation pathways and related TEA-fluxes as simulated with a more complete and complex numerical diagenetic model [Thullner et al., 2009]. Therefore, we reproduce the simulations of typical conditions along a global ocean hypsometry of Thullner et al. [2009] and compare our modelled TEA-fluxes with the results of the complex model as well as with observations from Middelburg et al. [1996]. To explore the global degradation of OM in the seafloor Thullner et al. [2009] quantified various diagenetic processes using the Biogeochemical Reaction Network Simulator [BRNS, Aguilera et al., 2005], a flexible simulation environment suitable for

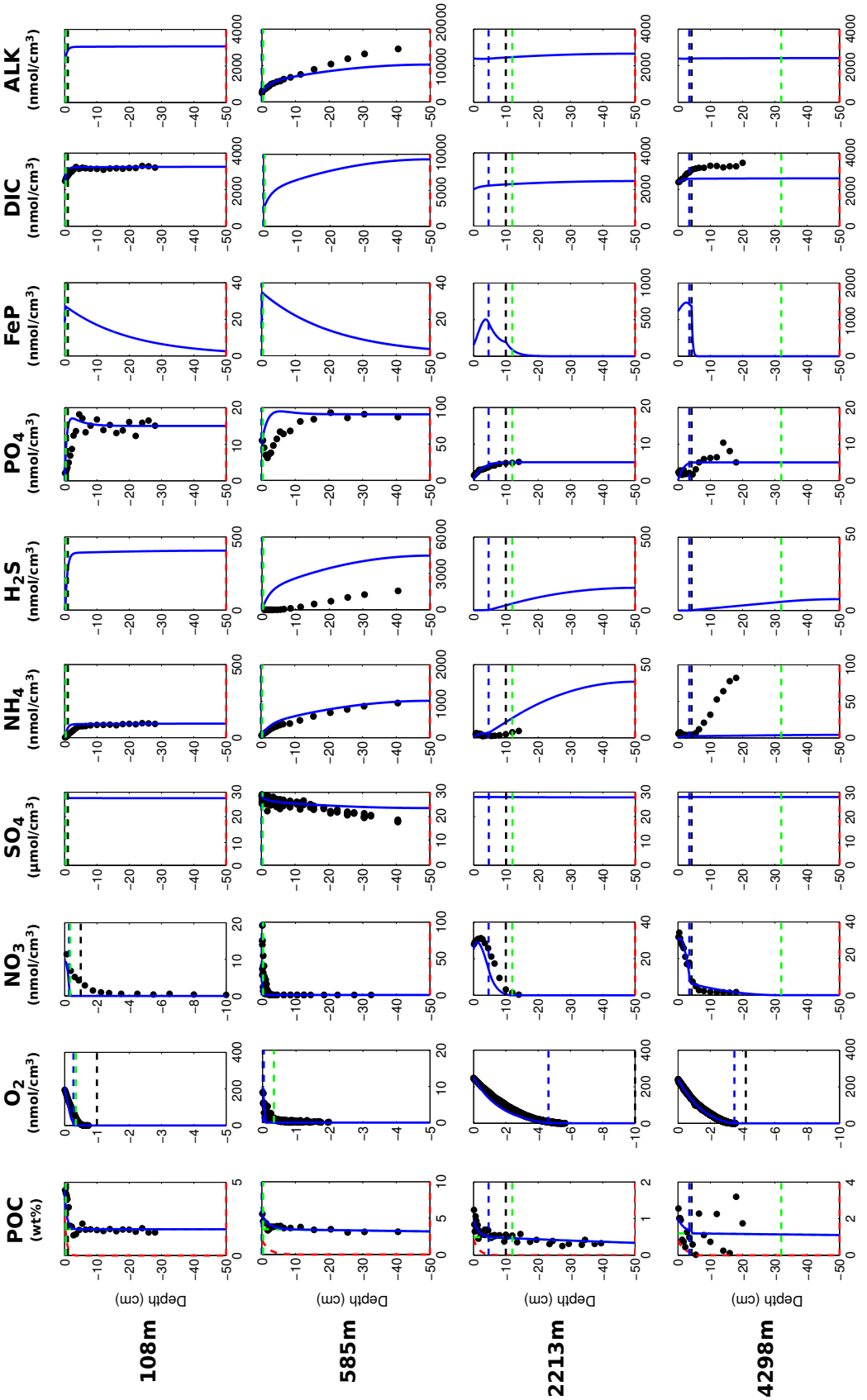

Figure 3.7: Modelled (curves) and measured (filled dots) solid phase and dissolved pore water profiles for four different sediment cores. Note that different scales are used for different stations. The blue POC curve represents the sum of the refractory (green) and labile (red) POC fraction. The horizontal dashed lines in each panel indicate the bioturbation depth (black) and the penetration depths of oxygen (blue), nitrate (green) and sulfate (red) as calculated by OMEN-SED.

reactive transport simulations of complex biogeochemical problems [e.g. Jourabchi et al., 2005; Thullner et al., 2005]. Thullner et al. [2009] used seafloor depth (SFD) as the master variable and calculated model parameters, such as w, D_{bio} and ϕ, from existing empirical relationships [e.g. Middelburg et al., 1997; Van Cappellen and Wang, 1995]. Organic matter degradation was described with a 1G approach, thus assuming a single pool of organic matter of uniform reactivity. The first order rate constant was related to the burial velocity, w (cm year^{-1}), following the empirical relationship of Boudreau [1997]:

$$k = 0.38 \cdot w^{0.59}. \tag{3.51}$$

This rate constant can be assumed as the mean reactivity of the organic matter fractions which are degraded in the upper, bioturbated $10-20$ cm of the sediments. Thus, more reactive fractions (degraded during days/weeks close to the SWI) and more refractory fractions (degraded on longer time scales deeper in the sediments) are not captured by this relationship [Boudreau, 1997]. BRNS simulations were performed using boundary conditions and parameters for depths representative for shelf, slope and deep sea sediments (i.e. SFD of 100m, 200m, 500m, 1000m, 2000m, 3500m and 5000m). In order to reproduce these results, OMEN-SED is configured here as a 1G model and boundary conditions and model parameters are defined as in Thullner et al. [2009, see Table 3.14]. As OMEN-SED assumes a fixed fraction (i.e. γ_{NH_4}, γ_{H_2S}) of reduced substances to be reoxidised, which exerts a large impact on the resulting SWI-fluxes (compare Section 3.3.1), two sets of simulations are performed in order to show the range of possible model outputs. In the first setup 95% of the reduced substances are reoxidised (i.e. $\gamma_{NH_4} = \gamma_{H_2S} = 0.95$) and in the second, less realistic case, only 5% are reoxidised (all other model parameters and boundary conditions are equal).

3.3.3.2 Results

Figure 3.8 compares simulated SWI-fluxes of TEAs (i.e. O_2, NO_3 and SO_4) along the global hypsometry using OMEN-SED (black lines) with the results of Thullner et al. [2009] (red lines). Observations for O_2 and NO_3 fluxes are taken from Middelburg et al. [1996]. Due to the applied empirical relations organic matter flux to the seafloor decreases by 2 orders of magnitude from 100 to 5000 m and its degradation rate constant by 1 order of magnitude (Table 3.14). Therefore, the rate of organic matter degradation is about 50 times greater at 100 m than at 5000 m [compare Thullner et al., 2009], thus resulting in a decrease of TEA-fluxes along the hypsometry (Figure 3.8). The 95%-reoxidation experiments (dots) show proportionally higher O_2 in-fluxes than the the 5%-reoxidation experiments (triangles) because more O_2 is utilised for in situ production of NO_3 and SO_4 in the sediments. This is also mirrored by the increased NO_3 out-flux and decreased SO_4 in-flux for shallower SFDs. This is in line with the results of Thullner et al. [2009] which showed that in situ production is an important pathway of SO_4 supply in the sediment, which is responsible for ~80% of the total OM degradation at depths between 100 and 2000 m (in our

Table 3.14: Seafloor depth dependency of key model parameters and boundary conditions [adapted from Thullner et al., 2009].

	Seafloor depth						
	100 m	200 m	500 m	1000 m	2000 m	3500 m	5000 m
Model parameters							
w^a (cm yr^{-1})	3.98×10^{-1}	3.60×10^{-1}	2.67×10^{-1}	1.62×10^{-1}	5.94×10^{-2}	1.32×10^{-2}	2.94×10^{-3}
$D_{\mathrm{bio}}{}^a$ (cm^2 yr^{-1})	27.5	25.1	19.0	12.1	4.83	1.23	0.310
ϕ^b	0.85	0.85	0.80	0.80	0.80	0.80	0.80
T^c (°C)	10.3	9.7	8.1	5.8	3.0	1.5	1.4
$\rho_{\mathrm{sed}}{}^c$ (g cm^{-3})	2.5	2.5	2.5	2.5	2.5	2.5	2.5
k^d (yr^{-1})	0.221	0.208	0.174	0.130	0.0718	0.0296	0.0122
Upper boundary conditions							
$\mathrm{POC_{flux}}{}^a$ (μmol cm^{-2}yr^{-1})	510	467	357	228	93.0	24.3	6.33
POC^e (wt%)	0.79	0.78	0.55	0.50	0.42	0.32	0.25
$\mathrm{O_{2,0}}{}^c$ (nmol cm^{-3})	132	129	121	114	116	135	141
$\mathrm{NO_{3,0}}{}^c$ (nmol cm^{-3})	17.3	18.6	22.1	26.5	31.0	31.6	31.6
$\mathrm{SO_{4,0}}{}^b$ (nmol cm^{-3})	28,000	28,000	28,000	28,000	28,000	28,000	28,000

[a] Derived from Middelburg et al. [1997].
[b] Derived from Van Cappellen and Wang [1995].
[c] Derived from Conkright et al. [2002].
[d] Derived from Boudreau [1997].
[e] Calculated with OMEN-SED from $\mathrm{POC_{flux}}$.

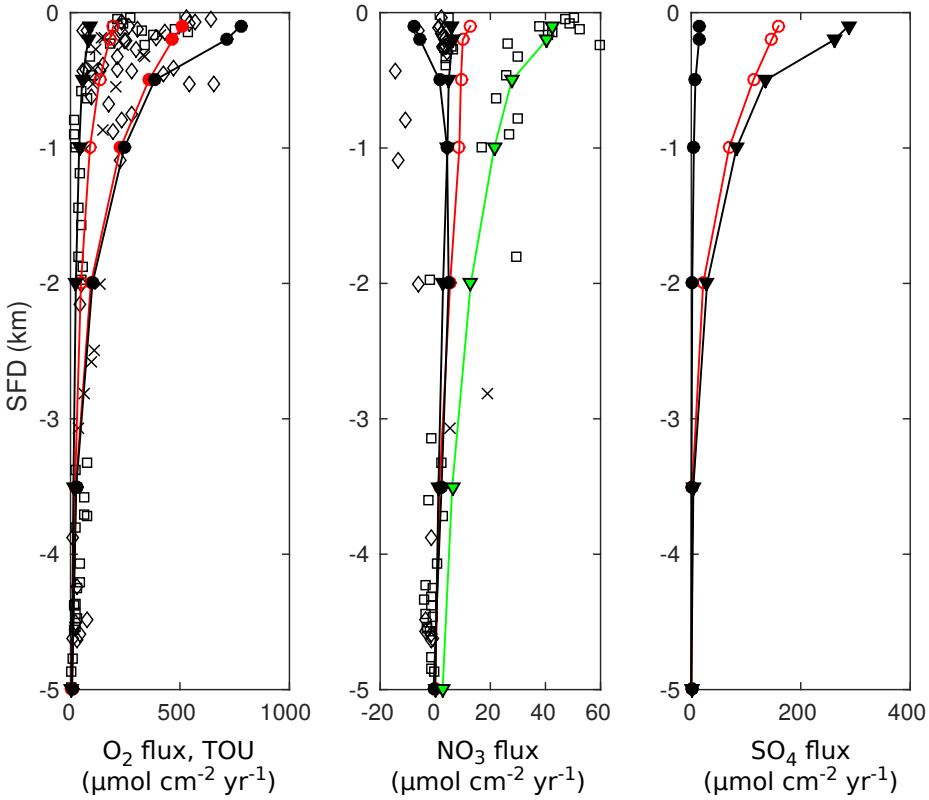

Figure 3.8: Fluxes of O_2, NO_3 and SO_4 to the sediment along the global hypsometry. Red lines (with open symbols) are modelled fluxes from Thullner et al. [2009] using BRNS; black lines are results from OMEN-SED (• : $\gamma_{NH_4} = \gamma_{H_2S} = 0.95$; ▼: $\gamma_{NH_4} = \gamma_{H_2S} = 0.05$). Observations of TEA fluxes are taken from Middelburg et al. [1996] (◇: Atlantic, □: Pacific, ×: Arctic/Indian Ocean). Also plotted in Figure (A) are the total oxygen uptake (TOU) estimates of Thullner et al. [2009] (filled red symbols). The green line indicates OMEN-SED results for low oxygen/high nitrate levels and the lower NC-ratio. Positive fluxes are directed from the ocean into the sediments.

results SO_4 is not used for OM degradation in OMEN-SED below 2000m). In general, Figure 3.8 shows that OMEN-SED captures the main trends in observed and numerically simulated TEA fluxes well. Results also confirm that higher γ-values better represent SWI-fluxes for most of the global hypsometry. A slight overestimation of shallow ocean SWI-fluxes (SFD < 200 m) for the high γ scenario indicates that slightly lower γ-values would better capture SWI-fluxes in these areas, where rapid oxygen consumption favours the escape of reduced species across the SWI.

In addition, observed O_2 fluxes in the upper 2000m are generally encompassed by our total range in predicted OMEN-SED fluxes. Oxygen fluxes for the deep-sea sediments, however, are slightly underestimated. These deviations can presumably be related to the assumed 1G description of organic matter degradation, which neglects the more labile OM pool. This highly reactive pool is degraded close to the sediment surface, thus promoting higher aerobic degradation

rates and higher O_2 fluxes. Nitrate fluxes in the upper 500m of the Atlantic Ocean are well predicted. However, as in Middelburg et al. [1996] the direction of calculated nitrate fluxes in the upper 1000m of the Pacific Ocean differ from the observations. Middelburg et al. [1996] related these discrepancies to the globally averaged model parameters and the applied boundary conditions. They could reduce the disagreements significantly by using more representative bottom water concentrations for the eastern Pacific and a higher flux of labile organic matter for their 2G model. By changing the boundary conditions and the N:C elemental ratio of organic matter for the whole hypsometry, it is possible to obtain a better model-data fit with OMEN-SED for the shallow Pacific Ocean (green line in Fig. 3.8B). Bohlen et al. [2012] report that the elemental N:C ratio strongly deviates from Redfield stoichiometry (0.151) with specifically lower values for the East Pacific Ocean. The use of their globally averaged value of 0.067 allows reconciling modelled and observed values provided that bottom water conditions are also changed to the low oxygen/high nitrate levels more likely to be found in the shallow Pacific Ocean (O_2 = 10 nmol cm^{-3} and NO_3 = 80 nmol cm^{-3}).

3.4 Scope of applicability and model limitations

Because of the high computational cost associated with resolving benthic dynamics, most Earth system Models of Intermediate Complexity (EMICs) and also some of the higher resolution Earth system models either completely neglect or merely include a highly simplified representation of benthic-pelagic exchange processes [Hülse et al., 2017]. However, benthic-pelagic coupling plays an important role for carbon cycling and the lack of its representation in EMICs compromises our ability to assess the response and recovery of the Earth system to major past, present and future carbon cycle and climate perturbations. As a consequence, there is a need for benthic biogeochemical models that are able to capture the main features of benthic biogeochemical dynamics, but that are, at the same time, computationally efficient enough to allow for a direct, dynamic coupling to ocean biogeochemical model. Therefore, we have developed OMEN-SED, a, one-dimensional analytical early diagenetic model that offers a predictive ability similar to complex, numerical diagenetic models at a significantly reduced computational cost.

OMEN-SED is thus not problem-specific. Its reaction network resolves the most pertinent benthic biogeochemical species as well as the most important processes that control their cycling and burial in marine sediments. OMEN-SED can thus be coupled to a wide range of regional to global ocean biogeochemical models, as well as EMICs and higher resolution Earth system models to investigate a wide range of research questions associated with past, present or future carbon and macro-nutrient cycling. For instance, OMEN-SED can be used to i) quantify benthic macro-nutrient recycling from the shallow coastal to the deep, open ocean, ii) investigate the role of benthic-pelagic coupling in the development of past or future ocean anoxia/euxinia, or to iii) estimate global organic carbon burial in marine sediments. In theory, its scope of applicability

thus ranges from the regional to the global and from the seasonal to the millennial timescale. In addition, the computational efficiency of OMEN-SED allows calculating quantitative sensitivity indices requiring large sample sizes such as variance- or density-based approaches. Therefore, OMEN-SED can also help quantitatively investigate sensitivity of benthic model output to systematic variations in model parameters when the model has been tuned to a site-specific problem.

However, OMEN-SED is inevitably associated with a certain degree of simplifications that may compromise the applicability of the model in its current version under certain circumstances. First, we have assumed steady state conditions to allow for an analytical solution of the coupled diagenetic equations. This steady-state assumption is only valid if the variability in boundary conditions and fluxes is generally longer than the characteristic timescales of the reaction-transport processes. As a consequence, OMEN-SED is well suited for the coupling to EMICs and the investigation of long-term dynamics in sediment-water exchange fluxes, for instance, during past extreme climate events. Yet, in its current version, OMEN-SED is not able to predict the transient response of benthic process rates and fluxes to short-term or seasonal variations of boundary conditions. Yet, future versions of OMEN-SED, could approximate non-steady state conditions by incorporating a time-step dependent relaxation between different steady states, similar to the schemes used in Ruardij and Van Raaphorst [1995] and Arndt and Regnier [2007]. Such a pseudo-transient approach would enable the application of OMEN-SED to systems characterised by high-frequency fluctuations in boundary conditions, such as the coastal ocean or estuaries.

Second, although the model explicitly simulates DIC and alkalinity production and, thus, has the potential to predict pH profiles within the sediment, a major limitation at this stage is the lack of an explicit description for $CaCO_3$ precipitation/dissolution coupled to OM decomposition, which also controls the inorganic carbon system [Krumins et al., 2013]. In addition, the current version of OMEN-SED does not yet explicitly resolve iron and manganese dynamics (although note, that iron is implicitly accounted for in the PO4 equation). This lack currently limits the applicability of OMEN-SED to iron- and manganese rich environments, such as coastal marine environments, upwelling regions or ferruginous oceans. In addition, it also compromises the ability of OMEN-SED in predicting H_2S fluxes in Fe-rich anoxic environments, where high iron porewater concentrations can deplete porewater H_2S by iron-sulfide mineral precipitation [e.g. Meyers, 2007]. Therefore, already planned future extensions of OMEN-SED include an explicit description of iron.

Finally, just as all global models, the global application of OMEN-SED is complicated by the lack of an objective, global framework for biogeochemical process parameterization. The sensitivity study presented here shows that this lack is particularly critical for OM degradation rate parameters (k_i,f_i) and the γ-values describing the completeness of secondary redox reactions. Model simulations along the global hypsometry (Section 3.3.3) have shown that high γ-values

generally capture the main SWI-flux features, but have also highlighted that slightly lower γ-values would result in a better fit of SWI-fluxes to observations of the shallow ocean. With respect to OM degradation rate constants, several alternative parametrisations are tested in the coupled OMEN-cGENIE framework and discussed in the following Chapter.

3.5 Conclusions

Here, we have described in detail and tested OMEN-SED, a new, analytical early diagenetic model resolving organic matter cycling and associated biogeochemical dynamics. OMEN-SED has been explictely designed for the coupling to EMICs and combines biogeochemical complexity with computational efficiency. It is the first analytical diagenetic model to explicitly represent oxic degradation, denitrification, sulfate reduction and implicitly methanogenesis, as well as the reoxidation of reduced substances, adsorption/desorption, as well as mineral precipitation//dissolution. Explicitly resolved pore water species include O_2, NO_3, NH_4, SO_4, H_2S, DIC and ALK and the solid phase includes two degradable fractions of organic matter, Fe-bound P and authigenic Ca-P minerals.

An extensive sensitive analysis, based on the density-based PAWN method [Pianosi and Wagener, 2015] emphasizes the importance of OM degradation rate parameters (k_i, f_i) and thus highlights the need for the development of an objective, global framework to parameterize OM degradation rate parameters. We have shown that the performance of OMEN-SED is similar to that of a fully formulated, multi-component numerical model. The new analytical model is able to reproduce observed pore water profiles across a wide range of depositional environments and captures observed global patterns of SWI-fluxes, oxygen penetration depths, biogeochemical reaction rates, as well as surface sediment organic matter contents (compare the following Chapter). Coupled to EMICs or higher resolution Earth system models, OMEN-SED is thus well suited to examine the role of sediments in global biogeochemical cycles in response to a wide range of past or future carbon cycle or climate perturbations over various timescales.

CHAPTER 4

COUPLING OMEN-SED TO cGENIE AND PRE-INDUSTRIAL MODEL SIMULATIONS

Contributions and acknowledgements
This chapter is adapted from a research article ready for submission for publication in Geoscientific Model Development. All co-authors (S. Arndt, S. Daines, P. Regnier and A. Ridgwell) provided assistance with editing and advised on aspects of this work. A. Ridgwell created the total burial flux fields. All other work presented in this chapter is my own.

4.1 Introduction

Earth system models track the biogeochemical dynamics of organic and inorganic carbon, essential nutrients and oxygen with the aim of investigating the evolution of the ocean's redox structure and carbon system and its feedbacks on global climate. This general aim thus defines a minimum set of state variables and reaction processes that need to be resolved for a realistic and efficient representation of the benthic-pelagic coupling in Earth system models (ESMs). Thus, a sediment model suitable for the coupling to an ESM and enabling a wide range of paleo questions to be addressed has to provide a robust quantification of organic (and inorganic) carbon burial fluxes, as well as benthic uptake/return fluxes of oxygen, growth-limiting nutrients and reduced species. As a consequence, the reaction network must account for the most important primary and secondary redox reactions, equilibrium reactions, mineral precipitation/dissolution and adsorption/desorption, resulting in a complex set of coupled reaction-transport equations. Yet, in most current Earth system models sediment-water dynamics are either neglected or treated in a very simplistic way as discussed in Chapter 2 and in the introduction of Chapter 3. To provide

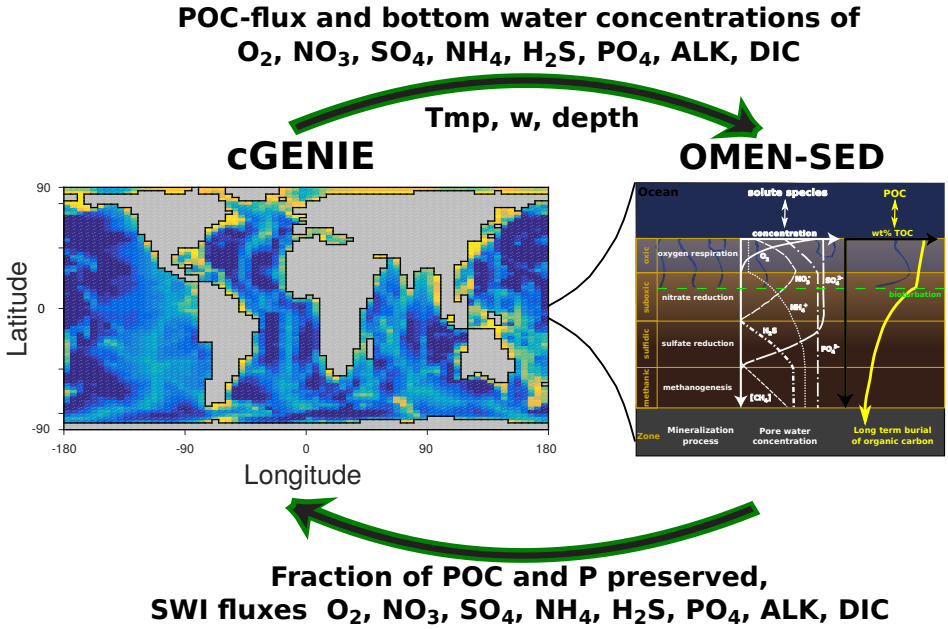

Figure 4.1: Schematic of the relationship between OMEN-SED and cGENIE. Arrows represent the information transferred between models.

a more realistic description of organic matter degradation and related biogeochemical dynamics in marine sediments which can be coupled to global Earth system models we have developed OMEN-SED , a new, one-dimensional, numerically efficient reactive transport model.

The diagenetic processes implemented in OMEN-SED are described in detail in the previous chapter and the performance of the stand-alone model is evaluated through comprehensive comparisons with observations and results from a more complex numerical model. In this chapter, in order to illustrate how a fully coupled ocean-sediment system can be configured and applied, the coupling of OMEN-SED to the carbon-centric version of the "GENIE" Earth system model [cGENIE, Ridgwell et al., 2007] is described. We start by providing a brief description of cGENIE and the coupling procedure (Section 4.2). The second part of the chapter (Section 4.3) starts with more theoretical considerations regarding the different time and reactivity scales that need to be considered when simulating organic matter degradation in the sediments compared to the water column. Building upon these theoretical considerations different parameterisations for the OM degradation rate constants are tested and simulated organic matter concentrations in the surface sediments are compared to a global database.

4.2 Coupling to the cGENIE Earth system model

cGENIE is a model of Intermediate Complexity based on the efficient climate model "C-GOLDSTEIN" of Edwards and Marsh [2005], featuring a frictional-geostrophic 3D-ocean circulation model cou-

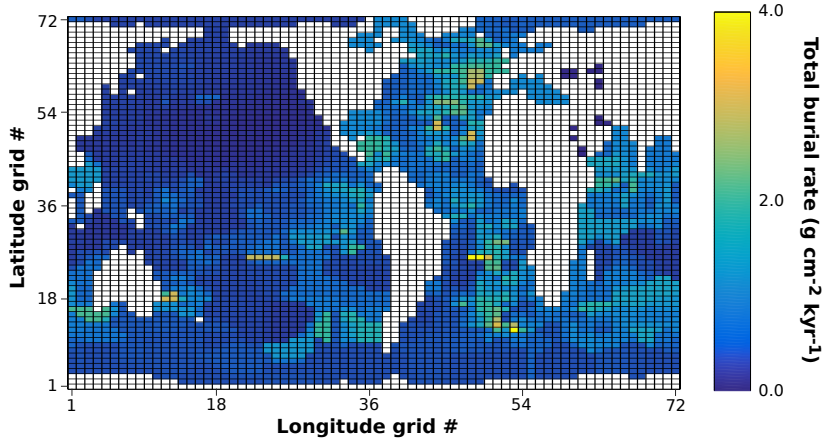

Figure 4.2: Distribution of prescribed total burial fluxes of detrital material, opal and $CaCO_3$ (in g cm^{-2} kyr^{-1}), re-gridded from the data compilation of Archer [1996a] using a method explained in the text. Note, latitude and longitude are shown in cGENIE grid-cells and not in degrees.

pled to a fast Energy-Moisture Balance 2D-atmosphere together with a dynamic-thermodynamic sea-ice component. The version of cGENIE used here includes the marine geochemical cycling of carbon, oxygen, phosphorus and sulfur [Ridgwell et al., 2007], preservation of carbonates in deep-sea sediments [SEDGEM, Ridgwell and Hargreaves, 2007] and terrestrial weathering [Colbourn et al., 2013]. The ocean model is implemented on a 36×36 equal-area horizontal grid with 16 vertical levels using the pre-industrial continental configuration and bathymetry as in Archer et al. [2009]. A finer grid (72×72) is used for the sediments [see Fig. 4.4C and Ridgwell and Hargreaves, 2007] and OMEN-SED is called by SEDGEM for each wet ocean grid point.

In our Earth system model set-up, we prescribe the burial sediment fluxes of detrital material, opal and $CaCO_3$, while leaving OMEN-SED to calculate organic matter preservation. This assumption serves two purposes. First, the run-time of the model is minimized as steady-state conditions are reached earlier, compared to the ca. 20-50 kyr adjustment time for surface sediment $CaCO_3$ [Ridgwell and Hargreaves, 2007]. Second, invariant flux fields remove feedbacks between OMEN-SED and the calculation of $CaCO_3$ preservation (changes in organic matter preservation affect $CaCO_3$ dissolution and hence burial rates which in turn affects weight percent of organic matter in the sediments) that would not only lengthen the sediment adjustment time but also make it impossible to carry out unbiased comparisons between different assumptions regarding organic matter reactivity in OMEN-SED.

We derive these fields form the data compilation of Archer [1996a] as follows. First, we re-grid the Archer [1996a] interpolated non carbonate mass accumulation rate field (NC_{flux}) to the 72×72 cGENIE sediment grid. This field includes detrital material plus opal (plus a minor contribution from organic matter). We could then directly calculate $\sum_{flux}$ (total burial flux of all components or total sediment accumulation rate) from this plus measurements of coretop

wt% $CaCO_3$ (C_{wtpct}) [Archer, 1996a] as $\sum_{\mathrm{flux}} = \mathrm{NC}_{\mathrm{flux}} \cdot (1 - \frac{C_{\mathrm{wtpct}}}{100})^{-1}$. However, some of the Archer [1996a] database C_{wtpct} values are both close to 100% and associated with high $\mathrm{NC}_{\mathrm{flux}}$, and hence would lead to unrealistically high values for $\sum_{\mathrm{flux}}$. We therefore impose a plausibility filter, by also re-gridding coretop wt% opal (O_{wtpct}) and quartz (Q_{wtpct}) and for grid points in which more than one component is reported and the sum exceeds 100 wt%, normalizing the individual components. (Note that for grid points with only a single solid component, no change is made.) We then calculate the individual solid component burial fluxes, and sum them up. To interpolate between the grid points associated with data, we iteratively average nearest (adjoining) neighbours. The distribution of the total burial flux $\sum_{\mathrm{flux}}$ (in g cm^{-2} kyr^{-1}) is shown in Figure 4.2.

Depending on the configuration of the overlying biogeochemical ocean model, processes can be included or excluded in OMEN-SED and stoichiometric factors (Tab. 3.10) need to be matched between models to ensure preservation of mass. As nitrogen is not modelled explicitly in the employed cGENIE configuration, $\mathrm{NC_i}$, $\mathrm{ALK}^{\mathrm{NIT}}$ and $\mathrm{ALK}^{\mathrm{DEN}}$ in OMEN-SED are set to zero. cGENIE, however, implicitly includes the effects of NH_4 release and its complete nitrification on alkalinity but neglects the impact of P release. Therefore, alkalinity stoichiometries for aerobic degradation, sulfate reduction and methanogenesis are changed to $\mathrm{ALK}^{\mathrm{OX}} = -16/106$, $\mathrm{ALK}^{\mathrm{SUL}} = 122/106$ and $\mathrm{ALK}^{\mathrm{MET}} = -16/106$, respectively (compare to default in Table 3.10).

Various biogeochemical tracers and parameters are transferred from SEDGEM to OMEN-SED (see Fig. 4.1) and are converted into the required units. Bottom water concentrations of solutes are converted from mol kg^{-1} to mol cm^{-3} and the depositional flux of POC ($\mathrm{POC}_{\mathrm{flux}}$) is converted from $\mathrm{cm}^3\,\mathrm{cm}^{-2}\,\mathrm{yr}^{-1}$ to mol $\mathrm{cm}^{-2}\,\mathrm{yr}^{-1}$ assuming an average density of POC of 1.0 g cm^{-3}. Within the water column in cGENIE, POC is partitioned into two fractions with different degradation length scales of ~590 m and 1000000 m, respectively. The labile pool thus degrades while sinking through the water column, whereas the refractory pool is assumed relatively unreactive [Ridgwell et al., 2007]. Thus, depending on seafloor depth, the partitioning of bulk POC reaching the sediments is different (Fig. 4.3A+B). This information is used by OMEN-SED to define the parameter f_1. Other parameters used from cGENIE are seafloor depth and local temperature. The advection/burial rate (w) is taken from the previous time-step of cGENIE, however, it is assured that w is not smaller than the detrital flux ($\mathrm{Det}_{\mathrm{flux}}$) to the sediments (e.g. $w < 0$ can occur if initially carbonate rich sediments are eroded during the spin-up of cGENIE). In case ($w \leq \mathrm{Det}_{\mathrm{flux}}$ & $\mathrm{Det}_{\mathrm{flux}} = 0.0$) all POC is remineralised at the ocean floor. Furthermore, a minimum value of $w = 0.4$ cm kyr^{-1} is imposed as OMEN-SED tends to be less stable for lower values. For comparison, this threshold is crossed for seafloor depths below 7000 m when applying the relationship between burial rate and water depth of Middelburg et al. [1997] and below 5200 m for the Burwicz et al. [2011] parameterisation. The bulk $\mathrm{POC}_{\mathrm{flux}}$ is separated into the labile and refractory component and the routine to find the steady-state solution for POC is called. Here, the two POC depositional fluxes are first converted into SWI concentrations ($\mathrm{POC}_i(z = 0)$, in mol cm^{-3}) by solving the flux

divergence equation:

$$\frac{\partial F}{\partial z} = -\frac{\partial}{\partial z}\left(-\xi D_i \frac{\partial \mathrm{POC}_i}{\partial z} + \xi w \mathrm{POC}_i\right) \tag{4.1}$$

for z=0. OMEN-SED then computes the fraction of POC preserved in the sediment (f_{POC}, see Eq. (3.6)) and subsequently calls the routines to find the steady-state solutions for the solute substances. Note, that in this initial coupling the calculated benthic uptake/return fluxes F_{C_i} of dissolved species C_i (compare Eq. (3.7)) are adjusted for the advective loss at the lower sediment boundary ($w \cdot C_i(z_\infty)$) to assure the conservation of mass in the coupled model:

$$F_{C_i} = \phi(0)\left(D_i \frac{\partial C_i(z)}{\partial z}\Big|_{z=0} - w\left[C_i(0) - C_i(z_\infty)\right]\right). \tag{4.2}$$

In case OMEN-SED computes unrealistic results for POC preservation (i.e. $f_{\mathrm{POC}} < 0.0$ or $f_{\mathrm{POC}} > 1.0$) we discard the results of OMEN-SED and all POC is remineralised at the ocean floor. For the modern ocean set-up, using the adjustments for w described above, this has not occurred and is just installed as a safety check. Finally, $\mathrm{f_{POC}}$ and the SWI-fluxes of solutes (F_{C_i}, in $\mathrm{mol\,cm^{-2}\,yr^{-1}}$) are returned to cGENIE. In case no POC is deposited on the seafloor (i.e. $\mathrm{POC_{flux}} = 0$), OMEN-SED is not executed and $\mathrm{f_{POC}}$ and F_{C_i} for all i are set to zero. In order to reduce memory requirements, the sediment profiles (e.g. as shown in Fig. 3.7 in the previous chapter) are not calculated in the FORTRAN version of OMEN-SED, however, the boundary conditions are saved and sediment profiles for specific grid-cells, ocean basins and ocean transects can be plotted at the end of each experiment using the stand-alone MATLAB version of OMEN-SED.

4.3 Parameterising the OM degradation rate constants in a global model

As shown in our sensitivity analysis (Section 3.3.1) and discussed by Arndt et al. [2013], the degradation rate constants for OM (k_i) are the most influential parameters and exert a dominant control on the SWI-flux of redox-sensitive elements as well as the preservation of organic matter. Yet, their spatial variability is unknown at the global scale and reported rate constants in the sediments can vary by about 10 orders of magnitude or more [Arndt et al., 2013; Middelburg et al., 1993]. Furthermore, when OMEN-SED is coupled to cGENIE, very different timescales have to be considered for OM degradation in the sediments compared to the water column (Fig. 4.3A+B) and thus the diagenetic rate constants cannot be easily implied by the assumed water column POC flux profiles in cGENIE. To illustrate this, lets consider the degradation of fresh, marine organic matter as it is transported and degraded along the ocean-sediment continuum. The bulk material is composed of a complex mixture of different organic carbon compounds that can be described by a reactivity continuum. Microbes preferentially degrade the more reactive organic matter compounds first [Emerson and Hedges, 1988; Lee et al., 2000; Wakeham et al., 1997], resulting in the preferential preservation of more unreactive compounds, rendering

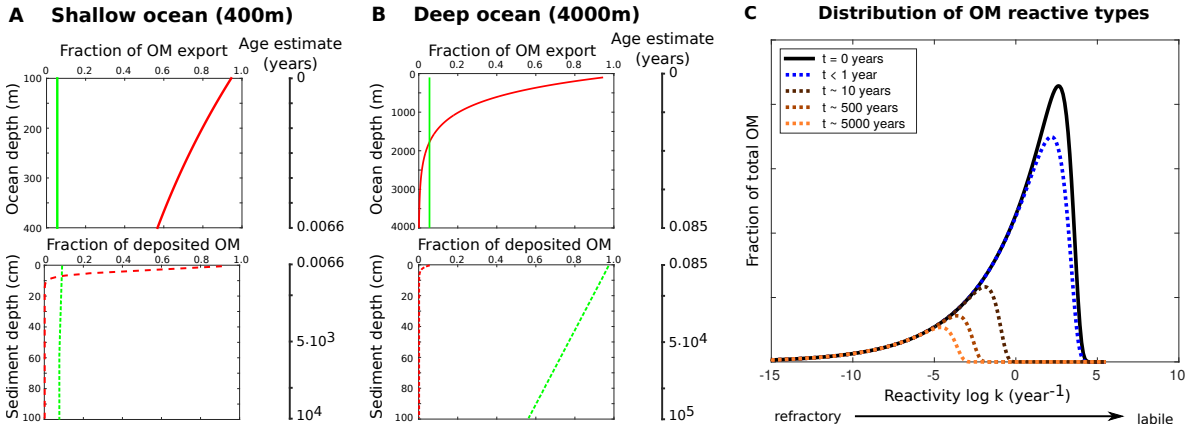

Figure 4.3: Idealised relationship of organic matter decomposition during remineralisation in the water column and the sediments. **A+B - Upper panels:** Water column development of the two organic matter fractions as represented in cGENIE for two ocean depths (red: labile OM with degradation length scale of 589m; green: refractory OM which is unreactive in the water column). The values are normalised to OM export at 100m. Age estimates for the OM since its export from the euphotic zone are calculated using a sinking velocity of 125m/day. **A+B - Lower panels:** Schematic representation of the development of the two OM fractions in the sediments (normalised to OM deposited on the seafloor). For the age estimates in the sediment column an advection rate of 0.01 and 0.001cm/yr is assumed, respectively. **C:** Idealised distribution functions of OM reactive types during remineralisation for different OM ages assuming a reactive continuum model for OM degradation. The initial distribution (at $t = 0$) represents fresh OM when it is exported from the euphotic zone [characterised by $a = 3e^{-4}$ yr^{-1} and $\nu = 0.125$ Boudreau et al., 2008].

the remaining mixture less and less reactive with time. Thus depending on the age of OM (or depth in the water and sediment column) the reactivity distribution of its compounds changes significantly (Fig. 4.3C) and the multi-G (2G in this case) approximation of this continuum has to take this shift into account. Fig. 4.3 illustrates these changes in the original reactivity distribution within a ocean-sediment framework. The reactivity distribution $t < 1$ year represents the organic matter mixture after it settled through the water column (Fig. 4.3C). Only the most reactive OM compounds are remineralised. This explains why the POC flux in the ocean can be represented with a 1G or pseudo 2G degradation model. In the sediments, however, much longer timescales have to be considered and a wider range of more unreactive compounds are degraded. As a consequence, significant changes in the reactivity distribution already take place in the upper millimetres of the sediments ($t \sim 10$ years, Fig. 4.3C). Therefore, a broader range of OM reactive types must be represented by the degradation model to capture the reactivity spectrum of OM in surface sediments, explaining why at least a pseudo 3G model [including two degradable and one refractory fraction Boudreau, 1997; Soetaert et al., 1996; Stolpovsky et al., 2015] is required. To complicate the situation even further, different sediment depths can represent very

different timescales. For instance, half a meter of sediment can be deposited within a year in a coastal setting, while it will represent thousands of years (if not more) of sedimentation in a deep ocean setting. Therefore, residence times and thus degradation rate timescales (or OM age) are mainly controlled by advection rates. For instance, assuming an advection rate of 0.01 cm/yr for the shallow ocean, OM at 5cm depth is has been degraded for approximately 500 years, whereas a deep ocean advection rate of 0.001 cm/year allowed for OM degradation of approximately 5000 years at the same depth. As a consequence, organic matter degradation in deep ocean sediments affects a much wider range of the reactivity continuum and our simple pseudo 3G approximation of the complex OM mixture needs to reflect this by allowing for different k and f values (Fig. 4.3C).

Thus defining appropriate OM degradation rate constants is a major challenge and source of uncertainty for diagenetic models. The rate constants in models are either determined through profile fitting for a specific site or, for global applications, they are related to a single, readily available characteristic (or master variable) of the local environmental conditions. For instance, considerable effort has been expended to relate the apparent rate constant for oxic and anoxic OM degradation to sedimentation rate (w) and various empirical relations have been proposed [Boudreau, 1997; Stolpovsky et al., 2015; Toth and Lerman, 1977; Tromp et al., 1995]. Nevertheless, these relationships are generally based and/or tested on limited data sets and their global applicability, especially under past or projected future environmental conditions is questionable [Arndt et al., 2013]. We hence test several alternative schemes in the coupled OMEN-cGENIE framework. Our objective is not to perform and discuss a detailed calibration of the coupled models as this is beyond the scope of this sediment model development paper. Rather we want to showcase the feasibility of the model coupling, illustrate the range of results and thus information that can be generated with OMEN-SED and verify that model results capture the main observed global benthic biogeochemical features.

4.3.1 Methodology

In this section we compare modelled mean POC weight percentages (wt%) in the upper 5cm of the sediments (POC_{5cm}) to the global distribution pattern of POC content in surface sediments (< 5cm sediment depth) of Seiter et al. [2004] using different parameterisations for the degradation rate constants k_1 and k_2. For our observational target we take the original POC distribution pattern in $1° \times 1°$ grid resolution [interpolated from > 5500 measurements, compare Seiter et al., 2004] and transform it onto the 72×72 SEDGEM grid (Figure 4.4). The regridding of the original POC distribution obviously affects the resolution of the data, especially for the continental margin, as some sites with higher POC wt% are lost in the regridding process (compare e.g. maximum values for the East Pacific and upwelling waters of the Namibian shelf, Figure 4.4A + B). The colour of the points in Figures 4.5 - 4.7 indicates the seafloor depth (SFD) of the respective cGENIE grid-cell. As the individual data-points are highly scattered and in order to see if a certain relation

between k_1 and k_2 performs better for specific ocean depths, the data-points are binned into 6 uniform depth-classes of 1000m each (respective mean POC wt% and SFD are represented by the triangles). The regression line (and the corresponding R^2-value) is calculated for the 6 bin-classes and included in the figures.

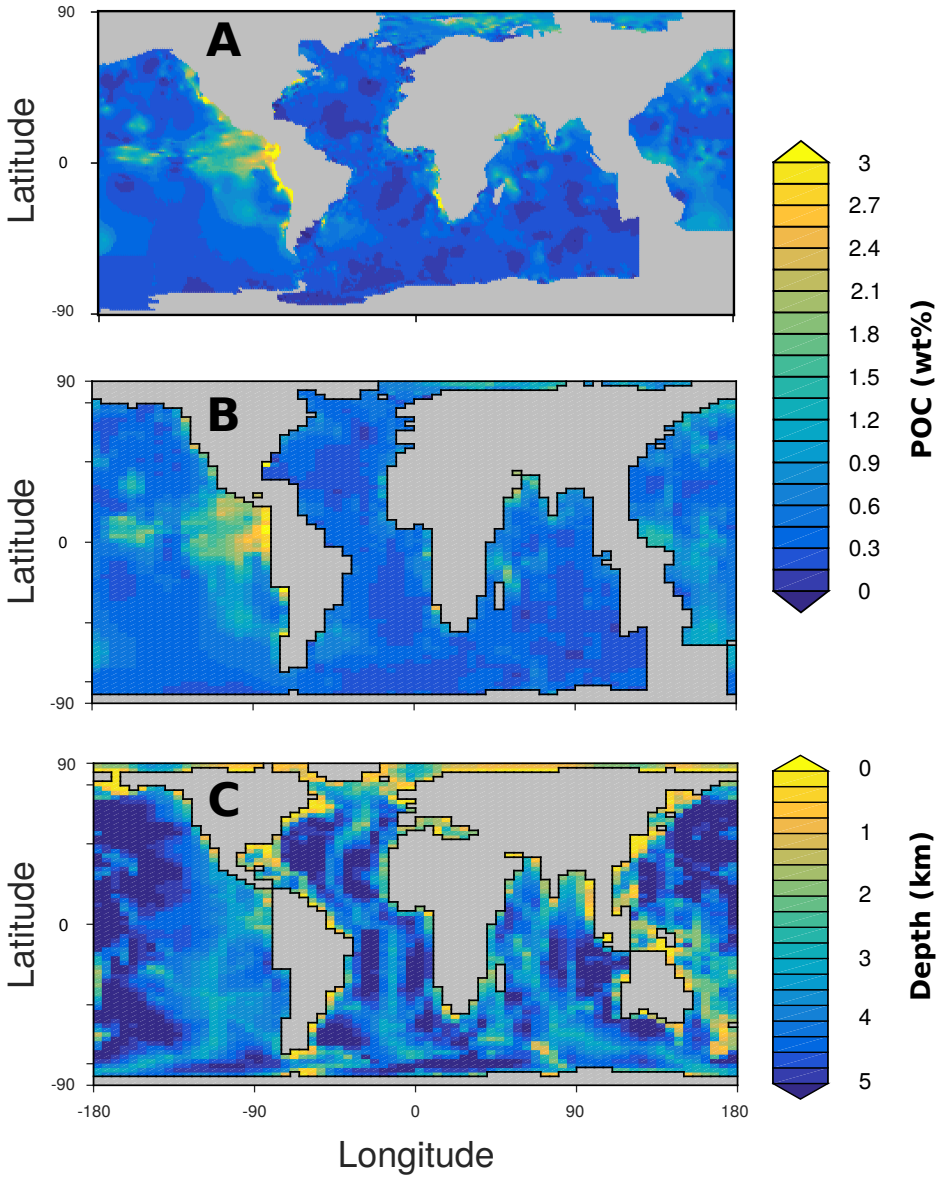

Figure 4.4: Observed distribution of sediment surface (< 5cm) POC wt% (A, B) and cGENIE bathymetry (C). (A) Original global distribution of POC wt% interpolated on a $1° \times 1°$ grid from more than 5500 individual data points [compare Seiter et al., 2004, for the interpolation procedure]. (B) Observed POC wt% data transformed onto the 72×72 SEDGEM grid. Grid points without any observations are left blank (grey). (C) Gridded continental configuration and ocean bathymetry of the 16-level, 72×72 equal-area cGENIE grid.

To parameterise the reactivity of organic matter in OMEN-SED two different schemes are tested and compared. First, spatially uniform degradation rate constants k_1 and k_2 are assumed. By simulating two different pools of POC in the water-column characterised by different degradation length scales [Ridgwell et al., 2007], cGENIE implicitly accounts for the decrease in mean POC reactivity with water-depth. The rate constants for the more refractory OM pool, k_2, is systematically varied between 0.004 and 0.006 year^{-1} and the more labile OM component, described by k_1, is assumed to degrade a multiple times faster (i.e. $x \in \{1.1, 1.2, 1.3, 1.5, 2\}$). However, although accounting for the decrease in mean POC reactivity with seafloor depth, this approach does not take into account the change in distribution of organic matter reactivity types caused by different burial velocities and thus different residence time scales in the sediments (Fig. 4.3). Therefore, the second approach uses the empirical relationship proposed by Boudreau [1997], which relates the apparent OM degradation rate constant in the upper sediments to the burial velocity, w (cm year^{-1}, see also Section 3.3.3):

$$k_{\text{app}} = 0.38 \cdot w^{0.59}. \tag{4.3}$$

Following Boudreau [1997] and Stolpovsky et al. [2015] it can be assumed that k_{app} represents the mean OM reactivity within the upper 10-20cm of the sediments. The following assumptions are made in order to calculate the two degradation rate constants for OMEN-SED:

$$k_{\text{app}} = f_1 \cdot k_1 + (1 - f_1) \cdot k_2 \tag{4.4}$$

$$k_1 = x \cdot k_2 \tag{4.5}$$

where x describes the relation between k_1 and k_2 and is subject to sensitivity experiments (with values of $x \in \{2, 5, 8, 10, 12, 15, 20, 25\}$). Note that the differences between k_1 and k_2 using this approach is significantly larger as in the globally uniform approach. As the fractions of labile and refractory OM reaching the sediments f_1 is known from cGENIE, k_1 and k_2 can be calculated independently for each grid-cell.

To simulate steady state sediment composition we configure the model as a “closed” system, i.e., one in which there is no loss of $CaCO_3$ through burial. The redox dependent P-cycle in OMEN-SED is not used in these experiments and all organic phosphorus is returned at the seafloor. To speed up the calculation and to assure that ocean redox changes caused by OMEN-SED do not impact the sediment composition of $CaCO_3$, we use the prescribed solid fields as described earlier. Apart from the prescribed fields and the 72×72 sediment grid the model is configured as in Archer et al. [2009] and atmospheric CO_2 is restored to a pre-industrial value of 278 ppmv. First a 20,000 year spinup is performed without OMEN-SED being coupled. All presented coupled cGENIE-OMEN simulations are run for 10,000 years to steady state from this spinup. OMEN-SED is called for each grid-cell in every time step, feeding back the resulting SWI-fluxes and the fraction of POC preserved in the sediments to cGENIE.

4.3.2 Results

4.3.2.1 Model-data comparison of organic matter concentrations

Figure 4.5 presents results for the spatially uniform degradation rate experiments. In general, using spatially uniform degradation rate constants 5 of the 6 bin-classes are located closer to the 1:1 line as in the experiments using the Boudreau [1997] relation (Fig. 4.6). Also the slope of some regression lines is close to 1.0 (e.g. $(k_2, x) \in \{(0.004, 1.5), (0.0045, 1.3), (0.005, 1.2), (0.005, 1.3), (0.0055, 1.1), (0.0055, 1.2), (0.006, 1.1)\}$), indicating that the simpler parameterisation adequately captures the relationship between between depth and observed POC wt% by bin-class. The reason for this is that BIOGEM provides a depth dependent POC flux and partitioning between the two fractions (Fig. 4.3). The shallowest bin-class (between 0 and 1000m) represents an exception, as OMEN-SED tends to overestimate POC preservation for this depth class. However, this could also be related to the regridding of the original POC distribution pattern of [Seiter et al., 2004] on to the SEDGEM grid, as some data grid-cells with higher POC wt% on the continental margin are lost due to the restricted SEDGEM resolution (compare Section 4.3). Overall, using this parameterisation, a relationship where the labile POC fraction degrades not more than 1.5 times faster than the refractory fraction fits the Seiter et al. [2004] data better than a larger spread between both POC pools (i.e. $x > 2.0$). We discuss later the implications of collapsing the k values in this specific calibration for long-term, geological carbon preservation.

Next the relationship of Boudreau [1997] and the assumptions of Eq. (4.4) and (4.5) are used to calculate k_1 and k_2. In Figure 4.6 (A-H) the relation between the two degradation rate constants (Eq. (4.5)) is changed globally, thus independent of the seafloor depth. The crossplots show that it is not possible to achieve a solution where all bin-classes fall onto, or close to, the 1:1 line. Also, the slope of the regression lines are generally much larger or smaller than 1.0 (with the exception of Figure 4.6C), indicating that the relationship between depth and observed POC wt% by bin-class is not adequately represented by the model. The R^2 values are strictly monotonically increasing for increasing x because a depth-dependency is artificially imposed for the modelled POC wt% through the relation between k_1 and k_2. When looking at the individual bin-classes it can be seen that shallow ocean depths are better represented by smaller differences between k_1 and k_2 (e.g. $k_1 = 5 \cdot k_2$ for SFD < 1000m, Figure 4.6B), and the deep ocean by a larger spread (e.g. $k_1 = 25 \cdot k_2$ for SFD > 3000m, Figure 4.6H). These results reflect the preferential degradation of more reactive organic matter types [Lee et al., 2000; Wakeham et al., 1997] and thus the change in the distribution functions of OM reactive types for different OM ages (Fig. 4.3C). In the shallow ocean bulk POC consists of fresher organic matter types on average and is therefore generally more reactive overall (i.e. higher k_{app} due to higher w in the model) as in the deep ocean. In addition, OM at 5cm sediment depth in the deep ocean is generally older as in the shallow ocean due to lower burial rates, therefore more reactive types are affected by degradation and a larger spread between k-values is needed to capture these dynamics (compare Fig. 4.3C).

Departing from our theoretical considerations (see discussion of Fig. 4.3C), we use these

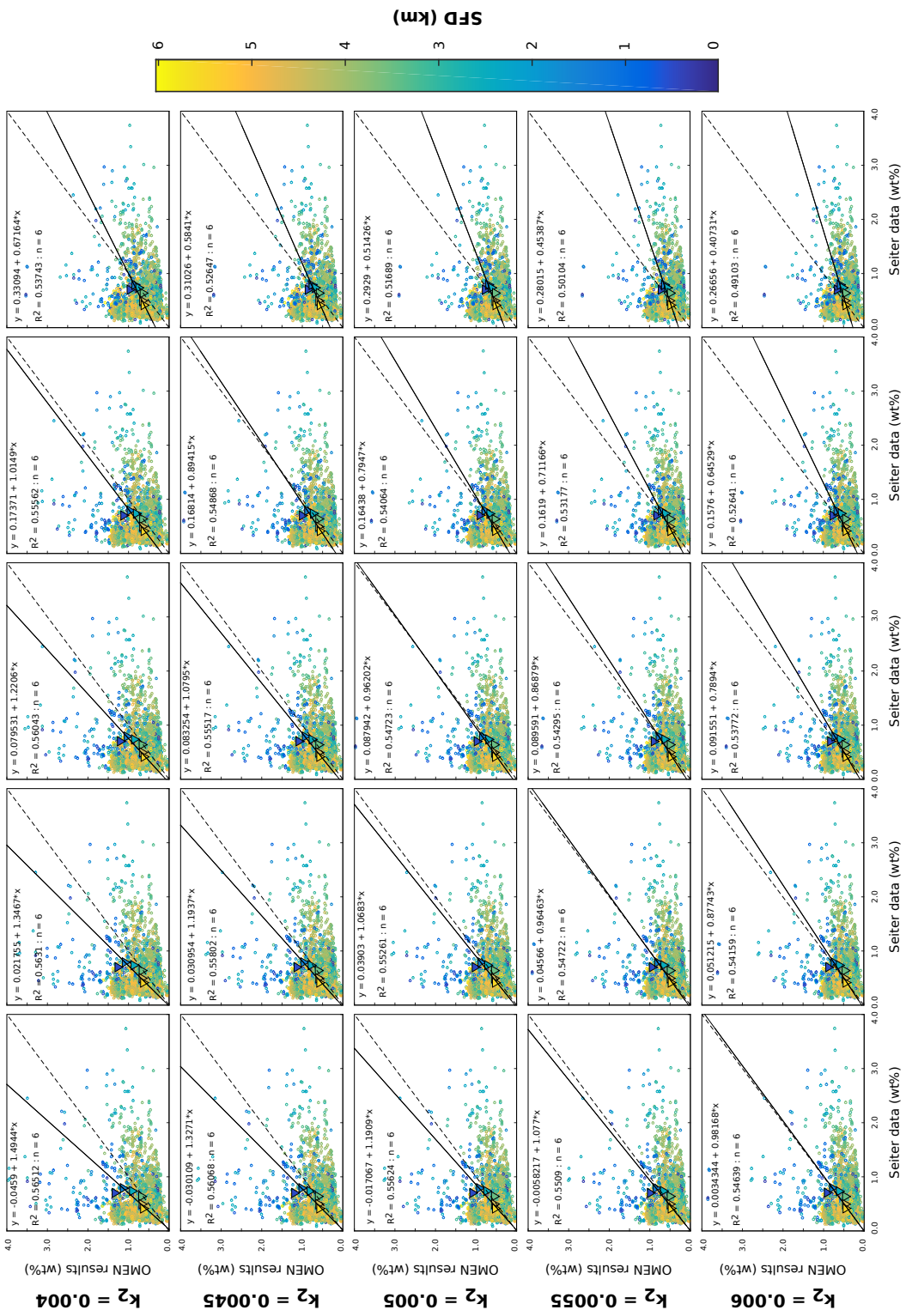

Figure 4.5: Crossplots comparing modelled and observed mean POC wt% in the upper 5 cm of the sediments using spatially uniform degradation rate constants k_1 and k_2. Data-points are binned into 6 uniform depth-classes of 1000m as in Fig. 4.6, each class is represented by a triangle. Grid-points with more than 4.0 POC wt% are not shown.

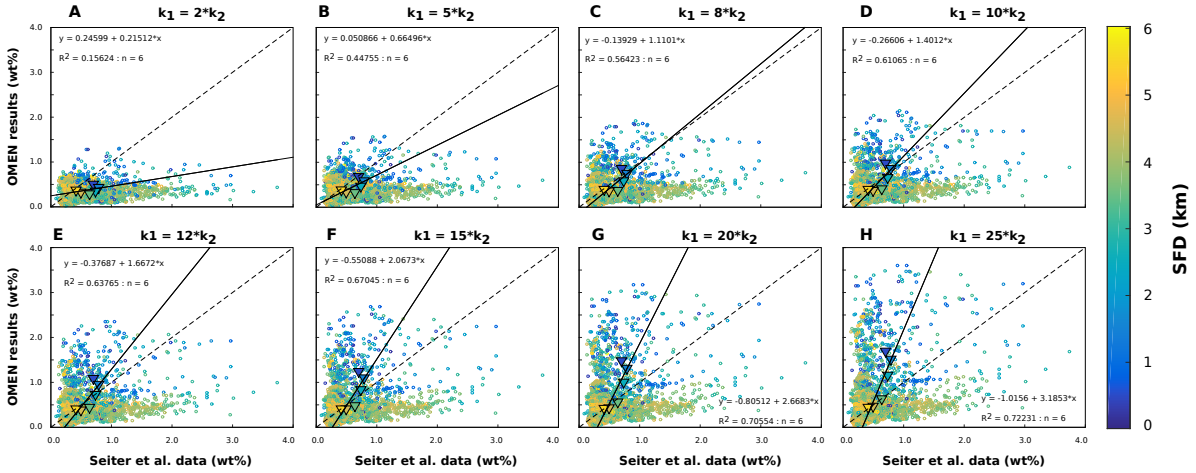

Figure 4.6: Crossplots comparing modelled and observed mean POC wt% in the upper 5 cm of the sediments using the relationship of Boudreau [1997] and the assumptions of Eq. (4.4) and (4.5) to calculate k_1 and k_2. Data-points are binned into 6 uniform depth-classes of 1000m, each class is represented by a triangle. Grid-points with more than 4.0 POC wt% are not shown.

observations to create a depth dependent relationship between the two degradation rate constants, where x in Eq. (4.5) is a function of SFD and takes values of $x = 5$ for SFD < 1000m, $x = 8$ for 1000m ≤ SFD < 2000m, $x = 12$ for 2000m ≤ SFD < 3000m and $x = 25$ for SFD ≥ 3000m for the 6 SFD bin-classes, respectively. In this depth dependent approach all bin-classes are close to the 1:1 line and the resulting regression model accounts for 92.6% of the variance of the modelled POC wt% around the observed mean of the bin-classes (Figure 4.7B). Furthermore, the slope of the regression line (0.9662) indicates that the relationship between depth and observed POC wt% for the bin-classes is well represented by the model. The histograms (Fig. 4.7C+D) visualize the difference between modelled and observed mean POC concentrations and demonstrate the high density of data points close to the 1:1 line. For the depth dependent approach, 92.5% of the cGENIE grid-cells show a difference between modelled and observed POC concentration of less than 1.0 POC wt%; in 79.9% of the grid-cells, the difference is less than 0.5 POC wt% (for the globally uniform approach the percentages are 95.37% and 70.95%, respectively).

Both experiments reproduce minimal POC concentrations in the subtropical gyres and generally higher concentrations along the continental margins (Fig. 4.7E+F). Both experiments, however, underestimate mean POC wt% in the surface sediments of the equatorial east Pacific and overestimate POC concentrations in the North Pacific and Southern Oceans (Fig. 4.7G+H). The depth dependent approach of Boudreau [1997] shows more spatial variability in POC preservation than the other parameterisation. In general, implementing lower, anaerobic degradation rate constants when bottom water oxygen concentrations fall below a threshold value could potentially improve the simulation of higher POC concentrations in areas with high POC input to the sediments [Palastanga et al., 2011].

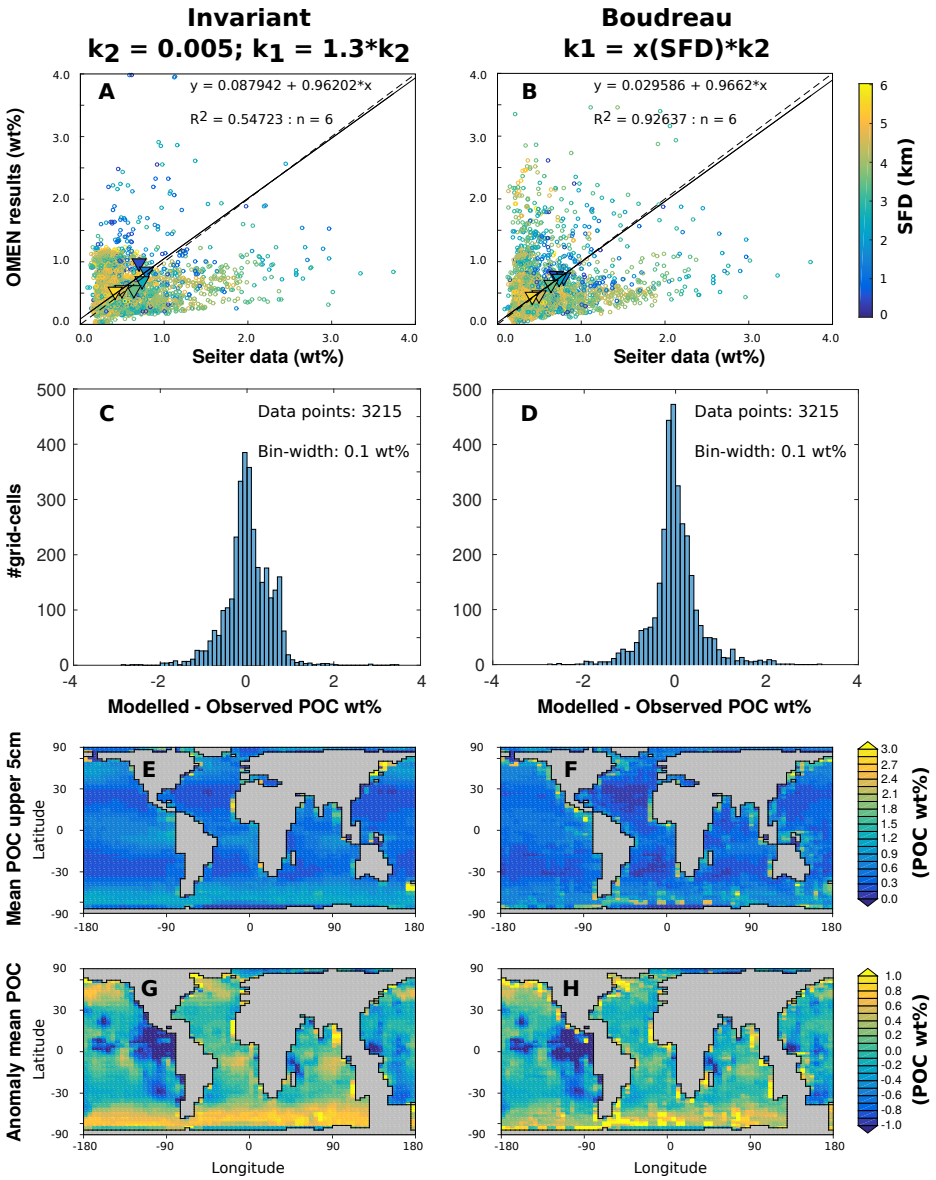

Figure 4.7: Mean POC concentrations in the upper 5cm of the sediments (POC_{5cm}) using the globally uniform model ($k_2 = 0.005$, $k_1 = 1.3 \cdot k_2$) and the depth dependent parameterisation $k_1 = x(\text{SFD}) \cdot k_2$ adapted from Boudreau [1997]. A+B: Crossplots as shown before in Fig. 4.5 and 4.6. C+D: Histograms of the residuals of modelled minus observed POC_{5cm}. E+F: POC_{5cm} as calculated with OMEN-SED. G+H: Difference map of POC_{5cm} as calculated with OMEN-SED and interpolated data from Seiter et al. [2004].

4.3.2.2 Simulated sediment-water interface fluxes and sediment characteristics

For the depth dependent Boudreau [1997] approach modelled SWI-fluxes and sediment characteristics are shown in Figure 4.8. Modelled total POC degradation (POC_{degr}) rates in the upper sediments decrease from the shelves to the deep sea by up to 2 orders of magnitude (Fig. 4.8B). This is in agreement with data from the literature [e.g. Burdige, 2007; Middelburg et al., 1997, 1993] and other model results [e.g. Thullner et al., 2009] which indicate that the highest degradation rates in marine sediments are found in the coastal ocean (SFD < 200 m). Oxygen fluxes into the sediments (Fig. 4.8C) range from 0.0 for the deep ocean and sites without OM deposition to values of about 300 μmol $cm^{-2}yr^{-1}$ for the shallow ocean with the highest POC degradation rates. Influx of SO_4 into the sediments is rather low (between 0.0 and 23.9 μmol $cm^{-2}yr^{-1}$) because in OMEN-SED 95% of produced H_2S is reoxidised to SO_4, therefore sulfate reduction is mainly driven by in situ sulfide oxidation. However, in general the coupled model fluxes fall well within the ranges predicted by the stand-alone global hypsometry experiments (O_2 between 0.0 and 800 μmol $cm^{-2}yr^{-1}$ and SO_4 between 0.0 and about 300 μmol $cm^{-2}yr^{-1}$, compare Section 3.3.3). In accordance with the total POC degradation rates the release of PO_4 shows a maximum value of 8.12 nmol $cm^{-2}yr^{-1}$ on the shelves (Fig. 4.8D). The relative contribution of aerobic POC degradation in the upper sediments increases from the shelves to the deep sea (Fig. 4.8G) which is also consistent with estimates from Thullner et al. [2009] who found that oxygen is responsible for less than 10% of POC_{degr} at 100 m SFD and for more than 80% in the deep sea.

The oxygen penetration depth in OMEN-SED increases from values below 1cm at the shelves to more than 10cm in the deep ocean (Fig. 4.8H and 4.9). Small oxygen penetration depths of a few millimetres are typical for bioturbated sediments in the coastal ocean [e.g. Wenzhöfer and Glud, 2002] and the oxygen penetration depth has been shown to increase rapidly with SFD to more than 10 cm in the deep sea [Glud, 2008; Meile and Van Cappellen, 2003]. Fischer et al. [2009] and D'Hondt et al. [2015] even found cores along a transect in the South Pacific gyre being oxygenated over their entire length (up to 8 m or even 75 m, respectively) which is consistent with our model results (not shown). Simulated mean oxygen penetration depths for the 6 depth bin-classes also agree well with observations compiled by Glud [2008] and Meile and Van Cappellen [2003, Fig. 4.9].

4.4 Conclusions

This Chapter describes the extension of the 3-D Earth system model cGENIE to include a mechanistic representation of benthic organic matter cycling and related biogeochemical dynamics. The inclusion of the module OMEN-SED has allowed us to make use of a global database of organic matter contents in the surface sediments in order to constrain our global model results. The calibrated model framework successfully simulates observed global patterns of surface sediment organic matter contents, SWI-fluxes, oxygen penetration depths and biogeochemical reaction

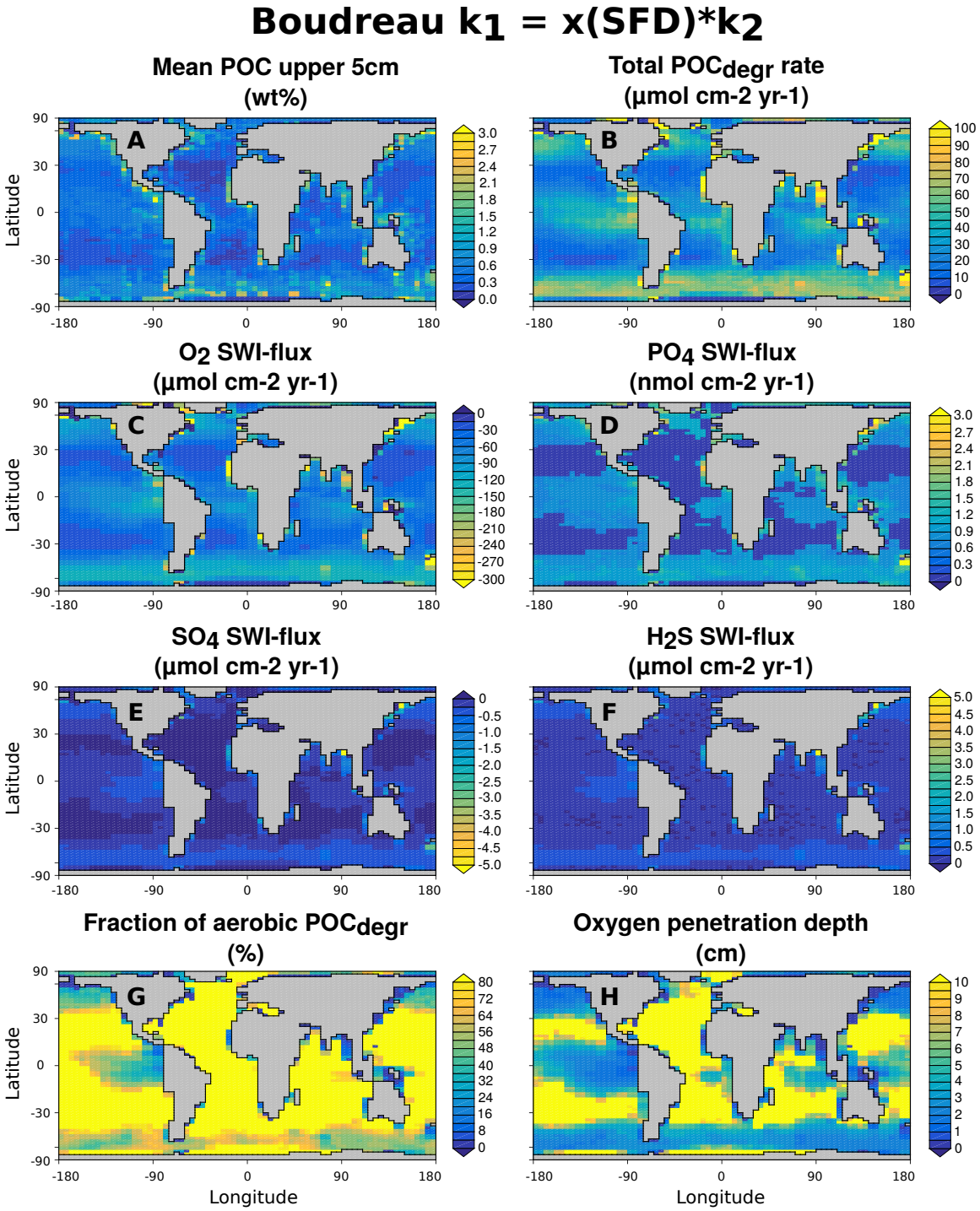

Figure 4.8: Sediment characteristics related to POC degradation and oxygen consumption for the depth dependent paramaterisation after Boudreau [1997] with $k_1 = x(\mathrm{SFD}) \cdot k_2$. Total $\mathrm{POC}_{\mathrm{degr}}$ rate and fraction of aerobic $\mathrm{POC}_{\mathrm{degr}}$ are the respective values for the first 5cm in the sediments.

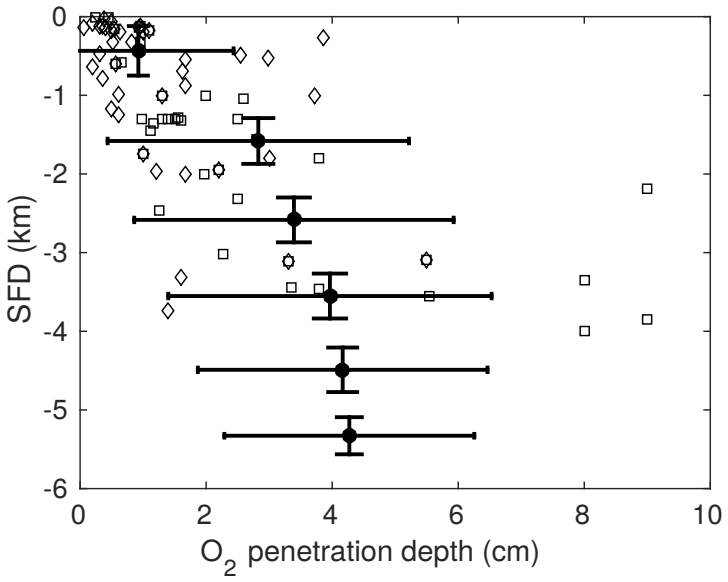

Figure 4.9: Seafloor depth versus O_2 penetration depth for the depth dependent paramaterisation after Boudreau [1997] with $k_1 = x(\text{SFD}) \cdot k_2$. Diamonds represent observations compiled by Meile and Van Cappellen [2003] and squares observations from Glud [2008]. Circles are the mean model results for the 6 SFD bin-classes (with standard deviations). Grid-cells where the entire sediment column is oxic (i.e. $z_{\text{ox}} = 100\text{cm}$) are not considered in these statistics (17, 32, 102, 300, 477 and 307 cells for the 6 bin-classes, respectively).

rates.

Due to its particular significance for the model output, different parameterisations for the degradation rate constant of organic matter are implemented in OMEN-SED. Compared are spatially uniform degradation rate constants as well as the empirical relationship of Boudreau [1997] which describes the apparent degradation rate constant as a function of sedimentation rate. The comparison between simulated OM contents and observations indicates that a depth and sedimentation rate dependent relationship provides the best fit, confirming more theoretical considerations regarding the different time and reactivity scales that need to be considered.

In order to simulate organic matter preservation in the upper sediments, such as the first 5 centimetres, the degradation rate constants for the labile and refractory OM pool are rather similar (i.e. they differ by less than two orders of magnitude). Instead, in order to simulate organic matter preservation in the deeper sediments and thus addressing questions concerning long-term, geological carbon burial the degradation rate constant for the refractory OM pool has to be scaled down. The resulting larger difference between degradation rate constants can be interpreted as being needed to capture the broader range of OM reactivities degraded over the entire sediment column (see Fig. 4.3).

However, more work is needed to develop and test different mechanistic parameterisations relating degradation rate constants to available environmental parameters (e.g. bottom water

oxygenation, sedimentation rate or seafloor depth) in order to represent the heterogeneous reactivity distribution of OM types due to preferential degradation and different time scales in the sediments. Because of its computational efficiency the coupled model framework presented here can be used to explore these questions using large simulation ensembles and objective statistical methods for sensitivity analysis. Furthermore, as all major parts of the global carbon cycle are included in the new model it is well suited to examine the role of sediments for global biogeochemical cycles and climate and for exploring feedbacks within the Earth system in response to a wide range of perturbations and over various timescales.

CHAPTER 5

DEVELOPMENT OF OCEAN ANOXIA AND EUXINIA DURING OAE2: THE ROLE OF BENTHIC-PELAGIC COUPLING.

Contributions and acknowledgements
This chapter is adapted from a research article in preparation for publication. S. Arndt and A. Ridgwell provided assistance with editing and advised on aspects of this work. All work presented in this chapter is my own.

5.1 Introduction

Oceanic Anoxic Events (OAEs) represent severe disturbances of the global carbon, oxygen and nutrient cycles of the ocean common to the Cretaceous period [e.g., Jenkyns, 1980, 2010; Schlanger and Jenkyns, 1976]. The archetypal example is the Cenomanian-Turonian boundary event (OAE2, ~ 93.5 Ma), which is characterized by extreme atmospheric CO_2 concentrations [Bice et al., 2006; Takashima et al., 2006], widespread bottom water anoxia [e.g., Brumsack, 2006; Goldberg et al., 2016; Owens et al., 2012], and photic zone euxinia [Kuypers et al., 2002; Pancost et al., 2004; Sinninghe Damsté and Köster, 1998] evidenced by various geochemical proxies. OAE2 is also characterized by a positive carbon isotope excursion detectable in sedimentary organic and inorganic $\delta^{13}C$ records [Fig. 5.1, Arthur et al., 1988; Schlanger and Jenkyns, 1976; Scholle and Arthur, 1980]. This excursion is caused by increased burial of ^{13}C-depleted organic matter (OM) in marine sediments, leading to an increase in the isotopic composition of the marine total dissolved inorganic carbon pool [phases A and B in Fig. 5.1, Arthur et al., 1988; Schlanger and Jenkyns, 1976]. The elevated rate of OM burial is indicated by laminated, thick organic carbon-rich layers (black shales) in the geological record [Arthur and Sageman, 1994; Stein et al., 1986]. The fate of

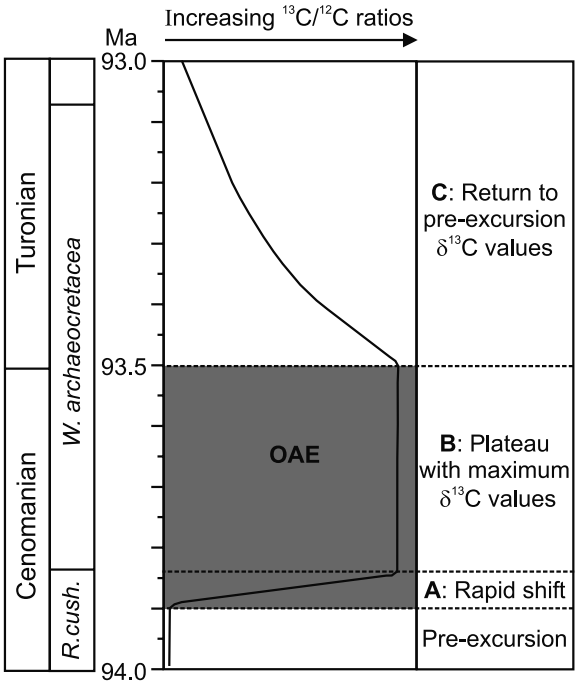

Figure 5.1: Idealized representation of the Cenomanian-Turonian stable carbon isotope excursion including three main phases (modified from Kuypers et al. [2002]). OAE2 is defined as the main phase of enhanced organic matter burial rates, indicated by the shaded area. Phase A represents a rapid increase in $\delta^{13}C$ values caused by increasing burial rates of ^{13}C-depleted organic matter in marine sediments. This is followed by a plateau of $\delta^{13}C$ values resulting from a maximum in OM burial rates (phase B). After OAE2, the $^{13}C/^{12}C$ ratio gradually decreases to background, pre-excursion values (phase C).

OM in the sediments is important for the genesis and persistence of OAE2 because it exerts a critical control on oxygen and nutrient levels in the ocean [Arndt et al., 2013; Mackenzie, 2005]. Over longer timescales burial of OM plays an important role for the recovery from OAE like conditions as it leads to net oxygen input to, and CO_2 removal from the atmosphere and ocean system [Berner, 2004]

Two mechanisms are generally proposed to explain the prolonged oceanic oxygen depletion during OAE2: (1) decreased oxygen supply to the deep ocean due to weaker overturning circulation [Bralower and Thierstein, 1984; Erbacher et al., 2001], and (2) increased oxygen demand in the water column resulting from enhanced primary productivity [Kuypers et al., 2002; Monteiro et al., 2012; Ozaki et al., 2011]. The observed increased OM burial is thought to be a result of both increased primary productivity and enhanced OM preservation in the sediments due to anoxic bottom waters [Jenkyns, 2010; Pedersen and Calvert, 1990]. Primary productivity may have been fuelled by increased nutrient availability and evidence for a rise in total phosphorus (P) accumulation rates in the sediments before the onset of OAE2 and a decrease during OAE2

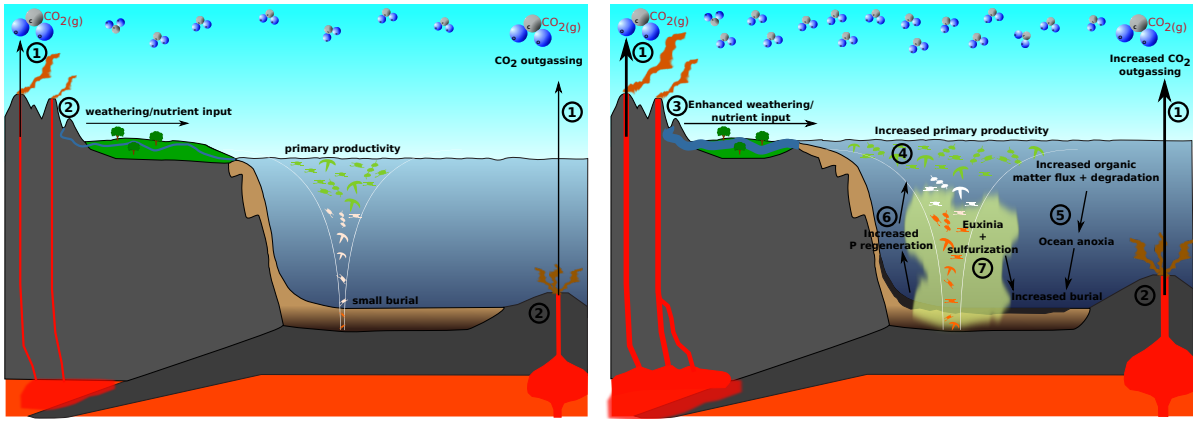

Figure 5.2: Schematic of potential feedbacks during OAE2. **Left:** Pre-OAE2, with background CO_2 outgassing (1) and nutrient input to the ocean (2). **Right:** Peak-OAE2, with increased volcanic CO_2 outgassing (1, 2) enhancing the nutrient input (2, 3) and primary productivity in the ocean (4). This leads to the development of ocean anoxia (5) and results in enhanced P regeneration from marine sediments (6), which in turn fuels PP (4). This further increases anoxia and develops into euxinia (7), increasing OM burial, therefore drawing down atmospheric CO_2 and re-oxygenating the ocean.

points towards the oceanic P cycle as being of particular importance [Kraal et al., 2010; Mort et al., 2007, 2008]. Potential sources for the initial P input include elevated weathering rates due to warmer temperatures [Blättler et al., 2011; Pogge von Strandmann et al., 2013], leaching of nutrients from flooded continental shelves due to sea level rise [Jones and Jenkyns, 2001; Voigt et al., 2006] and increased hydrothermal activity associated with large-scale submarine volcanism due to the formation of the Caribbean and/or Arctic Large Igneous provinces [Du Vivier et al., 2014; Snow et al., 2005]. Once bottom waters became anoxic, enhanced recycling of P relative to organic carbon from the sediments could have helped to sustain this initial boost in productivity, supposing the nutrients are upwelled into the photic zone [Kraal et al., 2010; Van Cappellen and Ingall, 1994]. The most important feedbacks considered responsible for OAE2 are summarised in Figure 5.2.

Even though OAE2 is the most studied of the oceanic anoxic events of the Cretaceous, considerable uncertainty about the spatial extent of anoxia and especially euxinia still remains. Sedimentary, biomarker and geochemical observations for ocean redox conditions suggest that prior to OAE2 solely the seafloor of the proto-North Atlantic Ocean was anoxic, whereas in the course of OAE2 anoxia spread over most of the worlds oceans (Table 5.1 and Fig. 5.3 b and c). Model-data comparison suggests that anoxia was spreading from 5% before the onset to at least 50% of the ocean volume during OAE2, with anoxic bottom waters covering most of the proto-Atlantic and Indian Oceans as well as the Tethys Sea and half of the Pacific Oceans [Monteiro et al., 2012]. Euxinia represents the most extreme anoxic condition, where free H_2S exists in the

Table 5.1: Evidence of seafloor anoxia and photic zone euxinia before and during OAE2. Adapted from Monteiro et al. [2012] who associate pre-OAE2 conditions with sediment observations immediately preceding the positive carbon isotope excursion and peak-OAE2 conditions with observations deposited during the peak of the excursion. Evidence for bottom water anoxia is represented by black dots(•), evidence for photic zone euxinia by black triangles (▲), evidence against by crosses (×) and question marks (?) indicate questionable evidence.

		Low Oxygen		**Euxinia**	
Label	Locations	Pre	Peak	Pre	Peak
A	Cape Hatteras (DSDP sites 105, 603B)	•?	•	–	▲
B	Newfoundland Basin (ODP Site 1276)	–	•	–	–
C	Hatteras Abyss (ODP Site 1276)	–	•	–	×?
D	Tarfaya Basin (Morocco)	•	•	▲	▲
E	Maracaibo Basin (Venezuela)	•	•	–	–
F	Demerara Rise (DSDP site 144, ODP Leg 207)	•	•	▲	▲
G	Cape Verde (DSDP sites 367, 368)	•	•	▲	▲
H	Angola Basin (DSDP site 530A)	×	•	×	▲
J	Eastbourne and Dover (UK)	×	×	–	–
K	Münsterland Basin (Germany)	×	×	–	–
L	Chrummflueschluch (Switzerland)	×	×	–	–
M	Vocontian Basin (France)	×	•	–	–
N	Galicia Margin (ODP Site 641)	–	•	–	▲?
P	Apennines (Italy)	×	•	–	▲?
Q	Oued Bahloul (Tunisia)	×	•	–	▲?
R	Levant Platform (Jordan)	×	•	×?	▲?
S	Tethyan Himalayas (Tibet)	×	•?	–	×?
T	Kerguelen Plateau (ODP site 1138)	–	•	–	–
U	Yezo Group (Japan)	×	•?	–	–
V	Mariana Basin (DSDP site 585)	×	•?	–	–
W	Shatsky and Hess Rises (DSDP sites 305, 310)	–	•?	–	–
X	Central South Pacific (DSDP site 463)	×	×	–	–

For references and explanation of the evidence please see Monteiro et al. [2012].

water column because sulfate has replaced oxygen and nitrate as the terminal electron acceptor (TEA) to remineralize organic matter. Observations for euxinia are more limited than for anoxia especially before the onset of OAE2 and for the Pacific and Indian Oceans (Fig. 5.3). However, it can be inferred that prior to OAE2 parts of the equatorial proto-Atlantic Ocean were already euxinic and that during OAE2 euxinic conditions also prevailed in parts of the proto-South and -North Atlantic Ocean [Kuypers et al., 2002; Pancost et al., 2004; Sinninghe Damsté and Köster, 1998] and might have reached the southern Tethys Ocean [Fig. 5.3 d and e, Monteiro et al., 2012; Sepúlveda et al., 2009]. Geochemical mass balance models suggest that euxinia affected between 2 - 10% of the global seafloor during OAE2 [Dickson et al., 2016; Owens et al., 2013, 2017].

Marine sediments play a crucial role for the global cycling of oxygen, phosphorus and sulfur as they take up TEAs from the water-column and represent the only relevant sink for P in the

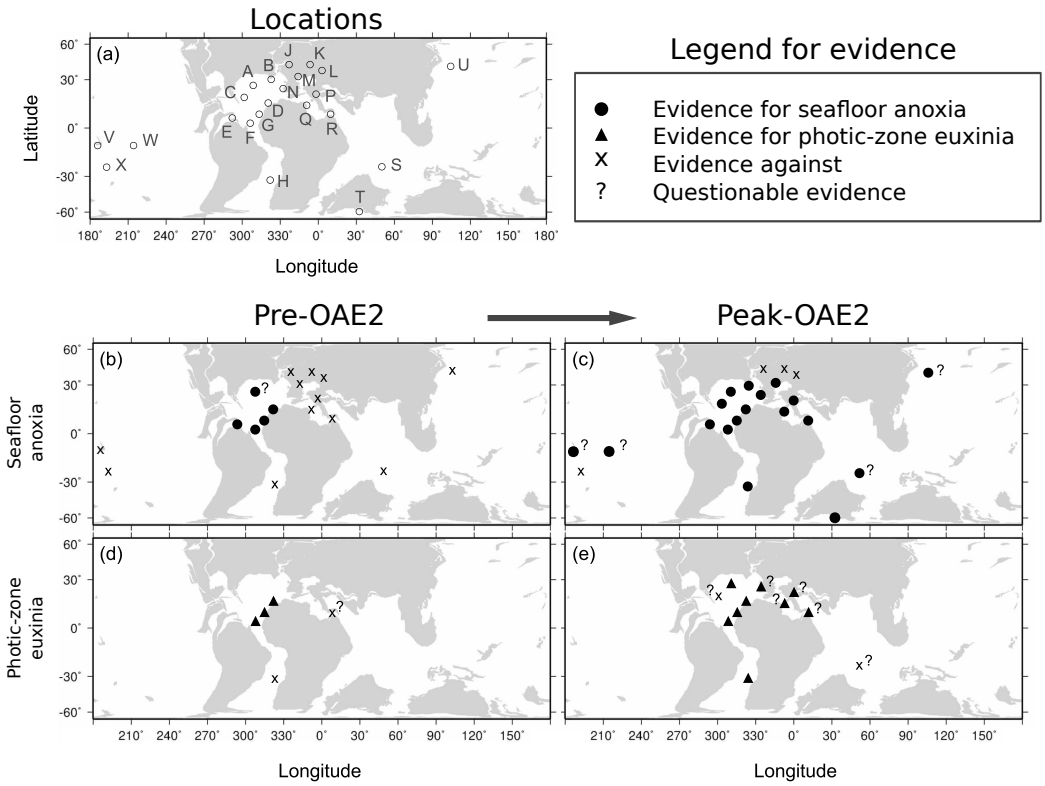

Figure 5.3: Global distribution of ocean redox evidence as reported in Table 5.1. Locations of the observations (a), evidence for seafloor anoxia (b, c) and photic zone euxinia (d, e) before and during OAE2. Figures and observations are adapted from Monteiro et al. [2012].

marine environment [Berner et al., 1993]. Most early diagenetic reactions can be related either directly or indirectly to the degradation of organic matter [e.g. Arndt et al., 2013; Boudreau and Ruddick, 1991; Middelburg et al., 1993]. The TEAs oxygen, nitrate and sulfate for instance are consumed to oxidize OM, resulting in the release of ammonium, hydrogen sulfide and phosphate to the pore water which might diffuse upward to the water column. As such, OM degradation in the sediments can profoundly affect the oxygen, sulfur and nutrient inventory of the ocean and thus its redox state [Lenton and Watson, 2000; Van Cappellen and Ingall, 1994].

For the genesis and persistence of OAE2 the recycling of phosphate from marine sediments might have also been of particular importance [Kraal et al., 2010; Van Cappellen and Ingall, 1994]. In the oxic part of the sediment, the produced PO_4 either diffuses upward to the water column or is adsorped to Fe oxides forming Fe-bound P [Slomp et al., 1996]. In the suboxic/anoxic zone, PO_4 is not only produced through organic matter degradation but is also released from the Fe-bound P pool due to the reduction of Fe oxides. Thus, the recycling of P from the sediments is strongly affected by local redox conditions as under oxygen depleted bottom waters and sediments, the reduction of Fe oxides liberates more P and may help to sustain increased productivity and

ocean anoxia [Kraal et al., 2010; Van Cappellen and Ingall, 1994]. This positive feedback between productivity, anoxia and P recycling from sediments has been suggested by various box-model [Bjerrum et al., 2006; Handoh and Lenton, 2003; Tsandev and Slomp, 2009; Wallmann, 2003] and laboratory studies [Kraal et al., 2010; Mort et al., 2007, 2008] alike to facilitate the persistence of anoxic conditions during OAE2.

Box-model studies have improved our mechanistic understanding of the feedbacks responsible for the development, persistence and/or termination of OAEs. They explored hypothesis under what conditions anoxia could have developed or declined, pointing towards changes in ocean circulation [Ruvalcaba Baroni et al., 2014], alterations of the phosphorus cycle [Bjerrum et al., 2006; Handoh and Lenton, 2003; Tsandev and Slomp, 2009] or imply that anoxia was linked to potential changes in the C:P Redfield ratio of marine OM under high atmospheric pCO_2 [Flögel et al., 2011]. Model-data comparisons are possibly the best approach to improve our understanding further and to evaluate competing mechanisms. However, the generally very limited data coverage makes a meaningful model-data comparison challenging and records from different proxies (with different sensitivities) or geographically distant locations are usually very difficult to assess in relation to each other. Spatially resolved global biogeochemical models can support the interpretation of paleo-records by explicitly representing a particular proxy and placing its distribution into a global, mechanistic framework. This facilitates more robust model-data comparisons and enables the modeller to make more quantitative assessments of the observations. Monteiro et al. [2012] use this strength of a 3D global biogeochemical model by comparing different geochemical proxy records for seafloor anoxia and photic zone euxinia to biogeochemical tracer simulations and are able to estimate the relative impact of different mechanisms for the de-oxygenation.

All aforementioned modelling studies highlight the significance of organic matter burial in marine sediments for the development and termination of OAE2, however, none of them uses an explicit sediment representation for OM degradation and preservation. The major hurdle is the complexity and high computational cost of simulating the essential redox reactions in marine sediments, which are critical to quantify the burial of OM and benthic recycling fluxes of chemical compounds. In order to close this knowledge gap, we developed a new, one-dimensional, numerically efficient model to represent OM preservation in marine sediments (OMEN-SED). OMEN-SED's computational efficiency allows its coupling to Earth system models of different complexities and therefore the investigation of coupled global biogeochemical dynamics over geological timescales.

This study explores, for the first time, the impact of using different representations for the benthic-pelagic coupling in a 3D-ocean-sediment model framework for the development of ocean anoxia and euxinia during OAE2. Equilibrium simulations are performed using the carbon-centric version of the "GENIE" Earth system model [cGENIE, Ridgwell et al., 2007] with four different lower boundary representations for the ocean. Compared are the very crude, but widely

adopted, Conservative and Reflective lower boundary approaches [see Hülse et al., 2017; Soetaert et al., 2000] with our new model OMEN-SED. Model results are constrained with observations for seafloor anoxia and photic zone euxinia [Monteiro et al., 2012].

5.2 Methods

5.2.1 The cGENIE Earth system model and OMEN-SED

For the model simulations in this chapter the carbon-centric version of the "GENIE" Earth system model [cGENIE Ridgwell et al., 2007] is used. cGENIE is a model of Intermediate Complexity based on the efficient climate model "C-GOLDSTEIN" of Edwards and Marsh [2005], featuring a frictional-geostrophic 3D-ocean circulation model coupled to a fast Energy-Moisture Balance 2D-atmosphere together with a dynamic-thermodynamic sea-ice component. The version of cGENIE used here includes the marine biogeochemical cycling of carbon, oxygen, phosphorus and sulfur as in Monteiro et al. [2012]. In contrast to Monteiro et al. [2012], nitrogen dynamics are not included in the cGENIE model employed here. cGENIE is implemented on a 36×36 equal-area horizontal grid with 16 vertical levels in the ocean and uses Cenomanian bathymetry and continental configuration as shown in Figure 5.4 which has been re-gridded from the higher resolution model FOAM [Donnadieu et al., 2006b]. Boundary conditions are adapted to represent Late Cretaceous conditions: (1) the annual average surface-ocean wind stress field is re-gridded from the Cenomanian FOAM experiment forced at 4.0× pre-industrial CO_2, (2) the solar constant is reduced by 0.56% and (3) the zonally averaged planetary albedo is re-gridded from the coupled general circulation model experiment of Hunter et al. [2008]. Despite its lower resolution, cGENIE is able to reproduce the main 3-D features of ocean dynamics of the Late Cretaceous such as ocean circulation and deep-water formation in the Southern Ocean and North Pacific [Poulsen et al., 2001; Trabucho-Alexandre et al., 2010]. Atmospheric CO_2 concentrations are restored to 2.0× pre-industrial value (556 ppmv) for the pre-OAE2 scenarios and 4.0× pre-industrial value (1112 ppmv) for the peak-OAE2 scenarios [Monteiro et al., 2012].

The cGENIE Earth system model is then extended with the new Organic Matter ENabled SEDiment model (OMEN-SED, see Chapter 3 and 4).The one-dimensional, analytic advection-diffusion-reaction model describes OM degradation and burial in the sediments as well as associated biogeochemical dynamics of the most important terminal electron acceptors (here O_2, SO_4) and methane (CH_4), related reduced substances (H_2S) and macronutrients (PO_4). Sediment-water interface fluxes of explicitly resolved pore water species are simulated as a function of bottom water concentrations, OM degradation rate constants, temperature and local sediment characteristics (i.e. bioturbation, advection and diffusion rate) and are returned to cGENIE in each time-step.

To simulate the preferential regeneration of phosphorus from the sediments under anoxic conditions a redox dependent P cycle is included in OMEN-SED. Thus, beside P release to pore

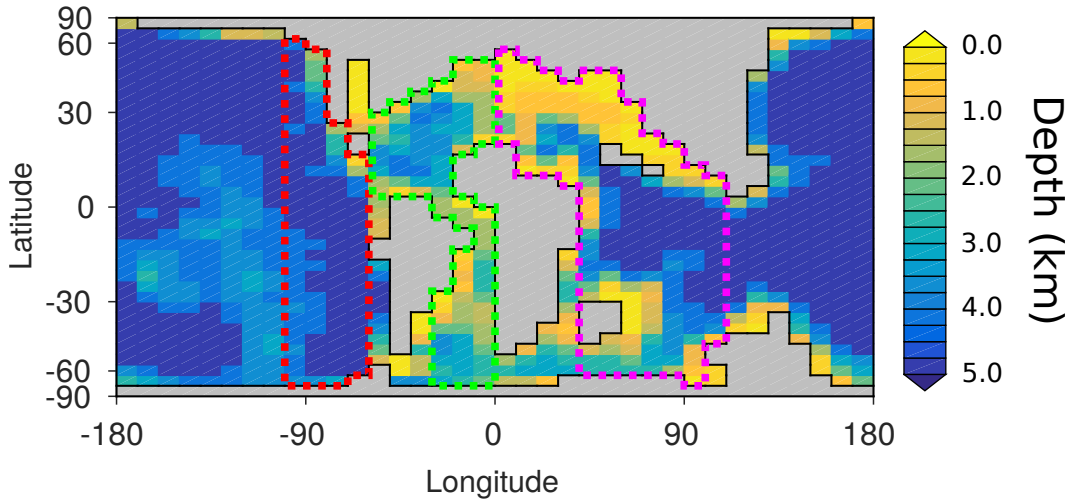

Figure 5.4: cGENIE ocean bathymetry for the Late Cretaceous, rescaled from the higher resolution model FOAM [Donnadieu et al., 2006b]. Dotted ocean provinces indicate the masks used for the zonal analysis (red: East Pacific Ocean, green: Atlantic Ocean, purple: Tethys Sea and Indian Ocean).

waters due to OM degradation, two additional, explicit P solid phases (Fe-bound P and authigenic fluorapatite) are considered. In the oxic part of the sediment column, P can be scavenged by sorption to Fe-oxides. In the anoxic part of the sediments this Fe-bound P can be released back to the pore water due to the reduction of these Fe-oxides [Slomp et al., 1996]. If concentrations of dissolved PO_4 become high enough in the anoxic sediments P is precipitated as authigenic fluorapatite [Ruttenberg and Berner, 1993]. In accordance with the underlying P model of Slomp et al. [1996], sorption and desorption of P to/from Fe-oxides as well as authigenic fluorapatite formation are described as first-order reactions with rate constants k_s , k_m and k_a, respectively. The rate of the respective process is calculated as the product of the rate constant and the difference between the current concentration (of PO_4 and Fe-bound P) and an equilibrium or asymptotic concentration Slomp et al. [1996]. The asymptotic Fe-bound P concentration (FeP^{∞}) and the equilibrium concentration for P sorption and authigenic fluorapatite formation ($PO_4{}^s$, $PO_4{}^a$) are adapted from the HAMOCC model of Palastanga et al. [2011, Table 5.2]. To maintain the P inventory in the model, any P lost at the bottom of the sediment column (either as an advective PO4 flux or in the form of Fe-P or authigenic fluorapatite) is restored at the uppermost ocean grid-cell. A complete description of OMEN-SED and the coupling to cGENIE can be found in Chapter 3 and 4.

In accordance with cGENIE, the sedimentary organic matter pool is composed of two discrete compound classes characterized by different degradation rate constants k_1 and k_2 (Table 5.2). We here use the results of the sensitivity analysis from the following Chapter 6 to parameterise the OM degradation rate constants (for a discussion on choosing appropriate constants for OAE2

Table 5.2: Parameter values used in OMEN-SED for the OAE2 scenarios. The P related rate constants and asymptotic/equilibrium concentrations are taken from the HAMOCC model of Palastanga et al. [2011]. All other parameters are as described in Chapter 3 and 4.

Parameter/Variable	Unit	Value	Description
k_1	yr^{-1}	0.0065	Degradation rate constant (labile OM)
k_2^{ox}	yr^{-1}	0.005	Oxic degradation rate constant (refractory OM)
k_2^{anox}	yr^{-1}	10^{-5}	Anoxic degradation rate constant (refractory OM)
k_s	yr^{-1}	36.5	Rate constant PO_4 sorption (margins)
k_s	yr^{-1}	3.65	Rate constant PO_4 sorption (deep sea)
k_m	yr^{-1}	0.19	Rate constant Fe-bound P release
k_a	yr^{-1}	0.37	Rate constant authigenic P precipitation
${PO_4}^s$	$\mathrm{mol\,cm}^{-3}$	$2.00 \cdot 10^{-9}$	Equilibrium conc. P sorption (margins)
${PO_4}^s$	$\mathrm{mol\,cm}^{-3}$	$12.00 \cdot 10^{-9}$	Equilibrium conc. P sorption (deep sea)
FeP^{∞}	$\mathrm{mol\,cm}^{-3}$	$5.2 \cdot 10^{-15}$	Asymptotic conc. for Fe-bound P (margins)
FeP^{∞}	$\mathrm{mol\,cm}^{-3}$	$5.2 \cdot 10^{-9}$	Asymptotic conc. for Fe-bound P (deep sea)
${PO_4}^a$	$\mathrm{mol\,cm}^{-3}$	$3.70 \cdot 10^{-9}$	Equilibrium conc. for authigenic P precipitation

see Section 6.2.2). As the quantitative constraints on OM reactivity during OAE2 are very limited we choose to employ spatially uniform rate constants depending on the oxygenation state of the seafloor. For an oxic depositional environment, rate constants for the refractory and labile OM pool are set to the "best" spatially uniform values as determined in Chapter 4 ($k_2 = 0.005$, $k_1 = 0.0065\ \mathrm{yr}^{-1}$). If bottom waters become anoxic [i.e $O_2 < 5.0\,\mu$M, e.g. Palastanga et al., 2011] the degradation rate constant describing the refractory OM pool is decreased to $k_2 = 10^{-5}$ [compare Chapter 6 and Arndt et al., 2009] as these compounds tend to degrade more slowly under anoxic conditions [LaRowe and Van Cappellen, 2011]. The reactivity of the labile OM pool remains unaltered as it has been shown that its reaction rate does not depend on the nature of the terminal electron acceptor [LaRowe and Van Cappellen, 2011].

5.2.2 Experiment setup

Equilibrium simulations for four versions of cGENIE with different lower boundary representations for the ocean are performed (Table 5.3). 1) The most simple setup, the *Conservative* lower boundary, essentially ignores the sediment-water interface as the burial flux of organic matter is set equal to its deposition flux. To account for mass preservation the "buried" OM is returned as a corresponding flux of solutes (i.e. DIC, PO_4 and alkalinity) from terrestrial carbonate weathering to the surface ocean [Colbourn et al., 2013]. 2) The other extreme lower boundary representation, the *Reflective* sediment boundary, simply assumes that organic matter reaching the bottom of the ocean degrades completely and the remineralisation products are returned instantaneously to the deepest ocean grid cell. A more detailed description of these lower boundary representations is given in Section 2.3.3.2. In order to explore the impact of P burial in (and its regeneration from) the sediments, two cGENIE setups coupled to different versions of the diagenesis model

Table 5.3: Four different lower boundary (sediment) representations used in cGENIE.

Sediment representation	Description
Conservative	All OM reaching the seafloor is buried. Losses from burial are restored as weathering flux of solutes.
Reflective	All OM reaching the seafloor is remineralised. Products are returned to the deepest ocean grid cell
OMEN-SED no PO_4	OMEN-SED without P-cycle - using a reflective boundary for P. Organic P is returned as PO4 to the deepest ocean grid cell.
OMEN-SED with PO_4	Complete OMEN-SED including the P-cycle with Fe-P and authigenic P. Buried P is restored at the uppermost ocean grid-cell

OMEN-SED are used. 3) In the first version, the sedimentary P cycle in OMEN-SED is excluded and all organic phosphorus raining down on the seafloor is instantaneously returned as phosphate to the lowest ocean grid-cell (i.e. using a reflective boundary for P). 4) The second setup uses the full version of OMEN-SED including the redox dependent cycling of P in the sediments.

For all four cGENIE versions the oceanic redox state for before and during OAE2 is reconstructed and compared to observations of seafloor anoxia and photic zone euxinia (Table 5.1 and Fig. 5.3). Simulated anoxic conditions in cGENIE are defined by O_2 concentrations lower than 10 μmol kg^{-1} and photic zone euxinia by the occurrence of H_2S at ocean depth between 80 and 200 m. Following Monteiro et al. [2012], pre-OAE2 conditions are simulated with 2× pre-industrial atmospheric CO_2 (556 ppmv) and peak-OAE2 conditions with 4× pre-industrial concentrations (1112 ppmv). To compare the four sediment representations under different degrees of ocean productivity and anoxia, the oceanic phosphate inventory is varied for the pre-OAE2 and peak-OAE2 scenarios. For pre-OAE2, oceanic phosphate is varied between 0.5 and 1.5 × modern concentrations and for peak-OAE2 between 1.5 and 2.5 × modern (with a modern values of PO_4 = 2.159 μmol kg^{-1}). Thus overall 12 pre-OAE2 and 12 peak-OAE2 experiments are run.

5.3 Model Results

5.3.1 Sediment representation and organic matter export

To a large degree the oxygenation state of the ocean is affected by remineralisation of organic matter in the ocean-sediment column which in turn is controlled by primary productivity in the upper ocean. Therefore, we first analyse changes in the global OM export production for the different sediment representations used in cGENIE when keeping the global PO_4 inventory of the ocean constant (Table 5.4). The four sediment representations can be divided into two groups depending on how they deal with phosphorus regeneration at the bottom of the ocean. First, representations which apply a reflective boundary for P at the bottom of the ocean (i.e. the Reflective boundary and the coupled OMEN-SED model excluding the P-cycle) and second

Table 5.4: Indicators for ocean redox state and organic matter export for the pre- and peak-OAE2 scenarios.

Experiment	Seafloor anoxia Area %	Global anoxia Volume %	Global mean O_2 μmol kg^{-1}	Global mean H_2S μmol kg^{-1}	Global OM export GtC yr^{-1}
Pre-OAE2 scenarios (2.0 × pre-industrial CO_2)					
	0.5× modern PO_4**:**				
Conservative	0.0	0.0	197.8	0.0	4.61
Reflective	0.7	0.0	190.1	0.0	3.84
OMEN-SED no PO_4	0.7	0.0	190.1	0.0	3.84
OMEN-SED with PO_4	3.3	0.9	177.3	0.0	4.57
	1.0× modern PO_4**:**				
Conservative	9.7	8.5	116.8	2.2	9.41
Reflective	11.0	8.4	103.9	3.5	7.82
OMEN-SED no PO_4	11.0	8.3	104.2	3.0	7.82
OMEN-SED with PO_4	18.1	15.2	82.3	5.7	9.47
	1.5× modern PO_4**:**				
Conservative	17.5	26.3	52.4	13.0	14.23
Reflective	47.3	49.3	40.2	18.2	11.82
OMEN-SED no PO_4	41.4	41.3	44.9	13.9	11.82
OMEN-SED with PO_4	61.3	55.8	33.9	20.7	13.76
Peak-OAE2 scenarios (4.0 × pre-industrial CO_2)					
	1.5× modern PO_4**:**				
Conservative	25.7	35.3	38.1	15.9	14.81
Reflective	67.4	59.7	30.5	23.7	12.27
OMEN-SED no PO_4	52.4	50.7	35.8	16.8	12.27
OMEN-SED with PO_4	72.9	63.1	27.6	23.9	14.15
	2.0× modern PO_4**:**				
Conservative	87.9	84.4	13.6	45.9	19.84
Reflective	88.1	83.1	15.5	63.1	16.43
OMEN-SED no PO_4	86.2	79.9	17.3	42.8	16.43
OMEN-SED with PO_4	89.2	84.4	14.0	61.2	19.30
	2.5× modern PO_4**:**				
Conservative	90.5	90.8	10.3	87.3	24.87
Reflective	90.6	89.1	11.5	108.4	20.59
OMEN-SED no PO_4	89.7	87.8	12.2	79.0	20.59
OMEN-SED with PO_4	92.0	90.4	10.3	106.7	24.64

representations which restore the P lost to burial in the sediments at the top of the ocean (i.e. the Conservative boundary and the coupled OMEN-SED model including the P-cycle, see Table 5.3). If P is restored at the top of the ocean it becomes instantaneously available for marine productivity, thus enhancing global OM export production (e.g. in the 0.5× PO_4 experiments from ~3.8 to 4.6 GtC yr^{-1}). The increase of OM export or the Conservative boundary is generally higher as here all P is restored at the ocean surface, while the complete OMEN-SED model partially regenerates P at the seafloor. Both representations using a reflective boundary for P show the same amount of OM export for all PO_4 scenarios (Table 5.4).

5.3.2 Sediment representation and the spatial extent of ocean anoxia and euxinia

Next, changes in seafloor anoxia and photic zone euxinia for the pre-OAE2 scenarios are discussed. Figures 5.5a and b show that oceanic phosphate concentrations of 0.5× modern are generally insufficient to trigger significant amounts of seafloor anoxia and photic zone euxinia. Increasing the concentration of PO_4 in the ocean to 1.0× modern values enhances global OM export by a factor of ~2 (Table 5.4). This in turn causes the anoxic seafloor area to expand for all four sediment representations over the entire proto-North Atlantic Ocean and and parts of the Tethys Sea (Fig. 5.5a). When using OMEN-SED with PO_4, seafloor anoxia spreads also into parts of the proto-South Atlantic and the southern East Pacific Ocean. All simulated patterns are in good agreement with the observations. The differing patterns of ocean anoxia caused by the sediment representations become more evident when an oceanic phosphate concentration of 1.5× modern is used. The Conservative boundary, even though showing the highest OM export, is characterised by the smallest expansion of seafloor anoxia (17.5%) as no organic matter is degraded at the ocean floor. Using a lower ocean boundary where OM is degraded at or in the sediments causes the geographical area of seafloor anoxia to increase to at least 41.4% (Fig. 5.5a). Results for OMEN-SED without PO_4 show a smaller expansion as the Reflective boundary because some OM reaching the ocean floor is preserved in the sediments. In general, the complete OMEN-SED model causes the largest expansion of seafloor anoxia, here mainly due to the increased marine productivity as buried P is restored at the ocean surface.

Photic zone euxinia starts to develop for oceanic PO_4 concentrations of 1.0× modern but regional changes are not as distinct in the pre-OAE2 scenarios (Fig. 5.5b) as the impact of the sediment representation is damped throughout the water column. Nevertheless, just the model using OMEN-SED with PO_4 is able to simulate euxinia at the Tarafaya and Cape Verde Basin (locations D and G) for the 1.0× PO_4 simulation and difference plots of photic zone euxinia reveal that H_2S concentrations are slightly higher for this model setup (Fig. 5.6A). Seafloor H_2S is, for obvious reasons, more sensitive to the sediment representation (Fig. 5.6B) and the geographical area is restricted to the extent of seafloor anoxia. Concentrations are lowest for the Conservative representation as the sediment boundary is completely ignored. Highest

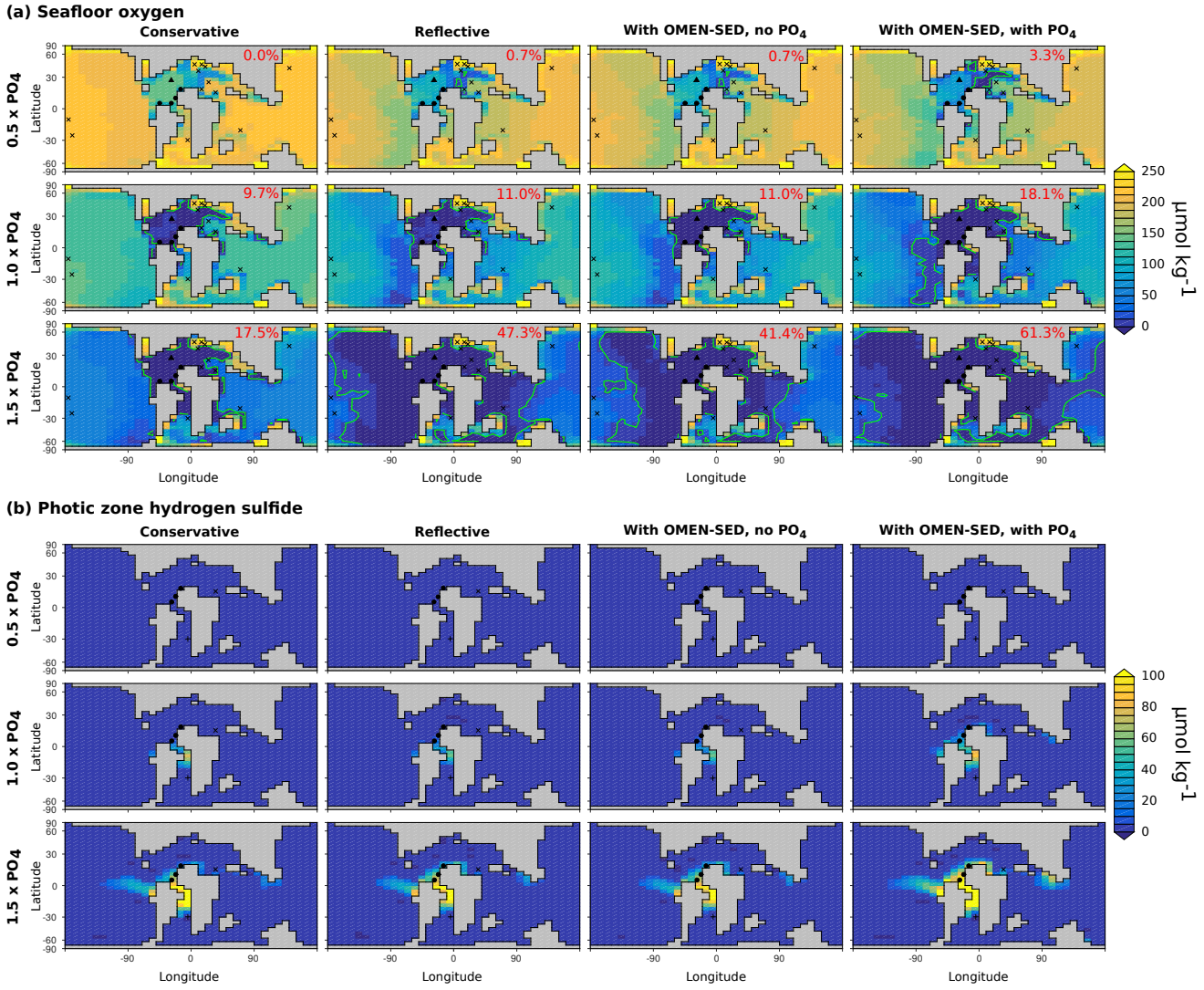

Figure 5.5: Pre-OAE2 model sensitivity of oceanic redox conditions with changing oceanic PO_4 concentration and sediment representation. (a) Sensitivity for seafloor anoxia showing simulated O_2 concentrations at the seafloor. Green contour indicates the model oxygen concentration of 10, μmmol kg^{-1}, indicating the region of seafloor anoxia. (b) Sensitivity for photic zone euxinia showing simulated H_2S concentration for the photic zone (80-200 m). Plotted on top of the model results are the observations of pre-OAE2 seafloor anoxia and photic zone euxinia (Table 5.1). Evidence for bottom water anoxia or photic zone euxinia is represented by black dots(•), evidence against by crosses (×) and questionable evidence is indicated by black triangles (▲). The fraction of anoxic seafloor area is indicated in red.

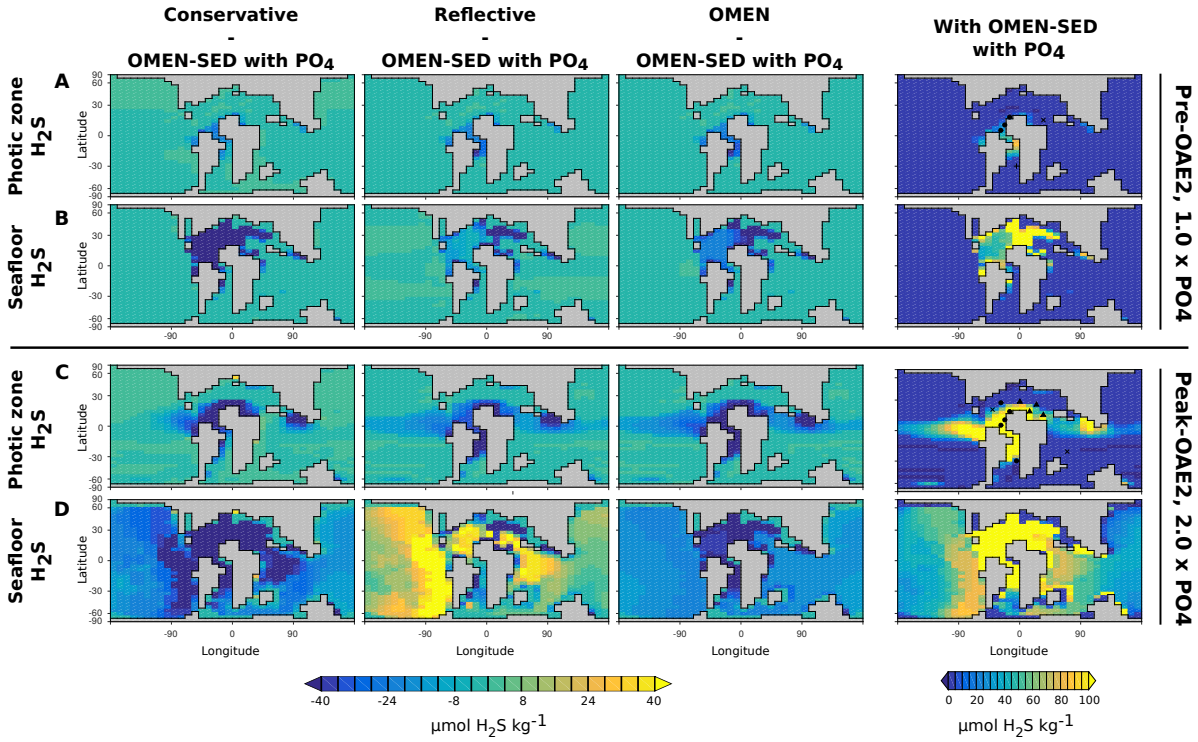

Figure 5.6: Anomaly plots for photic zone (A, C) and seafloor (B, D) euxinia for two example scenarios compared to the OMEN-SED with PO_4 model (right column).

concentrations are produced by the complete OMEN-SED model which are fuelled by H_2S production in the sediments due to enhanced OM degradation rates (see Section 5.3.3). The effect of the sediment representation for the development of euxinia in different ocean basins is analysed later in more detail.

For the minimum peak-OAE2 reconstruction (also using 1.5× modern PO_4) global OM export increases slightly due to higher temperatures caused by the doubling in atmospheric CO_2 (Table 5.4). The combination of enhanced temperatures and OM export causes the ocean to become more anoxic than in the comparable pre-OAE2 scenario. Depending on the employed sediment representation anoxia expands from 26.3 - 55.8% of the global ocean volume for the pre-OAE2 experiment to 35.3 - 63.1% for the peak-OAE2 experiment (Table 5.4). In all representations, except for the Conservative boundary, seafloor anoxia spreads over most of the proto-Atlantic and Indian Ocean as well as the Central and East Pacific Ocean and most of the Tethys Sea (Fig. 5.7). Increasing total oceanic PO_4 concentration to 2.5 × modern values enhances global OM export from a range of 12.27 - 14.81 to 20.59 - 24.87 GtC yr^{-1} (depending on the employed sediment representation). Consequently, anoxic conditions cover most of the global ocean with ~90% of the seafloor being anoxic and global mean O_2 concentrations dropping to values around 11 μmol kg^{-1} (Table 5.4).

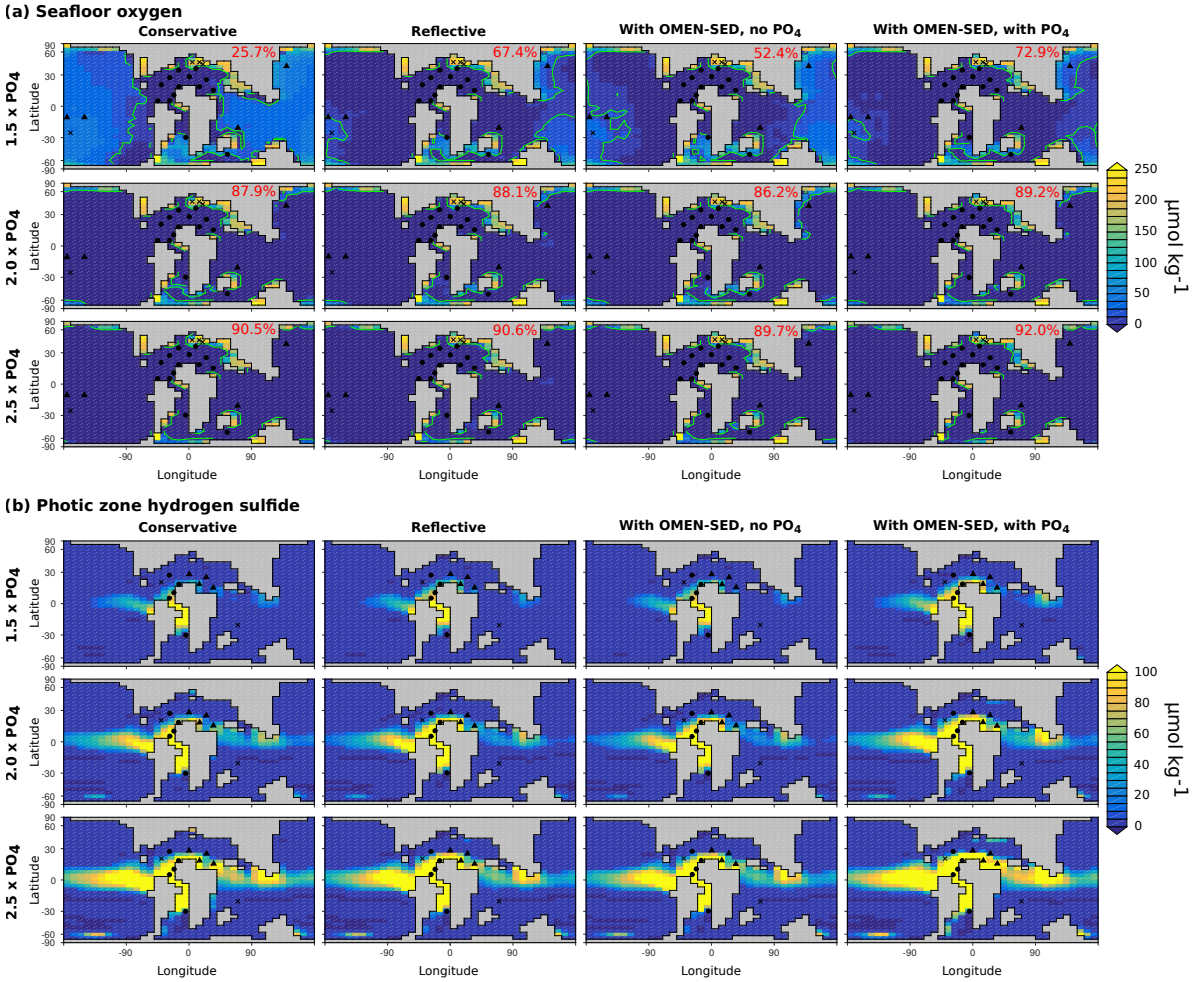

Figure 5.7: Peak-OAE2 model sensitivity of oceanic redox conditions with changing oceanic PO_4 concentration and sediment representation. Plotted on top of the model results are the observations of peak-OAE2 seafloor anoxia and photic zone euxinia (Table 5.1). Symbols for the evidence for bottom water anoxia and photic zone euxinia is as in Figure 5.5. The fraction of anoxic seafloor area is indicated in red.

Results also suggests that photic zone euxinia for an oceanic PO_4 concentration of 2.0 × modern spread over most of the equatorial regions and the entire, enclosed proto-Atlantic Ocean. The difference plots for photic zone euxinia reveal that H_2S concentrations for the sediment representation using OMEN-SED with PO_4 are again the highest (Fig. 5.6C). In contrast, seafloor euxinia is generally more pronounced in the model using the Reflective sediment boundary (Fig. 5.6D) and also global mean H_2S concentrations are higher (108.4 μmol kg^{-1}) compared with the complete OMEN-SED model (106.7 μmol kg^{-1}). Our results, thus suggest a threshold value for OM depositional flux to the sediments. Above the threshold, enhanced preservation of OM in the sediment model leads to a smaller diagenetic H_2S production in OMEN-SED compared to the complete degradation of OM at the Reflective boundary. However, at shallower ocean depths, especially in the Tethys Sea, the explicit sediment model still produces more seafloor euxinia. This is mainly due to very high H_2S sediment-water interface fluxes caused by high OM degradation rates at these depths (see Section 5.3.3). In particular, the increased availability and degradation of more labile OM at shallow ocean depths causes higher degradation rates and H_2S sediment-water interface fluxes (compare the sensitivity analysis in Chapter 3).

5.3.3 Organic matter degradation and sediment water interface fluxes in OMEN-SED

Next, sediment-water interface (SWI) fluxes and sediment characteristics simulated by the model setup using OMEN-SED including PO_4 dynamics are analysed. Therefore, results for one representative pre-OAE2 and one peak-OAE2 scenario are compared. As a result of the combined reconstruction of observations for seafloor anoxia and photic zone euxinia the 1.0 × PO_4 scenario is chosen as an analogue for pre-OAE2 conditions and the 2.0 × PO_4 scenario for peak-OAE2 conditions.

The main features of simulated SWI-fluxes can be explained by considering the patterns of OM degradation rates and OM burial in the sediments (Fig. 5.8A + B). Average OM degradation rates for peak-OAE2 are almost 200 μmol cm^{-2} yr^{-1} higher as for pre-OAE2. However, higher OM degradation rates for pre-OAE2 than peak-OAE2 are observed for some parts of the equatorial Pacific Ocean and at high latitudes. Here, a significant fraction of deposited OM is buried in the peak-OAE2 analogue. Highest degradation rates, for both scenarios, are simulated for the oxygenated margins with rates often exceeding 600 μmol cm^{-2} yr^{-1} (not shown). Due to oxic seafloor conditions in these areas, degradation rate constants in OMEN-SED are higher, thus all deposited OM is remineralised at the ocean margins (Fig. 5.8B).

For anoxic seafloor areas, OMEN-SED calculates zero O_2 uptake by the sediments (Figure 5.8C). All organic matter in these anoxic sediments is degraded by sulfate reduction which is also indicated by higher H_2S SWI-fluxes. Highest sediment O_2 uptake for both scenarios are simulated for the oxygenated margins of the oceans caused by very high OM degradation rates. However, not all OM is degraded aerobically at the ocean margins as can be inferred from very

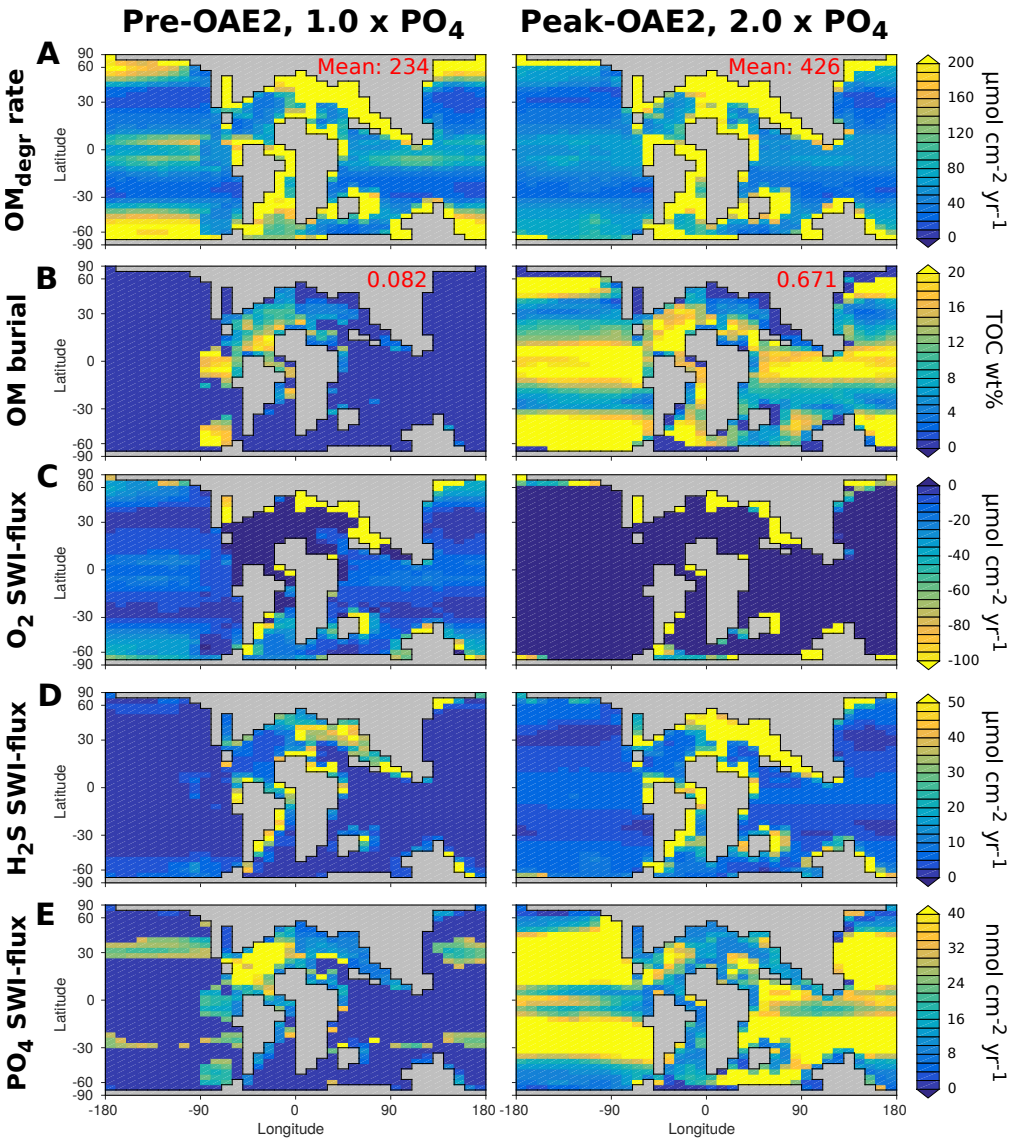

Figure 5.8: Simulated sediment characteristics and sediment-water interface fluxes for the representative pre-OAE2 (left) and peak-OAE2 scenario (right). Simulated total OM degradation (OM_{degr}) rate (A) represents the degradation rate for the entire sediment column (i.e. upper 1 m, the global mean rate is indicated in red on top of the plots). Simulated OM burial (B) represents the concentration of OM at a depth of 1 m in the sediment column (the rate of global OM burial in GtC yr^{-1} is indicated in red on top of the plots). Positive SWI-fluxes are directed from the sediments into the ocean.

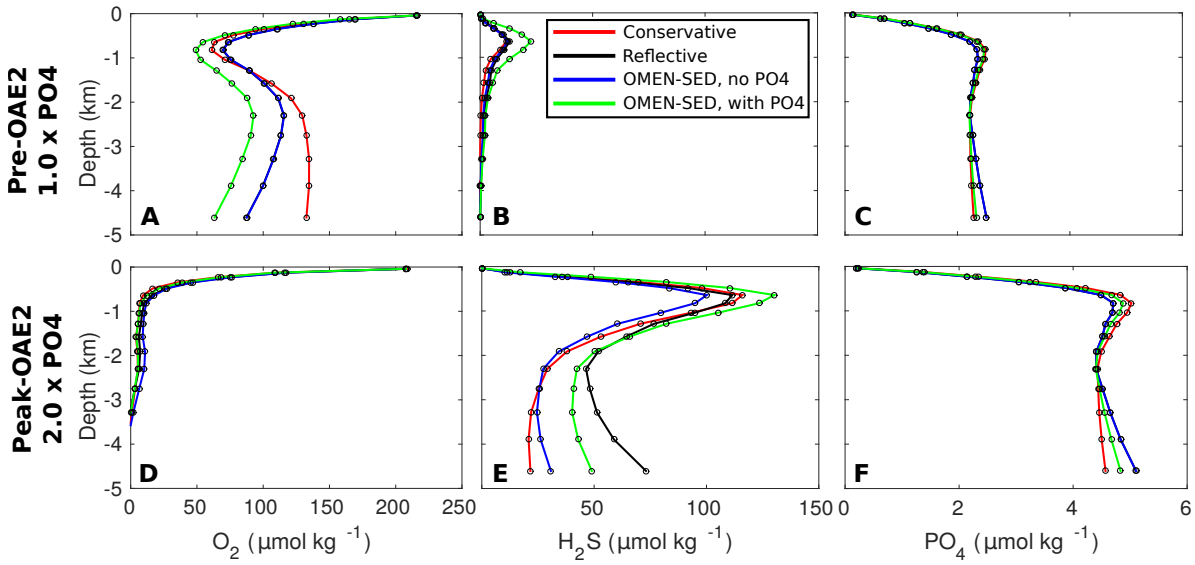

Figure 5.9: Globally averaged water column profiles of O_2, H_2S and PO_4 for 4 different sediment representations for the representative pre-OAE2 (top) and peak-OAE2 scenario (bottom).

high H_2S return fluxes from the sediments at these locations. Phosphate regeneration from the sediments is clearly enhanced in the more anoxic peak-OAE2 scenario (Fig. 5.8E). In the oxic part of the sediments Fe-P is formed therefore limiting the resulting SWI-flux of PO_4 (not shown). Under anoxic sediment conditions, in addition to PO_4 production through OM degradation, P is released from the Fe-P pool, thus causing enhanced P regeneration from the sediments. However, for very high OM degradations rates (e.g. in the Tethys Sea and parts of the proto-Atlantic Ocean) the regeneration of P is limited by the formation of authigenic fluorapatite.

5.3.4 Sediment representation and water column profiles on a global and basin wide scale

We have shown so far, that different sediment representations have an effect on the geographical extent of ocean anoxia and euxinia, especially at the seafloor. In the following, it is shown that also biogeochemical tracers throughout the entire water column are affected. Therefore, vertical water column profiles of O_2, H_2S and PO_4 for the four sediment representations are analysed. Results for the same representative pre-OAE2 and peak-OAE2 scenarios as in the previous Section are compared. First general differences are explained using globally averaged profiles. Thereafter, regional differences are analysed by focussing on zonally averaged profiles for the ocean provinces defined in Figure 5.4.

As all model configurations restore atmospheric oxygen to 0.2095 atm, O_2 concentrations at the surface ocean are equal for all sediment representations (Fig. 5.9A + D). In the upper 1 km of the water column the degradation of sinking organic matter reduces the oxygen concentration

rapidly for all four model configurations. For the pre-OAE2 scenario, the reduction is more pronounced for models which restore some or all of the P lost to burial in the sediments at the surface of the ocean (i.e the Conservative and the OMEN-SED with PO_4 representation). In the configuration using OMEN-SED with PO_4, the decline is further intensified through high O_2 uptake rates in sediments at the ocean margins (see Section 5.3.3). At deeper depths (> 2 km) the shape of the average profiles are increasingly affected by OM degradation at the seafloor. As a result, a second decline in oxygen concentrations is simulated for all configurations but the Conservative sediment representation. Consequently, the Conservative sediment representation exhibits the highest O_2 concentrations in the deep ocean.

The differences in H_2S profiles are best explained on the basis of the peak-OAE2 scenario (Fig. 5.9E). At shallower ocean depths (< 1 km) H_2S concentrations are highest for the OMEN-SED with PO_4 configuration. This is caused by two factors. First, higher marine productivity triggers enhanced H_2S production from sulfate reduction. Second, sediments at the shallower ocean margins are a source for H_2S due to very high OM degradation rates (compare Section 5.3.3). At deeper depths (> 2.5 km) H_2S concentrations are highest for the Reflective sediment representation as all OM is degraded at the seafloor in this configuration. Phosphate concentrations are not as sensitive on a global scale which can be explained by the fixed global PO_4 inventory of the ocean. However, results show that PO_4 concentrations in the model using OMEN-SED with PO_4 fall in between concentrations simulated by the more simple configurations (Fig. 5.9C + F). In the more simple configurations, organic P is completely restored at either the seafloor or the ocean surface, thus leading to higher/lower seafloor PO_4 concentrations, respectively.

Differences in zonally average water column profiles are more or less pronounced depending on the ocean province (Fig. 5.10 and 5.11). Results for the pre-OAE2 scenarios illustrate that zonally averaged O_2 profiles for the largely anoxic proto-Atlantic Ocean are rather similar and all sediment representations predict a decrease of O_2 with water depth to zero between 3 and 4 km (Fig. 5.10 a, left). In contrast, average O_2 concentrations for the other two ocean provinces are positive for the entire water-column. The offset between O_2 concentrations at deeper ocean depths (> 2 km) illustrates the different rates of O_2 consumption at the seafloor caused by the employed sediment representation. The proto-Atlantic Ocean is the only province with positive average H_2S concentrations throughout the water column (Fig. 5.10 a, middle). These are a result of sulfate reduction in the proto-North Atlantic basin (Fig. 5.11 a) which is predicted to be entirely anoxic (not shown). Only the Conservative boundary does not simulate anoxic and euxinic conditions for the proto-North Atlantic seafloor. Enhanced H_2S concentrations in the upper 1.5 km of the Tethys Sea are a result of OM degradation at the ocean margins and are intensified when the explicit P-cycle in OMEN-SED is used (Fig. 5.11 a).

Peak-OAE2 scenarios simulate zero average O_2 concentrations for ocean depths below 1 km in the Tethys Sea and Indian Ocean as well as in the East Pacific Ocean (Fig. 5.10 b). Oxygen penetrates deeper into the proto-Atlantic Ocean due to deep-water formation in the southern

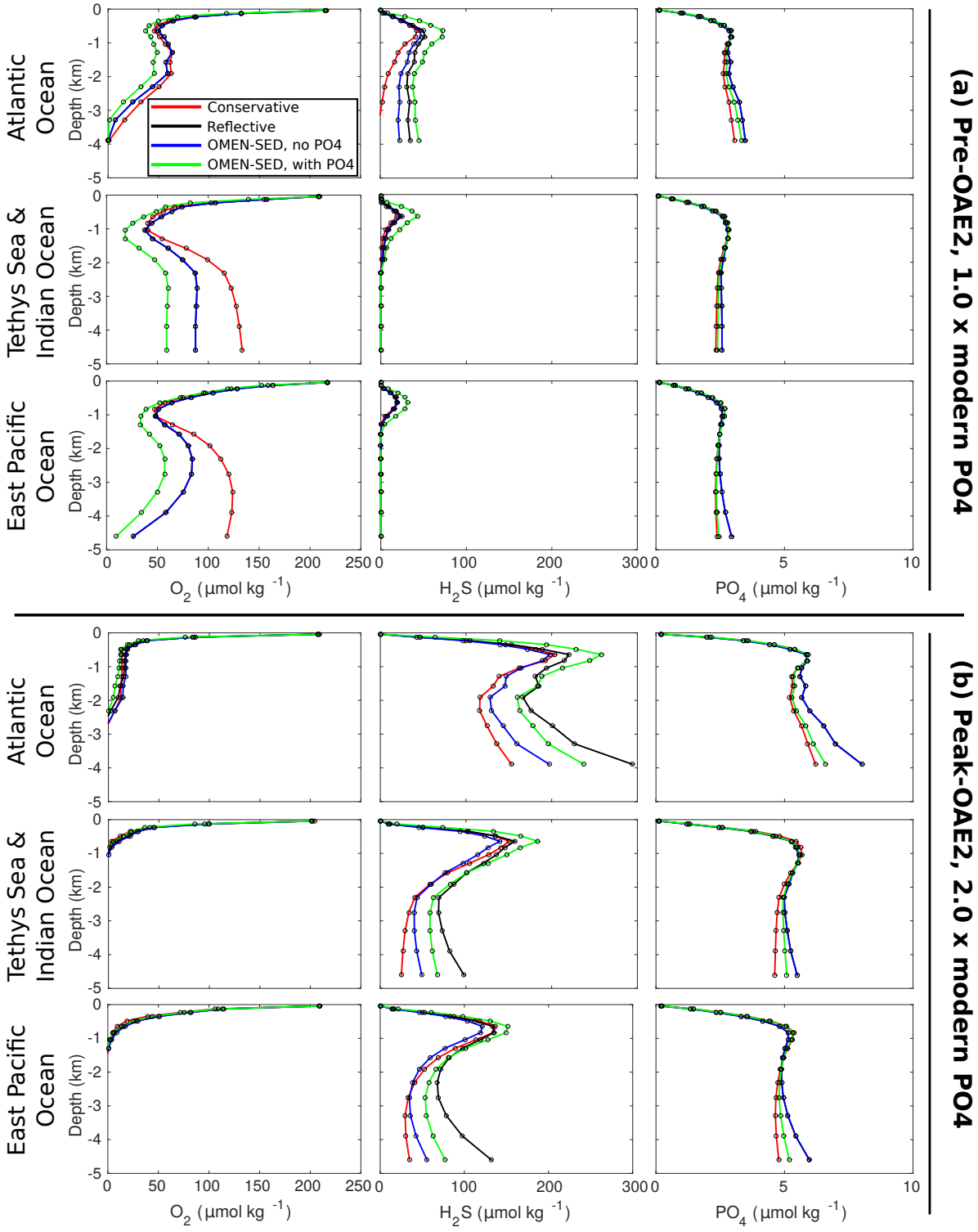

Figure 5.10: Zonally averaged profiles of water column properties for 4 different sediment representations for the representative pre-OAE2 (a) and peak-OAE2 scenario (b). Compared are O_2, H_2S and PO_4 profiles for the three ocean provinces as indicated in Figure 5.4.

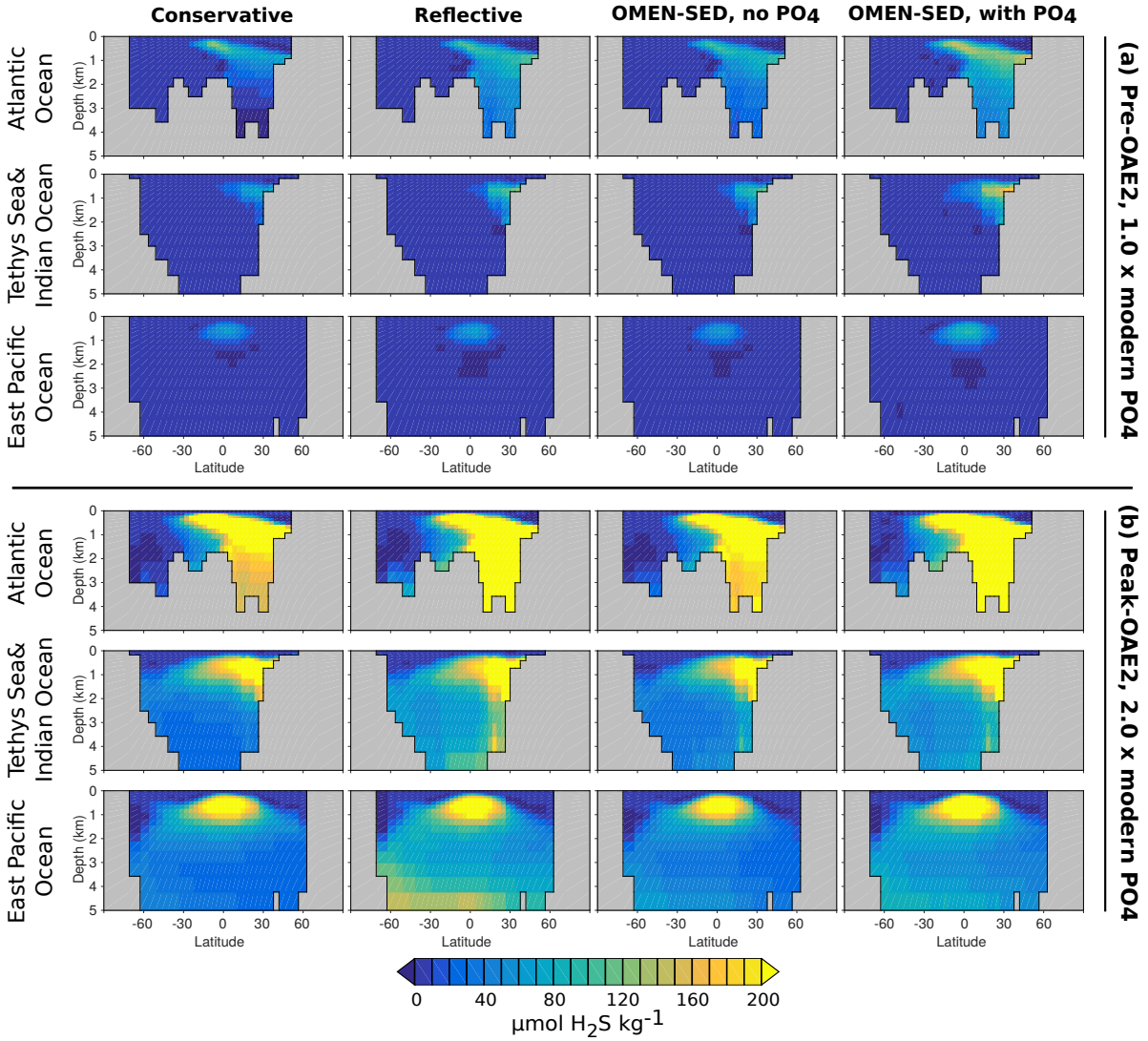

Figure 5.11: Zonal mean vertical H_2S profiles for the three ocean provinces as indicated in Figure 5.4 for the representative pre-OAE2 (a) and peak-OAE2 scenario (b).

parts of this province. Differences in the zonally averaged H_2S and PO_4 concentrations between sediment representations are specifically pronounced where OM export from the surface is high and at depths where OM degradation at the seafloor has a larger impact on the average concentration. Thus, largest differences are simulated in general for deeper ocean depths than about 3 km and in particular for the very productive and extremely euxinic conditions of the proto-Atlantic Ocean (Fig. 5.10 b, middle and right).

5.4 Discussion and Conclusions

This study focuses on the importance of benthic-pelagic coupling in Earth system models for simulating the oceanic redox state during the Cenomanian-Turonian boundary event (OAE2). Four structurally different representations of benthic-pelagic coupling are assessed for a range of oceanic PO_4 concentrations in order to reconstruct conditions before and during OAE2. The Earth system model cGENIE is configured with two very simple lower ocean boundaries (the Conservative and Reflective boundary) as well as two versions of the explicit sediment representation OMEN-SED (see Table 5.3). Model simulations of the oceanic redox state are constrained with observations for seafloor anoxia and photic zone euxinia.

Model results show that the employed sediment representation plays a crucial role for the onset and development of ocean anoxia and euxinia. The oxygenation of the ocean is particularly sensitive in the pre-OAE2 scenarios and the peak-OAE2 simulation with lower oceanic PO_4 concentrations (Fig. 5.5 and 5.7a). In the more productive peak-OAE2 scenarios the sediment representation strongly influences the expansion of euxinia in the ocean, while it is of minor importance for its oxygenation as global anoxia is already established by degradation of organic matter in the water column. The Conservative and Reflective sediment representation are the two end-member scenarios. The Reflective boundary overestimates the consumption of O_2 and the production of H_2S at the seafloor while the Conservative boundary underestimates respective rates. Thus the results show that the widely used Reflective lower boundary approach severely overestimates the expansion of seafloor euxinia.

Model simulations indicate that anoxia/euxinia develops and spreads due to OM degradation in oxygen minimum zones in the upper ocean and at the seafloor (e.g. Fig. 5.9 and 5.11). For lower PO_4 concentrations this is first evident in more productive and enclosed ocean basins like the proto-North Atlantic Ocean (Fig. 5.5 b), thus confirming observations [Monteiro et al., 2012] and more theoretical considerations regarding the causes of euxinia [Meyer and Kump, 2008]. When oceanic PO_4 concentrations are high enough both zones combine to establish anoxic/euxinic conditions in the entire water column (Fig. 5.11). Sediment-water interface fluxes calculated by the complete OMEN-SED model show that euxinia at the seafloor is specifically intensified in benthic areas with high OM degradation rates and thus high diffusive return fluxes of H_2S from the sediments (Fig. 5.8).

Upper ocean anoxia/euxinia is mainly driven by the biological pump, thus as a result of marine productivity and OM degradation in the water column. Results show that the employed sediment representation has important effects on marine productivity and OM export (Table 5.4). The four sediment representations can be divided into two groups depending on their parameterisation of P recycling from the sediments: First representations restoring P at the bottom of the ocean and second representations restoring it at the ocean surface. Depending on the location of nutrient recycling, this P is either instantly available for marine productivity thus causing enhanced OM export and ocean anoxia, or the recycled P depends on ocean circulation to be delivered back to the surface ocean. In the latter case a smaller fraction of recycled P is available for productivity in the surface ocean. Therefore, modellers should carefully considered where buried P is restored.

In addition, simulated sediment-water interface fluxes with OMEN-SED show enhanced P regeneration from anoxic sediments during peak-OAE2 (Fig. 5.8). The redox dependent regeneration of P from sediments is well documented but generally poorly quantified especially in ancient sediments [Ingall et al., 1993; Kraal et al., 2010; Slomp et al., 2004]. Therefore, future work with 3-dimensional Earth system models should concentrate on understanding the importance of the positive feedback between productivity, anoxia and P recycling from sediments for the genesis of OAE2. To test this idea transient simulations are required where the oceanic nutrient content can vary over time [e.g. Handoh and Lenton, 2003].

CHAPTER 6

ORGANIC MATTER BURIAL AND THE IMPACT OF SULFURIZATION DURING OAE2

Contributions and acknowledgements
This chapter is adapted from a research article in preparation for publication. S. Arndt and A. Ridgwell provided assistance with editing and advised on aspects of this work. All work presented in this chapter is my own.

6.1 Introduction

Even though the feedbacks triggering OAE2 are still under intense debate, the mechanisms responsible for its termination are even more enigmatic. The recovery from OAE2 requires mechanisms for the permanent removal of excess CO_2 from the atmosphere as well as for the reoxygenation of the ocean. On longer timescales the sediments may play a crucial role and the observed, globally increased organic matter (OM) burial is considered a dominant mechanism for the termination of OAE2 [Arthur et al., 1988; Kuypers et al., 1999, 2002; Wallmann, 2001]. Enhanced burial of OM removes CO_2 from the ocean/atmosphere system and thus induces global cooling. At the same time accumulating oxygen in the atmosphere and surface waters caused by increased OM burial (i.e. net photosynthetic oxygen production) has been shown to act as a negative feedback, eventually leading to the reoxygenation of the deeper ocean and a shut-down of the positive feedback of anoxia, P recycling and productivity [compare Fig. 6.1, Handoh and Lenton, 2003; Tsandev and Slomp, 2009].

Sediment cores from the proto-North Atlantic Ocean (locations A, D, E, F, G, Table 6.1) record relatively high total organic carbon (TOC) contents (or “black shales”) already before the onset

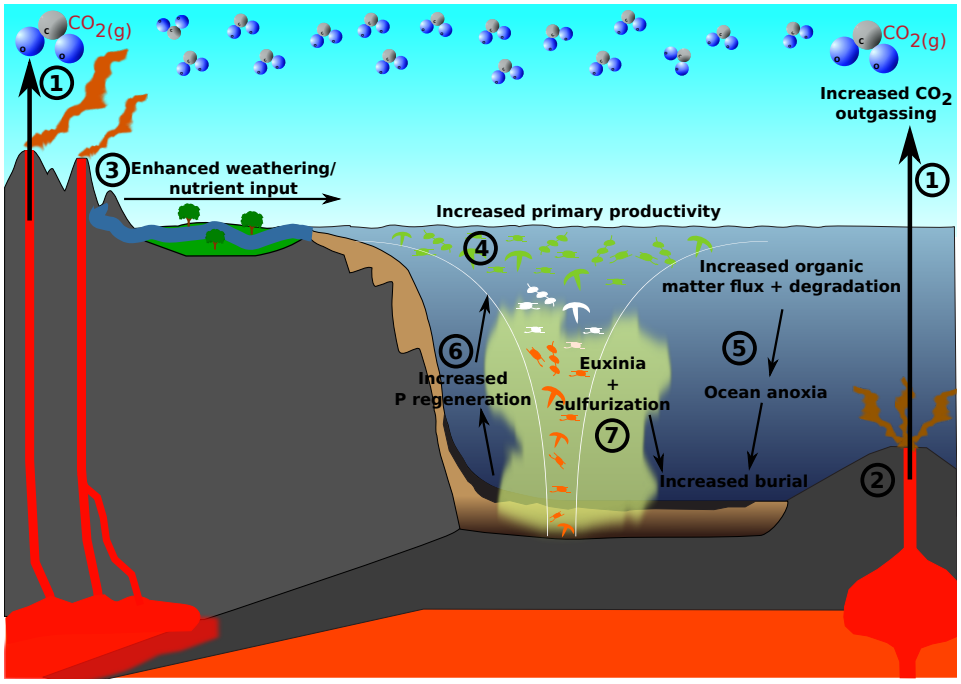

Figure 6.1: Schematic of potential feedbacks during OAE2, with increased volcanic CO_2 outgassing (1, 2) enhancing the nutrient input (2, 3) and primary productivity in the ocean (4). This leads to the development of ocean anoxia (5) and results in enhanced P regeneration from marine sediments (6), which in turn fuels PP (4). This further increases anoxia and develops into euxinia (7), increasing OM burial, therefore drawing down atmospheric CO_2 and re-oxygenating the ocean.

of OAE2, with values locally around 10 wt% [e.g. Kuypers et al., 2002; Sinninghe Damsté and Köster, 1998]. However, low TOC contents (generally < 1 wt%) and other evidence for an oxic seafloor environment have been found for the Tethys Sea (J, K, L, M, R), the proto-South Atlantic (H) as well as the Indian (S) and Pacific Oceans (U, V, X, compare Table 6.1 and Fig. 6.2). During OAE2, increased TOC contents and laminated black shales are recorded across much of the globe. Cores with specifically high TOC contents are found in the proto-North Atlantic Ocean (A, B, F, G), the proto-South Atlantic (H) and the Tethys Sea (N, P). In the Pacific Ocean, high TOC contents are recorded from oceanic plateaus (W: Shatsky and Hess rise 9.3 wt%) as well as from deep sea sites, such as the Mariana Basin [V: 10 wt%, Schlanger et al., 1987]. Mainly sediment cores from shallow waters in the northern Tethys Sea exhibit lower TOC contents (< 1 wt%) and other evidence for an oxic deposition environment (J, K, L). The site in the central South Pacific Ocean (X) also exhibits low TOC contents which could be either due to an oxic seafloor or due to its location in the South Pacific Gyre, which is characterised by low productivity and OM deposition at the seafloor [Ando et al., 2009].

To provide a first-order estimate of the magnitude of global organic matter burial during

Table 6.1: Observations of total organic carbon wt% (TOC wt%) during OAE2. Adapted from Monteiro et al. [2012]. For locations reporting a range of TOC wt% the mean value is used for model-data comparisons, for locations with maximum or minimum TOC wt% this value is used and if evidence reports "low TOC" a value of 0.25 TOC wt% is used (as this is the minimum value reported in the database).

		TOC wt%		Black shales	
Label	Locations	Pre	Peak	Pre	Peak
A	Cape Hatteras (DSDP sites 105, 603B)	< 10	3.5 - 26	✓	✓
B	Newfoundland Basin (ODP Site 1276)	–	13.4	–	✓
C	Hatteras Abyss (ODP Site 1276)	–	6	–	✓
D	Tarfaya Basin (Morocco)	2 - 5	1 - 20	✓	✓
E	Maracaibo Basin (Venezuela)	10 - 14	7 - 11	✓	✓
F	Demerara Rise (DSDP site 144, ODP Leg 207)	1 - 13	5 - 32.5	✓	✓
G	Cape Verde (DSDP sites 367, 368)	9	6.5 - 50	✓	✓
H	Angola Basin (DSDP site 530A)	low TOC	0.6 - 19.8	No	✓
J	Eastbourne and Dover (UK)	< 0.25	< 0.25	No	No
K	Münsterland Basin (Germany)	< 1	< 3	No	No
L	Chrummflueschluch (Switzerland)	low TOC	low TOC	No	No
M	Vocontian Basin (France)	< 1	5	No	✓
N	Galicia Margin (ODP Site 641)	–	6.5 - 11	–	✓
P	Apennines (Italy)	–	12 - 26	No	✓
Q	Oued Bahloul (Tunisia)	–	1 - 6	No	✓
R	Levant Platform (Jordan)	< 1	1.5 - 3	No	✓
S	Tethyan Himalayas (Tibet)	–	< 2	No	✓
T	Kerguelen Plateau (ODP site 1138)	–	< 3	–	✓
U	Yezo Group (Japan)	–	< 1	No	No
V	Mariana Basin (DSDP site 585)	–	10	No	✓
W	Shatsky and Hess Rise (DSDP sites 305, 310)	–	9.3	–	✓
X	Central South Pacific (DSDP site 463)	< 1	< 1	No	No

For references and explanation of the evidence please see Monteiro et al. [2012].

OAE2 Arthur et al. [1988] applied a carbon isotope mass balance modelling approach. They calculated a global excess burial of OM above the pre-OAE2 background of $\sim 0.32 \times 10^{13}$ mols C yr^{-1}. Assuming that atmospheric CO_2 during OAE2 was roughly 4 - 12 times higher than pre-industrial values [Bice et al., 2006; Sinninghe Damsté et al., 2010], this elevated rate of OM burial would have been sufficient to consume all CO_2 in the atmosphere within $\sim 60,000 - 180,000$ years [Arthur et al., 1988]. This simple budget calculation, even though resting on major assumptions, thus suggests that the increased OM burial may have had a significant effect on the reduction of atmospheric CO_2. The calculated durations are also consistent with estimates of Kuypers et al. [1999] who inferred from stable carbon isotope data of marine phytoplankton that the decrease in atmospheric CO_2 below 500 ppmv occurred in $\sim 60,000$ years. This apparently rapid recovery appears to be faster than can be explained by enhanced silicate and carbonate weathering alone and, thus, emphasises the important role of organic OM burial in terminating anoxic events.

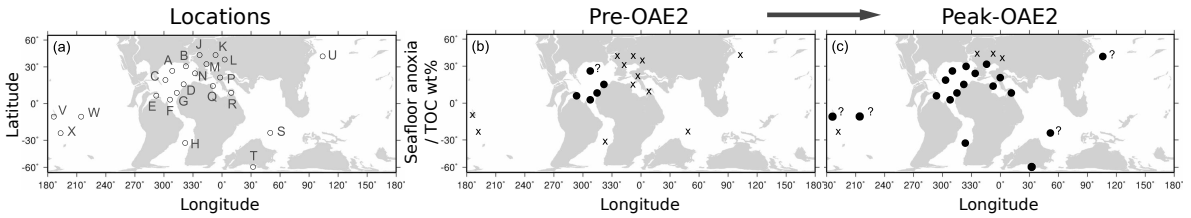

Figure 6.2: Global distribution of evidence for seafloor anoxia and TOC wt% as reported in Table 6.1. Locations of the observations (a) and evidence for seafloor anoxia before and during OAE2 (b, c). Figures and observations are adapted from Monteiro et al. [2012].

The process of OM burial, while widely recognised as important, is still poorly understood and the mechanisms leading to enhanced burial rates are intensely debated [e.g. Arndt et al., 2013; Canfield, 1994; Middelburg et al., 1993]. Traditionally, increased OM burial is related to increased productivity and/or increased preservation of OM due to reduced degradation rates in an anoxic/euxinic environment. However, the relative importance of both processes, especially under extreme conditions during Earth history, is difficult to assess. The estimation of paleoproductivity is complicated by the strong diagenetic overprint of proxies in the sediments [e.g. barite preservation may be reduced under anoxic conditions, Francois et al., 1995]. Even more important, our quantitative constraints on the reactivity of organic matter during OAE2 remains very limited. Apparent first-order degradation rate constants for Cretaceous black shales from Demerara Rise determined by inverse modelling reveal that OM reactivity was already low at the time of its deposition but values still span several orders of magnitude [$k \approx 10^{-4} - 10^{-6}$ yr^{-1}, Arndt et al., 2009]. In general, organic matter reactivity is controlled by a wide range of interlinked factors, such as temperature, physical protection, OM composition and the availability of terminal electron acceptors [Arndt et al., 2013; Canfield, 1994]. It is commonly accepted that elevated OM burial is related to anoxic conditions at the seafloor [Burdige, 2007; Canfield, 1989b; Demaison and Moore, 1980]. This relation is generally explained by lower free energy gains through anaerobic degradation of mid- to low-reactivity compounds [LaRowe and Van Cappellen, 2011], reduced bioturbation and grazing or the need for more complex bacterial consortia to degrade refractory organic matter compounds [which are thus degraded more slowly, Canfield, 1994; Hedges and Keil, 1995]. However, there is considerable debate about the influence of the redox state on diagenetic OM degradation rates [e.g. Arndt et al., 2013; Middelburg et al., 1993] and a number of studies report anoxic degradation rates similar to oxic rates in surface sediments [e.g. Henrichs and Reeburgh, 1987; Kristensen and Holmer, 2001; Lee, 1992]. The observed pattern may be explained by the degradation of different OM compounds characterised by different reactivities. Highly reactive, energetic (or labile) compounds degrade at a rate that does not depend on the nature of the terminal electron acceptor, while mid- to low energy (or refractory) compounds degrade faster under oxic conditions and degradation rates may even

become thermodynamically limited when only SO_4 is present [LaRowe and Van Cappellen, 2011].

Over the past decades an alternative OM preservation mechanism related to the extreme, euxinic conditions during OAE2 has been increasingly proposed to explain elevated organic matter preservation - sulfurization of organic matter [Arndt et al., 2009; Hebting et al., 2006; Raven et al., 2016; Sinninghe Damsté and Köster, 1998]. During sulfurization reactive organic matter compounds such as functionalized lipids and carbohydrates react with reduced inorganic sulfur species (e.g. H_2S) generating a sulfur cross-linked macromolecular network [Sinninghe Damsté et al., 1989a,b; van Dongen et al., 2003]. The resulting sulfur-rich organic matter compounds are more resistant to bacterial degradation and thus exhibit an enhanced preservation potential [Sinninghe Damsté and De Leeuw, 1990; Sinninghe Damsté et al., 1998]. Although sulfurization of OM is considered a globally significant process for preserving organic compounds on geologic time scales [see Sinninghe Damsté and De Leeuw, 1990; Werne et al., 2004, for reviews], the understanding whether it occurs already in the water column or solely in the sediments remains incomplete. Traditionally, it is argued that inorganic sulfur species react with organic matter during early diagenesis over time scales from a few decades to several thousand years [e.g. Urban et al., 1999; Wakeham et al., 1995]. However, a laboratory study by Adam et al. [1998] proposed that OM could become rapidly sulfurized by light induced reactions in the water column. Their experiments, using a variety of different organic compounds, were conducted under representative conditions for the photic zone (i.e. sunlight and low temperatures) and showed rapid sulfurization following the addition of reduced sulfur species (in particular H_2S). Support for rapid sulfurization is provided by Raven et al. [2016], who found that reduced sulfur can be incorporated into OM in the water column within days or less following phytoplankton blooms in the modern Cariaco Basin. As the majority of OM is degraded while it sinks through the water column, rapid sulfurization of sinking particles could affect a significantly larger OM pool than diagenetic sulfurization alone. Also van Dongen et al. [2006] hypothesized that enhanced euxinic conditions in the water column could be responsible for increased preservation of labile OM compounds, such as carbohydrates, in a Jurassic shelf sea. They argue that reduced degradation in the water column due to euxinic conditions would allow substantially more labile OM compounds to reach the sediments where they get sulfurized during early diagenesis.

The different time scales of sulfurization are not necessarily exclusive and it is likely that rapid sulfurization in the water column and slower diagenetic sulfurization are occurring simultaneously under appropriate environmental conditions [Wakeham et al., 1995; Werne et al., 2004]. In addition, specific sulfurization rates of individual organic compounds may vary substantially, with more labile compounds being more reactive towards reduced sulfur [Kok et al., 2000; Wakeham et al., 1995; Werne et al., 2000]. As a consequence, potential time scales for sulfurization are likely to range from days to thousands of years and rate constants might span several orders of magnitude. In one of the very few modelling studies incorporating OM sulfurization, Dale et al. [2009] used a second order rate constant of 0.2 $M^{-1}yr^{-1}$ (depending on the

concentration of H_2S and OM) to parametrise sulfurization in a diagenetic model of the modern Namibian shelf sediments. Considering the significantly shorter timescales in the water column and the availability of more labile OM which is more reactive towards sulfurization it thus can be inferred that rate constants in the water column are likely several orders of magnitude higher. To complicate the situation even further, very few quantitative assessments exist on the relative importance of water column versus diagenetic sulfurization and their significance for long term OM preservation. A notable exception is the work of Raven et al. [2016], who found that in Cariaco sediments even after 6000 years about half of the sulfur-rich organic matter compounds originated from rapid water column sulfurization. On a global basis, however, the extent to which OM sulfurization can enhance preservation is not quantified yet and its role for biogeochemical cycles and the termination of Cretaceous anoxic events has not been evaluated.

Here, we use the Earth system model cGENIE [Ridgwell et al., 2007] coupled to the new sediment model OMEN-SED as presented in Chapter 5 to investigate feedbacks between water column anoxia/euxinia and enhanced organic matter preservation in Cretaceous sediments. We quantify for the first time using a 3-dimensional Earth system model the amount of excess OM burial during OAE2 and investigate the potential role of OM sulfurization for the termination of OAE2. As in the previous chapter, the redox state of the ocean for before and during OAE2 is reconstructed by constraining model results with observations of seafloor anoxia and photic zone euxinia. In addition, appropriate degradation rate constants for the refractory OM pool (k_2) in OMEN-SED are determined by matching simulated OM contents in the sediments with observations of total organic carbon [TOC, Monteiro et al., 2012].

6.2 Methods

6.2.1 General model setup

All experiments in this chapter employ the late Cretaceous configuration (as in Chapter 5). The pre-OAE2 scenarios (*PRE_1PO4_E-4*, *PRE_1PO4_E-5* and *PRE_1PO4_E-6*) are used to calculate reasonable background organic matter burial rates during the Cretaceous (Table 6.2). Here, atmospheric CO_2 concentrations are restored to 2 times pre-industrial value (556 ppmv) and the ocean phosphate inventory is fixed to modern concentrations [PO_4 = 2.159 μM , compare Chapter 5 and Monteiro et al., 2012]. The peak-OAE2 experiments (Table 6.2) aim to reveal the effect of different preservation scenarios on the ocean redox structure and the excess burial rate of OM above the pre-OAE2 background. In all peak-OAE2 scenarios atmospheric CO_2 concentrations are restored to 4 times pre-industrial value (1112 ppmv). A sensitivity study is not performed for atmospheric CO_2 concentration, as Monteiro et al. [2012] showed that it has a minor effect on ocean productivity and anoxia in cGENIE. To find the best fit of model results to the compiled evidence of seafloor anoxia, photic zone euxinia and TOC content, the oceanic phosphate concentration is varied between 1.5 and 2.5 times modern values for the

Table 6.2: Experiment setup for this chapter, with 1.0 × modern PO_4 = 2.159 μM and 1.0 × pre-industrial atmospheric CO_2 = 278 ppmv.

Experiment	Atmospheric CO_2	Ocean [PO_4]	Anoxic k_2 (yr^{-1})	k_{sulf} ($M^{-1}\ yr^{-1}$)
Pre-OAE2 scenarios				
PRE_1PO4_E-4	2 × pre-industrial	1.0 × modern	10^{-4}	-
PRE_1PO4_E-5	2 × pre-industrial	1.0 × modern	10^{-5}	-
PRE_1PO4_E-6	2 × pre-industrial	1.0 × modern	10^{-6}	-
Peak-OAE2 scenarios without sulfurization				
PEAK_1.5PO4_E-4	4 × pre-industrial	1.5 × modern	10^{-4}	-
PEAK_1.5PO4_E-5	4 × pre-industrial	1.5 × modern	10^{-5}	-
PEAK_1.5PO4_E-6	4 × pre-industrial	1.5 × modern	10^{-6}	-
PEAK_2.0PO4_E-4	4 × pre-industrial	2.0 × modern	10^{-4}	-
PEAK_2.0PO4_E-5	4 × pre-industrial	2.0 × modern	10^{-5}	-
PEAK_2.0PO4_E-6	4 × pre-industrial	2.0 × modern	10^{-6}	-
PEAK_2.5PO4_E-4	4 × pre-industrial	2.5 × modern	10^{-4}	-
PEAK_2.5PO4_E-5	4 × pre-industrial	2.5 × modern	10^{-5}	-
PEAK_2.5PO4_E-6	4 × pre-industrial	2.5 × modern	10^{-6}	-
Peak-OAE2 scenarios with sulfurization				
PEAK_2.0PO4_SULF_E+1	4 × pre-industrial	2.0 × modern	10^{-5}	10^{1}
PEAK_2.0PO4_SULF_E+2	4 × pre-industrial	2.0 × modern	10^{-5}	10^{2}
PEAK_2.0PO4_SULF_E+3	4 × pre-industrial	2.0 × modern	10^{-5}	10^{3}
PEAK_2.0PO4_SULF_E+4	4 × pre-industrial	2.0 × modern	10^{-5}	10^{4}
PEAK_2.0PO4_SULF_E+5	4 × pre-industrial	2.0 × modern	10^{-5}	10^{5}
PEAK_2.0PO4_SULF_E+6	4 × pre-industrial	2.0 × modern	10^{-5}	10^{6}
PEAK_2.0PO4_SULF_E+7	4 × pre-industrial	2.0 × modern	10^{-5}	10^{7}

PEAK-experiments. In order to focus on the effects of carbon burial alone and to exclude the feedbacks related to phosphorus regeneration, OMEN-SED does not account for phosphorus dynamics in this chapter. Instead all organic phosphorus raining down on the seafloor gets instantaneously remineralized and returned to the deepest ocean grid-cell as phosphate (i.e. reflective P boundary).

6.2.2 The role of organic matter degradation in the sediments - finding an appropriate rate constant

Different degradation rate constants for the refractory OM pool (k_2) are explored to asses its impact on the ocean redox state and to find the best fit of simulated OM preservation to the compiled distribution of black shales (and respective TOC wt%, Table 6.1). Chapter 4 demonstrates that the best results for the modern ocean can be achieved by using depth

dependent, sedimentation rate-related OM degradation rate constants [the $k-w$ parameterisation after Boudreau, 1997]. However, this parameterisation [and the underlying empirical relationship of Boudreau, 1997] was derived from mainly oxic, modern ocean observations. Yet, the Cretaceous ocean is characterised by enhanced anoxia/euxinia, and black shales with very high organic matter concentrations are generally formed under relatively low sedimentation rates [e.g. Stein et al., 1986]. Thus, the empirically-found $k-w$ parameterisation might not be applicable under such unusual and extreme conditions. As in general, the quantitative constraints on OM degradation rate constants during OAE2 are very limited, we here employ spatially uniform rate constants in OMEN-SED and build upon degradation rate constants determined in Chapter 4. For an oxic depositional environment, rate constants for the refractory and labile OM pool are set to the "best" spatially uniform values as determined in Section 4.3 ($k_2 = 0.005$, $k_1 = 0.0065\ \mathrm{yr}^{-1}$). If bottom waters become anoxic [i.e $O_2 < 5.0\,\mu$M, e.g. Palastanga et al., 2011] the degradation rate constant describing the refractory (or mid- to low-reactivity) OM pool is decreased as these compounds tend to degrade more slowly under anoxic conditions [LaRowe and Van Cappellen, 2011]. Lower values, more representative for OM reactivity in Cretaceous black shales, are chosen here [i.e. $k_2 \in \{10^{-4}, 10^{-5}, 10^{-6}\}$, Arndt et al., 2009]. The reactivity of the labile (or highly reactive) OM pool remains unaltered as it has been shown that its reaction rate does not depend on the nature of the terminal electron acceptor [LaRowe and Van Cappellen, 2011]. As the faster degradation rate constant k_1 describing labile OM is mainly important for SWI-fluxes of solutes (see Section 3.3.1) whereas the slower degradation rate constant k_2 affects the preservation of OM, we expect simulated OM burial to be more sensitive than the redox state of the ocean towards variations in k_2.

6.2.3 The role of organic matter sulfurization

Finally, to asses the impact of organic matter sulfurization on ocean anoxia/euxinia and OM burial the peak-OAE2 scenarios including different sulfurization rate constants are run. Building upon our sensitivity analysis (Section 6.3.1) all sulfurization experiments use 2.0× PO_4 and an anoxic degradation rate constant for the refractory OM pool of $k_2 = 10^{-5}\,\mathrm{yr}^{-1}$. The general understanding is that mainly more labile OM compounds are sulfurized in the water-column or during early diagenesis as they are more reactive towards reduced sulfur [Sinninghe Damsté et al., 1989b; van Dongen et al., 2006; Werne et al., 2000]. Therefore, only the labile OM pool in cGENIE is subject to sulfurization. In the water column the reaction of labile OM (OM_l in M) with H_2S is described by the second order rate constant k_{sulf} (in $M^{-1}\ yr^{-1}$) and sulfurized organic matter (OM_{sulf}) is produced at a rate of:

$$\frac{d\mathrm{OM_{sulf}}}{dt} = \mathrm{k_{sulf}} \cdot [\mathrm{OM_l}] \cdot [\mathrm{H_2S}]. \tag{6.1}$$

The sulfurized OM pool is considered a separate, third fraction in OMEN-SED which is completely preserved and, thus, not subject to degradation. In our experiments the rate constant k_{sulf} is

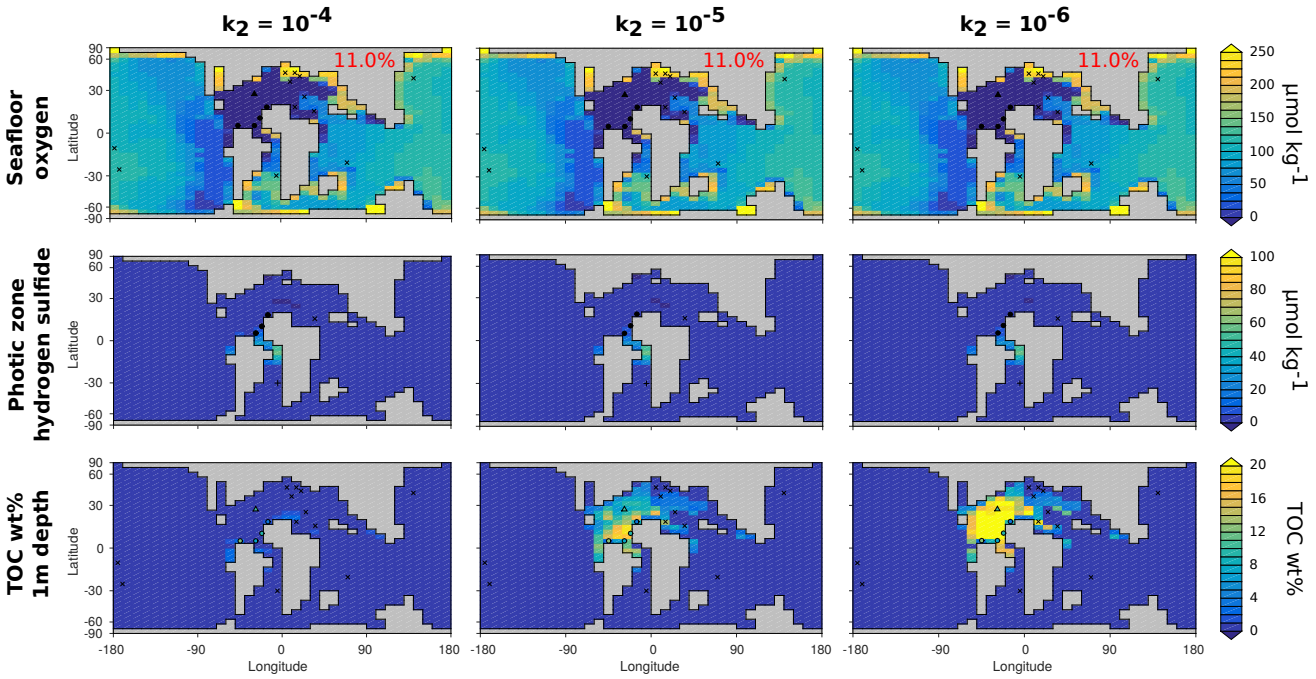

Figure 6.3: Pre-OAE2 model sensitivity of oceanic redox conditions and geological total organic carbon (TOC) preservation (TOC wt% at 1 m sediment depth) with changing anoxic organic matter degradation rate constant (k_2). Plotted on top of the model results are the observations of pre-OAE2 seafloor anoxia, photic zone euxinia (see Chapter 5) and TOC concentrations (Table 6.1). Evidence for bottom water anoxia or photic zone euxinia is represented by black dots(•), evidence against by crosses (×) and questionable evidence is indicated by black triangles (▲). The symbols for TOC wt% are the same as for seafloor anoxia, however, the colour indicates the measured TOC concentration at this location. The fraction of anoxic seafloor area is indicated in red.

varied from 10 to 10^7 M^{-1} yr^{-1} (Table 6.2). The minimum value is about one order of magnitude higher as the rate constant applied by Dale et al. [2009] for the Namibian shelf sediments and the maximum value of 10^7 M^{-1} yr^{-1} represents reaction kinetics similar to those of fast secondary redox reactions (e.g. H_2S reoxidation by O_2). Modelling sulfurization in OMEN-SED using a second order rate constant would complicate the analytical solution of the diagenetic equations. However, our approach of water-column sulfurization can also be considered to represent the decreased degradation of labile OM in the water column due to euxinic conditions and the subsequent sulfurization during early diagenesis as described by van Dongen et al. [2006].

Table 6.3: Indicators for ocean redox state and organic matter transport/preservation for the *PRE*- and *PEAK*-OAE2 experiments (not considering sulfurization)

Experiment	Seafloor anoxia Area %	Global anoxia Volume %	Global mean O_2 μmol kg^{-1}	Global mean H_2S μmol kg^{-1}	Global OM burial GtC yr^{-1}
Pre-OAE2					
1.0× modern PO_4: Export production: 7.821 GtC yr^{-1}, OM seafloor rain: 1.016 GtC yr^{-1}					
PRE_1PO4_E-4	11.0	8.4	104.0	3.5	0.007
PRE_1PO4_E-5	11.0	8.3	104.2	3.0	0.036
PRE_1PO4_E-6	11.0	8.2	104.2	2.7	0.049
Peak-OAE2					
1.5× modern PO_4: Export production: 12.272 GtC yr^{-1}, OM seafloor rain: 1.628 GtC yr^{-1}					
PEAK_1.5PO4_E-4	66.9	59.2	30.9	23.2	0.037
PEAK_1.5PO4_E-5	52.4	50.7	35.8	16.8	0.256
PEAK_1.5PO4_E-6	49.4	46.9	37.8	14.6	0.329
2.0× modern PO_4: Export production: 16.428 GtC yr^{-1}, OM seafloor rain: 2.181 GtC yr^{-1}					
PEAK_2.0PO4_E-4	88.0	82.8	15.7	61.1	0.087
PEAK_2.0PO4_E-5	86.2	79.9	17.3	42.8	0.530
PEAK_2.0PO4_E-6	83.8	77.8	18.9	34.8	0.718
2.5× modern PO_4: Export production: 20.589 GtC yr^{-1}, OM seafloor rain: 2.734 GtC yr^{-1}					
PEAK_2.5PO4_E-4	90.5	88.9	11.5	104.1	0.154
PEAK_2.5PO4_E-5	89.7	87.8	12.2	79.0	0.745
PEAK_2.5PO4_E-6	89.4	87.0	12.6	68.8	0.968

6.3 Results

6.3.1 The role of organic matter degradation in the sediments

Figure 6.3 illustrates the effect of different anoxic degradation rate constant on two ocean redox indicators and organic matter burial in the sediments for the pre-OAE2 scenario. Modelled seafloor anoxia and photic zone euxinia does not vary significantly with a decreasing degradation rate constant (Fig. 6.3, 1st & 2nd row) and also the change in global anoxia is negligible (Tab. 6.3). This is a consequence of the fixed degradation rate constant for the labile OM pool (k_1) which mainly controls the SWI-flux of O_2 and H_2S (compare the sensitivity analysis in Section 3.3.1). In contrast, the spatial distribution as well as the total amount of organic matter burial is very sensitive to the degradation rate constant. Decreasing the anoxic value of k_2 from 10^{-4} to 10^{-6} yr^{-1} increases the organic matter burial rate by a factor of 7 (from 0.007 to 0.049 GtC yr^{-1}, Tab. 6.3). High TOC wt% (around and above 10 wt%) are simulated for the proto-North Atlantic Ocean (location A, E, F, G) for the lower degradation rate constants, which is consistent with the observations (Tab. 6.1). Most of the Tethys Sea, especially shallow waters in the north, as well as the proto-South Atlantic, the Indian and Pacific Oceans are still characterised by lower or the

absence of organic matter burial which is in-line with the observations. The elevated OM burial in the proto-North Atlantic is a combination of seafloor anoxia and choosing an appropriate, anoxic degradation rate constant for the refractory OM pool.

For the peak-OAE2 scenarios, the effect of changes in the anoxic OM degradation rate constant is compared with changes in the oceanic nutrient content. Peak-OAE2 evidence is plotted on top of the model results (Fig. 6.4 and 6.5). For the peak-OAE2 conditions simulated productivity, OM export and OM rain to the seafloor is higher as in the pre-OAE2 scenarios (Table 6.3), thus changes in k_2 have a greater effect on the redox state of the ocean. Choosing a lower rate constant leads to significantly reduced OM degradation in the sediments and therefore less oxygen uptake from the water-column. As a consequence seafloor and global ocean anoxia is reduced (Fig. 6.4a and Table 6.3). This reoxygenation effect is most pronounced in the 1.5× PO_4 experiment and comparably smaller in the experiments with higher ocean nutrient content. In the very productive ocean (i.e. 2.0 and 2.5× PO_4), H_2S is building up significantly in the ocean (Table 6.3) and is oxidised by the net oxygen gain due to more OM burial, therefore diminishing its impact on reducing ocean anoxia. Even though, a smaller OM degradation rate constant reduces the mean oceanic H_2S concentration, this effect is not visible in simulated patterns of photic zone euxinia (Fig. 6.4b). These patterns are more sensitive to the oceanic phosphate inventory as they are mainly driven by OM degradation in the water column (see Chapter 5).

Global organic matter preservation increases when a lower degradation rate constant is used while keeping the oceanic phosphate inventory constant even though the anoxic seafloor area is decreased (Table 6.3 and Fig. 6.5). Due to the limited geographical expansion of seafloor anoxia in all 1.5× PO_4 experiments, the model is neither able to predict high TOC contents observed for the Angola Basin in the proto-South Atlantic Ocean (0.6 - 19.8 wt%, location H) nor for the equatorial Pacific Ocean (10 and 9.3 wt%, locations V and W). When keeping k_2 constant while increasing total oceanic PO_4 the elevated total OM preservation is caused by two factors. First, the higher nutrient inventory enhances global export production and therefore OM rain to the seafloor [Table 6.3 and Monteiro et al., 2012]. Second, as a result of this, anoxia geographically expands across the seafloor (Fig. 6.4a and Table 6.3), thus leading to more OM preservation in these areas due to the lower k_2-value applied in OMEN-SED. The model results suggest that a degradation rate constant of $k_2 = 10^{-4}$ is too high to create black-shales with high TOC contents observed in most of the proto-Atlantic Ocean and the Tethys Sea (Fig. 6.5). In contrast, for a value of $k_2 = 10^{-6}$ simulated organic matter contents generally exceed observed TOC contents. However, this is not surprising as simulated organic matter burial for the Cretaceous is compared with ~93.5 Ma old records of TOC content. Observations as well as modelling studies show that organic matter in these deeply buried (i.e. < 1 m), ancient black shales is still a source for ongoing microbial degradation [e.g. Arndt et al., 2006; Krumholz et al., 2002]. Therefore, OM concentrations are still decreased over time.

Figure 6.6 shows simulated TOC contents for the best peak-OAE2 scenarios (using $k_2 = 10^{-5}$

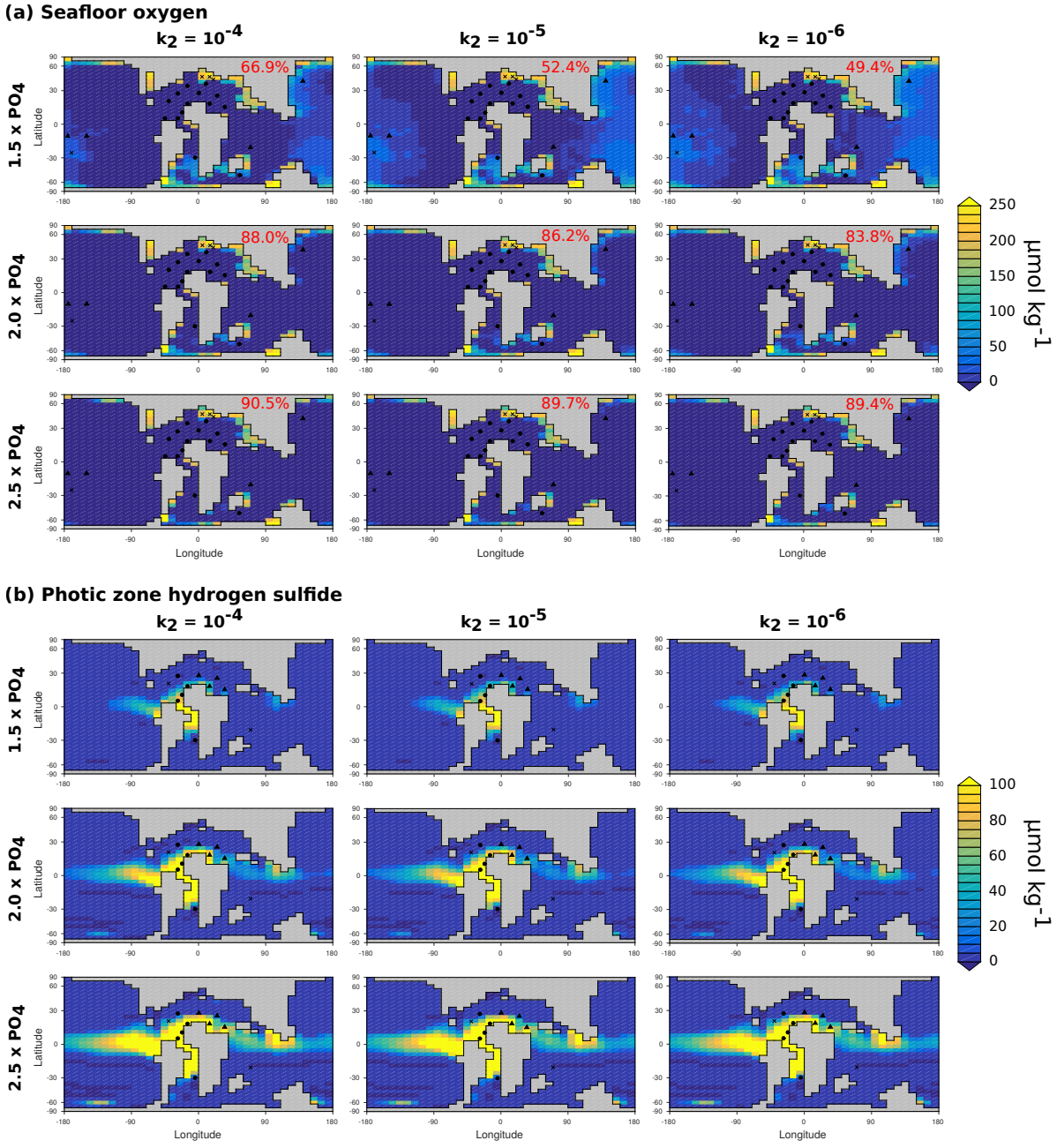

Figure 6.4: Peak-OAE2 model sensitivity of oceanic redox conditions with changing oceanic phosphate inventory and anoxic organic matter degradation rate constant (k_2). Plotted on top of the model results are the observations of peak-OAE2 seafloor anoxia and photic zone euxinia (see Chapter 5). The same symbols for the observations are used as in Fig. 6.3.

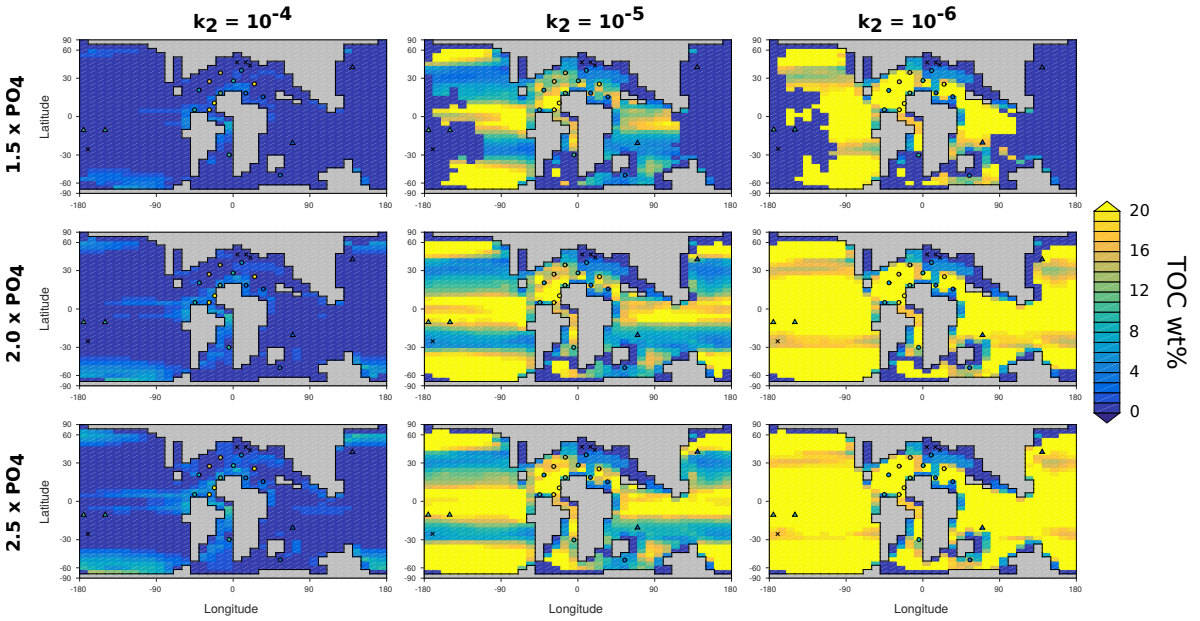

Figure 6.5: Peak-OAE2 model sensitivity of geological TOC preservation (TOC wt% at 1 m sediment depth) with changing oceanic phosphate inventory and anoxic organic matter degradation rate constant (k_2). Plotted on top of the model results are the observations of peak-OAE2 TOC content (see Table 6.1). Dots (∘) and triangles (△) indicate observations of black shales, with the colour representing the measured TOC concentration at this location. Crosses (×) indicate the absence of black shales and lower TOC concentrations.

and 10^{-6} with 2.0× PO_4, note the different colour scale compared to Fig. 6.5). The crossplots compare simulated TOC concentrations for the Cretaceous with observed present day TOC contents for the sediment cores of the database. Both experiments are able to reconstruct the spatial patterns of black shales with high TOC contents reasonably well. For the peak-OAE2 scenario using $k_2 = 10^{-5}$ also the concentrations simulated with OMEN-SED are in agreement with the observations (Fig. 6.6B). In this experiment black shales with TOC contents > 20 wt% are formed in parts of the proto-Atlantic Ocean and the Tethys Sea as well as in the high latitudes and most of the equatorial regions of the Pacific Ocean (Fig. 6.5). Simulated TOC concentrations for the proto-Atlantic Ocean generally match observations very well with the exception of location C, where model results are ~10 wt% too high, and location E, where the model underestimates concentrations by ~6 wt% (Fig. 6.6B). TOC content simulations for two locations in the southern Tethys Sea are too high (N and Q), yet, regardless of this misfit, both experiments still predict very low TOC concentrations for the shallow water sites in the northern Tethys Sea which is consistent with compiled observations (locations J, K, L). For the lower degradation constant ($k_2 = 10^{-6}$) simulated TOC concentrations are increasing for all locations of the database. However, the increase is not of the same magnitude for all locations. Specifically higher concentrations (> 10 wt%) are simulated for all sites in the Pacific Ocean (U, V, W, X), two

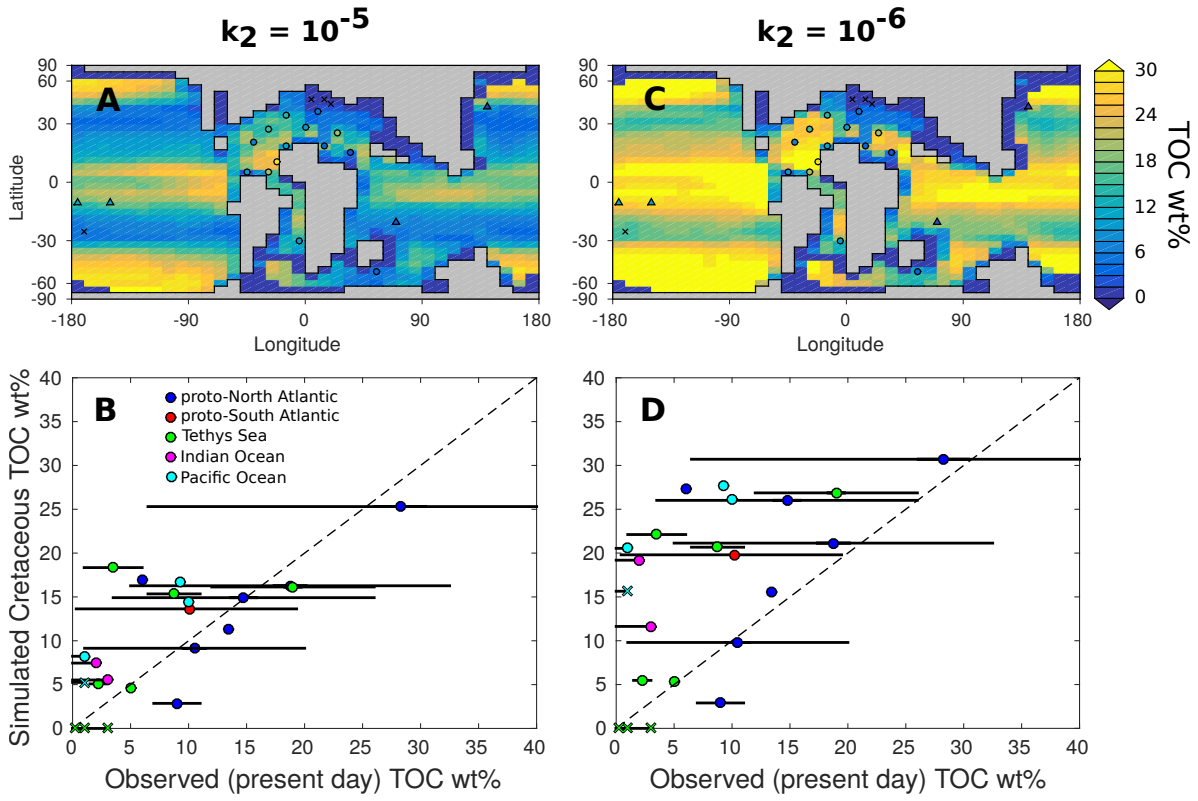

Figure 6.6: Model-data reconstruction of geological TOC preservation during peak-OAE2 using 2.0× PO_4 and a degradation rate constant of $k_2 = 10^{-5}$ (left) and $k_2 = 10^{-6}$ (right). **Top:** Maps of TOC wt% at 1 m sediment depth as in Fig. 6.5 (note the different colour scale). **Bottom:** Crossplots comparing simulated and observed TOC concentrations. The error bars indicate the ranges of TOC content reported for the specific location.

locations in the proto-North Atlantic Ocean (A, C) as well as locations in the Tethys Sea and Indian Ocean (P and S, respectively). It is worth noting, that observations from the Indian Ocean (locations S, T) as well as one observation in the Central Pacific Ocean (W) come from oceanic plateaus and might not be very representative given the low cGENIE resolution and bathymetry.

6.3.2 The role of organic matter sulfurization

Preliminary results indicate that sulfurization rate constants (k_{sulf}) of less than 10^5 M^{-1} yr^{-1} do not have a detectable impact on the redox state of the ocean (Table 6.4). Therefore, results of these experiments are not shown in figures of water column and sediment characteristics in this section. Figure 6.7 compares globally averaged water column profiles for the 3 sulfurization experiments using the highest sulfurization rate constants ($k_{sulf} \in \{10^5, 10^6, 10^7\}$) with the peak-OAE2 experiment without sulfurization. All OM flux profiles exhibit a similar shape although in the sulfurization experiments a higher flux (total and fraction of OM export flux, Fig. 6.7A+C)

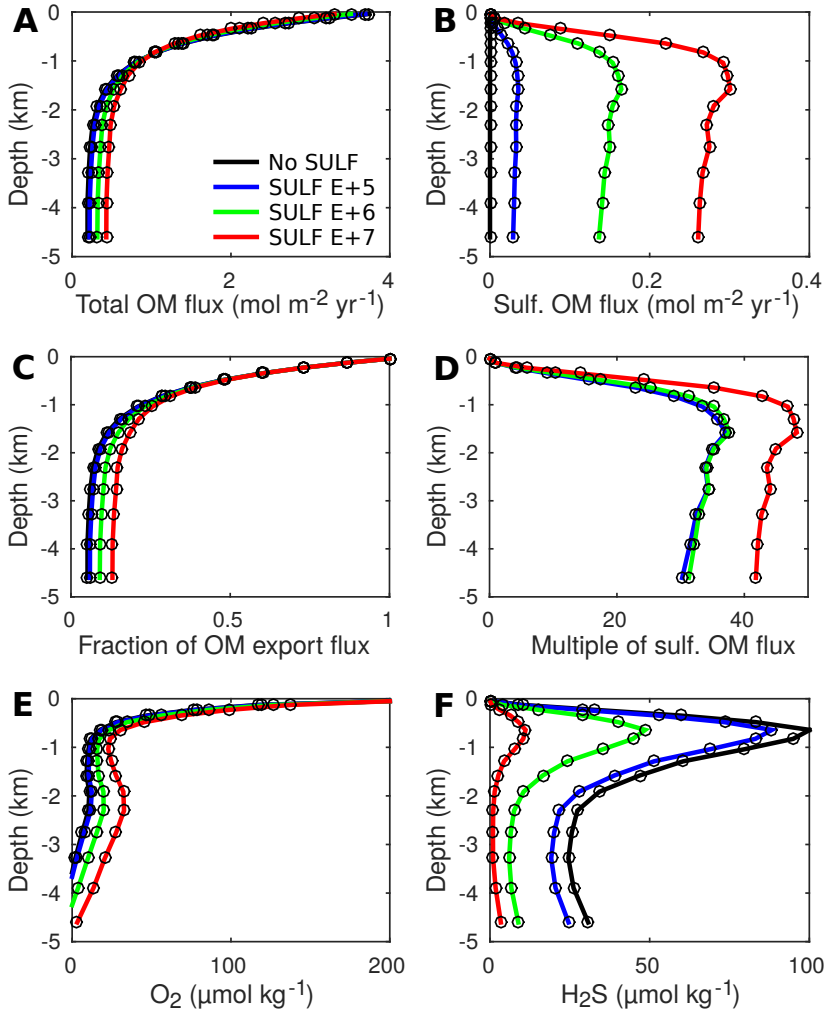

Figure 6.7: Globally averaged profiles of water column properties for 4 different sulfurization experiments. (A, B): Total OM and total sulfurized OM flux. (C): Global OM flux normalized to surface export flux (at 40 m). (D): Global sulfurized OM flux normalized to 127 m. (E, F): Global concentration profiles of oxygen and hydrogen sulfide.

is predicted at depths. The OM export production, however, decreases slightly for higher k_{sulf} (Table 6.4) because less OM is degraded in the upper ocean, therefore limiting the availability of nutrients for primary productivity. The sulfurized OM profiles visualize that most of the OM transformation takes place in the upper 1000 m of the water column where fluxes are up to 50 times higher as in the very surface ocean (Fig. 6.7D). This maximum in sulfurized OM flux is mainly due to very high H_2S concentrations at these depths (Fig. 6.7F) and because labile OM is still available for sulfurization. Globally averaged H_2S concentrations drop at all water depths for increasing sulfurization rate constants. This again is caused by two factors. First, H_2S is consumed by OM sulfurization and taken out of solution. Second, as a consequence, the bulk OM pool is more refractory, thus, leading to higher OM preservation and reduced H_2S production from OM degradation in the water column and the sediments. This decline in OM degradation is also mirrored in increasing global O_2 concentrations (Fig. 6.7E and Table 6.4).

The effect of OM sulfurization becomes even more evident when focusing on the geographical expansion of ocean anoxia and euxinia (Fig. 6.8). Model results suggests that enhanced OM preservation due to very rapid OM sulfurization could lead to a significant reoxygenation of the seafloor (from 86.2% to 58.7% anoxic area). In this maximum scenario, most of the seafloor of the East and Central Pacific Oceans as well as parts of the Indian and proto-South Atlantic Oceans are reoxygenated (Fig. 6.8A). Also, anoxia of the global ocean volume is decreasing from 79.7 to 48.0% reflecting reduced heterotrophic OM degradation in the water column as a result of a decrease in overall OM reactivity due to intense sulfurization. Even more significant is the reduction in water column euxinia, with photic zone euxinia almost completely disappearing and the part of the ocean volume with $[H_2S] > 10\,\mu\mathrm{mol\ kg^{-1}}$ dropping from 70.9 to 14.5% (Fig. 6.8C+E). The different responses of ocean anoxia and euxinia to increased sulfurization rate constants are indicators for non-linear feedbacks of the oxygen and sulfur cycle with changes in OM preservation.

Figure 6.9 illustrates the interactions between water column euxinia and OM fluxes for four different ocean provinces. The zonal average profiles of the no-sulfurization experiment (black) show fairly similar total OM fluxes but different degrees of water column euxinia. For all ocean provinces, higher sulfurization rate constants cause an increase in OM flux in the ocean (sulfurized and total) and a decline in water column euxinia. Due to different concentrations of H_2S in the ocean provinces, the sulfurization rate varies, causing highest sulfurized OM fluxes in the proto-Atlantic Ocean and lowest in the Central and West Pacific Ocean (Fig. 6.9A+C). For instance, in the $k_{\mathrm{sulf}} = 10^6$ scenario up to 70% of the total OM flux in the proto-Atlantic Ocean consists of sulfurized OM whereas in the Central and West Pacific Ocean only less than 34% of the OM is sulfurized (Fig. 6.9D). Consequently, in ocean provinces characterised by higher sulfurization rates more total organic matter is delivered to the seafloor (Fig. 6.9B) and hence buried in the sediments (Fig. 6.8F).

The spatially non-uniform increase of OM burial caused by rapid sulfurization can also be

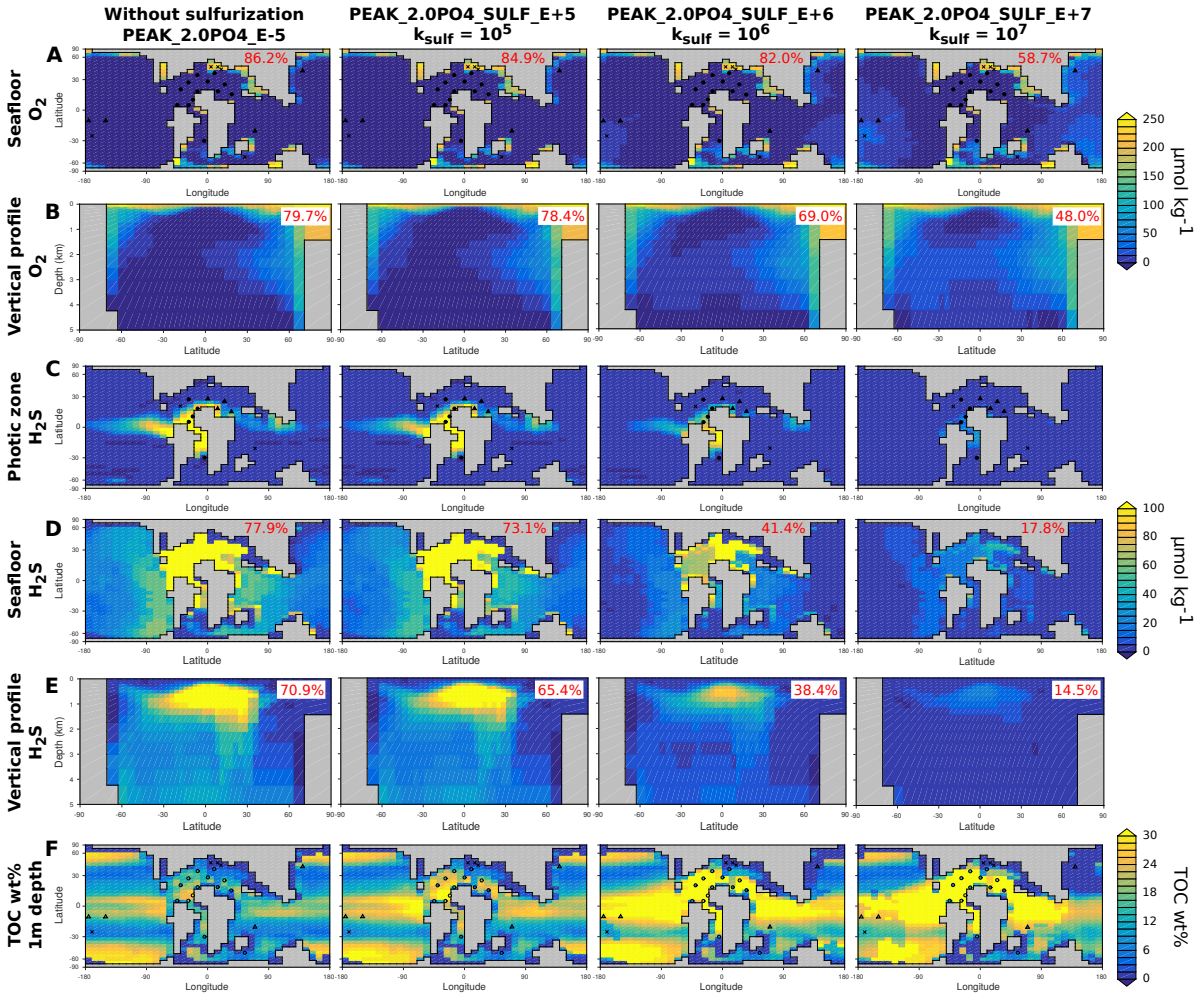

Figure 6.8: Model sensitivity of oceanic redox conditions and OM preservation with changing sulfurization rate constant. Vertical profiles of oxygen (B) and hydrogen sulfide (E) represents the average value across all longitudes. The percentages on top of the oxygen plots indicate the fraction of the anoxic seafloor area (A) and the global anoxic ocean volume (B). Respective percentages on top of the hydrogen sulfide plots (D, E) indicate H_2S concentrations higher than 10 μmol kg^{-1}.

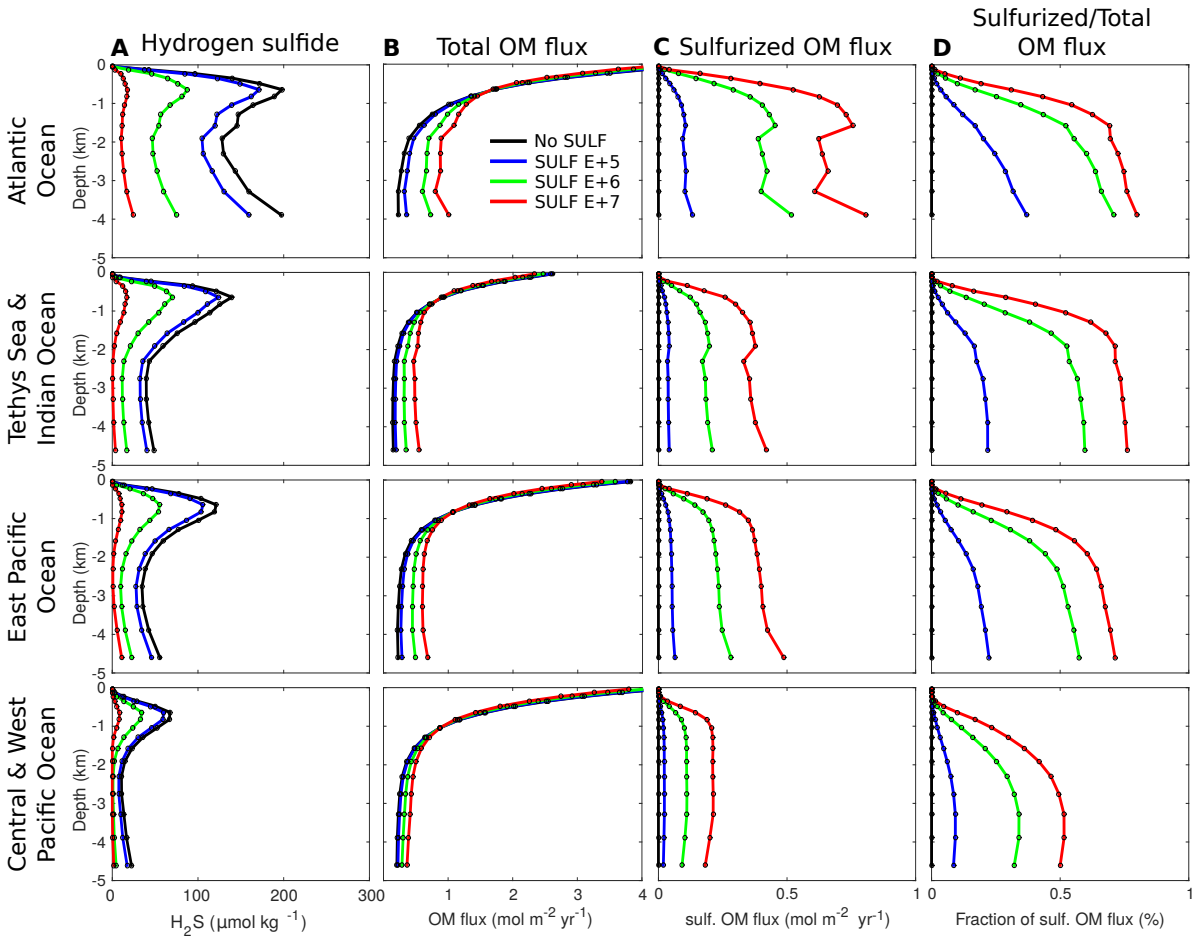

Figure 6.9: Zonally averaged profiles of water column euxinia and OM flux for 4 different sulfurization experiments. Compared are H_2S concentrations (A) and fluxes for total OM (B), sulfurized OM (C) and the ratio of sulfurized to total OM flux (D) for three ocean provinces.

seen in the model-data reconstruction (Fig. 6.10 A-D). Generally, for locations with observed black shales sulfurization increases OM preservation in between 8 and 18 wt%. The highest increases (of > 15 wt%) are simulated for locations in the proto-North Atlantic Ocean (A, B, C, D, F) and the Tethys Sea (N, P, Q). In the Indian and Pacific Ocean the increase is typically slightly lower (around 11-12 wt%), which is in line with comparably lower observed TOC contents in these basins (Table 6.1). Simulated TOC contents for locations lacking evidence for black shales are either only increased slightly by sulfurization (~3.5 wt%, site X), do still not preserve any TOC (locations J, K, L) or even show a decrease in OM preservation due to sulfurization (site U). This seemingly counter-intuitive observation can potentially be explained by limited availability of nutrients for primary productivity in certain parts of the ocean caused by an overall reduced OM degradation in the upper ocean. Preservation efficiencies of OM are specifically increased for the euxinic areas of the proto-Atlantic and East Pacific Oceans as well as large parts of the

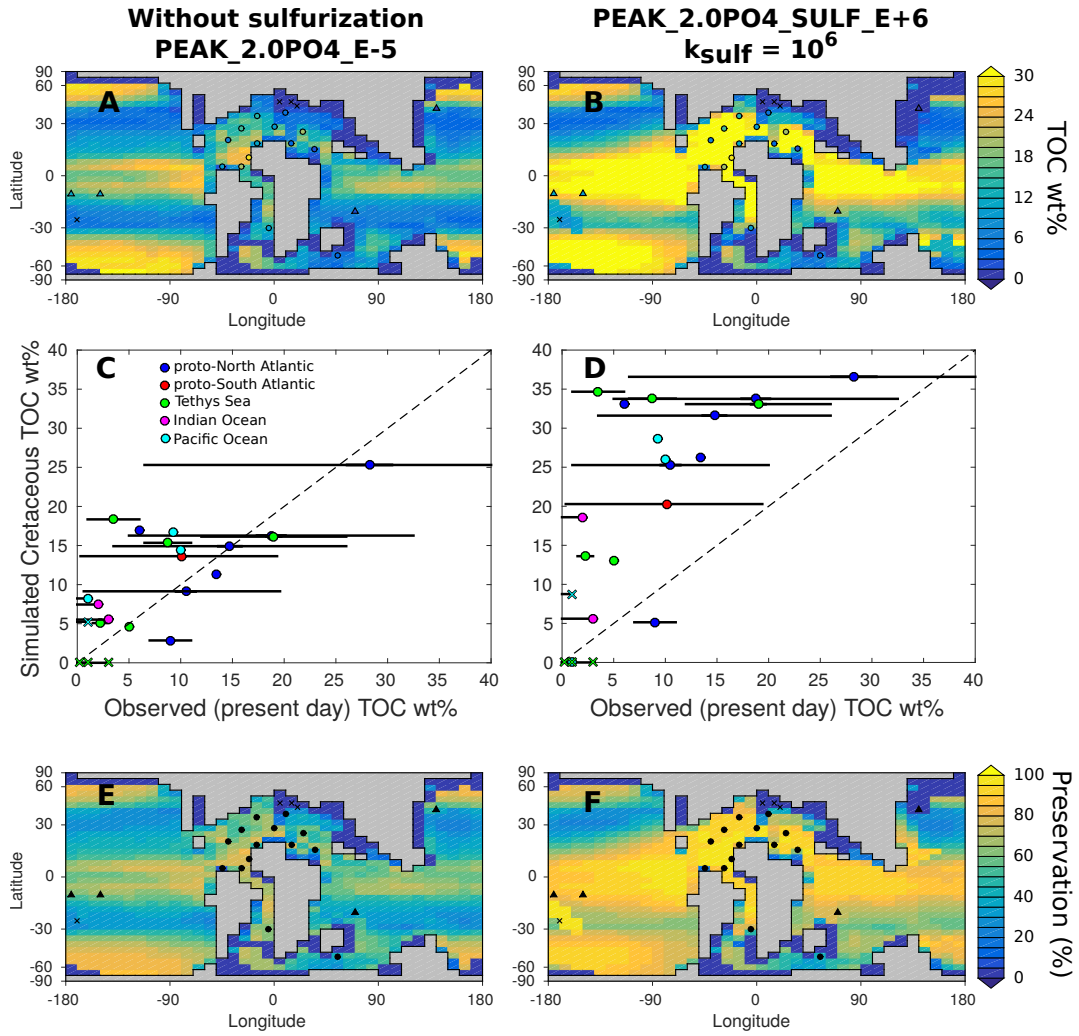

Figure 6.10: Impact of sulfurization on model-data reconstruction of geological TOC preservation during peak-OAE2. **Top:** Maps of TOC wt% at 1 m sediment depth as in Fig. 6.8F. **Middle:** Crossplots comparing simulated and observed TOC concentrations. The error bars indicate the ranges of TOC content reported for the specific location. **Bottom:** Preservation efficiency of organic matter calculated as the fraction between mean OM concentration in the first 5 cm and OM concentration at 1 m in the sediments.

Tethys Sea and most equatorial regions (Fig. 6.10 E+F). Note that preservation efficiencies are calculated as the fraction between mean OM concentrations in the first 5 cm and at 1 m in the sediments and are therefore slightly higher as if using the deposited OM at the seafloor.

6.4 Discussion

Our intention is not to advocate a particular choice of boundary conditions (i.e. atmospheric CO_2, oceanic PO_4 concentrations) or model parameters (OM degradation or sulfurization rate constants) to reconstruct OAE2 conditions but simply to illustrate that general trends of ocean redox conditions and organic matter preservation during the Cretaceous can be readily achieved with a 3D Earth system model of the coupled ocean-sediment system that includes the most important biogeochemical cycles. More specifically, we explore the influence of euxinia on OM sulfurization and associated enhanced OM preservation, as well as its feedbacks with ocean biogeochemistry. The feedback mechanisms responsible for enhanced OM preservation during peak-OAE2 are set in motion in our model by a doubling of the phosphate inventory in the ocean. This nutrient increase could have come from elevated phosphorus weathering rates caused by higher atmospheric CO_2 and is frequently suggested as an important initial trigger for OAE2 [e.g. Handoh and Lenton, 2003; Jenkyns, 2010; Monteiro et al., 2012; Pogge von Strandmann et al., 2013; Tsandev and Slomp, 2009]. The magnitude of increased weathering rates needed to double the marine phosphate inventory is consistent with paleo-weathering rates for OAE2 derived from strontium and calcium isotopic data [Blättler et al., 2011].

Doubling the oceanic phosphate concentration (from 1.0 to 2.0× PO_4) stimulates biological production and consequently increases organic matter export from the surface and OM rain to the seafloor in almost the same proportion (from 7.821 to 16.428 and 1.016 to 2.181 GtC yr^{-1}, respectively, Table 6.4). Concurrent with the productivity increase is a decline in oceanic oxygen concentration due to increased respiratory demand in deeper waters. In contrast to OM export and rain rate to the seafloor, global OM burial increases by a factor of ~ 15 (from 0.036 to 0.530 GtC yr^{-1}) illustrating the effect of an expanded anoxic seafloor area on OM burial (Table 6.4). This factor compares well with an increase of OM burial to 13 times pre-OAE2 values calculated by Tsandev and Slomp [2009]. Increased heterotrophic sulfate reduction rates in the euxinic water column stimulate the production of H_2S which can react with labile OM compounds, making them more resistant to bacterial degradation [Sinninghe Damsté and De Leeuw, 1990; Werne et al., 2004]. Model results indicate that OM sulfurization becomes a globally significant processes (i.e. increasing global OM burial by > 5%) when sulfurization is kinetically fast (i.e. $k_{sulf} > 10^5$). In this minimum scenario OM sulfurization increases OM burial and, thus, the overall excess OM burial above the pre-OAE2 background by a factor of 1.3 (or 3.6 for the maximum scenario $k_{sulf} = 10^7$). Simulated OM preservation efficiencies are specifically enhanced in euxinic areas of the ocean (e.g. the proto-Atlantic and East Pacific Oceans as well as parts of the Tethys Sea and equatorial

Table 6.4: Changes in ocean redox conditions and organic matter burial in the sediments for the pre-OAE2 and peak-OAE2 analogues as well as the sulfurization experiments.

Experiment	Seafloor anoxia (Area %)	Global anoxia (Volume %)	Global mean O_2 (μmol kg^{-1})	Global mean H_2S (μmol kg^{-1})	Global OM export (GtC yr^{-1})	Global OM rain (GtC yr^{-1})	Global OM burial (GtC yr^{-1})	Global Excess OM burial (GtC yr^{-1})
Pre-OAE2								
PRE_1PO4_E-5	11.0	8.3	104.2	3.0	7.821	1.016	0.036	-
Peak-OAE2								
Without sulfurization								
PEAK_2.0PO4_E-5	86.2	79.9	17.3	42.8	16.428	2.181	0.530	0.494
With sulfurization								
PEAK_2.0PO4_SULF_E+1	86.2	79.9	17.3	42.8	16.427	2.181	0.530	0.494
PEAK_2.0PO4_SULF_E+2	86.2	79.9	17.3	42.8	16.427	2.181	0.531	0.495
PEAK_2.0PO4_SULF_E+3	86.2	79.9	17.3	42.7	16.425	2.182	0.533	0.497
PEAK_2.0PO4_SULF_E+4	86.0	79.8	17.4	41.9	16.403	2.193	0.551	0.515
PEAK_2.0PO4_SULF_E+5	84.9	78.4	18.4	35.9	16.214	2.288	0.698	0.662
PEAK_2.0PO4_SULF_E+6	82.0	69.0	24.4	16.3	15.409	2.666	1.239	1.203
PEAK_2.0PO4_SULF_E+7	58.7	48.0	34.4	3.4	14.505	3.059	1.798	1.762

regions). Depending on the rate constant k_{sulf}, calculated preservation efficiencies range from 70 to 100% in these areas. These values compare well with predicted preservation efficiencies for OAE2 black shale organic matter from Demerara Rise [79 to 89%, Arndt et al., 2009]. As a consequence, over longer timescales, sulfurization of OM leads to enhanced CO_2 removal from the atmosphere and net photosynthetic oxygen production which causes a reoxygenation of the ocean and a reduction of water column euxinia.

The simulated excess OM burial rate of 0.494 GtC yr^{-1} for the no-sulfurization scenario translates to 4.1×10^{13} mols C yr^{-1} and is thus one order of magnitude higher than the excess burial rate of 0.32×10^{13} mols C yr^{-1} calculated by Arthur et al. [1988] who applied a carbon isotope mass balancing approach. Assuming atmospheric CO_2 during OAE2 to be 12 times higher than pre-industrial values [Bice et al., 2006; Sinninghe Damsté et al., 2010] it would thus take only ~ 15,000 years to consume all CO_2 in the atmosphere at our rate of excess OM burial. This time scale is significantly shorter than the one calculated by [Arthur et al., 1988] who proposed ~ 180,000 years to strip the Cretaceous atmosphere of CO_2. Our time scale is also shorter than results of Kuypers et al. [1999] who calculated a duration for the reduction of atmospheric CO_2 to background values of ~ 60,000 years. However, it needs to be considered that our results are more representative for the maximum extent of ocean anoxia/euxinia, thus simulating maximum OM burial rates during the peak-OAE2 event. These rates would not be sustained for the complete recovery phase from peak-OAE2. It is more likely, that burial rates would gradually decrease from this maximum rate while the ocean gets oxidised, thus slowing down the CO_2 drawdown over time.

6.5 Conclusions

Marine sediments act as the ultimate sink for organic matter, preserving carbon from the atmospheric and oceanic reservoirs. This process is important as it exerts an important control on atmospheric CO_2 concentrations and oxygen levels in the ocean [Berner, 2004]. Although globally increased organic matter burial is considered a primary cause for the reduction of atmospheric CO_2 and the reoxygenation of the ocean during OAE2, the mechanisms causing increased OM burial are still intensely debated and a precise quantification of this carbon sink is still missing. In this study, a 3D Earth system model is used for the first time to quantitatively assess excess OM burial rates during OAE2 compared to background Cretaceous values. In addition, the potential role of OM sulfurization as an emergency recovery mechanism from an extreme greenhouse world is investigated.

Although, our model results are inevitably associated with a certain degree of uncertainty, it is the first 3D Earth system model to confirm observations from the geological record that globally enhanced burial rates of organic matter during OAE2 are a primary mechanism that caused significant reduction in atmospheric CO_2. Our results imply that feedbacks between carbon,

oxygen, phosphorus and sulfur cycles in the ocean-sediment system lead to enhanced organic matter preservation during OAE2 compared to background Cretaceous values. At our simulated maximum excess OM burial rate, it would take only ~ 15,000 years to consume all CO_2 in the atmosphere of the Cretaceous. The sensitivity analysis shows that choosing the degradation rate constant for the refractory OM pool k_2 in OMEN-SED is crucial for reconstructing observed total organic carbon contents. We find that the coupled model framework is able reproduce patterns of black shales with high TOC content as observed in the geological record for OAE2. Our model results also imply that rapid sulfurization of organic matter in the water column has the potential to intensify OM burial and the reoxygenation of the ocean. Consequently, sulfurization can be an initially very efficient mechanism for drawing down CO_2 and inducing the termination of OAE2. Exact timescales are difficult to predict as the recovery (i.e. the reoxygenation of the ocean) will decrease the efficiency of the sulfurized OM sink and thus slow down CO_2 sequestration. Better estimates would require transient simulations. Future progress towards understanding feedbacks causing the termination of OAE2 also demand the representation of CO_2 feedbacks whereby changes in atmospheric concentrations in response to enhanced rates of OM burial have further effects on global biogeochemical cycles. For instance, lower atmospheric CO_2 would suppress terrestrial P weathering and P inputs into the ocean. Decreased primary productivity would then allow for reoxygenation of the ocean and the shut-down of the feedback loop between anoxia, P recycling and high primary productivity.

CHAPTER 7

SUMMARY AND FUTURE WORK

7.1 Summary of main findings

The work presented in this thesis reviews, evaluates and extends the current representation of marine carbon cycling in paleoclimate Earth system models. The particular focus is on the representation of benthic-pelagic coupling and modelling of organic matter degradation and related biogeochemical processes in marine sediments. The newly developed analytical diagenetic model OMEN-SED is coupled to the cGENIE Earth system model and is applied to study the impacts of organic matter burial and diagenetic processes for the development and termination of the Cenomanian-Turonian oceanic anoxic event (OAE2). As such, this thesis covers four important components of the modelling process: (1) A comprehensive review and evaluation of modelling approaches is conducted in order to identify gaps in current modelling frameworks (Chapter 2). (2) A new, analytical model for organic matter diagenesis in marine sediments is developed (and validated) in order to close one of the gaps identified before (Chapter 3). (3) The new diagenetic model is coupled to a global Earth system model and the coupled framework is tested and validated against observations from the modern ocean (Chapter 4). (4) The new global modelling framework is applied in the paleo-context, where its results are compared to simpler parameterisations of the benthic-pelagic coupling (Chapter 5). Finally, the modelling framework is applied in an OAE2 case-study to investigate new research hypotheses (Chapter 5). In the following, the main results of the research chapters of this thesis are summarised.

Chapter 2 provides a comprehensive overview of how marine carbon cycling and the biological carbon pump is treated in available paleoclimate models and critically evaluates their ability to help interpret past marine carbon cycle and climate dynamics. To this end, the chapter first provides an overview of commonly used paleoclimate models and some of their associated paleo-

applications, drawing from a wide range of global carbon cycle box models and Earth system Models of Intermediate Complexity (EMICs). Secondly, the chapter reviews and evaluates the three dominant processes involved in the cycling of organic and inorganic carbon in the marine system and how they are represented in models, namely: biological productivity at the ocean surface, remineralisation/dissolution of particulate carbon within the water column, and the benthic-pelagic coupling at the seafloor. Illustrative examples using the Earth system model cGENIE are employed to show how different parameterisations of water-column and sediment processes can lead to significantly different model projections. The compilation reveals the prevalence of static parameterisations of marine particulate organic carbon flux among existing paleoclimate models, which are commonly empirically derived from present-day observations. Another identified issue is the current oversimplified sediment representation in paleoclimate models, which are often not able to model the properties needed for a comparison to proxy-observations. Although such approaches tend to represent carbon transfer in the modern ocean-sediment system well, they are potentially compromised in their ability to reflect the true degree of freedom and strength of feedbacks with respect to past climate events, particularly those characterised by environmental boundary conditions that differ fundamentally from today.

Chapter 3 presents the first version of OMEN-SED (Organic Matter ENabled SEDiment model), a new, one-dimensional analytical early diagenetic model resolving organic matter cycling and associated biogeochemical dynamics in marine sediments designed to be coupled to Earth system models. OMEN-SED explicitly describes organic matter cycling as well as associated dynamics of the most important terminal electron acceptors (i.e. O_2 , NO_3, SO_4) and methane (CH_4), related reduced substances (NH_4, H_2S), macronutrients (PO_4) and associated pore water quantities (ALK, DIC). Its reaction network accounts for the most important primary and secondary redox reactions, equilibrium reactions, mineral dissolution and precipitation, as well as adsorption and desorption processes associated with organic matter dynamics that affect the dissolved and solid species explicitly resolved in the model. In addition, a representation of the formation and burial of Fe-bound P and authigenic Ca-P minerals is included in order to represent a redox-dependent sedimentary P cycle. Thus, OMEN-SED is able to capture the main features of diagenetic dynamics in marine sediments and, therefore, offers similar predictive abilities than a complex, numerical diagenetic model. Yet, its computational efficiency allows its coupling to global Earth system models and therefore the investigation of coupled global biogeochemical dynamics over a wide range of climate relevant timescales. Chapter 3 provides a detailed description of the new sediment model, as well as an extensive sensitivity analysis using a novel method which considers the entire cumulative distribution functions of the model outputs. In addition, OMEN-SED's performance is evaluated through comprehensive comparisons with observations and results from a more complex numerical model. Results show that solid phase and dissolved pore water profiles for different ocean depths are reproduced with good accuracy and simulated terminal electron acceptor fluxes fall well within the range of globally observed

fluxes.

Chapter 4 illustrates the application of OMEN-SED in an Earth system model framework by coupling it to the global model cGENIE. Thereby, the first spatially resolved Earth system model is created mechanistically accounting for oxic degradation, denitrification, sulfate reduction and implicitly methanogenesis, as well as the reoxidation of reduced substances, adsorption/desorption, as well as mineral precipitation/dissolution in marine sediments. A sensitivity analysis is performed with the coupled model framework, comparing globally invariant degradation rate constants for organic matter as well as the empirical relationship of Boudreau [1997] which describes the apparent degradation rate constant as a function of sedimentation rate. The comparison between simulated organic matter contents and observations indicates that a depth and sedimentation rate dependent relationship provides the best fit, confirming more theoretical considerations regarding the different time and reactivity scales that need to be considered in the sediments. Simulated sediment characteristics of the calibrated model framework, such as organic matter degradation rates, oxygen penetration depths and sediment-water interface fluxes are generally in good agreement with observations and in line with what one would expect on a global scale. Coupled to an Earth system model, OMEN-SED is thus a powerful tool that will not only help elucidate the role of benthic-pelagic exchange processes in the evolution and, in particular, the termination of a wide range of climate events, but will also allow a direct comparison of model output with the sedimentary record - the most important climate archive on Earth.

In Chapter 5 the new Earth system model framework is applied to examine the importance of benthic-pelagic coupling for the development of ocean anoxia and euxinia during OAE2. A suite of experiments with a hierarchy of lower ocean boundary representations of increasing complexity coupled to cGENIE is presented. The representations range from very simple, but widely adopted, Conservative and Reflective lower boundary approaches, where sediment interactions are essentially ignored (all organic matter is either instantaneously remineralised or buried in the sediments), to more complex explicit sediment representations simulated with OMEN-SED. Results show that the lower boundary representation plays a crucial role for benthic-pelagic exchange fluxes of dissolved species and thus for the onset of anoxia and euxinia. The two simple representations either over- or underestimate the consumption of oxygen and the productions of H_2S. Results using OMEN-SED generally fall in between these extreme scenarios. Model simulations illustrate that anoxia/euxinia develops from oxygen minimum zones in the photic zone and at the seafloor. When marine productivity is high enough, both areas combine and establish anoxic/euxinic conditions in the entire water column. Furthermore, simulated sediment-water interface fluxes with OMEN-SED show enhanced P regeneration from the sediments in response to seafloor oxygen depletion during peak-OAE2 which could further intensify marine productivity. Future work with cGENIE should concentrate on understanding the importance of the positive feedback between P recycling from anoxic sediments, primary productivity and anoxia for the

genesis of OAE2 as this is still a poorly quantified process.

In Chapter 6 the coupled cGENIE - OMEN-SED modelling framework is applied to investigate the role of organic matter burial in Earth's recovery dynamics from OAE2. Thus, for the first time a 3D Earth system model is employed to quantitatively interpret the coupled biogeochemical recovery of the Earth system from a perturbation of the global carbon cycle and the associated global warming during OAE2. In addition, a new mechanism is investigated which has been increasingly proposed to explain the elevated organic matter burial rates observed during OAE2 - sulfurization of organic matter. During sulfurization, more labile organic matter compounds react with reduced inorganic sulfur species (e.g. H_2S), resulting in the formation of organic sulfur compounds which are less prone to bacterial degradation. Although studies indicate the global significance of this process and its potential relevance for organic matter burial and climate cooling a quantitative investigation of its importance is still lacking. Model simulations in Chapter 6 reveal three important results. First, they imply that feedbacks between carbon, oxygen, phosphorus and sulfur cycles in the ocean-sediment system lead to significantly enhanced organic matter preservation during OAE2 compared to background Cretaceous values. Second, the model can reproduce geographical patterns of organic matter-rich black shales as observed in the geological record for OAE2. Third, results indicate that rapid organic matter sulfurization in the water column has the potential to intensify organic matter burial and thus the reoxygenation of the ocean. Consequently, sulfurization can be an initially very efficient mechanism for drawing down CO_2 and inducing the termination of OAE2.

7.2 Future work

Findings and results presented in this thesis offer the opportunity for new research questions which can be broadly separated into three groups. First, future OMEN-SED model developments to include more processes and to overcome some of the limitations discussed in Chapter 3 and 4. Second, the results obtained for OAE2 could be pursued through at least two related studies and third, OMEN-SED could be coupled to other model types and applied to completely new research questions.

7.2.1 Future OMEN-SED developments

Implementation of an explicit Fe-cycle

The next step will be to implement an explicit Fe-cycle in OMEN-SED by including three additional biogeochemical tracers in the modelling framework, namely Fe(III), Fe(II) and pyrite or FeS_2). Organic matter degradation via Fe(III)-reduction and related production of Fe(II) will follow the general pattern of the other degradation and reoxidation pathways. The oxidation of Fe(II) by O_2 will be analogous to H_2S oxidation in OMEN-SED. Reactive Fe-minerals also represent an important sink for pore water H_2S through the process of sedimentary pyrite

formation [e.g. Berner, 1984; Canfield, 1989a; Canfield et al., 1992]. Therefore, we plan to include this process in a similar manner as the current precipitation of apatite in OMEN-SED. For simplicity, we will not model the intermediate production of iron monosulfides (FeS) but assume the reaction of iron minerals with H_2S readily produces pyrite. These processes will further improve the mechanistic representation of diagenetic processes in Earth system models and will enable us to explore the significance of feedbacks between the cycling of iron, phosphorous and sulfur on a global scale in general and for organic matter preservation during OAEs in particular [Meyers, 2007].

Implementation of an explicit $CaCO_3$-cycle

Another important biogeochemical cycle for the functioning of the Earth system which is currently ignored in OMEN-SED is that of calcium carbonate [$CaCO_3$, Ridgwell and Zeebe, 2005]. Precipitation and dissolution of $CaCO_3$ depends on the saturation state of pore waters with respect to calcite, itself related to primary and secondary redox-reactions and its effects on pore water alkalinity and dissolved inorganic carbon concentrations [Hales, 2003]. Organic matter driven release of CO_2 decreases the carbonate ion concentration (CO_3^{2-}) and can be very distinct in pore waters as transport is generally limited to diffusion [Emerson and Bender, 1981]. An explicit, steady-state representation of $CaCO_3$ dynamics and its relationship with alkalinity and DIC is challenging to develop. One way of implementing it would be to adapt a similar approach to Jourabchi et al. [2005] where the rate of dissolution depends on the degree of undersaturation of the pore waters. Another approach would be to include $CaCO_3$ dynamics in a (potentially) more simplified way as has been presented previously by Boudreau [1987] or Archer et al. [2002].

7.2.2 Possible future OAE applications

Comparing recovery dynamics from OAEs and the PETM

The newly developed model framework could be applied to evaluate and compare the recovery dynamics of the Earth system from different greenhouse climates during Earth history. In particular the significance of organic matter burial and sulfurisation as an “emergency” recovery mechanism and its impact on the benthic-pelagic coupling could be compared. It would be interesting to compare the dynamics of climate recovery during OAE2 with other extreme events as for instance the Paleocene-Eocene Thermal Maximum [PETM ~55 Ma, Zachos et al., 2005] or the Toarcian OAE [~183 Ma, Jenkyns, 2010]. All three events are characterised by similarities and differences in their recovery dynamics. All events represent warming transients, are associated with high organic matter preservation in the sediments and show rates of recovery of the $\delta^{13}C$ record to be more rapid than if caused by enhanced silicate weathering alone, thus calling for the importance of organic matter burial [e.g. Bains et al., 2000; Bowen and Zachos, 2010; Cohen et al., 2007]. However, for the Cenomanian-Turonian and Toarcian OAEs the isotopic

recovery to background values is achieved more rapidly compared to the PETM, where the recovery can be separated into two stages. The second stage proceeds more slowly, thus indicative for slower silicate weathering feedbacks being responsible as well [Kelly et al., 2005]. The new model framework could be applied to compare quantitatively for the first time the significance of organic matter burial for the recovery dynamics from these topical extreme events. Furthermore, the model could be used to evaluate if the more rapid recovery from OAEs is caused by the more widespread euxinic conditions and therefore more efficient organic matter burial due to sulfurisation.

Transient OAE2 simulation

With the new coupled cGENIE - OMEN-SED framework we have created the first three-dimensional Earth system model accounting for all important modes of Earth system recovery from a condition of elevated atmospheric CO_2 concentrations. The new model is able to represent positive feedbacks between PO_4 concentration, biological production, anoxia and benthic P regeneration which is important to develop and maintain the state of ocean anoxia/euxinia [Van Cappellen and Ingall, 1994]. At the same time the model now incorporates a mechanistic representation of organic matter preservation in the sediments. Therefore, increased organic matter burial rates (intensified through sulfurization) leads to reduced oxygen consumption in the marine environment, thus decreased anoxia and ultimately a drawdown of atmospheric CO_2 concentrations. Therefore it should be possible to run transient OAE2 simulations, initiated for instance by an increased phosphorous weathering rate, and to test if feedbacks between the coupled marine biogeochemical cycles in a 3-D Earth system model are able to simulate the development and termination of OAE2. As mentioned earlier, in order to test this idea, cGENIE needs to be configured as an “open system”, where atmospheric oxygen and carbon dioxide concentrations as well as the oceanic inventory of phosphate can change over time.

7.2.3 Possible model couplings and new applications

Coupling to a regional model of the Amazon shelf

The Amazon River, the world’s largest river in terms of water discharge [Dai et al., 2009], represents an important organic matter and nutrient source for the ocean which significantly influences the local ecosystem structure [Goes et al., 2014]. This in turn has significant impacts on the efficiency of the biological carbon pump, leading to oceanic carbon sequestration in areas influenced by the Amazon River [Cooley and Yager, 2006]. The combination of strong coastal currents, tides and wind-driven waves causes periodic reworking of the shelf sediments, thus increasing its oxygen exposure time. Consequently, organic matter degradation rates along the Amazon coastline are some of the highest for estuarine or shelf environments, with terrestrial and marine organic matter contributing to diagenetic degradation [Aller and Blair, 2006]. The

understanding of this very dynamic and nonsteady-state environment rests mainly on a limited number of field studies. Furthermore, the impact of the Amazon River on biogeochemistry in the Atlantic Ocean and the global carbon budget has not yet been quantified with a numerical model. To close this knowledge gap, Domitille Louchard (PhD student, ETH) is applying the Regional Oceanic Modeling System [ROMS, Shchepetkin and McWilliams, 2005], a 3D numerical ocean circulation model, to simulate the Atlantic basin using a dynamic grid resolution. The telescopic grid features the highest resolution (4km) at the mouth of the Amazon in order to represent coastal currents as well as eddy and advective transport processes. The ocean circulation model will be coupled to the Biogeochemical Elemental Cycling model [BEC, Moore et al., 2001] which will be extended with an terrestrial organic matter pool, characterised by a different degradation rate constant. In order to determine the fate of the different organic matter sources and the role of diagenetic processes for the nutrient budget of the Atlantic Ocean OMEN-SED will be coupled to the ROMS-BEC framework. In preparation, the explicit Fe-cycle has to be included in OMEN-SED and in order to account for the dynamic and nonsteady-state conditions on the Amazon shelf, parameterisations for deposition/erosion as well as corrections for the steady-state assumption need to be explored [compare e.g. Arndt and Regnier, 2007].

Applications in the ChAOS and PISCES projects

OMEN-SED could also be used in two ongoing projects investigating the impacts of climate change on the rapidly changing Arctic environment and the Patagonian coast line. The Changing Arctic Ocean Seafloor project (ChAOS) explores the effects of the retreating sea ice cover on the carbon and nutrient dynamics of the Arctic Ocean and its feedbacks with the local ecosystem. In the Arctic Ocean benthic-pelagic processes and its feedbacks with the water column are more pronounced than in the open ocean and are crucial for marine productivity and long-term carbon sequestration from the ocean-atmosphere system [Stein and MacDonald, 2004]. However, major uncertainties exist how a reduced sea ice cover will affect diagenetic processes and related carbon and nutrient cycles [Macdonald et al., 2015]. Modelling these responses is made very challenging due to the incomplete mechanistic understanding of the Arctic Ocean seafloor. In addition, most regional biogeochemical models do not represent the complexity of the benthic-pelagic coupling. Even though, the Arctic Ocean sea floor represents a very dynamic environment also affected by significant inter-annual sea ice cover variability [Kay et al., 2011], OMEN-SED could be used to determine upper and lower boundaries for potential sediment-water exchange fluxes and to guide experiments with more complex diagenetic models. For this purpose, OMEN-SED could be readily used as a stand-alone version driven by output of the NEMO-MEDUSA modelling framework [Aumont et al., 2015; Yool et al., 2011] which is used in the ChAOS project.

The second project investigates Patagonian Ice field Shrinkage impacts on Coastal and fjord EcosystemS (PISCES) along the Chilean coast line. Here, the fjord hydrodynamics will be described by the 2D vertically resolved MIT-GCM [Marshall et al., 1997] and the water column

biogeochemistry by the Carbon-Generic Estuary Model [C-GEM, Volta et al., 2014]. As in C-GEM the complete organic matter pool is remineralised either aerobically or via denitrification the coupling to OMEN-SED would improve the representation of the lower boundary of the modelling framework. To investigate the sensitivity of the fjord's nutrient budget to future riverine fluxes a series of steady state experiments are planned where C-GEM will be forced with various fluxes and boundary conditions. At the same time, comparing results of the two lower boundary conditions would improve our understanding of the importance of the benthic-pelagic representation for modelling estuarine systems.

APPENDIX A

A.1 Paleoclimate Earth Sytem Model Applications

Table A.1: **Paleoclimate model applications (EMICs)** (ordered from higher to lower ocean resolution) with a relation to the biological pump. Study-time reflects the broad modelled time in the experiments (not the official timing of the event).

Model	Event	Study-Time	References
EMIC			
Bern 2.5D	Younger Dryas	ca. 13.0 – 11.0 kyr BP	Marchal et al. [1999a,b, 2001]
	Heinrich events & Last deglaciation	ca. 60 – 12 kyr BP	Marchal et al. [1998a]
Bern 3D	Holocene	ca. 8 kyr BP – present	Brovkin et al. [2016]; Menviel and Joos [2012]
	LGM and deglaciation	20.0 kyr BP – present	Tschumi et al. [2011, 2008]
	Last glacial period	ca. 70 – 30 kyr BP	Parekh et al. [2008]
	Last glacial cycle	125 kry BP – present	Menviel et al. [2012]
	Emian interglacial	126 – 115 kyr BP	Brovkin et al. [2016]
CLIMBER-2	Holocene	ca. 8 kyr BP – present	Brovkin et al. [2016]; Kleinen et al. [2015]
	8.2 kyr BP event	8.2 kyr BP	Brovkin et al. [2002a]
	Last deglaciation	ca. 18 – 9 kyr BP	Bouttes et al. [2012a]
	LGM	ca. 21 kyr BP	Bouttes et al. [2009]; Brovkin et al. [2007, 2002b] Bouttes et al. [2010, 2011, 2012b]
	Emian interglacial	ca. 125 kyr BP	Duplessy et al. [2007]
		ca. 126 – 116 kyr BP	Brovkin et al. [2016]; Kleinen et al. [2015]
	Glacial cycles	126 kyr BP – present	Brovkin et al. [2012]
	MIS 11 interglacial	420 – 380 kyr BP	Kleinen et al. [2015]
GENIE	Holocene	8 – 0.5 kyr BP	Brovkin et al. [2016]
	Younger Dryas	13.5 – 11.5 kyr BP	Singarayer et al. [2008]
	Emian interglacial	126 – 115 kyr BP	Brovkin et al. [2016]
	Eocene hyperthermal	49.2 Ma	Kirtland Turner and Ridgwell [2013]
		ca. 50 Ma	Norris et al. [2013]
	Early Eocene	ca. 55 Ma	Meyer and Kump [2008]; Pälike et al. [2012] Anagnostou et al. [2016]
	PETM	ca. 55.8 Ma	Panchuk et al. [2008]; Ridgwell [2007] Cui et al. [2011]; Ridgwell and Schmidt [2010] Kirtland Turner and Ridgwell [2016] Zeebe et al. [2016]
	OAE2	93.5 Ma	Monteiro et al. [2012]
	Cretaceous	101 Ma	Meyer and Kump [2008]
	End-Permian	ca. 252 Ma	Meyer and Kump [2008]; Meyer et al. [2008] Cui et al. [2015, 2013]
	Last 400 Ma	400 Ma – present	Goodwin et al. [2009]

Table A.2: **Table A.1 (continued)**

Model	Event	Study-Time	References
GEOCLIM	Cretaceous	145.5 - 65.5 Ma	Donnadieu et al. [2006a]
	Jurassic	199.6 – 145.5 Ma	Donnadieu et al. [2006a]
	Triassic	251.0 – 199.6 Ma	Donnadieu et al. [2006a]; Goddéris et al. [2008]
	Late Neoproterozoic	580.0 Ma	Donnadieu et al. [2004]
	Neoproterozoic	1,000 – 542.0 Ma	Le Hir et al. [2008]
LOVECLIM	Last deglaciation	ca. 21 – 10 kyr BP	Menviel et al. [2011]
	LGM	ca. 22.5 kyr BP	Menviel et al. [2014, 2008a,b]
	Interglacials	universally	Menviel et al. [2010]
	Emian interglacial	ca. 129 – 118 kyr BP	Duplessy et al. [2007]
MESMO	Younger Dryas	ca. 12.9 – 11.7 kyr BP	Matsumoto and Yokoyama [2013]
	Heinrich 1	ca. 17.5 – 14.5 kyr BP	Matsumoto and Yokoyama [2013]
	LGM	ca. 22.5 kyr BP	Sun and Matsumoto [2010]
			Matsumoto et al. [2014]
	Glacial cycles	ca. 400 kry BP – present	Ushie and Matsumoto [2012]
MoBidiC	LGM	ca. 22.5 kyr BP	Crucifix [2005]
	Heinrich events	ca. 60 – 12 kyr BP	Crucifix [2005]
	& Last deglaciation		
UVic	Last deglaciation	ca. 20 – 15 kyr BP	Schmittner and Lund [2015]
	Last deglaciation	23 kyr BP – present	Simmons et al. [2015]
	LGM	ca. 21 kyr BP	Fraile et al. [2009]; Menviel et al. [2014]
			Schmittner and Somes [2016]
	DO-event 8 & 12	ca. 37 & 45 kyr BP	Ewen et al. [2004]
	DO-event	universally	Schmittner [2005]; Schmittner et al. [2007]
	Panama seaway closure	ca. 14 – 3 Ma	Schneider and Schmittner [2006]
	Antarctic Glaciation	ca. 33.7 Ma	Pagani et al. [2011]
	PETM	ca. 55.8 Ma	Bralower et al. [2014]; Meissner et al. [2014]
			Alexander et al. [2015]
	End-Permian	ca. 252 Ma	Montenegro et al. [2011]

Table A.3: **Paleoclimate model applications (Box models)** (ordered from higher to lower ocean resolution) with a relation to the biological pump. Study-time reflects the broad modelled time in the experiments (not the official timing of the event).

Model	Event	Study-Time	References
Box			
BICYCLE	Last deglaciation	21 – 10 kyr BP	Köhler et al. [2005]
	Glacial cycles	120 kyr BP – present	Köhler et al. [2006]
	Glacial cycles	740 kyr BP – present	Köhler and Fischer [2006]
			Köhler et al. [2010]
	Mid Pleistocene Transition	2 Ma – present	Köhler and Bintanja [2008]
CYCLOPS	LGM	ca. 22.5 kyr BP	Keir [1988]; Michel et al. [1995]
			Galbraith et al. [2015]; Sigman et al. [2003]
	Last deglaciation	ca. 30 kyr BP – present	Keir [1991]; Sigman et al. [1998]
	Glacial cycle	150 kyr BP – present	Hain et al. [2010]; Keir [1990]
DCESS	LGM	ca. 22.5 kyr BP	Lambert et al. [2015]
	PETM	ca. 55.8 Ma	Shaffer et al. [2016]
LOSCAR	Mid-Miocene	16.8 – 13.8 Ma	Armstrong McKay et al. [2014]
	MECO	ca. 40 Ma	Sluijs et al. [2013]
	Paleocene-Eocene	62 – 48 Ma	Komar et al. [2013]
	Early Eocene	ca. 55 Ma	Pälike et al. [2012]
	PETM	ca. 55.8 Ma	Zeebe and Zachos [2007]; Zeebe et al. [2009]
			Uchikawa and Zeebe [2010]
			Komar and Zeebe [2011]
			Zeebe and Zachos [2013]
			Penman et al. [2014]; Zeebe et al. [2016]
MBM	Glacial cycle	ca. 150 kyr BP – present	Munhoven and François [1994, 1996]
			Munhoven [2007]
PANDORA	Glacial-Interglacial CO_2	universally	Broecker and Peng [1986, 1987, 1989]
			Broecker et al. [1990]
SUE	since LGM	ca. 22.5 kyr BP – today	Ridgwell et al. [2003b]
	Glacial cycles	400 kyr BP – present	Ridgwell [2001]; Ridgwell et al. [2002]
	Snowball Earth	around 650 Ma	Ridgwell et al. [2003a]
	Phanerozoic	600 Ma – present	Ridgwell [2005]

APPENDIX B

APPENDIX B

B.1 OMEN-SED reaction network

Table B.1: Primary pathways of organic matter degradation, secondary redox reactions and stoichiometries implemented in the reaction network.

Pathway	Stoichiometry
	Primary Redox reactions
Aerobic degradation	$(CH_2O)_x(NH_3)_y(H_3PO_4)_z + (x+2y)O_2 + (y+2z)HCO_3^- \rightarrow (x+y+2z)CO_2 + yNO_3^- + zHPO_4^{2-} + (x+2y+2z)H_2O$
Denitrification	$(CH_2O)_x(NH_3)_y(H_3PO_4)_z + \frac{(4x+3y)}{5}NO_3^- \rightarrow \frac{(2x+4y)}{5}N_2 + \frac{(x-3y+10z)}{5}CO_2 + \frac{(4x+3y-10z)}{5}HCO_3^- + zHPO_4^{2-} + \frac{(3x+6y+10z)}{5}H_2O$
Sulfate reduction	$(CH_2O)_x(NH_3)_y(H_3PO_4)_z + \frac{x}{2}SO_4^{2-} + (y-2z)CO_2 + (y-2z)H_2O \rightarrow \frac{x}{2}H_2S + (x+y-2z)HCO_3^- + yNH_4^+ + zHPO_4^{2-}$
Methanogenesis	$(CH_2O)_x(NH_3)_y(H_3PO_4)_z + (y-2z)H_2O \rightarrow \frac{x}{2}CH_4 + \frac{x-2y+4z}{2}CO_2 + (x-2z)HCO_3^- + yNH_4^+ + zHPO_4^{2-}$
	Secondary Redox reactions
Nitrification	$NH_4^+ + 2O_2 + 2HCO_3^- \rightarrow NO_3^- + 2CO_2 + 3H_2O$
Sulfide oxidation	$H_2S + 2O_2 + 2HCO_3^- \rightarrow SO_4^{2-} + 2CO_2 + 2H_2O$
AOM	$CH_4 + CO_2 + SO_4^{2-} \rightarrow 2HCO_3^- + H_2S$
	Adsorption reactions and mineral precipitation
NH_4 adsorption	$NH_4^+ \xrightarrow{K_{NH_4}} NH_4^+(ads)$
P ad-/desorption	$PO_4^{2-} \xrightarrow{K_{PO_4}^{I,II}} PO_4^{2-}(ads); \qquad PO_4^{2-} \xrightarrow{k_s} Fe-bound\ P \xrightarrow{k_m} PO_4^{2-}$
CFA precipitation	$PO_4^{2-} \xrightarrow{k_a} CFA$

B.2 Sensitivity Analysis

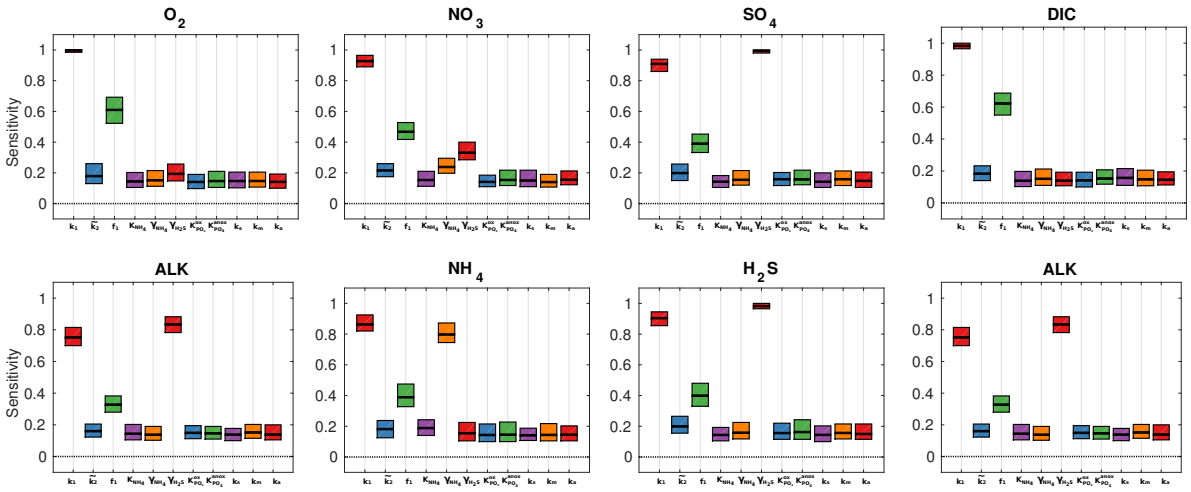

Figure B.1: Box plot of parameter sensitivities for the calculated SWI-fluxes for the 4000m oxic condition. Average sensitivities (black lines) and 90% confidence intervals using $N = 11200$ model evaluations and $Nboot = 100$ bootstrap resamples.

BIBLIOGRAPHY

Adam, P., Philippe, E., and Albrecht, P. (1998). Photochemical Sulfurization of Sedimentary Organic Matter: A Widespread Process Occurring at Early Diagenesis in Natural Environments? *Geochimica et Cosmochimica Acta*, 62(2):265–271.

Aguilera, D. R., Jourabchi, P., Spiteri, C., and Regnier, P. (2005). A knowledge-based reactive transport approach for the simulation of biogeochemical dynamics in earth systems. *Geochemistry, Geophysics, Geosystems*, 6(7):Q07012.

Alexander, K., J. Meissner, K., and J. Bralower, T. (2015). Sudden spreading of corrosive bottom water during the Palaeocene-Eocene Thermal Maximum. *Nature Geoscience*, 8(6):458–461. 00001.

Alldredge, A. L. and Cohen, Y. (1987). Can microscale chemical patches persist in the sea? microelectrode study of marine snow, fecal pellets. *Science*, 235(4789):689–691.

Allemand, D., Tambutté, E., Zoccola, D., and Tambutté, S. (2011). Coral Calcification, Cells to Reefs. In Dubinsky, Z. and Stambler, N., editors, *Coral Reefs: An Ecosystem in Transition*, pages 119–150. Springer Netherlands.

Aller, R. C. (1984). The importance of relict burrow structures and burrow irrigation in controlling sedimentary solute distributions. *Geochimica et Cosmochimica Acta*, 48(10):1929–1934.

Aller, R. C. (1988). Benthic fauna and biogeochemical processes in marine sediments: the role of burrow structures. In Blackburn, T. and Sorensen, J., editors, *Nitrogen cycling in coastal marine environments*, pages 301–338. Scope, Chichester.

Aller, R. C. and Blair, N. E. (2006). Carbon remineralization in the Amazon-Guianas tropical mobile mudbelt: A sedimentary incinerator. *Continental Shelf Research*, 26(17):2241–2259.

Alverson, K. D., Bradley, R. S., and Pedersen, T. F. (2003). *Paleoclimate, Global Change and the Future*. Springer Science & Business Media.

Anagnostou, E., John, E. H., Edgar, K. M., Foster, G. L., Ridgwell, A., Inglis, G. N., Pancost, R. D., Lunt, D. J., and Pearson, P. N. (2016). Changing atmospheric CO2 concentration was the primary driver of early Cenozoic climate. *Nature*, advance online publication. 00000.

Anderson, L. A. and Sarmiento, J. L. (1994). Redfield ratios of remineralization determined by nutrient data analysis. *Global Biogeochemical Cycles*, 8(1):65–80.

Andersson, J. H., Wijsman, J. W. M., Herman, P. M. J., Middelburg, J. J., Soetaert, K., and Heip, C. (2004). Respiration patterns in the deep ocean. *Geophysical Research Letters*, 31(3).

Ando, A., Nakano, T., Kaiho, K., Kobayashi, T., Kokado, E., and Khim, B.-K. (2009). Onset of Seawater 87sr/86sr Excursion Prior to Cenomanian-Turonian Oceanic Anoxic Event 2? New Late Cretaceous Strontium Isotope Curve from the Central Pacific Ocean. *Journal of Foraminiferal Research*, 39(4):322–334.

Archer, D. (1996a). A data-driven model of the global calcite lysocline. *Global Biogeochemical Cycles*, 10(3):511–526.

Archer, D. and Devol, A. (1992). Benthic oxygen fluxes on the Washington shelf and slope: A comparison of in situ microelectrode and chamber flux measurements. *Limnology and Oceanography*, 37(3):614–629.

Archer, D., Eby, M., Brovkin, V., Ridgwell, A., Cao, L., Mikolajewicz, U., Caldeira, K., Matsumoto, K., Munhoven, G., Montenegro, A., and Tokos, K. (2009). Atmospheric Lifetime of Fossil Fuel Carbon Dioxide. *Annual Review of Earth and Planetary Sciences*, 37(1):117–134.

Archer, D., Kheshgi, H., and Maier-Reimer, E. (1998). Dynamics of fossil fuel CO2 neutralization by marine CaCO3. *Global Biogeochemical Cycles*, 12(2):259–276.

Archer, D. and Maier-Reimer, E. (1994). Effect of deep-sea sedimentary calcite preservation on atmospheric co2 concentration. *Nature*, 367(6460):260–263.

Archer, D., Winguth, A., Lea, D., and Mahowald, N. (2000a). What caused the glacial/interglacial atmospheric pCO2 cycles? *Reviews of Geophysics*, 38(2):159–189.

Archer, D. E. (1991). Modeling the calcite lysocline. *Journal of Geophysical Research*, 96(C9):17037–17050.

Archer, D. E. (1996b). An atlas of the distribution of calcium carbonate in sediments of the deep sea. *Global Biogeochemical Cycles*, 10(1):159–174.

Archer, D. E., Eshel, G., Winguth, A., Broecker, W., Pierrehumbert, R., Tobis, M., and Jacob, R. (2000b). Atmospheric pCO_2 sensitivity to the biological pump in the ocean. *Global Biogeochem. Cy.*, 14(4):1219–1230.

Archer, D. E., Morford, J. L., and Emerson, S. R. (2002). A model of suboxic sedimentary diagenesis suitable for automatic tuning and gridded global domains. *Global Biogeochemical Cycles*, 16(1):17–1.

Armstrong, R. A., Lee, C., Hedges, J. I., Honjo, S., and Wakeham, S. G. (2001). A new, mechanistic model for organic carbon fluxes in the ocean based on the quantitative association of POC with ballast minerals. *Deep Sea Research Part II: Topical Studies in Oceanography*, 49(1–3):219–236.

Armstrong McKay, D. I., Tyrrell, T., Wilson, P. A., and Foster, G. L. (2014). Estimating the impact of the cryptic degassing of Large Igneous Provinces: A mid-Miocene case-study. *Earth and Planetary Science Letters*, 403:254–262.

Arndt, S., Brumsack, H.-J., and Wirtz, K. W. (2006). Cretaceous black shales as active bioreactors: A biogeochemical model for the deep biosphere encountered during ODP Leg 207 (Demerara Rise). *Geochimica et Cosmochimica Acta*, 70(2):408–425.

Arndt, S., Hetzel, A., and Brumsack, H.-J. (2009). Evolution of organic matter degradation in cretaceous black shales inferred from authigenic barite: A reaction-transport model. *Geochimica et Cosmochimica Acta*, 73(7):2000–2022.

Arndt, S., Jørgensen, B., LaRowe, D., Middelburg, J., Pancost, R., and Regnier, P. (2013). Quantifying the degradation of organic matter in marine sediments: A review and synthesis. *Earth-Science Reviews*, 123:53–86.

Arndt, S. and Regnier, P. (2007). A model for the benthic-pelagic coupling of silica in estuarine ecosystems: sensitivity analysis and system scale simulation. *Biogeosciences*, 4(3):331–352.

Arndt, S., Regnier, P., Goddéris, Y., and Donnadieu, Y. (2011). GEOCLIM reloaded (v 1.0): a new coupled earth system model for past climate change. *Geosci. Model Dev.*, 4(2):451–481.

Arrieta, J. M., Mayol, E., Hansman, R. L., Herndl, G. J., Dittmar, T., and Duarte, C. M. (2015). Dilution limits dissolved organic carbon utilization in the deep ocean. *Science*, 348(6232):331–333.

Arthur, M. and Sageman, B. (1994). Marine Black Shales: Depositional Mechanisms and Environments of Ancient Deposits. *Annual Review of Earth and Planetary Sciences*, 22(1):499–551.

Arthur, M. A., Dean, W., Pollastro, R., Scholle, P., and Claypool, G. (1985). Comparative geochemical and mineralogical studies of two cyclic transgressive pelagic limestone units, cretaceous western interior basin, u.s. *In: Pratt, L.M., et al. (Ed.), Fine-Grained Deposits and Biofacies of the Cretaceous Western Interior Seaway: Evidence of Cyclic Sedimentary Processes. Soc. For Sediment. Geol.*, pages 16–27.

Arthur, M. A., Dean, W. E., and Pratt, L. M. (1988). Geochemical and climatic effects of increased marine organic carbon burial at the cenomanian/turonian boundary. *Nature*, 335(6192):714–717.

Arthur, M. A., Schlanger, S. O., and Jenkyns, H. C. (1987). The cenomanian-turonian oceanic anoxic event, II. palaeoceanographic controls on organic-matter production and preservation. *Geological Society, London, Special Publications*, 26(1):401–420.

Aumont, O., Ethé, C., Tagliabue, A., Bopp, L., and Gehlen, M. (2015). PISCES-v2: an ocean biogeochemical model for carbon and ecosystem studies. *Geosci. Model Dev.*, 8(8):2465–2513. 00009.

Bacastow, R. B. and Maier-Reimer, E. (1990). Ocean-circulation model of the carbon cycle. *Clim. Dynam.*, 4(2):95–125.

Bains, S., Norris, R. D., Corfield, R. M., and Faul, K. L. (2000). Termination of global warmth at the Palaeocene/Eocene boundary through productivity feedback. *Nature*, 407(6801):171–174.

Barker, S., Higgins, J. A., and Elderfield, H. (2003). The future of the carbon cycle: review, calcification response, ballast and feedback on atmospheric CO2. *Philosophical Transactions of the Royal Society of London A: Mathematical, Physical and Engineering Sciences*, 361(1810):1977–1999.

Berelson, W. M. (2001). Particle settling rates increase with depth in the ocean. *Deep Sea Research Part II: Topical Studies in Oceanography*, 49(1-3):237–251.

Berger, W. H. (1967). Foraminiferal ooze: Solution at depths. *Science*, 156(3773):383–385.

Berner, R. (1977). Sedimentation and dissolution of pteropods in the ocean. *The fate of fossil fuel CO2 in the oceans. Plenum Press, New York, pp 243ą260*.

Berner, R. A. (1964a). An idealized model of dissolved sulfate distribution in recent sediments. *Geochimica et Cosmochimica Acta*, 28(9):1497–1503.

Berner, R. A. (1964b). An idealized model of dissolved sulfate distribution in recent sediments. *Geochimica et Cosmochimica Acta*, 28(9):1497–1503.

Berner, R. A. (1980a). *Early Diagenesis: A Theoretical Approach*. Princeton University Press.

Berner, R. A. (1980b). A rate model for organic matter decomposition during bacterial sulfate reduction in marine sediments. In *Biogéochimie de la matière organique à l'interface eau-sédiment marin*, volume 293 of *Colloques Internationaux du CNRS*, pages 35–44. Centre National de la Recherche Scientifique, Paris.

Berner, R. A. (1984). Sedimentary pyrite formation: An update. *Geochimica et Cosmochimica Acta*, 48(4):605–615.

Berner, R. A. (1990). Atmospheric carbon dioxide levels over phanerozoic time. *Science*, 249(4975):1382–1386.

Berner, R. A. (1991). A model for atmospheric CO_2 over Phanerozoic time. *Am. J. Sci.*, 291(4):339–376.

Berner, R. A. (2004). *The Phanerozoic Carbon Cycle: CO2 and O2*. Oxford University Press.

Berner, R. A. and Caldeira, K. (1997). The need for mass balance and feedback in the geochemical carbon cycle. *Geology*, 25(10):955–956.

Berner, R. A., Canfield, D. E., et al. (1989). A new model for atmospheric oxygen over phanerozoic time. *Am. J. Sci*, 289(4):333–361.

Berner, R. A. and Honjo, S. (1981). Pelagic Sedimentation of Aragonite: Its Geochemical Significance. *Science*, 211(4485):940–942.

Berner, R. A. and Morse, J. W. (1974). Dissolution kinetics of calcium carbonate in sea water; IV, theory of calcite dissolution. *American Journal of Science*, 274(2):108–134.

Berner, R. A., Ruttenberg, K. C., Ingall, E. D., and Rao, J.-L. (1993). The Nature of Phosphorus Burial in Modern Marine Sediments. In Wollast, R., Mackenzie, F. T., and Chou, L., editors, *Interactions of C, N, P and S Biogeochemical Cycles and Global Change*, number 4 in NATO ASI Series, pages 365–378. Springer Berlin Heidelberg.

Bernhardt, K. (2008). Finding Alternatives and Reduced Formulations for Process-Based Models. *Evolutionary Computation*, 16(1):63–88. 00008.

Beven, K. J., Aspinall, W. P., Bates, P. D., Borgomeo, E., Goda, K., Hall, J. W., Page, T., Phillips, J. C., Rougier, J. T., Simpson, M., Stephenson, D. B., Smith, P. J., Wagener, T., and Watson, M. (under review). Epistemic uncertainties and natural hazard risk assessment - Part 1: A review of the issues. *Nat. Hazards Earth Syst. Sci. Discuss.*, 2015:7333–7377.

Bice, K. L., Birgel, D., Meyers, P. A., Dahl, K. A., Hinrichs, K. U., and Norris, R. D. (2006). A multiple proxy and model study of cretaceous upper ocean temperatures and atmospheric CO2 concentrations. *Paleoceanography*, 21(2).

Biddanda, B. and Benner, R. (1997). Carbon, nitrogen, and carbohydrate fluxes during the production of particulate and dissolved organic matter by marine phytoplankton. *Limnology and Oceanography*, 42(3):506–518.

Billen, G. (1982). An idealized model of nitrogen recycling in marine sediments. *American journal of Science*, 282(4):512–541.

Bishop, J. (1989). Regional extremes in particulate matter composition and flux: effects on the chemistry of the ocean interior. *In: Productivity of the Ocean: Present and Past*, 44:117–137.

Bjerrum, C. J., Bendtsen, J., and Legarth, J. J. F. (2006). Modeling organic carbon burial during sea level rise with reference to the Cretaceous. *Geochemistry, Geophysics, Geosystems*, 7(5):Q05008. 00042.

Blättler, C. L., Jenkyns, H. C., Reynard, L. M., and Henderson, G. M. (2011). Significant increases in global weathering during Oceanic Anoxic Events 1a and 2 indicated by calcium isotopes. *Earth and Planetary Science Letters*, 309(1-2):77–88.

Bohlen, L., Dale, A. W., and Wallmann, K. (2012). Simple transfer functions for calculating benthic fixed nitrogen losses and C:N:P regeneration ratios in global biogeochemical models. *Global Biogeochemical Cycles*, 26(3):GB3029.

Boudreau, B. P. (1984). On the equivalence of nonlocal and radial-diffusion models for porewater irrigation. *Journal of Marine Research*, 42(3):731–735.

Boudreau, B. P. (1986). Mathematics of tracer mixing in sediments; I, Spatially-dependent, diffusive mixing. *American Journal of Science*, 286(3):161–198.

Boudreau, B. P. (1987). A steady-state diagenetic model for dissolved carbonate species and pH in the porewaters of oxic and suboxic sediments. *Geochimica et Cosmochimica Acta*, 51(7):1985–1996.

Boudreau, B. P. (1991). Modelling the sulfide-oxygen reaction and associated pH gradients in porewaters. *Geochimica et Cosmochimica Acta*, 55(1):145–159.

Boudreau, B. P. (1996). A method-of-lines code for carbon and nutrient diagenesis in aquatic sediments. *Computers & Geosciences*, 22(5):479–496.

Boudreau, B. P. (1997). *Diagenetic models and their implementation*, volume 505. Springer Berlin.

Boudreau, B. P. (1998). Mean mixed depth of sediments: The wherefore and the why. *Limnology and Oceanography*, 43(3):524–526.

Boudreau, B. P., Arnosti, C., Jørgensen, B. B., and Canfield, D. E. (2008). Comment on "Physical Model for the Decay and Preservation of Marine Organic Carbon". *Science*, 319(5870):1616–1616.

Boudreau, B. P., Mucci, A., Sundby, B., Luther, G. W., and Silverberg, N. (1998). Comparative diagenesis at three sites on the Canadian continental margin. *Journal of Marine Research*, 56(6):1259–1284.

Boudreau, B. P. and Ruddick, B. R. (1991). On a reactive continuum representation of organic matter diagenesis. *American Journal of Science*, 291(5):507–538. 00187.

Boudreau, B. P. and Westrich, J. T. (1984). The dependence of bacterial sulfate reduction on sulfate concentration in marine sediments. *Geochimica et Cosmochimica Acta*, 48(12):2503–2516.

Bouttes, N., Paillard, D., and Roche, D. (2010). Impact of brine-induced stratification on the glacial carbon cycle. *Climate of the Past*, 6(5):575–589.

Bouttes, N., Paillard, D., Roche, D., Waelbroeck, C., Kageyama, M., Lourantou, A., Michel, E., and Bopp, L. (2012a). Impact of oceanic processes on the carbon cycle during the last termination. *Climate of the Past*, 8(1):149–170.

Bouttes, N., Paillard, D., Roche, D. M., Brovkin, V., and Bopp, L. (2011). Last glacial maximum CO2 and δ13C successfully reconciled. *Geophysical Research Letters*, 38(2).

Bouttes, N., Roche, D. M., and Paillard, D. (2009). Impact of strong deep ocean stratification on the glacial carbon cycle. *Paleoceanography*, 24(3):PA3203.

Bouttes, N., Roche, D. M., and Paillard, D. (2012b). Systematic study of the impact of fresh water fluxes on the glacial carbon cycle. *Climate of the Past*, 8(2):589–607. 00007.

Bowen, G. J. and Zachos, J. C. (2010). Rapid carbon sequestration at the termination of the Palaeocene-Eocene Thermal Maximum. *Nature Geoscience*, 3(12):866–869.

Boyd, P. W. and Trull, T. W. (2007). Understanding the export of biogenic particles in oceanic waters: Is there consensus? *Progress in Oceanography*, 72(4):276–312.

Bradley, J. A., Anesio, A. M., and Arndt, S. (2016). Bridging the divide: a model-data approach to Polar and Alpine microbiology. *FEMS microbiology ecology*, 92(3).

Bralower, T. J., Meissner, K. J., Alexander, K., and Thomas, D. J. (2014). The dynamics of global change at the Paleocene-Eocene thermal maximum: A data-model comparison. *Geochemistry, Geophysics, Geosystems*, 15(10):3830–3848. 00005.

Bralower, T. J. and Thierstein, H. R. (1984). Low productivity and slow deep-water circulation in mid-Cretaceous oceans. *Geology*, 12(10):614–618.

Broecker, W. (2003). The oceanic caco3 cycle. *Treatise on Geochemistry*, 6:529–549.

Broecker, W. S. (1982). Ocean chemistry during glacial time. *Geochimica et Cosmochimica Acta*, 46(10):1689–1705.

Broecker, W. S. and Peng, T.-H. (1986). Carbon cycle : 1985. glacial to interglacial changes in the operation of the global carbon cycle. *Radiocarbon*, 28(2A):309–327.

Broecker, W. S. and Peng, T.-H. (1987). The role of $CaCO_3$ compensation in the glacial to interglacial atmosphere CO_2 change. *Global Biogeochem. Cycles*, 1(1):15–29.

Broecker, W. S. and Peng, T.-H. (1989). The cause of the glacial to interglacial atmospheric CO_2 change : A polar alkalinity hypothesis. *Global Biogeochem. Cycles*, 3(3):215–239.

Broecker, W. S., Peng, T.-H., Trumbore, S., Bonani, G., and Wolfli, W. (1990). The distribution of radiocarbon in the glacial ocean. *Global Biogeochem. Cycles*, 4(1):103–117.

Brovkin, V., Bendtsen, J., Claussen, M., Ganopolski, A., Kubatzki, C., Petoukhov, V., and Andreev, A. (2002a). Carbon cycle, vegetation, and climate dynamics in the holocene: Experiments with the CLIMBER-2 model. *Global Biogeochemical Cycles*, 16(4):1139.

Brovkin, V., Brücher, T., Kleinen, T., Zaehle, S., Joos, F., Roth, R., Spahni, R., Schmitt, J., Fischer, H., Leuenberger, M., Stone, E. J., Ridgwell, A., Chappellaz, J., Kehrwald, N., Barbante, C., Blunier, T., and Dahl Jensen, D. (2016). Comparative carbon cycle dynamics of the present and last interglacial. *Quaternary Science Reviews*, 137:15–32. 00000.

Brovkin, V., Ganopolski, A., Archer, D., and Munhoven, G. (2012). Glacial co 2 cycle as a succession of key physical and biogeochemical processes. *Climate of the Past*, 8(1):251–264.

Brovkin, V., Ganopolski, A., Archer, D., and Rahmstorf, S. (2007). Lowering of glacial atmospheric CO2 in response to changes in oceanic circulation and marine biogeochemistry. *Paleoceanography*, 22(4):PA4202.

Brovkin, V., Hofmann, M., Bendtsen, J., and Ganopolski, A. (2002b). Ocean biology could control atmospheric δ13c during glacial-interglacial cycle. *Geochemistry, Geophysics, Geosystems*, 3(5):1–15.

Brumsack, H.-J. (2006). The trace metal content of recent organic carbon-rich sediments: Implications for Cretaceous black shale formation. *Palaeogeography, Palaeoclimatology, Palaeoecology*, 232(2-4):344–361.

Buesseler, K. O. and Boyd, P. W. (2009). Shedding light on processes that control particle export and flux attenuation in the twilight zone of the open ocean. *Limnology and Oceanography*, 54(4):1210.

Burdige, D. J. (2006). *Geochemistry of marine sediments*, volume 398. Princeton University Press Princeton.

Burdige, D. J. (2007). Preservation of Organic Matter in Marine Sediments: Controls, Mechanisms, and an Imbalance in Sediment Organic Carbon Budgets? *Chemical Reviews*, 107(2):467–485.

Burwicz, E. B., Rüpke, L. H., and Wallmann, K. (2011). Estimation of the global amount of submarine gas hydrates formed via microbial methane formation based on numerical reaction-transport modeling and a novel parameterization of Holocene sedimentation. *Geochimica et Cosmochimica Acta*, 75(16):4562–4576.

Canfield, D. E. (1989a). Reactive iron in marine sediments. *Geochimica et Cosmochimica Acta*, 53(3):619–632.

Canfield, D. E. (1989b). Sulfate reduction and oxic respiration in marine sediments: implications for organic carbon preservation in euxinic environments. *Deep Sea Research Part A. Oceanographic Research Papers*, 36(1):121–138. 00374.

Canfield, D. E. (1994). Factors influencing organic carbon preservation in marine sediments. *Chemical Geology*, 114(3–4):315–329.

Canfield, D. E., Kristensen, E., and Thamdrup, B. (2005). *Aquatic Geomicrobiology*. Gulf Professional Publishing.

Canfield, D. E., Raiswell, R., and Bottrell, S. H. (1992). The reactivity of sedimentary iron minerals toward sulfide. *American Journal of Science*, 292(9):659–683.

Cao, L., Eby, M., Ridgwell, A., Caldeira, K., Archer, D., Ishida, A., Joos, F., Matsumoto, K., Mikolajewicz, U., Mouchet, A., Orr, J. C., Plattner, G.-K., Schlitzer, R., Tokos, K., Totterdell, I., Tschumi, T., Yamanaka, Y., and Yool, A. (2009). The role of ocean transport in the uptake of anthropogenic CO2. *Biogeosciences*, 6(3):375–390.

Cappellen, P. V. and Wang, Y. (1996). Cycling of iron and manganese in surface sediments; a general theory for the coupled transport and reaction of carbon, oxygen, nitrogen, sulfur, iron, and manganese. *American Journal of Science*, 296(3):197–243.

Chalikov, D. V. and Verbitsky, M. Y. (1984). A new earth climate model. *Nature*, 308(5960):609–612.

Ciais, P., Sabine, C., Bala, G., Bopp, L., Brovkin, V., Canadell, J., Chhabra, A., DeFries, R., Galloway, J., Heimann, M., et al. (2014). Carbon and other biogeochemical cycles. In *Climate change 2013: the physical science basis. Contribution of Working Group I to the Fifth Assessment Report of the Intergovernmental Panel on Climate Change*, pages 465–570. Cambridge University Press.

Claussen, M., Mysak, L., Weaver, A., Crucifix, M., Fichefet, T., Loutre, M.-F., Weber, S., Alcamo, J., Alexeev, V., Berger, A., Calov, R., Ganopolski, A., Goosse, H., Lohmann, G., Lunkeit, F., Mokhov, I., Petoukhov, V., Stone, P., and Wang, Z. (2002). Earth system models of intermediate complexity: closing the gap in the spectrum of climate system models. *Climate Dynamics*, 18(7):579–586.

Cohen, A. S., Coe, A. L., and Kemp, D. B. (2007). The Late Palaeocene-Early Eocene and Toarcian (Early Jurassic) carbon isotope excursions: a comparison of their time scales, associated environmental changes, causes and consequences. *Journal of the Geological Society*, 164(6):1093–1108.

Colbourn, G., Ridgwell, A., and Lenton, T. M. (2013). The Rock Geochemical Model (RokGeM) v0.9. *Geosci. Model Dev.*, 6(5):1543–1573.

Conkright, M. E., Locarnini, R. A., Garcia, H. E., O'Brien, T. D., Boyer, T. P., Stephens, C., and Antonov, J. I. (2002). *World Ocean Atlas 2001: Objective analyses, data statistics, and figures: CD-ROM documentation*. US Department of Commerce, National Oceanic and Atmospheric Administration, National Oceanographic Data Center, Ocean Climate Laboratory.

Cooley, S. R. and Yager, P. L. (2006). Physical and biological contributions to the western tropical North Atlantic Ocean carbon sink formed by the Amazon River plume. *Journal of Geophysical Research: Oceans*, 111(C8):C08018.

Cox, P. M., Betts, R. A., Jones, C. D., Spall, S. A., and Totterdell, I. J. (2000). Acceleration of global warming due to carbon-cycle feedbacks in a coupled climate model. *Nature*, 408(6809):184–187.

Crucifix, M. (2005). Distribution of carbon isotopes in the glacial ocean: A model study. *Paleoceanography*, 20(4):PA4020.

Cui, Y., Kump, L., and Ridgwell, A. (2015). Spatial and temporal patterns of ocean acidification during the end–permian mass extinction–an earth system model evaluation. *Volcanism and Global Environmental Change, Cambridge University Press, United Kingdom*, pages 291–306.

Cui, Y., Kump, L. R., and Ridgwell, A. (2013). Initial assessment of the carbon emission rate and climatic consequences during the end-permian mass extinction. *Palaeogeography, Palaeoclimatology, Palaeoecology*, 389:128–136.

Cui, Y., Kump, L. R., Ridgwell, A. J., Charles, A. J., Junium, C. K., Diefendorf, A. F., Freeman, K. H., Urban, N. M., and Harding, I. C. (2011). Slow release of fossil carbon during the palaeocene-eocene thermal maximum. *Nature Geoscience*, 4(7):481–485.

Dai, A., Qian, T., Trenberth, K. E., and Milliman, J. D. (2009). Changes in Continental Freshwater Discharge from 1948 to 2004. *Journal of Climate*, 22(10):2773–2792.

Dalan, F., Stone, P. H., Kamenkovich, I. V., and Scott, J. R. (2005). Sensitivity of the ocean's climate to diapycnal diffusivity in an EMIC. part i: Equilibrium state. *Journal of Climate*, 18(13):2460–2481.

Dale, A. W., Brüchert, V., Alperin, M., and Regnier, P. (2009). An integrated sulfur isotope model for Namibian shelf sediments. *Geochimica et Cosmochimica Acta*, 73(7):1924–1944.

Dauwe, B., Middelburg, J. J., Herman, P. M. J., and Heip, C. H. R. (1999). Linking diagenetic alteration of amino acids and bulk organic matter reactivity. *Limnology and Oceanography*, 44(7):1809–1814.

Davies, A. M. (1994). On the complementary nature of observational data, scientific understanding and model complexity: the need for a range of models. *Journal of Marine Systems*, 5(6):406–408.

de Graciansky, P. C., Deroo, G., Herbin, J. P., Montadert, L., Müller, C., Schaaf, A., and Sigal, J. (1984). Ocean-wide stagnation episode in the late cretaceous. *Nature*, 308(5957):346–349.

De La Rocha, C. L., Nowald, N., and Passow, U. (2008). Interactions between diatom aggregates, minerals, particulate organic carbon, and dissolved organic matter: Further implications for the ballast hypothesis. *Global Biogeochemical Cycles*, 22(4).

Demaison, G. and Moore, G. (1980). Anoxic environments and oil source bed genesis. *Organic Geochemistry*, 2(1):9–31.

Devol, A. H. and Christensen, J. P. (1993). Benthic fluxes and nitrogen cycling in sediments of the continental margin of the eastern North Pacific. *Journal of Marine Research*, 51(2):345–372.

D'Hondt, S., Inagaki, F., Zarikian, C. A., Abrams, L. J., Dubois, N., Engelhardt, T., Evans, H., Ferdelman, T., Gribsholt, B., Harris, R. N., Hoppie, B. W., Hyun, J.-H., Kallmeyer, J., Kim, J., Lynch, J. E., McKinley, C. C., Mitsunobu, S., Morono, Y., Murray, R. W., Pockalny, R., Sauvage, J., Shimono, T., Shiraishi, F., Smith, D. C., Smith-Duque, C. E., Spivack, A. J., Steinsbu, B. O., Suzuki, Y., Szpak, M., Toffin, L., Uramoto, G., Yamaguchi, Y. T., Zhang, G.-l., Zhang, X.-H., and Ziebis, W. (2015). Presence of oxygen and aerobic communities from sea floor to basement in deep-sea sediments. *Nature Geoscience*, 8(4):299–304.

Dickson, A. J., Jenkyns, H. C., Porcelli, D., van den Boorn, S., and Idiz, E. (2016). Basin-scale controls on the molybdenum-isotope composition of seawater during Oceanic Anoxic Event 2 (Late Cretaceous). *Geochimica et Cosmochimica Acta*, 178:291–306.

Donnadieu, Y., Godderis, Y., Pierrehumbert, R., Dromart, G., Fluteau, F., and Jacob, R. (2006a). A GEOCLIM simulation of climatic and biogeochemical consequences of pangea breakup. *Geochemistry Geophysics Geosystems*, 7:Q11019.

Donnadieu, Y., Pierrehumbert, R., Jacob, R., and Fluteau, F. (2006b). Modelling the primary control of paleogeography on Cretaceous climate. *Earth and Planetary Science Letters*, 248(1,Äì2):426–437.

Donnadieu, Y., Ramstein, G., Goddéris, Y., and Fluteau, F. (2004). Global Tectonic Setting and Climate of the Late Neoproterozoic: A Climate-Geochemical Coupled Study. In Jenkins, G. S., McMenamin, r. A. S., McKay, C. P., and Sohl, L., editors, *The Extreme Proterozoic: Geology, Geochemistry, and Climate*, pages 79–89. American Geophysical Union.

Du Vivier, A. D. C., Selby, D., Sageman, B. B., Jarvis, I., Gröcke, D. R., and Voigt, S. (2014). Marine 187os/188os isotope stratigraphy reveals the interaction of volcanism and ocean circulation during Oceanic Anoxic Event 2. *Earth and Planetary Science Letters*, 389:23–33.

Ducklow, H. W., Quinby, H. L., and Carlson, C. A. (1995). Bacterioplankton dynamics in the equatorial Pacific during the 1992 El Nino. *Deep Sea Research Part II: Topical Studies in Oceanography*, 42(2-3):621–638.

Dunne, J. P., Sarmiento, J. L., and Gnanadesikan, A. (2007). A synthesis of global particle export from the surface ocean and cycling through the ocean interior and on the seafloor. *Global Biogeochemical Cycles*, 21(4).

Duplessy, J. C., Roche, D. M., and Kageyama, M. (2007). The deep ocean during the last interglacial period. *Science*, 316(5821):89–91.

Eby, M., Weaver, A. J., Alexander, K., Zickfeld, K., Abe-Ouchi, A., Cimatoribus, A. A., Crespin, E., Drijfhout, S. S., Edwards, N. R., Eliseev, A. V., Feulner, G., Fichefet, T., Forest, C. E., Goosse, H., Holden, P. B., Joos, F., Kawamiya, M., Kicklighter, D., Kienert, H., Matsumoto, K., Mokhov, I. I., Monier, E., Olsen, S. M., Pedersen, J. O. P., Perrette, M., Philippon-Berthier, G., Ridgwell, A., Schlosser, A., Schneider von Deimling, T., Shaffer, G., Smith, R. S., Spahni, R., Sokolov, A. P., Steinacher, M., Tachiiri, K., Tokos, K., Yoshimori, M., Zeng, N., and Zhao, F. (2013). Historical and idealized climate model experiments: an intercomparison of earth system models of intermediate complexity. *Clim. Past*, 9(3):1111–1140.

Eby, M., Zickfeld, K., Montenegro, A., Archer, D., Meissner, K. J., and Weaver, A. J. (2009). Lifetime of anthropogenic climate change: Millennial time scales of potential CO2 and surface temperature perturbations. *Journal of Climate*, 22(10):2501–2511.

Edwards, N. R. and Marsh, R. (2005). Uncertainties due to transport-parameter sensitivity in an efficient 3-d ocean-climate model. *Climate Dynamics*, 24(4):415–433.

Emerson, S. (1985). Organic carbon preservation in marine sediments. *The Carbon Cycle and Atmospheric CO: Natural Variations Archean to Present*, pages 78–87.

Emerson, S. and Bender, M. L. (1981). Carbon fluxes at the sediment-water interface of the deep-sea: calcium carbonate preservation. *Journal of Marine Research*, 39:139–162.

Emerson, S. and Hedges, J. I. (1988). Processes controlling the organic carbon content of open ocean sediments. *Paleoceanography*, 3(5):621–634.

Emerson, S., Jahnke, R., and Heggie, D. (1984). Sediment-water exchange in shallow water estuarine sediments. *Journal of Marine Research*, 42(3):709–730.

Epping, E., van der Zee, C., Soetaert, K., and Helder, W. (2002). On the oxidation and burial of organic carbon in sediments of the Iberian margin and Nazaré Canyon (NE Atlantic). *Progress in Oceanography*, 52(2-4):399–431.

Eppley, R. W. and Peterson, B. J. (1979). Particulate organic matter flux and planktonic new production in the deep ocean. *Nature*, 282:677–680.

Erbacher, J., Huber, B. T., Norris, R. D., and Markey, M. (2001). Increased thermohaline stratification as a possible cause for an ocean anoxic event in the Cretaceous period. *Nature*, 409(6818):325–327.

Ewen, T. L., Weaver, A. J., and Schmittner, A. (2004). Modelling carbon cycle feedbacks during abrupt climate change. *Quaternary Science Reviews*, 23(3-4):431–448.

Fabry, V. J. (1989). Aragonite production by pteropod molluscs in the subarctic pacific. *Deep Sea Research Part A. Oceanographic Research Papers*, 36(11):1735–1751.

Falkowski, P., Scholes, R. J., Boyle, E., Canadell, J., Canfield, D., Elser, J., Gruber, N., Hibbard, K., Högberg, P., Linder, S., Mackenzie, F. T., Iii, B. M., Pedersen, T., Rosenthal, Y., Seitzinger, S., Smetacek, V., and Steffen, W. (2000). The global carbon cycle: A test of our knowledge of earth as a system. *Science*, 290(5490):291–296.

Falkowski, P. G., Barber, R. T., and Smetacek, V. (1998). Biogeochemical controls and feedbacks on ocean primary production. *Science*, 281(5374):200–206.

Feely, R. A., Sabine, C. L., Lee, K., Berelson, W., Kleypas, J., Fabry, V. J., and Millero, F. J. (2004). Impact of anthropogenic CO2 on the CaCO3 system in the oceans. *Science*, 305(5682):362–366.

Fiadeiro, M. (1980). The alkalinity of the deep pacific. *Earth and Planetary Science Letters*, 49(2):499–505.

Fischer, J. P., Ferdelman, T. G., D'Hondt, S., Røy, H., and Wenzhöfer, F. (2009). Oxygen penetration deep into the sediment of the South Pacific gyre. *Biogeosciences*, 6(8):1467–1478.

Flögel, S., Wallmann, K., Poulsen, C. J., Zhou, J., Oschlies, A., Voigt, S., and Kuhnt, W. (2011). Simulating the biogeochemical effects of volcanic CO2 degassing on the oxygen-state of the deep ocean during the Cenomanian/Turonian Anoxic Event (OAE2). *Earth and Planetary Science Letters*, 305(3,Äì4):371–384.

Forster, A., Schouten, S., Moriya, K., Wilson, P. A., and Damsté, J. S. S. (2007). Tropical warming and intermittent cooling during the Cenomanian/Turonian oceanic anoxic event 2: Sea surface temperature records from the equatorial atlantic. *Paleoceanography*, 22(1).

Fraile, I., Schulz, M., Mulitza, S., Merkel, U., Prange, M., and Paul, A. (2009). Modeling the seasonal distribution of planktonic foraminifera during the Last Glacial Maximum. *Paleoceanography*, 24(2):PA2216.

Francois, R., Honjo, S., Krishfield, R., and Manganini, S. (2002). Factors controlling the flux of organic carbon to the bathypelagic zone of the ocean. *Global Biogeochemical Cycles*, 16(4):34–1–34–20.

Francois, R., Honjo, S., Manganini, S. J., and Ravizza, G. E. (1995). Biogenic barium fluxes to the deep sea: Implications for paleoproductivity reconstruction. *Global Biogeochemical Cycles*, 9(2):289–303.

Friedlingstein, P., Cox, P., Betts, R., Bopp, L., von Bloh, W., Brovkin, V., Cadule, P., Doney, S., Eby, M., Fung, I., Bala, G., John, J., Jones, C., Joos, F., Kato, T., Kawamiya, M., Knorr, W., Lindsay, K., Matthews, H. D., and Raddatz, T. (2006). Climate-carbon cycle feedback analysis: Results from the c4mip model intercomparison. *Journal of Climate*, 19(14):3337–3353.

Friedlingstein, P., Dufresne, J.-L., Cox, P. M., and Rayner, P. (2003). How positive is the feedback between climate change and the carbon cycle? *Tellus B*, 55(2):692–700.

Galbraith, E. D., Kwon, E. Y., Bianchi, D., Hain, M. P., and Sarmiento, J. L. (2015). The impact of atmospheric pco2 on carbon isotope ratios of the atmosphere and ocean. *Global Biogeochem. Cycles*, 29(3):307–324.

Gangstø, R., Joos, F., and Gehlen, M. (2011). Sensitivity of pelagic calcification to ocean acidification. *Biogeosciences*, 8(2):433–458.

Gillooly, J. F., Brown, J. H., West, G. B., Savage, V. M., and Charnov, E. L. (2001). Effects of Size and Temperature on Metabolic Rate. *Science*, 293(5538):2248–2251.

Glud, R. N. (2008). Oxygen dynamics of marine sediments. *Marine Biology Research*, 4(4):243–289.

Goddéris, Y., Donnadieu, Y., de Vargas, C., Pierrehumbert, R. T., Dromart, G., and van de Schootbrugge, B. (2008). Causal or casual link between the rise of nannoplankton calcification and a tectonically-driven massive decrease in late triassic atmospheric CO2? *Earth and Planetary Science Letters*, 267(1–2):247–255.

Goddéris, Y. and Joachimski, M. (2004). Global change in the Late Devonian: modelling the Frasnian-Famennian short-term carbon isotope excursions. *Palaeogeography, Palaeoclimatology, Palaeoecology*, 202(3-4):309–329.

Goes, J. I., Gomes, H. d. R., Chekalyuk, A. M., Carpenter, E. J., Montoya, J. P., Coles, V. J., Yager, P. L., Berelson, W. M., Capone, D. G., Foster, R. A., Steinberg, D. K., Subramaniam, A., and Hafez, M. A. (2014). Influence of the Amazon River discharge on the biogeography of phytoplankton communities in the western tropical north Atlantic. *Progress in Oceanography*, 120:29–40.

Goldberg, T., Poulton, S. W., Wagner, T., Kolonic, S. F., and Rehkämper, M. (2016). Molybdenum drawdown during Cretaceous Oceanic Anoxic Event 2. *Earth and Planetary Science Letters*, 440:81–91.

Goloway, F. and Bender, M. (1982). Diagenetic models of interstitial nitrate profiles in deep sea suboxic sediments1. *Limnology and Oceanography*, 27(4):624–638.

Goodwin, P., Williams, R. G., Ridgwell, A., and Follows, M. J. (2009). Climate sensitivity to the carbon cycle modulated by past and future changes in ocean chemistry. *Nature Geoscience*, 2(2):145–150.

Goosse, H., Brovkin, V., Fichefet, T., Haarsma, R., Huybrechts, P., Jongma, J., Mouchet, A., Selten, F., Barriat, P.-Y., Campin, J.-M., Deleersnijder, E., Driesschaert, E., Goelzer, H., Janssens, I., Loutre, M.-F., Morales Maqueda, M. A., Opsteegh, T., Mathieu, P.-P., Munhoven, G., Pettersson, E. J., Renssen, H., Roche, D. M., Schaeffer, M., Tartinville, B., Timmermann, A., and Weber, S. L. (2010). Description of the earth system model of intermediate complexity LOVECLIM version 1.2. *Geosci. Model Dev.*, 3(2):603–633.

Gupta, N. S., Briggs, D. E. G., Collinson, M. E., Evershed, R. P., Michels, R., Jack, K. S., and Pancost, R. D. (2007). Evidence for the in situ polymerisation of labile aliphatic organic compounds during the preservation of fossil leaves: Implications for organic matter preservation. *Organic Geochemistry*, 38(3):499–522.

Gypens, N., Lancelot, C., and Soetaert, K. (2008). Simple parameterisations for describing n and p diagenetic processes: Application in the north sea. *Progress in Oceanography*, 76(1):89–110.

Hain, M. P., Sigman, D. M., and Haug, G. H. (2010). Carbon dioxide effects of Antarctic stratification, North Atlantic Intermediate Water formation, and subantarctic nutrient drawdown during the last ice age: Diagnosis and synthesis in a geochemical box model. *Global Biogeochemical Cycles*, 24(4):GB4023.

Hain, M. P., Sigman, D. M., and Haug, G. H. (2014). The Biological Pump in the Past. In *Treatise on Geochemistry (Second Edition)*, pages 485–517. Elsevier, Oxford.

Hales, B. (2003). Respiration, dissolution, and the lysocline. *Paleoceanography*, 18(4):1099.

Hales, B. and Emerson, S. (1997). Evidence in support of first-order dissolution kinetics of calcite in seawater. *Earth and Planetary Science Letters*, 148(1-2):317–327.

Handoh, I. C. and Lenton, T. M. (2003). Periodic mid-Cretaceous oceanic anoxic events linked by oscillations of the phosphorus and oxygen biogeochemical cycles. *Global Biogeochemical Cycles*, 17(4).

Hansell, D., Carlson, C., Repeta, D., and Schlitzer, R. (2009). Dissolved organic matter in the ocean: A controversy stimulates new insights. *Oceanography*, 22(4):202–211.

Hansell, D. A. (2013). Recalcitrant dissolved organic carbon fractions. *Annual Review of Marine Science*, 5(1):421–445.

Hansell, D. A. and Carlson, C. A. (2014). *Biogeochemistry of Marine Dissolved Organic Matter*. Academic Press.

Hansell, D. A., Carlson, C. A., and Schlitzer, R. (2012). Net removal of major marine dissolved organic carbon fractions in the subsurface ocean. *Global Biogeochemical Cycles*, 26(1):GB1016.

Hartnett, H. E., Keil, R. G., Hedges, J. I., and Devol, A. H. (1998). Influence of oxygen exposure time on organic carbon preservation in continental margin sediments. *Nature*, 391(6667):572–575.

Hebting, Y., Schaeffer, P., Behrens, A., Adam, P., Schmitt, G., Schneckenburger, P., Bernasconi, S. M., and Albrecht, P. (2006). Biomarker evidence for a major preservation pathway of sedimentary organic carbon. *Science*, 312(5780):1627–1631.

Hedges, J. I., Baldock, J. A., Gélinas, Y., Lee, C., Peterson, M., and Wakeham, S. G. (2001). Evidence for non-selective preservation of organic matter in sinking marine particles. *Nature*, 409(6822):801–804.

Hedges, J. I. and Keil, R. G. (1995). Sedimentary organic matter preservation: an assessment and speculative synthesis. *Marine Chemistry*, 49(2-3):81–115.

Heinze, C., Maier-Reimer, E., Winguth, A. M. E., and Archer, D. (1999). A global oceanic sediment model for long-term climate studies. *Global Biogeochemical Cycles*, 13(1):221–250.

Heinze, M. and Ilyina, T. (2015). Ocean biogeochemistry in the warm climate of the late Paleocene. *Climate of the Past*, 11:63–79.

Henrichs, S. M. and Reeburgh, W. S. (1987). Anaerobic mineralization of marine sediment organic matter: Rates and the role of anaerobic processes in the oceanic carbon economy. *Geomicrobiology Journal*, 5(3–4):191–237.

Hensen, C., Zabel, M., and Schulz, H. N. (2006). Benthic Cycling of Oxygen, Nitrogen and Phosphorus. In Schulz, H. D. and Zabel, M., editors, *Marine Geochemistry*, pages 207–240. Springer Berlin Heidelberg.

Henson, S. A., Sanders, R., and Madsen, E. (2012). Global patterns in efficiency of particulate organic carbon export and transfer to the deep ocean. *Global Biogeochemical Cycles*, 26(1).

Henson, S. A., Sanders, R., Madsen, E., Morris, P. J., Le Moigne, F., and Quartly, G. D. (2011). A reduced estimate of the strength of the ocean's biological carbon pump. *Geophysical Research Letters*, 38(4):L04606. 00050.

Holden, P., Edwards, N., Müller, S., Oliver, K., Death, R., and Ridgwell, A. (2013). Controls on the spatial distribution of oceanic δ13cdic. *Biogeosciences*, 10(3):1815–1833.

Honjo, S., Manganini, S. J., Krishfield, R. A., and Francois, R. (2008). Particulate organic carbon fluxes to the ocean interior and factors controlling the biological pump: A synthesis of global sediment trap programs since 1983. *Progress in Oceanography*, 76(3):217–285.

Hülse, D., Arndt, S., Wilson, J. D., Munhoven, G., and Ridgwell, A. (2017). Understanding the causes and consequences of past marine carbon cycling variability through models. *Earth-Science Reviews*, 171:349–382.

Hunter, S. J., Valdes, P. J., Haywood, A. M., and Markwick, P. J. (2008). Modelling Maastrichtian climate: investigating the role of geography, atmospheric CO2 and vegetation. *Clim. Past Discuss.*, 2008:981–1019.

Ibach, L. E. J. (1982). Relationship between sedimentation rate and total organic carbon content in ancient marine sediments. *AAPG Bulletin*, 66(2):170–188.

Iglesias-Rodriguez, M. D., Armstrong, R., Feely, R., Hood, R., Kleypas, J., Milliman, J. D., Sabine, C., and Sarmiento, J. (2002). Progress made in study of ocean's calcium carbonate budget. *Eos, Transactions American Geophysical Union*, 83(34):365–375.

Ilyina, T., Six, K. D., Segschneider, J., Maier-Reimer, E., Li, H., and Nunez-Riboni, I. (2013). Global ocean biogeochemistry model HAMOCC: Model architecture and performance as component of the MPI-Earth system model in different CMIP5 experimental realizations. *Journal of Advances in Modeling Earth Systems*, 5(2):287–315.

Ingall, E. and Jahnke, R. (1994). Evidence for enhanced phosphorus regeneration from marine sediments overlain by oxygen depleted waters. *Geochimica et Cosmochimica Acta*, 58(11):2571–2575. 00302.

Ingall, E. D., Bustin, R. M., and Van Cappellen, P. (1993). Influence of water column anoxia on the burial and preservation of carbon and phosphorus in marine shales. *Geochimica et Cosmochimica Acta*, 57(2):303–316.

Jannasch, H. W. (1994). The microbial turnover of carbon in the deep-sea environment. *Global and Planetary Change*, 9(3-4):289–295.

Jansen, H., Zeebe, R. E., and Wolf-Gladrow, D. A. (2002). Modeling the dissolution of settling CaCO3 in the ocean. *Global Biogeochemical Cycles*, 16(2):11–1.

Jarvis, I., Lignum, J. S., Gröcke, D. R., Jenkyns, H. C., and Pearce, M. A. (2011). Black shale deposition, atmospheric CO2 drawdown, and cooling during the Cenomanian-Turonian Oceanic Anoxic Event. *Paleoceanography*, 26(3):n/a–n/a.

Jenkyns, H. C. (1980). Cretaceous anoxic events: from continents to oceans. *Journal of the Geological Society*, 137(2):171–188.

Jenkyns, H. C. (2010). Geochemistry of oceanic anoxic events. *Geochemistry, Geophysics, Geosystems*, 11(3).

Jiao, N., Herndl, G. J., Hansell, D. A., Benner, R., Kattner, G., Wilhelm, S. W., Kirchman, D. L., Weinbauer, M. G., Luo, T., Chen, F., and Azam, F. (2010). Microbial production of recalcitrant dissolved organic matter: long-term carbon storage in the global ocean. *Nature Reviews Microbiology*, 8(8):593–599.

John, E. H., Wilson, J. D., Pearson, P. N., and Ridgwell, A. (2014). Temperature-dependent remineralization and carbon cycling in the warm eocene oceans. *Palaeogeography, Palaeoclimatology, Palaeoecology*, 413:158–166.

Jones, C. E. and Jenkyns, H. C. (2001). Seawater Strontium Isotopes, Oceanic Anoxic Events, and Seafloor Hydrothermal Activity in the Jurassic and Cretaceous. *American Journal of Science*, 301(2):112–149.

Jones, N. S., Ridgwell, A., and Hendy, E. J. (2015). Evaluation of coral reef carbonate production models at a global scale. *Biogeosciences*, 12(5):1339–1356. 00005.

Jørgensen, B. B. (1978). A comparison of methods for the quantification of bacterial sulfate reduction in coastal marine sediments: II Calculation from mathematical models. *Geomicrobiology Journal*, 1:29–47.

Jørgensen, B. B. and Kasten, S. (2006). Sulfur Cycling and Methane Oxidation. In Schulz, P. D. H. D. and Zabel, D. M., editors, *Marine Geochemistry*, pages 271–309. Springer Berlin Heidelberg.

Jourabchi, P., Cappellen, P. V., and Regnier, P. (2005). Quantitative interpretation of pH distributions in aquatic sediments: A reaction-transport modeling approach. *American Journal of Science*, 305(9):919–956.

Kageyama, M., Braconnot, P., Harrison, S. P., Haywood, A. M., Jungclaus, J., Otto-Bliesner, B. L., Peterschmitt, J.-Y., Abe-Ouchi, A., Albani, S., Bartlein, P. J., Brierley, C., Crucifix, M., Dolan, A., Fernandez-Donado, L., Fischer, H., Hopcroft, P. O., Ivanovic, R. F., Lambert, F., Lunt, D. J., Mahowald, N. M., Peltier, W. R., Phipps, S. J., Roche, D. M., Schmidt, G. A., Tarasov, L., Valdes, P. J., Zhang, Q., and Zhou, T. (2016). PMIP4-CMIP6: The contribution of the Paleoclimate Modelling Intercomparison Project to CMIP6. *Geosci. Model Dev. Discuss.*, 2016:1–46.

Kay, J. E., Holland, M. M., and Jahn, A. (2011). Inter-annual to multi-decadal Arctic sea ice extent trends in a warming world. *Geophysical Research Letters*, 38(15):L15708.

Keil, R. and Hedges, J. (1993). Sorption of organic matter to mineral surfaces and the preservation of organic matter in coastal marine sediments. *Chemical Geology*, 107(3):385–388.

Keir, R. S. (1980). The dissolution kinetics of biogenic calcium carbonates in seawater. *Geochimica et Cosmochimica Acta*, 44(2):241–252.

Keir, R. S. (1988). On the Late Pleistocene ocean geochemistry and circulation. *Paleoceanography*, 3(4):413–445.

Keir, R. S. (1990). Reconstructing the ocean carbon system variation during the last 150,000 years according to the Antarctic nutrient hypothesis. *Paleoceanography*, 5(3):253–276.

Keir, R. S. (1991). The effect of vertical nutrient redistribution on surface ocean δ^{13}C. *Global Biogeochemical Cycles*, 5(4):351–358.

Keller, D. P., Oschlies, A., and Eby, M. (2012). A new marine ecosystem model for the University of Victoria Earth System Climate Model. *Geosci. Model Dev.*, 5(5):1195–1220. 00018.

Kelly, D. C., Zachos, J. C., Bralower, T. J., and Schellenberg, S. A. (2005). Enhanced terrestrial weathering/runoff and surface ocean carbonate production during the recovery stages of the Paleocene-Eocene thermal maximum. *Paleoceanography*, 20(4):PA4023.

Kennedy, M. J., Pevear, D. R., and Hill, R. J. (2002). Mineral Surface Control of Organic Carbon in Black Shale. *Science*, 295(5555):657–660.

Kirchman, D. L., Lancelot, C., Fasham, M., Legendre, L., Radach, G., and Scott, M. (1993). Dissolved Organic Matter in Biogeochemical Models of the Ocean. In Evans, G. T. and Fasham, M. J. R., editors, *Towards a Model of Ocean Biogeochemical Processes*, number 10 in NATO ASI Series. Springer Berlin Heidelberg.

Kirtland Turner, S. and Ridgwell, A. (2013). Recovering the true size of an eocene hyperthermal from the marine sedimentary record. *Paleoceanography*, 28(4):700–712.

Kirtland Turner, S. and Ridgwell, A. (2016). Development of a novel empirical framework for interpreting geological carbon isotope excursions, with implications for the rate of carbon injection across the PETM. *Earth and Planetary Science Letters*, 435:1–13.

Klaas, C. and Archer, D. E. (2002). Association of sinking organic matter with various types of mineral ballast in the deep sea: Implications for the rain ratio. *Global Biogeochemical Cycles*, 16(4):63–1—63–14.

Kleinen, T., Brovkin, V., and Munhoven, G. (2015). Carbon cycle dynamics during recent interglacials. *Climate of the Past Discussions*, 11(3):1945–1983.

Kleypas, J. A. and Langdon, C. (2006). Coral reefs and changing seawater carbonate chemistry. *Coastal and Estuarine Studies: Coral Reefs and Climate Change Science and Management*, 61:73–110.

Kohfeld, K. E., Quéré, C. L., Harrison, S. P., and Anderson, R. F. (2005). Role of Marine Biology in Glacial-Interglacial CO2 Cycles. *Science*, 308(5718):74–78.

Köhler, P. and Bintanja, R. (2008). The carbon cycle during the mid pleistocene transition: the southern ocean decoupling hypothesis. *Climate of the Past*, 4(4):311–332.

Köhler, P. and Fischer, H. (2006). Simulating low frequency changes in atmospheric CO2 during the last 740 000 years. *Climate of the Past*, 2(2):57–78.

Köhler, P., Fischer, H., Munhoven, G., and Zeebe, R. E. (2005). Quantitative interpretation of atmospheric carbon records over the last glacial termination. *Global Biogeochemical Cycles*, 19(4).

Köhler, P., Fischer, H., and Schmitt, J. (2010). Atmospheric δ13co2 and its relation to pCO2 and deep ocean δ13c during the late Pleistocene. *Paleoceanography*, 25(1):PA1213.

Köhler, P., Muscheler, R., and Fischer, H. (2006). A model-based interpretation of low-frequency changes in the carbon cycle during the last 120,000 years and its implications for the reconstruction of atmospheric delta c-14. *Geochemistry Geophysics Geosystems*, 7:Q11N06.

Kok, M. D., Rijpstra, W. I. C., Robertson, L., Volkman, J. K., and Sinninghe Damsté, J. S. (2000). Early steroid sulfurisation in surface sediments of a permanently stratified lake (Ace Lake, Antarctica). *Geochimica et Cosmochimica Acta*, 64(8):1425–1436.

Kolmogorov, A. (1933). Sulla determinazione empirica di una leggi di distribuzione. *Giorn. 1st Ital. Attuari, 4*, 91.

Komar, N. and Zeebe, R. E. (2011). Oceanic calcium changes from enhanced weathering during the Paleocene-Eocene thermal maximum: No effect on calcium-based proxies. *Paleoceanography*, 26(3):PA3211.

Komar, N., Zeebe, R. E., and Dickens, G. R. (2013). Understanding long-term carbon cycle trends: The late Paleocene through the early Eocene. *Paleoceanography*, 28(4):650–662.

Kraal, P., Slomp, C. P., Forster, A., and Kuypers, M. M. M. (2010). Phosphorus cycling from the margin to abyssal depths in the proto-Atlantic during oceanic anoxic event 2. *Palaeogeography, Palaeoclimatology, Palaeoecology*, 295(1-2):42–54.

Kriest, I., Khatiwala, S., and Oschlies, A. (2010). Towards an assessment of simple global marine biogeochemical models of different complexity. *Progress in Oceanography*, 86(3-4):337–360.

Kriest, I. and Oschlies, A. (2013). Swept under the carpet: organic matter burial decreases global ocean biogeochemical model sensitivity to remineralization length scale. *Biogeosciences*, 10(12):8401–8422.

Kriest, I., Oschlies, A., and Khatiwala, S. (2012). Sensitivity analysis of simple global marine biogeochemical models. *Global Biogeochemical Cycles*, 26(2):GB2029.

Kristensen, E. and Holmer, M. (2001). Decomposition of plant materials in marine sediment exposed to different electron acceptors (O2, NO3-, and SO42-), with emphasis on substrate origin, degradation kinetics, and the role of bioturbation. *Geochimica et Cosmochimica Acta*, 65(3):419–433.

Krom, M. D. and Berner, R. A. (1980). Adsorption of phosphate in anoxic marine sediments1. *Limnology and Oceanography*, 25(5):797–806.

Krumholz, L. R., Harris, S. H., and Suflita, J. M. (2002). Anaerobic Microbial Growth from Components of Cretaceous Shales. *Geomicrobiology Journal*, 19(6):593–602.

Krumins, V., Gehlen, M., Arndt, S., Van Cappellen, P., and Regnier, P. (2013). Dissolved inorganic carbon and alkalinity fluxes from coastal marine sediments: Model estimates for different shelf environments and sensitivity to global change. *Biogeosciences*.

Kujawinski, E. B. (2011). The Impact of Microbial Metabolism on Marine Dissolved Organic Matter. *Annual Review of Marine Science*, 3(1):567–599.

Kump, L. R., Brantley, S. L., and Arthur, M. A. (2000). Chemical weathering, atmospheric CO2, and climate. *Annual Review of Earth and Planetary Sciences*, 28(1):611–667.

Kuypers, M. M. M., Pancost, R. D., and Damsté, J. S. S. (1999). A large and abrupt fall in atmospheric CO2 concentration during Cretaceous times. *Nature*, 399(6734):342–345. 00243.

Kuypers, M. M. M., Pancost, R. D., Nijenhuis, I. A., and Sinninghe Damsté, J. S. (2002). Enhanced productivity led to increased organic carbon burial in the euxinic North Atlantic basin during the late Cenomanian oceanic anoxic event. *Paleoceanography*, 17(4):1051.

Kwon, E. Y., Primeau, F., and Sarmiento, J. L. (2009). The impact of remineralization depth on the air-sea carbon balance. *Nature Geoscience*, 2(9):630–635.

Lam, P. J., Doney, S. C., and Bishop, J. K. B. (2011). The dynamic ocean biological pump: Insights from a global compilation of particulate organic carbon, CaCO3, and opal concentration profiles from the mesopelagic. *Global Biogeochemical Cycles*, 25(3).

Lambert, F., Tagliabue, A., Shaffer, G., Lamy, F., Winckler, G., Farias, L., Gallardo, L., and De Pol-Holz, R. (2015). Dust fluxes and iron fertilization in Holocene and Last Glacial Maximum climates. *Geophysical Research Letters*, 42(14):2015GL064250.

LaRowe, D. E. and Van Cappellen, P. (2011). Degradation of natural organic matter: A thermodynamic analysis. *Geochimica et Cosmochimica Acta*, 75(8):2030–2042.

Lasaga, A. C. (1981). Rate laws of chemical reactions. *In: Lasaga, A., Kirkpatrick, R.J. (Eds.), Reviews in Mineralogy; (United States)*, 8:1–68.

Laws, E. A., Falkowski, P. G., Smith, W. O., Ducklow, H., and McCarthy, J. J. (2000). Temperature effects on export production in the open ocean. *Global Biogeochemical Cycles*, 14(4):1231–1246.

Le Hir, G., Goddéris, Y., Donnadieu, Y., and Ramstein, G. (2008). A geochemical modelling study of the evolution of the chemical composition of seawater linked to a "snowball" glaciation. *Biogeosciences*, 5(1):253–267.

Le Moigne, F. A. C., Pabortsava, K., Marcinko, C. L. J., Martin, P., and Sanders, R. J. (2014). Where is mineral ballast important for surface export of particulate organic carbon in the ocean? *Geophysical Research Letters*, 41(23):2014GL061678.

Le Moigne, F. A. C., Sanders, R. J., Villa-Alfageme, M., Martin, A. P., Pabortsava, K., Planquette, H., Morris, P. J., and Thomalla, S. J. (2012). On the proportion of ballast versus non-ballast associated carbon export in the surface ocean. *Geophysical Research Letters*, 39(15):L15610.

Lee, C. (1992). Controls on organic carbon preservation: The use of stratified water bodies to compare intrinsic rates of decomposition in oxic and anoxic systems. *Geochimica et Cosmochimica Acta*, 56(8):3323–3335.

Lee, C., Wakeham, S. G., and I. Hedges, J. (2000). Composition and flux of particulate amino acids and chloropigments in equatorial pacific seawater and sediments. *Deep Sea Research Part I: Oceanographic Research Papers*, 47(8):1535–1568.

Lenton, T. M. and Watson, A. J. (2000). Redfield revisited: 1. Regulation of nitrate, phosphate, and oxygen in the ocean. *Global Biogeochemical Cycles*, 14(1):225–248.

Li, Y.-H. and Gregory, S. (1974). Diffusion of ions in sea water and in deep-sea sediments. *Geochimica et Cosmochimica Acta*, 38(5):703–714.

Locarnini, R., Mishonov, A., Antonov, J., Boyer, T., Garcia, H., Baranova, O., Zweng, M., Paver, C., Reagan, J., Johnson, D., et al. (2013). World ocean atlas 2013. vol. 1: Temperature. *A. Mishonov, Technical Ed. NOAA Atlas NESDIS*, 73:40.

Logan, B. E. and Hunt, J. R. (1987). Advantages to microbes of growth in permeable aggregates in marine systems. *Limnol. Oceanogr*, 32(5):1034–1048.

Longhurst, A., Sathyendranath, S., Platt, T., and Caverhill, C. (1995). An estimate of global primary production in the ocean from satellite radiometer data. *Journal of Plankton Research*, 17(6):1245–1271.

López-Urrutia, A., Martin, E. S., Harris, R. P., and Irigoien, X. (2006). Scaling the metabolic balance of the oceans. *Proceedings of the National Academy of Sciences*, 103(23):8739–8744.

Lunt, D. J., Huber, M., Anagnostou, E., Baatsen, M. L. J., Caballero, R., DeConto, R., Dijkstra, H. A., Donnadieu, Y., Evans, D., Feng, R., Foster, G. L., Gasson, E., von der Heydt, A. S., Hollis, C. J., Inglis, G. N., Jones, S. M., Kiehl, J., Kirtland Turner, S., Korty, R. L., Kozdon, R., Krishnan, S., Ladant, J.-B., Langebroek, P., Lear, C. H., LeGrande, A. N., Littler, K., Markwick, P., Otto-Bliesner, B., Pearson, P., Poulsen, C. J., Salzmann, U., Shields, C., Snell, K., Stärz, M., Super, J., Tabor, C., Tierney, J. E., Tourte, G. J. L., Tripati, A., Upchurch, G. R., Wade, B. S., Wing, S. L., Winguth, A. M. E., Wright, N. M., Zachos, J. C., and Zeebe, R. E. (2017). The DeepMIP contribution to PMIP4: experimental design for model simulations of the EECO, PETM, and pre-PETM (version 1.0). *Geosci. Model Dev.*, 10(2):889–901.

Lutz, M., Dunbar, R., and Caldeira, K. (2002). Regional variability in the vertical flux of particulate organic carbon in the ocean interior. *Global Biogeochemical Cycles*, 16(3):11–1–11–18.

Ma, W. and Tian, J. (2014). Modeling the contribution of dissolved organic carbon to carbon sequestration during the last glacial maximum. *Geo-Marine Letters*, 34(5):471–482.

Ma, Z., Gray, E., Thomas, E., Murphy, B., Zachos, J., and Paytan, A. (2014). Carbon sequestration during the Palaeocene-Eocene Thermal Maximum by an efficient biological pump. *Nature Geoscience*, 7(5):382–388.

Macdonald, R. W., Kuzyk, Z. Z. A., and Johannessen, S. C. (2015). The vulnerability of Arctic shelf sediments to climate change. *Environmental Reviews*, 23(4):461–479.

Mackenzie, F. T. (2005). *Sediments, Diagenesis, and Sedimentary Rocks: Treatise on Geochemistry, Second Edition*. Elsevier. 00000.

Mackenzie, F. T., Lerman, A., and Andersson, A. J. (2004). Past and present of sediment and carbon biogeochemical cycling models. *Biogeosciences*, 1(1):11–32.

Maier-Reimer, E. (1993). Geochemical cycles in an ocean general circulation model. preindustrial tracer distributions. *Global Biogeochemical Cycles*, 7(3):645–677.

Marchal, O., Stocker, T. F., and Joos, F. (1998a). Impact of oceanic reorganizations on the ocean carbon cycle and atmospheric carbon dioxide content. *Paleoceanography*, 13(3):225–244.

Marchal, O., Stocker, T. F., and Joos, F. (1998b). A latitude-depth, circulation-biogeochemical ocean model for paleoclimate studies. development and sensitivities. *Tellus B*, 50(3):290–316.

Marchal, O., Stocker, T. F., and Joos, F. (1999a). Physical and biogeochemical responses to freshwater-induced thermohaline variability in a zonally averaged ocean model. In Clark, U., Webb, S., and Keigwin, D., editors, *Geophysical Monograph Series*, volume 112, pages 263–284. American Geophysical Union, Washington, D. C.

Marchal, O., Stocker, T. F., Joos, F., Indermühle, A., Blunier, T., and Tschumi, J. (1999b). Modelling the concentration of atmospheric CO2 during the younger dryas climate event. *Climate Dynamics*, 15(5):341–354.

Marchal, O., Stocker, T. F., and Muscheler, R. (2001). Atmospheric radiocarbon during the younger dryas: production, ventilation, or both? *Earth and Planetary Science Letters*, 185(3–4):383–395.

Marinov, I., Gnanadesikan, A., Sarmiento, J. L., Toggweiler, J. R., Follows, M., and Mignone, B. K. (2008). Impact of oceanic circulation on biological carbon storage in the ocean and atmospheric pCO2. *Global Biogeochemical Cycles*, 22(3):GB3007.

Marsay, C. M., Sanders, R. J., Henson, S. A., Pabortsava, K., Achterberg, E. P., and Lampitt, R. S. (2015). Attenuation of sinking particulate organic carbon flux through the mesopelagic ocean. *Proceedings of the National Academy of Sciences*, 112(4):1089–1094.

Marsh, R., Müller, S. A., Yool, A., and Edwards, N. R. (2011). Incorporation of the C-GOLDSTEIN efficient climate model into the GENIE framework: "eb_go_gs" configurations of GENIE. *Geosci. Model Dev.*, 4(4):957–992.

Marshall, J., Adcroft, A., Hill, C., Perelman, L., and Heisey, C. (1997). A finite-volume, incompressible Navier Stokes model for studies of the ocean on parallel computers. *Journal of Geophysical Research: Oceans*, 102(C3):5753–5766.

Martin, J. H., Fitzwater, S. E., Michael Gordon, R., Hunter, C. N., and Tanner, S. J. (1993). Iron, primary production and carbon-nitrogen flux studies during the JGOFS North Atlantic bloom experiment. *Deep Sea Research Part II: Topical Studies in Oceanography*, 40(1-2):115–134. 00276.

Martin, J. H., Knauer, G. A., Karl, D. M., and Broenkow, W. W. (1987). VERTEX: carbon cycling in the northeast pacific. *Deep Sea Research Part A. Oceanographic Research Papers*, 34(2):267–285.

Matsumoto, K. (2007). Biology-mediated temperature control on atmospheric pCO2 and ocean biogeochemistry. *Geophysical Research Letters*, 34(20):L20605.

Matsumoto, K., Chase, Z., and Kohfeld, K. (2014). Different mechanisms of silicic acid leakage and their biogeochemical consequences. *Paleoceanography*, 29(3):2013PA002588.

Matsumoto, K. and Yokoyama, Y. (2013). Atmospheric δ14c reduction in simulations of Atlantic overturning circulation shutdown. *Global Biogeochemical Cycles*, 27(2):296–304.

McGuffie, K. and Henderson-Sellers, A. (2005). *A Climate Modelling Primer*. John Wiley & Sons.

Meile, C. and Van Cappellen, P. (2003). Global estimates of enhanced solute transport in marine sediments. *Limnology and Oceanography*, 48(2):777–786.

Meissner, K. J., Bralower, T. J., Alexander, K., Jones, T. D., Sijp, W., and Ward, M. (2014). The Paleocene-Eocene Thermal Maximum: How much carbon is enough? *Paleoceanography*, 29(10):946–963. 00003.

Melesse, A. M. and Hanley, R. S. (2005). Artificial neural network application for multi-ecosystem carbon flux simulation. *Ecological Modelling*, 189(3-4):305–314. 00070.

Menviel, L., England, M. H., Meissner, K. J., Mouchet, A., and Yu, J. (2014). Atlantic-Pacific seesaw and its role in outgassing CO2 during Heinrich events. *Paleoceanography*, 29(1):58–70. 00018.

Menviel, L. and Joos, F. (2012). Toward explaining the holocene carbon dioxide and carbon isotope records: Results from transient ocean carbon cycle-climate simulations. *Paleoceanography*, 27(1).

Menviel, L., Joos, F., and Ritz, S. (2012). Simulating atmospheric CO_2, ^{13}C and the marine carbon cycle during the last glacial-interglacial cycle: possible role for a deepening of the mean remineralization depth and an increase in the oceanic nutrient inventory. *Quaternary Science Reviews*, 56:46–68.

Menviel, L., Timmermann, A., Mouchet, A., and Timm, O. (2008a). Climate and marine carbon cycle response to changes in the strength of the Southern Hemispheric westerlies. *Paleoceanography*, 23(4):PA4201.

Menviel, L., Timmermann, A., Mouchet, A., and Timm, O. (2008b). Meridional reorganizations of marine and terrestrial productivity during heinrich events. *Paleoceanography*, 23(1):PA1203.

Menviel, L., Timmermann, A., Timm, O. E., and Mouchet, A. (2010). Climate and biogeochemical response to a rapid melting of the West Antarctic Ice Sheet during interglacials and implications for future climate. *Paleoceanography*, 25(4):PA4231.

Menviel, L., Timmermann, A., Timm, O. E., and Mouchet, A. (2011). Deconstructing the last glacial termination: the role of millennial and orbital-scale forcings. *Quaternary Science Reviews*, 30(9–10):1155–1172.

Meyer, K. M. and Kump, L. R. (2008). Oceanic Euxinia in Earth History: Causes and Consequences. *Annual Review of Earth and Planetary Sciences*, 36(1):251–288. 00175.

Meyer, K. M., Kump, L. R., and Ridgwell, A. (2008). Biogeochemical controls on photic-zone euxinia during the end-permian mass extinction. *Geology*, 36(9):747–750.

Meyers, S. R. (2007). Production and preservation of organic matter: The significance of iron. *Paleoceanography*, 22(4):PA4211.

Meysman, F. J. R., Middelburg, J. J., Herman, P. M. J., and Heip, C. H. R. (2003). Reactive transport in surface sediments. II. Media: an object-oriented problem-solving environment for early diagenesis. *Computers & Geosciences*, 29(3):301–318.

Michel, E., Labeyrie, L. D., Duplessy, J.-C., Gorfti, N., Labracherie, M., and Turon, J.-L. (1995). Could deep subantarctic convection feed the world deep basins during the last glacial maximum? *Paleoceanography*, 10(5):927–941.

Middelburg, J. J. (1989). A simple rate model for organic matter decomposition in marine sediments. *Geochimica et Cosmochimica Acta*, 53(7):1577–1581.

Middelburg, J. J. and Meysman, F. J. R. (2007). Burial at sea. *Science*, 316(5829):1294–1295.

Middelburg, J. J., Soetaert, K., and Herman, P. M. (1997). Empirical relationships for use in global diagenetic models. *Deep Sea Research Part I: Oceanographic Research Papers*, 44(2):327–344.

Middelburg, J. J., Soetaert, K., Herman, P. M. J., and Heip, C. H. R. (1996). Denitrification in marine sediments: A model study. *Global Biogeochemical Cycles*, 10(4):661–673.

Middelburg, J. J., Vlug, T., Jaco, F., and van der Nat, W. A. (1993). Organic matter mineralization in marine systems. *Global and Planetary Change*, 8(1):47–58.

Millero, F. J. (2007). The marine inorganic carbon cycle. *Chemical Reviews*, 107(2):308–341.

Milliman, J. D. (1993). Production and accumulation of calcium carbonate in the ocean: Budget of a nonsteady state. *Global Biogeochemical Cycles*, 7(4):927–957.

Milliman, J. D. and Droxler, A. W. (1996). Neritic and pelagic carbonate sedimentation in the marine environment: Ignorance is not bliss. *Geologische Rundschau*, 85(3):496–504.

Milliman, J. D., Troy, P. J., Balch, W. M., Adams, A. K., Li, Y. H., and Mackenzie, F. T. (1999). Biologically mediated dissolution of calcium carbonate above the chemical lysocline? *Deep Sea Research Part I: Oceanographic Research Papers*, 46(10):1653–1669.

Monteiro, F. M., Pancost, R. D., Ridgwell, A., and Donnadieu, Y. (2012). Nutrients as the dominant control on the spread of anoxia and euxinia across the cenomanian-turonian oceanic anoxic event (OAE2): Model-data comparison. *Paleoceanography*, 27(4).

Montenegro, A., Spence, P., Meissner, K. J., Eby, M., Melchin, M. J., and Johnston, S. T. (2011). Climate simulations of the Permian-Triassic boundary: Ocean acidification and the extinction event. *Paleoceanography*, 26(3):PA3207. 00014.

Moore, J. K., Doney, S. C., Kleypas, J. A., Glover, D. M., and Fung, I. Y. (2001). An intermediate complexity marine ecosystem model for the global domain. *Deep Sea Research Part II: Topical Studies in Oceanography*, 49(1):403–462.

Morse, J. W. and Arvidson, R. S. (2002). The dissolution kinetics of major sedimentary carbonate minerals. *Earth-Science Reviews*, 58(1-2):51–84.

Morse, J. W., Arvidson, R. S., and Lüttge, A. (2007). Calcium carbonate formation and dissolution. *Chemical Reviews*, 107(2):342–381.

Morse, J. W. and Berner, R. A. (1972). Dissolution kinetics of calcium carbonate in sea water; i, a kinetic origin for the lysocline. *American Journal of Science*, 272(9):840–851.

Morse, J. W. and He, S. (1993). Influences of t, s and PCO2 on the pseudo-homogeneous precipitation of CaCO3 from seawater: implications for whiting formation. *Marine Chemistry*, 41(4):291–297.

Mort, H. P., Adatte, T., Föllmi, K. B., Keller, G., Steinmann, P., Matera, V., Berner, Z., and Stüben, D. (2007). Phosphorus and the roles of productivity and nutrient recycling during oceanic anoxic event 2. *Geology*, 35(6):483–486. 00135.

Mort, H. P., Adatte, T., Keller, G., Bartels, D., Föllmi, K. B., Steinmann, P., Berner, Z., and Chellai, E. H. (2008). Organic carbon deposition and phosphorus accumulation during Oceanic Anoxic Event 2 in Tarfaya, Morocco. *Cretaceous Research*, 29(5-6):1008–1023.

Mouchet, A. and François, L. M. (1996). Sensitivity of a global oceanic carbon cycle model to the circulation and to the fate of organic matter: Preliminary results. *Physics and Chemistry of the Earth*, 21(5-6):511–516.

Munhoven, G. (2007). Glacial-interglacial rain ratio changes: Implications for atmospheric and ocean-sediment interaction. *Deep Sea Research Part II: Topical Studies in Oceanography*, 54(5-7):722–746.

Munhoven, G. and François, L. M. (1994). Glacial-interglacial changes in continental weathering : Possible implications for atmospheric CO_2. In Zahn, R., Pedersen, T. F., Kaminski, M. A., and Labeyrie, L., editors, *Carbon Cycling in the Glacial Ocean : Constraints on the Ocean's Role in Global Change*, volume 17 of *NATO ASI Series I : Global Environmental Change*, pages 39–58. Springer-Verlag, Berlin.

Munhoven, G. and François, L. M. (1996). Glacial-interglacial variability of atmospheric CO_2 due to changing continental silicate rock weathering : A model study. *J. Geophys. Res.*, 101(D16):21423–21437.

Najjar, R. G., Jin, X., Louanchi, F., Aumont, O., Caldeira, K., Doney, S. C., Dutay, J.-C., Follows, M., Gruber, N., Joos, F., Lindsay, K., Maier-Reimer, E., Matear, R. J., Matsumoto, K., Monfray, P., Mouchet, A., Orr, J. C., Plattner, G.-K., Sarmiento, J. L., Schlitzer, R., Slater, R. D., Weirig, M.-F., Yamanaka, Y., and Yool, A. (2007). Impact of circulation on export production, dissolved organic matter, and dissolved oxygen in the ocean: Results from Phase II of the Ocean Carbon-cycle Model Intercomparison Project (OCMIP-2). *Global Biogeochemical Cycles*, 21(3):GB3007.

Najjar, R. G., Sarmiento, J. L., and Toggweiler, J. R. (1992). Downward transport and fate of organic matter in the ocean: Simulations with a general circulation model. *Global Biogeochemical Cycles*, 6(1):45–76.

Nihoul, J. C. J. (1994). Do not use a simple model when a complex one will do. *Journal of Marine Systems*, 5(6):401–406.

Norris, R. D., Turner, S. K., Hull, P. M., and Ridgwell, A. (2013). Marine ecosystem responses to cenozoic global change. *Science*, 341(6145):492–498.

Oreskes, N., Shrader-Frechette, K., and Belitz, K. (1994). Verification, Validation, and Confirmation of Numerical Models in the Earth Sciences. *Science*, 263(5147):641–646.

Owens, J. D., Gill, B. C., Jenkyns, H. C., Bates, S. M., Severmann, S., Kuypers, M. M. M., Woodfine, R. G., and Lyons, T. W. (2013). Sulfur isotopes track the global extent and dynamics of euxinia during Cretaceous Oceanic Anoxic Event 2. *Proceedings of the National Academy of Sciences*, 110(46):18407–18412.

Owens, J. D., Lyons, T. W., Hardisty, D. S., Lowery, C. M., Lu, Z., Lee, B., and Jenkyns, H. C. (2017). Patterns of local and global redox variability during the Cenomanian-Turonian Boundary Event (Oceanic Anoxic Event 2) recorded in carbonates and shales from central Italy. *Sedimentology*, 64(1):168–185.

Owens, J. D., Lyons, T. W., Li, X., Macleod, K. G., Gordon, G., Kuypers, M. M. M., Anbar, A., Kuhnt, W., and Severmann, S. (2012). Iron isotope and trace metal records of iron cycling in the proto-North Atlantic during the Cenomanian-Turonian oceanic anoxic event (OAE-2). *Paleoceanography*, 27(3):PA3223.

Ozaki, K., Tajima, S., and Tajika, E. (2011). Conditions required for oceanic anoxia/euxinia: Constraints from a one-dimensional ocean biogeochemical cycle model. *Earth and Planetary Science Letters*, 304(1-2):270–279.

Pagani, M., Huber, M., Liu, Z., Bohaty, S. M., Henderiks, J., Sijp, W., Krishnan, S., and DeConto, R. M. (2011). The Role of Carbon Dioxide During the Onset of Antarctic Glaciation. *Science*, 334(6060):1261–1264.

Palastanga, V., Slomp, C. P., and Heinze, C. (2011). Long-term controls on ocean phosphorus and oxygen in a global biogeochemical model. *Global Biogeochemical Cycles*, 25(3):GB3024.

Pälike, H., Lyle, M. W., Nishi, H., Raffi, I., Ridgwell, A., Gamage, K., Klaus, A., Acton, G., Anderson, L., Backman, J., Baldauf, J., Beltran, C., Bohaty, S. M., Bown, P., Busch, W., Channell, J. E. T., Chun, C. O. J., Delaney, M., Dewangan, P., Dunkley Jones, T., Edgar, K. M., Evans, H., Fitch, P., Foster, G. L., Gussone, N., Hasegawa, H., Hathorne, E. C., Hayashi, H., Herrle, J. O., Holbourn, A., Hovan, S., Hyeong, K., Iijima, K., Ito, T., Kamikuri, S.-i., Kimoto, K., Kuroda, J., Leon-Rodriguez, L., Malinverno, A., Moore Jr, T. C., Murphy, B. H., Murphy, D. P., Nakamura, H., Ogane, K., Ohneiser, C., Richter, C., Robinson, R., Rohling, E. J., Romero, O., Sawada, K., Scher, H., Schneider, L., Sluijs, A., Takata, H., Tian, J., Tsujimoto, A., Wade, B. S., Westerhold, T., Wilkens, R., Williams, T., Wilson, P. A., Yamamoto, Y., Yamamoto, S., Yamazaki, T., and Zeebe, R. E. (2012). A cenozoic record of the equatorial pacific carbonate compensation depth. *Nature*, 488(7413):609–614.

Panchuk, K., Ridgwell, A., and Kump, L. R. (2008). Sedimentary response to paleocene-eocene thermal maximum carbon release: A model-data comparison. *Geology*, 36(4):315–318.

Pancost, R. D., Crawford, N., Magness, S., Turner, A., Jenkyns, H. C., and Maxwell, J. R. (2004). Further evidence for the development of photic-zone euxinic conditions during Mesozoic oceanic anoxic events. *Journal of the Geological Society*, 161(3):353–364.

Parekh, P., Joos, F., and Müller, S. A. (2008). A modeling assessment of the interplay between aeolian iron fluxes and iron-binding ligands in controlling carbon dioxide fluctuations during Antarctic warm events. *Paleoceanography*, 23(4):PA4202.

Passow, U. (2004). Switching perspectives: Do mineral fluxes determine particulate organic carbon fluxes or vice versa? *Geochemistry, Geophysics, Geosystems*, 5(4).

Pedersen, T. F. and Calvert, S. E. (1990). Anoxia vs. productivity: What controls the formation of organic-carbon-rich sediments and sedimentary rocks? (1). *AAPG Bulletin*, 74(4):454–466.

Penman, D. E., Hönisch, B., Zeebe, R. E., Thomas, E., and Zachos, J. C. (2014). Rapid and sustained surface ocean acidification during the Paleocene-Eocene Thermal Maximum. *Paleoceanography*, 29(5):2014PA002621. 00032.

Perry, C. T., Spencer, T., and Kench, P. S. (2008). Carbonate budgets and reef production states: a geomorphic perspective on the ecological phase-shift concept. *Coral Reefs*, 27(4):853–866.

Petoukhov, V. (1980). A zonal climate model of heat and moisture exchange in the atmosphere over the underlying layers of ocean and land in: Golitsyn gs, yaglom am (eds) physics of the atmosphere and the problem of climate.

Petoukhov, V., Claussen, M., Berger, A., Crucifix, M., Eby, M., Eliseev, A. V., Fichefet, T., Ganopolski, A., Goosse, H., Kamenkovich, I., Mokhov, I. I., Montoya, M., Mysak, L. A., Sokolov, A., Stone, P., Wang, Z., and Weaver, A. J. (2005). EMIC intercomparison project (EMIP-CO2): comparative analysis of EMIC simulations of climate, and of equilibrium and transient responses to atmospheric CO2 doubling. *Climate Dynamics*, 25(4):363–385.

Pianosi, F., Beven, K., Freer, J., Hall, J. W., Rougier, J., Stephenson, D. B., and Wagener, T. (2016). Sensitivity analysis of environmental models: A systematic review with practical workflow. *Environmental Modelling & Software*, 79:214–232.

Pianosi, F., Sarrazin, F., and Wagener, T. (2015). A Matlab toolbox for Global Sensitivity Analysis. *Environmental Modelling & Software*, 70:80–85.

Pianosi, F. and Wagener, T. (2015). A simple and efficient method for global sensitivity analysis based on cumulative distribution functions. *Environmental Modelling & Software*, 67:1–11.

Pianosi, F., Wagener, T., Rougier, J., Freer, J., and Hall, J. (2014). Sensitivity analysis of environmental models: A systematic review with practical workflow. In *Vulnerability, Uncertainty, and Risk*, pages 290–299. American Society of Civil Engineers.

Plattner, G.-K., Knutti, R., Joos, F., Stocker, T. F., von Bloh, W., Brovkin, V., Cameron, D., Driesschaert, E., Dutkiewicz, S., Eby, M., Edwards, N. R., Fichefet, T., Hargreaves, J. C., Jones, C. D., Loutre, M. F., Matthews, H. D., Mouchet, A., Müller, S. A., Nawrath, S., Price, A., Sokolov, A., Strassmann, K. M., and Weaver, A. J. (2008). Long-Term Climate Commitments Projected with Climate-Carbon Cycle Models. *Journal of Climate*, 21(12):2721–2751.

Pogge von Strandmann, P. A. E., Jenkyns, H. C., and Woodfine, R. G. (2013). Lithium isotope evidence for enhanced weathering during Oceanic Anoxic Event 2. *Nature Geoscience*, 6(8):668–672.

Poulsen, C. J., Barron, E. J., Arthur, M. A., and Peterson, W. H. (2001). Response of the mid-cretaceous global oceanic circulation to tectonic and CO2 forcings. *Paleoceanography*, 16(6):576–592.

Ragueneau, O., Tréguer, P., Leynaert, A., Anderson, R. F., Brzezinski, M. A., DeMaster, D. J., Dugdale, R. C., Dymond, J., Fischer, G., Francois, R., Heinze, C., Maier-Reimer, E., Martin-Jézéquel, V., Nelson, D. M., and Quéguiner, B. (2000). A review of the Si cycle in the modern ocean: recent progress and missing gaps in the application of biogenic opal as a paleoproductivity proxy. *Global and Planetary Change*, 26(4):317–365.

Randall, D. A., Wood, R. A., Bony, S., Colman, R., Fichefet, T., Fyfe, J., Kattsov, V., Pitman, A., Shukla, J., Srinivasan, J., et al. (2007). Climate models and their evaluation. *In: Climate change 2007: The Physical Science Basis. Contribution of Working Group I to the Fourth Assessment Report of the Intergovernmental Panel on Climate Change*, 323.

Raven, M. R., Sessions, A. L., Adkins, J. F., and Thunell, R. C. (2016). Rapid organic matter sulfurization in sinking particles from the Cariaco Basin water column. *Geochimica et Cosmochimica Acta*, 190:175–190. 00000.

Redfield, A. C. (1963). The influence of organisms on the composition of seawater. *The sea*, 2:26–77.

Regaudie-de Gioux, A. and Duarte, C. M. (2012). Temperature dependence of planktonic metabolism in the ocean. *Global Biogeochemical Cycles*, 26(1):GB1015.

Regnier, P., Dale, A. W., Arndt, S., LaRowe, D. E., Mogollon, J., and Van Cappellen, P. (2011). Quantitative analysis of anaerobic oxidation of methane (AOM) in marine sediments: A modeling perspective. *Earth-Science Reviews*, 106(1):105–130.

Regnier, P., Wollast, R., and Steefel, C. I. (1997). Long-term fluxes of reactive species in macrotidal estuaries: Estimates from a fully transient, multicomponent reaction-transport model. *Marine Chemistry*, 58(1-2):127–145.

Reimers, C. E., Lange, C. B., Tabak, M., and Bernhard, J. M. (1990). Seasonal spillover and varve formation in the Santa Barbara Basin, California. *Limnology and Oceanography*, 35(7):1577–1585.

Reimers, C. E., Ruttenberg, K. C., Canfield, D. E., Christiansen, M. B., and Martin, J. B. (1996). Porewater pH and authigenic phases formed in the uppermost sediments of the Santa Barbara Basin. *Geochimica et Cosmochimica Acta*, 60(21):4037–4057.

Ridgwell, A. (2005). A Mid Mesozoic Revolution in the regulation of ocean chemistry. *Marine Geology*, 217(3-4):339–357.

Ridgwell, A. (2007). Interpreting transient carbonate compensation depth changes by marine sediment core modeling. *Paleoceanography*, 22(4):PA4102.

Ridgwell, A. and Arndt, S. (2014). Why dissolved organic matter: Doc in ancient oceans and past climate change. *In: Hansell, D.A., Carlson, C.A. (Eds.), Biogeochemistry of Marine Dissolved Organic Matter*, pages 1–20.

Ridgwell, A. and Hargreaves, J. C. (2007). Regulation of atmospheric CO2 by deep-sea sediments in an earth system model. *Global Biogeochemical Cycles*, 21(2).

Ridgwell, A., Hargreaves, J. C., Edwards, N. R., Annan, J. D., Lenton, T. M., Marsh, R., Yool, A., and Watson, A. (2007). Marine geochemical data assimilation in an efficient Earth System Model of global biogeochemical cycling. *Biogeosciences*, 4(1):87–104. 00090.

Ridgwell, A. and Schmidt, D. N. (2010). Past constraints on the vulnerability of marine calcifiers to massive carbon dioxide release. *Nature Geoscience*, 3(3):196–200.

Ridgwell, A. and Zeebe, R. E. (2005). The role of the global carbonate cycle in the regulation and evolution of the earth system. *Earth and Planetary Science Letters*, 234(3-4):299–315.

Ridgwell, A. J. (2001). *Glacial-interglacial perturbations in the global carbon cycle.* Ph.D., University of East Anglia.

Ridgwell, A. J., Kennedy, M. J., and Caldeira, K. (2003a). Carbonate Deposition, Climate Stability, and Neoproterozoic Ice Ages. *Science*, 302(5646):859–862.

Ridgwell, A. J., Watson, A. J., and Archer, D. E. (2002). Modeling the response of the oceanic Si inventory to perturbation, and consequences for atmospheric CO2. *Global Biogeochemical Cycles*, 16(4):1071. 00050.

Ridgwell, A. J., Watson, A. J., Maslin, M. A., and Kaplan, J. O. (2003b). Implications of coral reef buildup for the controls on atmospheric CO2 since the Last Glacial Maximum. *Paleoceanography*, 18(4):1083. 00071.

Riebesell, U., Körtzinger, A., and Oschlies, A. (2009). Sensitivities of marine carbon fluxes to ocean change. *Proceedings of the National Academy of Sciences*, 106(49):20602–20609.

Roth, R., Ritz, S. P., and Joos, F. (2014). Burial-nutrient feedbacks amplify the sensitivity of atmospheric carbon dioxide to changes in organic matter remineralisation. *Earth Syst. Dynam.*, 5(2):321–343.

Ruardij, P. and Van Raaphorst, W. (1995). Benthic nutrient regeneration in the ERSEM ecosystem model of the north sea. *Netherlands Journal of Sea Research*, 33(3-4):453–483.

Ruttenberg, K. C. (1993). Reassessment of the oceanic residence time of phosphorus. *Chemical Geology*, 107(3):405–409.

Ruttenberg, K. C. and Berner, R. A. (1993). Authigenic apatite formation and burial in sediments from non-upwelling, continental margin environments. *Geochimica et Cosmochimica Acta*, 57(5):991–1007.

Ruvalcaba Baroni, I., Topper, R. P. M., van Helmond, N. A. G. M., Brinkhuis, H., and Slomp, C. P. (2014). Biogeochemistry of the North Atlantic during oceanic anoxic event 2: role of changes in ocean circulation and phosphorus input. *Biogeosciences*, 11(4):977–993.

Sageman, B. B., Murphy, A. E., Werne, J. P., Ver Straeten, C. A., Hollander, D. J., and Lyons, T. W. (2003). A tale of shales: the relative roles of production, decomposition, and dilution in the accumulation of organic-rich strata, middle-upper devonian, appalachian basin. *Chemical Geology*, 195(1-4):229–273.

Sarmiento, J. L., Dunne, J., Gnanadesikan, A., Key, R. M., Matsumoto, K., and Slater, R. (2002). A new estimate of the CaCO3 to organic carbon export ratio. *Global Biogeochemical Cycles*, 16(4):1107.

Sarmiento, J. L. and Gruber, N. (2006). *Ocean biogeochemical dynamics*, volume 1015. Princeton University Press Princeton.

Sarmiento, J. L., Murnane, R., Quere, C. L., Keeling, R., and Williams, R. G. (1995). Air-Sea CO2 transfer and the carbon budget of the North Atlantic. *Philosophical Transactions of the Royal Society of London B: Biological Sciences*, 348(1324):211–219.

Sarmiento, J. L., Slater, R. D., Fasham, M. J. R., Ducklow, H. W., Toggweiler, J. R., and Evans, G. T. (1993). A seasonal three-dimensional ecosystem model of nitrogen cycling in the north atlantic euphotic zone. *Global Biogeochemical Cycles*, 7(2):417–450.

Sarmiento, J. L. and Toggweiler, J. R. (1984). A new model for the role of the oceans in determining atmospheric p_{CO_2}. *Nature*, 308:621–624.

Schlanger, S. and Jenkyns, H. (1976). Cretaceous Oceanic Anoxic Events: Causes and consequences. *Geologie en Mijnbouw*, 55(3-4):179–184.

Schlanger, S. O., Arthur, M. A., Jenkyns, H. C., and Scholle, P. A. (1987). The cenomanian-turonian oceanic anoxic event, i. stratigraphy and distribution of organic carbon-rich beds and the marine Œ¥13C excursion. *Geological Society, London, Special Publications*, 26(1):371–399.

Schmittner, A. (2005). Decline of the marine ecosystem caused by a reduction in the Atlantic overturning circulation. *Nature*, 434(7033):628–633.

Schmittner, A., Galbraith, E. D., Hostetler, S. W., Pedersen, T. F., and Zhang, R. (2007). Large fluctuations of dissolved oxygen in the Indian and Pacific oceans during Dansgaard-Oeschger oscillations caused by variations of North Atlantic Deep Water subduction. *Paleoceanography*, 22(3):PA3207.

Schmittner, A. and Lund, D. C. (2015). Early deglacial Atlantic overturning decline and its role in atmospheric CO2 rise inferred from carbon isotopes (δ13c). *Clim. Past*, 11(2):135–152.

Schmittner, A., Oschlies, A., Giraud, X., Eby, M., and Simmons, H. L. (2005). A global model of the marine ecosystem for long-term simulations: Sensitivity to ocean mixing, buoyancy

forcing, particle sinking, and dissolved organic matter cycling. *Global Biogeochemical Cycles*, 19(3):n/a–n/a.

Schmittner, A. and Somes, C. J. (2016). Complementary constraints from carbon (13c) and nitrogen (15n) isotopes on the glacial ocean's soft-tissue biological pump. *Paleoceanography*, 31(6):2015PA002905.

Schneider, B. and Schmittner, A. (2006). Simulating the impact of the Panamanian seaway closure on ocean circulation, marine productivity and nutrient cycling. *Earth and Planetary Science Letters*, 246(3-4):367–380.

Schneider, R. R., Schulz, H. D., and Hensen, C. (2006). Marine carbonates: Their formation and destruction. In Schulz, P. D. H. D. and Zabel, D. M., editors, *Marine Geochemistry*, pages 311–337. Springer Berlin Heidelberg.

Scholle, P. A. and Arthur, M. A. (1980). Carbon isotope fluctuations in cretaceous pelagic limestones: Potential stratigraphic and petroleum exploration tool. *AAPG Bull.*, 64:1.

Schulz, H. D. (2006). Quantification of Early Diagenesis: Dissolved Constituents in Pore Water and Signals in the Solid Phase. In Schulz, P. D. H. D. and Zabel, D. M., editors, *Marine Geochemistry*, pages 73–124. Springer Berlin Heidelberg.

Seiter, K., Hensen, C., Schröter, J., and Zabel, M. (2004). Organic carbon content in surface sediments‚Äîdefining regional provinces. *Deep Sea Research Part I: Oceanographic Research Papers*, 51(12):2001–2026.

Sepúlveda, J., Wendler, J., Leider, A., Kuss, H.-J., Summons, R. E., and Hinrichs, K.-U. (2009). Molecular isotopic evidence of environmental and ecological changes across the Cenomanian-Turonian boundary in the Levant Platform of central Jordan. *Organic Geochemistry*, 40(5):553–568.

Sexton, P. F., Norris, R. D., Wilson, P. A., Pälike, H., Westerhold, T., Röhl, U., Bolton, C. T., and Gibbs, S. (2011). Eocene global warming events driven by ventilation of oceanic dissolved organic carbon. *Nature*, 471(7338):349–352.

Shaffer, G. (1993). Effects of the marine biota on global carbon cycling. In Heimann, M., editor, *The Global Carbon Cycle*, number 15 in NATO ASI Series, pages 431–455. Springer Berlin Heidelberg.

Shaffer, G. (1996). Biogeochemical cycling in the global ocean: 2. new production, redfield ratios, and remineralization in the organic pump. *Journal of Geophysical Research: Oceans*, 101(C2):3723–3745.

Shaffer, G., Huber, M., Rondanelli, R., and Pepke Pedersen, J. O. (2016). Deep time evidence for climate sensitivity increase with warming. *Geophysical Research Letters*, 43(12):2016GL069243.

Shaffer, G., Malskaer Olsen, S., and Pepke Pedersen, J. O. (2008). Presentation, calibration and validation of the low-order, DCESS earth system model (version 1). *Geosci. Model Dev.*, 1(1):17–51.

Shchepetkin, A. F. and McWilliams, J. C. (2005). The regional oceanic modeling system (ROMS): a split-explicit, free-surface, topography-following-coordinate oceanic model. *Ocean Modelling*, 9(4):347–404.

Sigman, D. M. and Boyle, E. A. (2000). Glacial/interglacial variations in atmospheric carbon dioxide. *Nature*, 407(6806):859–869.

Sigman, D. M., Lehman, S. J., and Oppo, D. W. (2003). Evaluating mechanisms of nutrient depletion and 13c enrichment in the intermediate-depth Atlantic during the last ice age. *Paleoceanography*, 18(3):1072.

Sigman, D. M., McCorkle, D. C., and Martin, W. R. (1998). The calcite lysocline as a constraint on glacial/interglacial low-latitude production changes. *Global Biogeochem. Cycles*, 12(3):409–427.

Simmons, C. T., Matthews, H. D., and Mysak, L. A. (2015). Deglacial climate, carbon cycle and ocean chemistry changes in response to a terrestrial carbon release. *Climate Dynamics*, pages 1–13.

Singarayer, J. S., Richards, D. A., Ridgwell, A., Valdes, P. J., Austin, W. E. N., and Beck, J. W. (2008). An oceanic origin for the increase of atmospheric radiocarbon during the younger dryas. *Geophysical Research Letters*, 35(14):L14707.

Sinninghe Damsté, J. S. and De Leeuw, J. W. (1990). Analysis, structure and geochemical significance of organically-bound sulphur in the geosphere: State of the art and future research. *Organic Geochemistry*, 16(4–6):1077–1101.

Sinninghe Damsté, J. S., Eglinton, T. I., De Leeuw, J. W., and Schenck, P. (1989a). Organic sulphur in macromolecular sedimentary organic matter: I. structure and origin of sulphur-containing moieties in kerogen, asphaltenes and coal as revealed by flash pyrolysis. *Geochimica et Cosmochimica Acta*, 53(4):873–889.

Sinninghe Damsté, J. S., Kok, M. D., Köster, J., and Schouten, S. (1998). Sulfurized carbohydrates: an important sedimentary sink for organic carbon? *Earth and Planetary Science Letters*, 164(1–2):7–13.

Sinninghe Damsté, J. S. and Köster, J. (1998). A euxinic southern north atlantic ocean during the Cenomanian/Turonian oceanic anoxic event. *Earth and Planetary Science Letters*, 158(3–4):165–173.

Sinninghe Damsté, J. S., Rijpstra, W. C., Kock-van Dalen, A., De Leeuw, J. W., and Schenck, P. (1989b). Quenching of labile functionalised lipids by inorganic sulphur species: Evidence for the formation of sedimentary organic sulphur compounds at the early stages of diagenesis. *Geochimica et Cosmochimica Acta*, 53(6):1343–1355.

Sinninghe Damsté, J. S., van Bentum, E. C., Reichart, G.-J., Pross, J., and Schouten, S. (2010). A CO2 decrease-driven cooling and increased latitudinal temperature gradient during the mid-Cretaceous Oceanic Anoxic Event 2. *Earth and Planetary Science Letters*, 293(1-2):97–103.

Six, K. D. and Maier-Reimer, E. (1996). Effects of plankton dynamics on seasonal carbon fluxes in an ocean general circulation model. *Global Biogeochemical Cycles*, 10(4):559–583.

Slomp, C., Malschaert, J., and Van Raaphorst, W. (1998). The role of adsorption in sediment-water exchange of phosphate in north sea continental margin sediments. *Limnology and Oceanography*, 43(5):832–846.

Slomp, C. P., Epping, E. H., Helder, W., and Van Raaphorst, W. (1996). A key role for iron-bound phosphorus in authigenic apatite formation in north atlantic continental platform sediments. *Journal of Marine Research*, 54(6):1179–1205.

Slomp, C. P., Thomson, J., and de Lange, G. J. (2004). Controls on phosphorus regeneration and burial during formation of eastern Mediterranean sapropels. *Marine Geology*, 203(1):141–159.

Sluijs, A., Zeebe, R. E., Bijl, P. K., and Bohaty, S. M. (2013). A middle Eocene carbon cycle conundrum. *Nature Geoscience*, 6(6):429–434.

Smirnov, N. V. (1939). On the estimation of the discrepancy between empirical curves of distribution for two independent samples. *Bull. Math. Univ. Moscou*, 2(2).

Smith, S. (1984). Phosphorus versus nitrogen limitation in the marine environment. *LIMNOLOGY*.

Snow, L. J., Duncan, R. A., and Bralower, T. J. (2005). Trace element abundances in the Rock Canyon Anticline, Pueblo, Colorado, marine sedimentary section and their relationship to Caribbean plateau construction and oxygen anoxic event 2. *Paleoceanography*, 20(3):PA3005.

Soetaert, K. and Herman, P. M. J. (1995). Nitrogen dynamics in the Westerschelde estuary (SW Netherlands) estimated by means of the ecosystem model MOSES. *Hydrobiologia*, 311(1-3):225–246.

Soetaert, K., Herman, P. M. J., and Middelburg, J. J. (1996). A model of early diagenetic processes from the shelf to abyssal depths. *Geochimica et Cosmochimica Acta*, 60(6):1019–1040.

Soetaert, K., Hofmann, A. F., Middelburg, J. J., Meysman, F. J. R., and Greenwood, J. (2007). The effect of biogeochemical processes on pH. *Marine Chemistry*, 105(1-2):30–51.

Soetaert, K., Middelburg, J. J., Herman, P. M. J., and Buis, K. (2000). On the coupling of benthic and pelagic biogeochemical models. *Earth-Science Reviews*, 51(1-4):173–201.

Solomatine, D. and Wagener, T. (2011). Hydrological modeling. In Wilderer, P., editor, *Treatise on Water Science*, volume 2, pages 435–457. Oxford: Academic Press.

Stein, R. and MacDonald, R. W., editors (2004). *The Organic Carbon Cycle in the Arctic Ocean*. Springer Berlin Heidelberg, Berlin, Heidelberg.

Stein, R., Rullkötter, J., and Welte, D. H. (1986). Accumulation of organic-carbon-rich sediments in the Late Jurassic and Cretaceous Atlantic Ocean ‚Äî A synthesis. *Chemical Geology*, 56(1-2):1–32.

Stolpovsky, K., Dale, A. W., and Wallmann, K. (2015). Toward a parameterization of global-scale organic carbon mineralization kinetics in surface marine sediments. *Global Biogeochemical Cycles*, 29(6):2015GB005087.

Stumm, W. and Morgan, J. J. (2012). *Aquatic Chemistry: Chemical Equilibria and Rates in Natural Waters*. John Wiley & Sons.

Suess, E. (1980). Particulate organic carbon flux in the oceans-surface productivity and oxygen utilization. *Nature*, 288(5788):260–263.

Sun, X. and Matsumoto, K. (2010). Effects of sea ice on atmospheric pCO2: A revised view and implications for glacial and future climates. *Journal of Geophysical Research: Biogeosciences*, 115(G2):G02015.

Tagliabue, A., Aumont, O., DeAth, R., Dunne, J. P., Dutkiewicz, S., Galbraith, E., Misumi, K., Moore, J. K., Ridgwell, A., Sherman, E., Stock, C., Vichi, M., Voelker, C., and Yool, A. (2016). How well do global ocean biogeochemistry models simulate dissolved iron distributions? *Global Biogeochemical Cycles*, 30(2):149–174.

Takashima, R., Nishi, H., Huber, B. T., and Leckie, R. M. (2006). Greenhouse World and the Mesozoic Ocean. *Oceanography*, 19(4):64–74.

Tambutté, S., Holcomb, M., Ferrier-Pagés, C., Reynaud, S., Tambutté, E., Zoccola, D., and Allemand, D. (2011). Coral biomineralization: From the gene to the environment. *Journal of Experimental Marine Biology and Ecology*, 408(1-2):58–78.

Teal, L., Bulling, M., Parker, E., and Solan, M. (2010). Global patterns of bioturbation intensity and mixed depth of marine soft sediments. *Aquatic Biology*, 2(3):207–218.

Thullner, M., Dale, A. W., and Regnier, P. (2009). Global-scale quantification of mineralization pathways in marine sediments: A reaction-transport modeling approach. *Geochemistry, Geophysics, Geosystems*, 10(10).

Thullner, M., Van Cappellen, P., and Regnier, P. (2005). Modeling the impact of microbial activity on redox dynamics in porous media. *Geochimica et Cosmochimica Acta*, 69(21):5005–5019.

Tjiputra, J. F., Roelandt, C., Bentsen, M., Lawrence, D. M., Lorentzen, T., Schwinger, J., Seland, Ø., and Heinze, C. (2013). Evaluation of the carbon cycle components in the Norwegian Earth System Model (NorESM). *Geosci. Model Dev.*, 6(2):301–325. 00057.

Toth, D. J. and Lerman, A. (1977). Organic matter reactivity and sedimentation rates in the ocean. *American Journal of Science*, 277(4):465–485.

Trabucho-Alexandre, J., Tuenter, E., Henstra, G. A., van der Zwan, K. J., van de Wal, R. S. W., Dijkstra, H. A., and de Boer, P. L. (2010). The mid-cretaceous north atlantic nutrient trap: Black shales and OAEs. *Paleoceanography*, 25.

Tréguer, P. J. and Rocha, C. L. D. L. (2013). The World Ocean Silica Cycle. *Annual Review of Marine Science*, 5(1):477–501.

Tromp, T. K., Van Cappellen, P., and Key, R. M. (1995). A global model for the early diagenesis of organic carbon and organic phosphorus in marine sediments. *Geochimica et Cosmochimica Acta*, 59(7):1259–1284. 00164.

Trull, T., Bray, S., Buesseler, K., Lamborg, C., Manganini, S., Moy, C., and Valdes, J. (2008). In situ measurement of mesopelagic particle sinking rates and the control of carbon transfer to the ocean interior during the vertical flux in the global ocean (vertigo) voyages in the north pacific. *Deep Sea Research Part II: Topical Studies in Oceanography*, 55(14):1684–1695.

Tsandev, I. and Slomp, C. (2009). Modeling phosphorus cycling and carbon burial during Cretaceous Oceanic Anoxic Events. *Earth and Planetary Science Letters*, 286(1-2):71–79.

Tschumi, T., Joos, F., Gehlen, M., and Heinze, C. (2011). Deep ocean ventilation, carbon isotopes, marine sedimentation and the deglacial CO2 rise. *Clim. Past*, 7(3):771–800.

Tschumi, T., Joos, F., and Parekh, P. (2008). How important are Southern Hemisphere wind changes for low glacial carbon dioxide? A model study. *Paleoceanography*, 23(4):PA4208.

Tsunogai, S. and Noriki, S. (1991). Particulate fluxes of carbonate and organic carbon in the ocean. is the marine biological activity working as a sink of the atmospheric carbon? *Tellus B*, 43(2):256–266.

Tyrrell, T. (1999). The relative influences of nitrogen and phosphorus on oceanic primary production. *Nature*, 400(6744):525–531.

Tziperman, E., Halevy, I., Johnston, D. T., Knoll, A. H., and Schrag, D. P. (2011). Biologically induced initiation of neoproterozoic snowball-earth events. *Proceedings of the National Academy of Sciences*, 108(37):15091–15096.

Uchikawa, J. and Zeebe, R. E. (2010). Examining possible effects of seawater pH decline on foraminiferal stable isotopes during the Paleocene-Eocene Thermal Maximum. *Paleoceanography*, 25(2):PA2216.

Ullman, W. J. and Aller, R. C. (1982). Diffusion coefficients in nearshore marine sediments. *Limnology and Oceanography*, 27(3):552–556.

Urban, N. R., Ernst, K., and Bernasconi, S. (1999). Addition of sulfur to organic matter during early diagenesis of lake sediments. *Geochimica et Cosmochimica Acta*, 63(6):837–853.

Ushie, H. and Matsumoto, K. (2012). The role of shelf nutrients on glacial-interglacial CO2: A negative feedback. *Global Biogeochemical Cycles*, 26(2):GB2039.

Van Cappellen, P. and Berner, R. A. (1988). A mathematical model for the early diagenesis of phosphorus and fluorine in marine sediments; apatite precipitation. *American Journal of Science*, 288(4):289–333.

Van Cappellen, P. and Ingall, E. D. (1994). Benthic phosphorus regeneration, net primary production, and ocean anoxia: A model of the coupled marine biogeochemical cycles of carbon and phosphorus. *Paleoceanography*, 9(5):677–692.

Van Cappellen, P. and Wang, Y. (1995). Metal cycling in surface sediments: modeling the interplay of transport and reaction. *Metal contaminated aquatic sediments*, pages 21–64.

van Dongen, B. E., Schouten, S., and Sinninghe Damsté, J. S. (2003). Sulfurization of Carbohydrates Results in a Sulfur-Rich, Unresolved Complex Mixture in Kerogen Pyrolysates. *Energy & Fuels*, 17(4):1109–1118.

van Dongen, B. E., Schouten, S., and Sinninghe Damsté, J. S. (2006). Preservation of carbohydrates through sulfurization in a Jurassic euxinic shelf sea: Examination of the Blackstone Band TOC cycle in the Kimmeridge Clay Formation, UK. *Organic Geochemistry*, 37(9):1052–1073.

van Weering, T. C. E., de Stigter, H. C., Boer, W., and de Haas, H. (2002). Recent sediment transport and accumulation on the NW Iberian margin. *Progress in Oceanography*, 52(2):349–371.

Vanderborght, J.-P. and Billen, G. (1975). Vertical distribution of nitrate concentration in interstitial water of marine sediments with nitrification and denitrification. *Limnology and Oceanography*, 20(6):953–961.

Vanderborght, J.-P., Wollas, R., and Bitten, G. (1977). Kinetic models of diagenesis in disturbed sediments. Part 2. Nitrogen diagenesis. *Limnology and Oceanography*, 22(5):794–803.

Vecsei, A. (2004). A new estimate of global reefal carbonate production including the fore-reefs. *Global and Planetary Change*, 43(1-2):1–18.

Voigt, S., Gale, A. S., and Voigt, T. (2006). Sea-level change, carbon cycling and palaeoclimate during the Late Cenomanian of northwest Europe; an integrated palaeoenvironmental analysis. *Cretaceous Research*, 27(6):836–858.

Volk, T. and Hoffert, M. I. (1985). Ocean carbon pumps : Analysis of relative strengths and efficiencies in ocean-driven atmospheric CO_2 changes. In Sundquist, E. T. and Broecker, W. S., editors, *The Carbon Cycle and Atmospheric CO_2 : Natural Variations Archean to Present*, volume 32 of *Geophys. Monogr. Ser.*, pages 99–110. AGU, Washington, DC.

Volta, C., Arndt, S., Savenije, H. H. G., Regnier, P., and Laruelle, G. G. (2014). C-GEM (v 1.0): A new, cost-efficient biogeochemical model for estuaries and its application to a funnel-shaped system. *Geoscientific Model Development, 7 (4), 2014*.

Wagener, T. and Gupta, H. V. (2005). Model identification for hydrological forecasting under uncertainty. *Stochastic Environmental Research and Risk Assessment*, 19(6):378–387.

Wakeham, S. G., Hedges, J. I., Lee, C., Peterson, M. L., and Hernes, P. J. (1997). Compositions and transport of lipid biomarkers through the water column and surficial sediments of the equatorial pacific ocean. *Deep Sea Research Part II: Topical Studies in Oceanography*, 44(9–10):2131–2162.

Wakeham, S. G., Sinninghe Damsté, J. S., Kohnen, M. E. L., and De Leeuw, J. W. (1995). Organic sulfur compounds formed during early diagenesis in Black Sea sediments. *Geochimica et Cosmochimica Acta*, 59(3):521–533.

Walker, J. C. G. and Opdyke, B. C. (1995). Influence of variable rates of neritic carbonate deposition on atmospheric carbon dioxide and pelagic sediments. *Paleoceanography*, 10(3):415–427.

Wallmann, K. (2001). Controls on the cretaceous and cenozoic evolution of seawater composition, atmospheric CO2 and climate. *Geochimica et Cosmochimica Acta*, 65(18):3005–3025.

Wallmann, K. (2003). Feedbacks between oceanic redox states and marine productivity: A model perspective focused on benthic phosphorus cycling. *Global Biogeochemical Cycles*, 17(3):1084.

Wang, Y. and Van Cappellen, P. (1996). A multicomponent reactive transport model of early diagenesis: Application to redox cycling in coastal marine sediments. *Geochimica et Cosmochimica Acta*, 60(16):2993–3014. 00283.

Washington, W. M. and Parkinson, C. C. L. (2005). *An introduction to three-dimensional climate modeling*. University Science Books.

Weber, T., Cram, J. A., Leung, S. W., DeVries, T., and Deutsch, C. (2016). Deep ocean nutrients imply large latitudinal variation in particle transfer efficiency. *Proceedings of the National Academy of Sciences*, 113(31):8606–8611.

Wenzhöfer, F. and Glud, R. N. (2002). Benthic carbon mineralization in the Atlantic: a synthesis based on in situ data from the last decade. *Deep Sea Research Part I: Oceanographic Research Papers*, 49(7):1255–1279.

Werne, J. P., Hollander, D. J., Behrens, A., Schaeffer, P., Albrecht, P., and Sinninghe Damsté, J. S. (2000). Timing of early diagenetic sulfurization of organic matter: a precursor-product relationship in Holocene sediments of the anoxic Cariaco Basin, Venezuela. *Geochimica et Cosmochimica Acta*, 64(10):1741–1751.

Werne, J. P., Hollander, D. J., Lyons, T. W., and Sinninghe Damsté, J. S. (2004). Organic sulfur biogeochemistry: Recent advances and future research directions. In *Special Paper 379: Sulfur Biogeochemistry - Past and Present*, volume 379, pages 135–150. Geological Society of America. DOI: 10.1130/0-8137-2379-5.135.

Werne, J. P., Lyons, T. W., Hollander, D. J., Schouten, S., Hopmans, E. C., and Sinninghe Damsté, J. S. (2008). Investigating pathways of diagenetic organic matter sulfurization using compound-specific sulfur isotope analysis. *Geochimica et Cosmochimica Acta*, 72(14):3489–3502.

Wilson, J. D., Barker, S., and Ridgwell, A. (2012). Assessment of the spatial variability in particulate organic matter and mineral sinking fluxes in the ocean interior: Implications for the ballast hypothesis. *Global Biogeochemical Cycles*, 26(4).

Winguth, A. M. E., Thomas, E., and Winguth, C. (2012). Global decline in ocean ventilation, oxygenation, and productivity during the Paleocene-Eocene Thermal Maximum: Implications for the benthic extinction. *Geology*, 40(3):263–266.

Wolf-Gladrow, D. A., Zeebe, R. E., Klaas, C., Körtzinger, A., and Dickson, A. G. (2007). Total alkalinity: The explicit conservative expression and its application to biogeochemical processes. *Marine Chemistry*, 106(1-2):287–300.

Yamanaka, Y. and Tajika, E. (1996). The role of the vertical fluxes of particulate organic matter and calcite in the oceanic carbon cycle: Studies using an ocean biogeochemical general circulation model. *Global Biogeochemical Cycles*, 10(2):361–382.

Yamanaka, Y. and Tajika, E. (1997). Role of dissolved organic matter in the marine biogeochemical cycle: Studies using an ocean biogeochemical general circulation model. *Global Biogeochemical Cycles*, 11(4):599–612.

Yool, A., Popova, E. E., and Anderson, T. R. (2011). Medusa-1.0: a new intermediate complexity plankton ecosystem model for the global domain. *Geosci. Model Dev.*, 4(2):381–417.

Zachos, J. C., Röhl, U., Schellenberg, S. A., Sluijs, A., Hodell, D. A., Kelly, D. C., Thomas, E., Nicolo, M., Raffi, I., Lourens, L. J., McCarren, H., and Kroon, D. (2005). Rapid Acidification of the Ocean During the Paleocene-Eocene Thermal Maximum. *Science*, 308(5728):1611–1615.

Zeebe, R. E. (2012). LOSCAR: Long-term Ocean-atmosphere-Sediment CArbon cycle Reservoir model v2.0.4. *Geosci. Model Dev.*, 5(1):149–166.

Zeebe, R. E., Ridgwell, A., and Zachos, J. C. (2016). Anthropogenic carbon release rate unprecedented during the past 66 million years. *Nature Geoscience*, 9(4):325–329.

Zeebe, R. E. and Wolf-Gladrow, D. (2001). *CO2 in Seawater: Equilibrium, Kinetics, Isotopes: Equilibrium, Kinetics, Isotopes*. Elsevier.

Zeebe, R. E. and Zachos, J. C. (2007). Reversed deep-sea carbonate ion basin gradient during Paleocene-Eocene thermal maximum. *Paleoceanography*, 22(3):PA3201.

Zeebe, R. E. and Zachos, J. C. (2013). Long-term legacy of massive carbon input to the Earth system: Anthropocene versus Eocene. *Philosophical Transactions of the Royal Society of London A: Mathematical, Physical and Engineering Sciences*, 371(2001):20120006.

Zeebe, R. E., Zachos, J. C., and Dickens, G. R. (2009). Carbon dioxide forcing alone insufficient to explain Palaeocene-Eocene Thermal Maximum warming. *Nature Geoscience*, 2(8):576–580.

Zickfeld, K., Eby, M., Weaver, A. J., Alexander, K., Crespin, E., Edwards, N. R., Eliseev, A. V., Feulner, G., Fichefet, T., Forest, C. E., Friedlingstein, P., Goosse, H., Holden, P. B., Joos, F., Kawamiya, M., Kicklighter, D., Kienert, H., Matsumoto, K., Mokhov, I. I., Monier, E., Olsen, S. M., Pedersen, J. O. P., Perrette, M., Philippon-Berthier, G., Ridgwell, A., Schlosser, A., Schneider Von Deimling, T., Shaffer, G., Sokolov, A., Spahni, R., Steinacher, M., Tachiiri, K., Tokos, K. S., Yoshimori, M., Zeng, N., and Zhao, F. (2013). Long-Term Climate Change Commitment and Reversibility: An EMIC Intercomparison. *Journal of Climate*, 26(16):5782–5809.